Diagnostic and Therapeutic MEMS (Micro-Electro-Mechanical Systems) Devices for the Identification and Treatment of Human Disease

by

Jennie Hewitt Appel Podlevsky

A Dissertation Presented in Partial Fulfillment
of the Requirements for the Degree
Doctor of Philosophy

Approved April 2018 by the
Graduate Supervisory Committee:

Junseok Chae, Chair
Michael Goryll
Michael Kozicki
Mehdi Nikkhah

ARIZONA STATE UNIVERSITY

May 2018

ABSTRACT

Early detection and treatment of disease is paramount for improving human health and wellness. Micro-scale devices promote new opportunities for the rapid, cost-effective, and accurate identification of altered biological states indicative of disease early-onset; these devices function at a scale more sensitive to numerous biological processes. The application of Micro-Electro-Mechanical Systems (MEMS) in biomedical settings has recently emerged and flourished over course of the last two decades, requiring a deep understanding of material biocompatibility, biosensing sensitively/selectively, biological constraints for artificial tissue/organ replacement, and the regulations in place to ensure device safety. Capitalizing on the inherent physical differences between cancerous and healthy cells, our ultra-thin silicone membrane enables earlier identification of bladder cancer—with a 70% recurrence rate. Building on this breakthrough, we have devised an array to multiplex this sample-analysis in real-time as well as expanding beyond bladder cancer. The introduction of new materials—with novel properties—to augment current and create innovative medical implants requires the careful analysis of material impact on cellular toxicity, mutagenicity, reactivity, and stability. Finally, the achievement of replacing defective biological systems with implanted artificial equivalents that must function within the same biological constraints, have consistent reliability, and ultimately show the promise of improving human health as demonstrated by our hydrogel check valve. The ongoing proliferation, expanding prevalence, and persistent improvement in MEMS devices through greater sensitivity, specificity, and integration with biological processes will undoubtedly bolster medical science with novel MEMS-based diagnostics and therapeutics.

Dedicated to my family whose love and support made all of this possible.

My husband, Joshua Podlevsky; my brothers, David Appel, Phillip Nalwalker, and Jeremy Nalwalker; my sister Kaitlyn Romero; my stepmom Marla Eva; my mother-in-law Helen Podlevsky; my godmother Jane McGriff; my mother Kim McRae and my father, Arthur Appel.

ACKNOWLEDGMENTS

I am grateful for my fellow lab members and their continuous and insightful discussion, the myriad of undergraduates who exchanged untold hours of persistent and monotonous work for practical laboratory training, and my advisor who kept me in line and demanded high quality work and creative solutions (instead of ever allowing for the easy way out).

I would like to thank Drs. Michael Goryll, Michael Kozicki, and Mehdi Nikkhah for serving as my committee, enhancing my knowledge/skillsets by their thoughtful consideration and critic of my research.

I would also like to thank CSSER personal, especially Carrie Sinclair, Todd Eller, and Stefan Myhajlenko, for their thoughtful guidance, creative solutions and willingness to explore unconventional techniques. Additionally, Dr. Liao and his research team for their inclusive and welcoming research environment and for answering my numerous questions on bladder cancer.

I wish to thank the National Science Foundation for the funding which made this work possible as well as the selection committees for the Fulton foundation, ARCS foundation, international switching symposium, and the Dean's fellowship for their generous support of my research pursuits.

TABLE OF CONTENTS

Page

APPENDIX Page

LIST OF TABLES

Table Page

LIST OF FIGURES

Figure Page

Figure Page

CHAPTER 1

INTRODUCTION

1.1. Micro Electro Mechanical Systems: the Rise of Micro-Technology

In 1959 Nobel laureate, Richard Feynman, gave his legendary talk “There is Plenty of Room at the Bottom”, his overarching theme—what is possible when we can manipulate matter at the atomic scale (Feynman, 1959). He challenged his audience to imagine a car no longer than a millimeter or an encyclopedia written on the tip of a pen. In the hopes that these challenges would aspire new techniques for interacting with the microscopic world he even offered financial compensation to the first people who accomplished those goals. While one of these goals, the millimeter car, was achieved by conventional means by a highly skilled craftsman within a few months, the other was nearly forgotten until the development of electron beam lithography, nearly 15 years later. While these challenges did not spur the development of novel microscale manufacturing techniques as Dr. Feynman had intended. The development of the silicon processing industry effectively prompted both the integrated circuit and micro electro mechanical systems (MEMS)(Ko, 2007). Integrated circuitry required advanced understanding of the manipulation of silicon in order to dope, pattern, and etch surfaces to form transistors. Additionally, the scaling down of transistors with the advancement of batch fabrication techniques set the stage for further development within silicon processing.

Silicon was initially thought to be a brittle and unwieldy mechanical material, however, in 1982 Petersen published a comprehensive review effectively negating that opinion and introducing the field of MEMS(Petersen, 1982). While the term MEMS is

not universal it generally refers to microscale devices fabricated using silicon processing techniques and includes micromachining, bulk, and surface machining. More specifically, techniques such as photolithography, thin-film deposition, chemical vapor deposition, thermal growth, wet etching, and deep reactive ion etching are integrated together to yield a wide variety of microscale sensors and actuators. MEMS devices operate using two underlying principles either an electrical input results in a physical action—an actuator—or a physical action results in an electrical output—a sensor (figure 1.1.). Often MEMS devices cannot be simply classified as either a sensor or an actuator, they often combine these concepts into a fully integrated system.

MEMS devices have infiltrated numerous aspects of modern society, vehicles, projection systems, telecommunications, inkjet printing, and even biomedical applications (Eddy & Sparks, 1998; Ko, 2007; Takaki, Takenaka, Morimoto, Konuma, & Hirabayashi, 2012). The devices used in these industries typically have the smallest component range from 1 to 100 μm (figure 1.2.). When scaling devices from a macro—typically meters long—to microscale the underlying physics shifts where capillary, stiction, and electrostatic forces have significantly more impact that inertial forces. This can be highly advantageous or lead to cautious device release techniques. Often capillary forces are large enough at the micro/nanoscale to allow for flow without external pump systems. Conversely, when releasing MEMS devices using liquids stiction often leads to the collapse of suspended structures such as cantilever beams, but this can be avoided with thoughtful preparation and the use of supercritical CO_2 techniques. Furthermore, electrostatic actuation allows for the simple application of a voltage differential to induce the movement of a micro-mirror in optical MEMS. Coupled with the traditional

advantages seen in the semiconductor industry, low lost mass production and high yield MEMS devices have become a key feature in numerous modern technologies.

1.2. Biomedical MEMS: More Than the Sum of Its Parts

Techniques commonly combined in biomedical MEMS were used as early as 1967 by Carter *et al*. however, the field itself slowly gained traction and became independent in the early 1990s. This early work used thermally evaporated islands of palladium to explore cell spreading and cell membrane formation; capitalizing on traditional silicon processing techniques to understand biological concepts (Carter, 1967). This work was expanded upon using micro-fabricated groves to encourage directional cell growth (Brunette, 1986). Furthermore, the use of MEMS technology to understand cellular mechanics continued with the development of microscale cantilevers, microneedle arrays, and atomic force microscopy all examining cell-substrate interactions (Galbraith & Heetz, 1997; Małgorzata Lekka et al., 2012; Tan et al., 2003). The underlying principles of both micro-cantilevers and micro-needle arrays are very similar. When cells adhere to either they spread, ultimately bending the structures; given the known dimensions and flexibility of these substrates the resulting cell traction forces are easily derived. These early devices employed microfabrication techniques in order to examine cellular phenomenon. However, the field of biomedical MEMS has expanded beyond this initial iteration to not only examine cell-based mechanisms but explore bio-sensing, organ modeling, DNA sequencing, disease diagnosis, and treatment.

Often bio-sensing and disease diagnosis operate concurrently, where a biosensor detects a biomarker for a specific disease. The earliest MEMS chemical sensors, 1979, were gas chromatography systems using micro-fabricated fluidic systems to differentiate

and isolate various particles in gaseous form. In this work they hypothesize further applications toward implantable biomedical devices (Terry, Jerman, & Angell, 1979). This early suggestion of combining silicon fabrication techniques toward a biological sensor could be considered the first biomedical MEMS device. This pioneering research spurred the interdisciplinary combination of fluidics, microbiology, material science and engineering to generate a wide variety of biomedical MEMS devices in the form of lab-on-a-chip, and micro total analysis systems (micro-TAS). Further development has led to resonators (film bulk acoustic (W. Xu, Appel, Chae, & Member, 2012), surface acoustic wave (Voiculescu & Nurashikin, 2012), quartz crystal (Marx, 2003), etc.) using mass or viscosity induced resonance change, optical (fluorescent (Hastie et al., 2013), light quenching (X. Sun et al., 2017)) induced changes, electrochemical (potentiometric (Qu, Xia, Bian, Sun, & Han, 2009))induced changed all selectively triggered by the presence of disease specific biomarkers (figure 1.3.).

However, bio-sensing can also expand beyond disease diagnosis to provide physicians valuable data regarding blood oxygen levels, and intraocular or aortic pressure. Often these devices are either implantable or wearable. Devices measuring blood oxygen, have been in the medical field since the early 1940s however they were often unstable due to early light sources, use at the ear, and low accuracy (Millikan, 1942). But with the advent of silicon processing and MEMS technology, these optical sensors were drastically improved and integrated into modern medicine. Currently, a similar optical technique is being pursued as a microscale implant (Fiala, Bingger, Foerstert, Heilmann, & Beyersdorti, 2010; Theodor et al., 2014). Interestingly, implantable intraocular pressure sensors were in development before the wide adoption

of silicon processing techniques, (figure 1.4.) (Collins, 1967). In 1967, Collins reported the development of diameter bubble tonometer (in the range 2 - 6 mm) and their success monitoring the intraocular pressure of rabbits for over a year (Collins, 1967). While these devices were fabricated using traditional, non-silicon processing based, techniques they did prompt the development and interest of the MEMS community inspiring the development of sensor embedded contact lenses for continuous intraocular pressure measurement (Cooper, Beale, & Constable, 1979; Greene & Gilman, 1974; M. Leonardi, Leuenberger, Bertrand, Bertsch, & Renaud, 2003; Matteo Leonardi, Pitchon, Bertsch, & Renaud, 2009), ultimately leading to device commercialization and approval by the United States Food and Drug Administration (FDA) (Dunbar, Shen, & Aref, 2017). While these devices are not traditionally considered bio-sensors they have become a subset of the biomedical MEMS field that is rapidly expanding into commercial applications.

Another contribution to the biomedical MEMS field is the subfield of "organ-on-a-chip", similar to lab-on-a-chip concepts where cells can be studied on an individual basis, the organ-on-a-chip concept attempts to understand organ function in a well-controlled in vitro model(Perestrelo, Águas, Rainer, & Forte, 2015). However, before organ-on-a-chip can be fully appreciated the development of polydimethylsiloxane (PDMS) based microfluidics must be introduced. PDMS is a transparent, non-toxic, biocompatible, gas permeable, polymer (Mata, Fleischman, & Roy, 2005), which is ubiquitous within biomedical MEMS. Generally, silicon wafers, post-micromachining, are used as PDMS molds to form microfluidic, pillar, or other complex structures (Duffy, Mcdonald, Schueller, & Whitesides, 1998; McDonald et al., 2000; Qin, Xia, &

Whitesides, 1996). PDMS microfluidics led to the development of the first organ-on-a-chip, a lung-on-a-chip microsystem which induced cyclic mechanical strain on cells cultured within the device and modeled the impact of "breathing" airborne nanoparticles (Huh et al., 2010). Other organ-on-a-chip concepts include the modeling of arteries (Yasotharan, Pinto, Sled, Bolz, & Günther, 2015), kidney function (Wilmer et al., 2016), neurovascular systems (Alcendor et al., 2013), ocular drug treatments (Dodson, Echevarria, Li, Sappington, & Edd, 2016) and even modeling occlusion-based failure modes for hydrocephalus shunts (C. Harris, Pearson, Hadley, & Zhu, 2015). Generally, these projects aim to closely emulate physiological conditions to improve and reduce costs associated with drug screening or toxicology studies as well as expand understanding of complex organ systems and diseases.

Microfluidics has become synonymous with biomedical MEMS and DNA sequencing was one of the early applications of microfluidics and has become a competitive commercial application. A commercial application of particular interest to the biomedical MEMS community is the techniques developed by BioNano Genomics (Hastie et al., 2013). They developed a micro/nano fluidic array designed to linearized pre-treated DNA fragments for visualization using fluorescent microscopy. This array is fabricated using an innovative shadow mask protocol to get pillars in a size gradient before the nanofluidic channels to effectively linearize the DNA strands (Cao, Tegenfeldt, Austin, & Chou, 2002; Cao, Yu, et al., 2002; Tegenfeldt et al., 2004). Other capillary electrophoresis techniques have integrated MEMS technology in fabricating their capillary channels (Harrison et al., 1993; Harrison, Manz, Fan, & Widmer, 1992; Simpson et al., 1998; J. Wang, Chatrathi, Tian, & Polsky, 2000) as well as the

development of nano-pore based sequencing which aims to “thread” DNA through a 1 to 10 nm pore (Jain et al., 2018). An ionic current flows across the nano-pore, as a DNA strand is threaded through the pore the ionic current varies in response to the DNA sequence giving a specific change in current for each molecule (Jain et al., 2018). Microfluidics and therefore, biomedical MEMS is essential to modern DNA sequencing and has led to the development of numerous companies which rely upon capillary chips to provide valuable sequencing data.

Biomedical MEMS therapeutics can generally be considered biosensors, however these biosensors aim to not only sense biological abnormalities but counteract them. This is demonstrated by the concept of an artificial pancreas—which has been partially achieved by continuous glucose monitoring systems—an implanted glucose sensing element detects an increase in glucose levels, this information is sent to an external insulin pump which then injects insulin to counteract the increased glucose levels. One such device being produced by Glysens Inc. is a wireless implantable continuous glucose monitoring system (Lucisano, Routh, Lin, & Gough, 2017). This device employs an array of platinum electrodes with corresponding silver/silver chloride reference electrodes to monitor the two-step enzymatic reaction of glucose oxidase and catalase which is compared to an oxygen sensing reference (Gough, Kumosa, Routh, Lin, & Lucisano, 2010; Gough et al., 2003). This device is still in preliminary human trials and with continued success should be approved for continuous glucose monitoring. CardioMEMS Inc. employs a similar MEMS therapeutic based on one of the earliest MEMS devices, a membrane pressure sensor, strategically coupled to wireless technology and placed within the pulmonary artery to monitor blood pressure at that specific location (Potkay,

2008). This device has been approved by the FDA for human use, and provides life-saving blood pressure information to physicians to detect worsening heart failure before the onset of symptoms allowing for the adjustment of medications to improve overall patient outcomes(Abraham et al., 2011) (Abraham et al., 2016). Other such implantable systems aim to integrate MEMS sensing technology such as hydrocephalus shunts coupled to MEMS intracranial pressure sensors (B. J. Kim et al., 2016) and nanoparticle drug delivery schemes (Meng & Sheybani, 2014) to directly provide medication at tumor sites. These devices are still in development; however, they have the potential to transform the medical industry and the regulation system surrounding it.

1.3. Medical Devices and the FDA: the Path to an Implantable Device

In the early 1960s, intrauterine devices (IUDs) were under development in the United States and being used internationally. At this time, all medical devices ranging from contact lenses to surgical thread, were unregulated. IUDs were designed to induce foreign body response at the entrance to the uterus, which would in turn, reduce the rate of conception. It was hypothesized that a larger contact surface area would induce an even greater foreign body response and improve the overall device functionality, the Dalkon Shield was conceived. In 1971, this device was introduced to the general public and an aggressive marketing campaign lead to approximately 2.2 million devices sold in the United States and 1.7 million internationally (Roepke & Schaff, 2014).

Within three years, studies were published citing the Dalkon Shield induced pelvic infections, septic abortions and death. In particular, noting that the material chosen for the string, effectively wicked bacteria into the uterus leading to an increased infection rate. In 1975 the FDA formally cited the string as a hazard (Roepke & Schaff, 2014) and

Dalkon Shields stopped being sold however no device recall was issued, and devices were still marketed internationally. Later studies determined that the Dalkon Shield induced at least ten thousand adverse events, ranging from pelvic infections to septic abortions, hysterectomies and at least 18 deaths (Roepke & Schaff, 2014). This directly led to an amendment of the Food, Drug, and Cosmetic Act of 1938, the Medical Device Regulation Act (Roepke & Schaff, 2014). This act established the classification of medical devices, the establishment of quality and functionality standards, and the requirement of pre-market approval depending on the classification of the device in question.

This amendment, expanding the FDA regulatory power to include medical devices, radically changed the research and development of diagnostic and therapeutic devices. Prior to the 1976 medical device regulation act, implanted devices were simply researched, developed, and manufactured. Clinical trials were performed but not necessary to market and sell medical devices, even implantable devices. After the medical device regulation act passed all medical devices were classified based on the amount of risk associated with each device. Class 1 devices, such as dental floss, are the least risky devices and require the least amount of regulatory controls. Class 2 devices, such as condoms, require greater regulation to ensure device safety and effectiveness. Finally, class 3 devices, such as replacement heart valves, require the most regulation with devices being evaluated by the FDA before marketing.

The ramifications of the medical device regulation act on the research and development of implantable medical devices has shifted the overall industry away from an academic environment towards the private sector. This shift has immensely altered a

device's path to market. The FDA provides oversight of the medical device industry and the research required to implant devices in human patients. This necessitates a balance within the field of medical devices between academic research and industry device development. Rarely do academic researchers take a FDA regulated device from conception to market. A few exceptions to this rule are the biomedical MEMS companies CardioMEMS, which was the first implantable MEMS pressure sensor and BioNano Genomics, a micro / nano fluidics structure which enables the sequencing of long strands of DNA to better map genomes.

1.4. Material Biocompatibility: a Vital Step Towards Implantable Devices

History has shown, time and again, the toxic effect of neglecting or misunderstanding material biocompatibility. Lead, mercy, silver, and even radium were found in occupational environments or commercial products leading to plumbism (lead), mad hatter's disease (mercy), argyria (silver) and tumor growth (radium) (W. R. Lee, 1968; Nowack, Krug, & Height, 2011; Tsatalis et al., 2017). These historical examples show the significance of evaluating material biocompatibility particularly when designing implantable devices. While there are numerous definitions of biocompatibility, the most widely excepted version states that a biocompatible material will induce a known and predicable biological response when tested. This can range from bio-inert materials such as cobalt-chrome alloys (Navarro, Michiardi, Castan, & Planell, 2008), which do not induce any biological response to bio-degradable materials, calcium phosphate, which induce a specific and well characterized biological response (Amini, Wallace, & Nukavarapu, 2011). Evaluating newly developed materials has become both a regulatory and scientific pursuit. Many regulatory agencies including the FDA and the

environmental protection agency enact public policy for both occupational and medicinal hazards which impact human exposure to toxic materials. Furthermore, biocompatibility is fascinating from a scientific perspective as the fields of nanomaterials and biology converge.

Regulation and material biocompatibility couple in the form of standards. Both the International Standards Organization and the American Society for Testing and Materials have extensive biocompatibility determination protocols. These range from irritant testing to in vitro cell culture methods to subcutaneous or full implantation-based evaluations. This comprehensive look at material biocompatibility also encourages exploration of the mechanisms behind geno- or cytotoxicity, as well as the systemic examination of material degradation. This systemic approach investigates how a biological environment breaks down materials and the impact of degradation on secondary and tertiary organ systems such as the liver or kidneys, which typically filter small particles out of the blood stream. While the aforementioned standards provide a vital reference point, they are only the starting point of determining biocompatibility.

Bulk materials normally known to be innocuous can become toxic when shape, size, or surface charge change (Jiang, Kim, Rutka, & Chan, 2008). Thus, the biocompatibility of nanoscale spheres, sheets, and tubes of various materials have been studied since the early 1970s (Couvreur, Tulkens, Roland, Trouet, & Speiser, 1977). For example despite being generally considered fully biocompatible gold can become toxic if in the form of less than 1.4 nm spherical particles (Alkilany & Murphy, 2010; Pan et al., 2009). Similarly, conflicting reports of graphene and graphene oxide toxicity varies based on if the materials are fixed onto a substrate or allowed to float freely. In the first case

these materials are generally found to be biocompatible (G. Y. Chen, Pang, Hwang, Tuan, & Hu, 2012), however in the second case, these atomically thin sheets can effectively slice cell membranes making free floating graphene highly toxic (K.-h. Liao, Y.-s. Lin, C. W. Macosko, & C. L. Haynes, 2011). Nano-rods or tubes have also been investigated in terms of biocompatibility and found toxic in specific concentrations and dimensions (Pardo, Shuster-Meiseles, Levin-Zaidman, Rudich, & Rudich, 2014; Z. Sun et al., 2011). These distinctions have led to numerous conflicting reports which have only increased as some of the traditional methods of examining cultured cell viability have also been shown to be susceptible to interference by nanoparticles.

Gross cellular viability is typically evaluated using commercially available reagents and protocols. These generally come in the form of colorimetric assays which respond to changes in cellular processes. Two of the most common are methylthiazolyldiphenyl-tetrazolium bromide (MTT) and water-soluble tetrazolium salt (WST-8). These assays rely on extracellular dehydrogenases to induce color change, however, both assays are susceptible to nanoparticle interference, particularly the MTT assay is often inaccurate if carbon based nanoparticles are being evaluated (Teo, Chng, Sofer, & Pumera, 2014). As these are somewhat indirect measures of cellular viability other commercial protocols rely on dual-fluorescent binding to either viable cell membranes (calcein-acetoxymethyl) or exposed cell nuclei (ethidium homodimer-1). Mechanistic cell viability can be examined by investigating apoptotic or necrotic triggers for cell death. One such mechanism is reactive oxygen species formation, in excess, reactive oxygen species can lead to either cell death pathway, however it is necessary in small amounts for cell signaling. After cellular viability is established more holistic

evaluations can be performed through the use of irritant, subcutaneous, and animal implantation testing.

1.5. Bioengineering: Devices to Replace Organs, a Hydrocephalus Example

Diseases and ageing can be considered degradation of a biological system, from an engineering standpoint we can replace this degradation with an improved non-biological implant, simply replace an arthritic hip with a prosthesis. In some cases these replacements can even improve upon the natural design (Lechler & Lilja, 2008). Other situations spur from disease, requiring devices to bypass defective regions or replace organ function. This will be exemplified by the case of hydrocephalus shunts and alternative treatments which will be addressed in more detail in chapter 5. In order to design a treatment, we must first understand the biological context surrounding the disease state. In the case of hydrocephalus there is a flaw in the cerebrospinal fluid (CSF) flow pathway which leads to an accumulation of CSF within the brain. This flaw, in certain types of hydrocephalus, is in the arachnoid granulations—biological one-way valves which regulate CSF flow from the intracranial space into the superior sagittal sinus. Historically this disease was treated by simply drilling a hole in the skull and draining excess CSF (Aschoff, Kremer, Hashemi, & Kunze, 1999; Khamlichi, 1998). At the time there was not a sterile method of performing this technique and mortality rates are assumed to be near 100% until the 1890s. This method of simply removing excess fluid became the norm until the 1950s when implantable shunt systems were developed to regulate CSF flow internally.

In the case of hydrocephalus, the disease state is straightforward, this allows for system modeling. There has been much progress in understanding the complex fluid

dynamic behavior within the intracranial space. The greatest insights have been provided by computational models derived from magnetic resonance imaging (MRI) scans of both healthy controls and hydrocephalic patients. These models reveal the complex interplay of fluid across the brain, the ventricles, and subarachnoid space (Buishas, Gould, & Linninger, 2014; Andreas A. Linninger, Sweetman, & Penn, 2009; Andreas A Linninger et al., 2005; Sweetman & Xenos, 2011). While these computational models provide important insights, it has remained difficult to apply these models to physical device testing conditions for the interface of the subarachnoid space and superior sagittal sinus. Several research groups have pursued bench top phantom models of CSF flow. These models are gross depictions of intracranial fluids dynamics. Of these physical models, the most advanced and physiologically relevant has come from the 'Interface Group' based out of the University of Zurich. Their initial attempt was a life size model of the intracranial space that includes the brain, ventricles, and subarachnoid space(Bottan, Poulikakos, & Kurtcuoglu, 2012; Bottan et al., 2013). This model has been used to mimic the intracranial pressures observed in healthy individuals, the CSF flow pattern produced by the ventricles and the resulting localized normal pressure in the subarachnoid space (Bottan et al., 2012; Bottan et al., 2013). Their more recent bench top model more closely mimics the effects of body orientation on hydrocephalus shunt system performance, particularly investigating cases of over drainage (Gehlen, Kurtcuoglu, & Daners, 2016). In addition to modeling, we can also examine healthy tissues to understand the design parameters vital to restoring CSF flow.

After the system is fully understood, a design to replace the malfunctioning organ, in this case, arachnoid granulations can be pursued. Accurately replicating the function of

arachnoid granulations is the ultimate goal of treating hydrocephalus. The flow-pressure characteristics for functioning arachnoid granulations resembles the current-voltage characteristics of diodes with a forward current applied. When the ‘threshold voltage’ or cracking pressure is reached, flow through the arachnoid granulation starts and when that flow is reversed the AG remains closed with little to no leakage. Grzybowski *et al*. reported this unidirectional flow of extracted arachnoid granulations. High fluidic conductivity was measured when following the natural CSF flow pathway from the subarachnoid space to the superior sagittal sinus. While reversing the natural flow pathway, a very low fluidic conductivity corresponding to near zero flow was measured (Grzybowski, Holman, Katz, & Lubow, 2006). With this understanding of arachnoid granulation function, the development of devices which mimic that function can begin.

Abraham, W. T., Adamson, P. B., Bourge, R. C., Aaron, M. F., Costanzo, M. R., Stevenson, L. W., & Strickland, W. (2011). Wireless pulmonary artery haemodynamic monitoring in chronic heart failure : a randomised controlled trial. Lancet, 377, 658-666. doi:10.1016/S0140-6736(11)60101-3

Abraham, W. T., Stevenson, L. W., Bourge, R. C., Lindenfeld, J. A., Bauman, J. G., & Adamson, P. B. (2016). Sustained efficacy of pulmonary artery pressure to guide adjustment of chronic heart failure therapy : complete follow-up results from the CHAMPION randomised trial. The Lancet, 387, 453-461. doi:10.1016/S0140-6736(15)00723-0

Alcendor, D. J., Block III, F. E., Cliff, D. E., Daniels, J. S., Ellacott, K. L. J., Goodwin, C. R., . . . Wikswo, J. P. (2013). Neurovascular unit on a chip : implications for translational applications. Stem Cell Research and Therapy, 4, 1-5.

Alkilany, A. M., & Murphy, C. J. (2010). Toxicity and cellular uptake of gold nanoparticles : what we have learned so far ? Journal of nanoparticle research, 12, 2313-2333. doi:10.1007/s11051-010-9911-8

Amini, A. R., Wallace, J. S., & Nukavarapu, S. P. (2011). Short-Term and Long-Term Effects of Orthopedic Biodegradable Implants. Journal of Long Term Effects of Medical Implants, 21, 93-122.

Aschoff, A., Kremer, P., Hashemi, B., & Kunze, S. (1999). The scientific history of hydrocephalus and its treatment. neurosurgical Review, 22, 67-93.

Bottan, S., Poulikakos, D., & Kurtcuoglu, V. (2012). Phantom model of physiologic intracranial pressure and cerebrospinal fluid dynamics. IEEE Transactions on Biomedical Engineering, 59, 1532-1538. doi:10.1109/TBME.2012.2187448

Bottan, S., Schmid Daners, M., de Zelicourt, D., Fellner, N., Poulikakos, D., & Kurtcuoglu, V. (2013). Assessment of intracranial dynamics in hydrocephalus: effects of viscoelasticity on the outcome of infusion tests. Journal of neurosurgery, 119, 1511-1519. doi:10.3171/2013.8.JNS122497

Brunette, D. M. (1986). Fibroblasts on Micromachined Substrata Orient Hierarchically to Grooves of Different Dimensions. Experimental cell research, 164, 11-26.

Buishas, J., Gould, I. G., & Linninger, A. A. (2014). A computational model of cerebrospinal fluid production and reabsorption driven by Starling forces. Croatian medical journal, 55, 481-497. doi:10.3325/cmj.2014.55.481

Cao, H., Tegenfeldt, J. O., Austin, R. H., & Chou, S. Y. (2002). Gradient nanostructures for interfacing microfluidics and nanofluidics. Applied Physics Letters, 81, 3058-3060. doi:10.1063/1.1515115

Cao, H., Yu, Z., Wang, J., Tegenfeldt, J. O., Austin, R. H., Chen, E., . . . Chou, S. Y. (2002). Fabrication of 10 nm enclosed nanofluidic channels. Applied Physics Letters, 81, 2002-2004. doi:10.1063/1.1489102

Carter, S. B. (1967). A Method of Confining Single Cells to Study Individual Cell Reactions and Clone Formation. Experimental cell research, 48, 189-193.

Chen, G. Y., Pang, D. W. P., Hwang, S. M., Tuan, H. Y., & Hu, Y. C. (2012). A graphene-based platform for induced pluripotent stem cells culture and differentiation. Biomaterials, 33, 418-427. doi:10.1016/j.biomaterials.2011.09.071

Collins, C. C. (1967). Miniature Passive Pressure Transensor for Implanting in the Eye. IEEE transactions on bio-medical engineering, 14, 74-83.

Cooper, R. L., Beale, D. G., & Constable, I. (1979). Passive radiotelemetry of intraocular pressure in vivo: calibration and validation of continual scleral guard-ring applanation transensors in the dog and rabbit. Investigative Ophthalmology and Visual Science, 18, 930-938.

Couvreur, P., Tulkens, P., Roland, M., Trouet, A., & Speiser, P. (1977). Nanocapsules: A New Type of Lysosomotropic Carrier. Federation of European Biochemical Societies Letters, 84, 0-3.

Dodson, K. H., Echevarria, F. D., Li, D., Sappington, R. M., & Edd, J. F. (2016). Retina-on-a-chip: a microfluidic platform for point access signaling studies. Biomedical Microdevices, 17. doi:10.1007/s10544-015-0019-x.Retina-on-a-chip

Duffy, D. C., Mcdonald, J. C., Schueller, O. J. A., & Whitesides, G. M. (1998). Rapid Prototyping of Microfluidic Systems in Poly(dimethylsiloxane). Analytical Chemistry, 70, 4974-4984.

Dunbar, G. E., Shen, B. Y., & Aref, A. A. (2017). The Sensimed Triggerfish contact lens sensor: efficacy, safety, and patient perspectives. Clinical Ophthalmology, 11, 875-882.

Eddy, D. S., & Sparks, D. R. (1998). Application of MEMS Technology in Automotive Sensors and Actuators. Proceedings of the IEEE.

Feynman, R. P. (1959). There's Plenty of Room at the Bottom: An Invitation to Enter a New World of Physics. In. American Physical Society.

Fiala, J., Bingger, P., Foerstert, K., Heilmann, C., & Beyersdorti, F. (2010). Implantable Sensor for Blood Pressure Determination via Pulse Transit Time. IEEE Sensors.

Galbraith, C. G., & Heetz, M. I. P. S. (1997). A micromachined device provides a new bend on fibroblast traction forces. Proceedings of the National Academy of Sciences of the United States of America, 94, 9114-9118.

Gehlen, M., Kurtcuoglu, V., & Daners, M. S. c. (2016). Patient Specific Hardware-in-the-Loop Testing of Cerebrospinal Fluid Shunt Systems. IEEE transactions on bio-medical engineering, 63, 348-358. doi:10.1109/TBME.2015.2457681

Gough, D. A., Kumosa, L. S., Routh, T. L., Lin, J. T., & Lucisano, J. Y. (2010). Function of an Implanted Tissue Glucose Sensor for More than 1 Year in Animals. Science Translational Medicine, 2.

Gough, D. A., Makale, M. T., Lin, J. T., Calou, R. E., Tsai, A. G., Chen, P. C., . . . Gough, D. A. (2003). Tissue window chamber system for validation of implanted oxygen sensors of implanted oxygen sensors. American Journal of Physiology - Heart and Circulatory Physiology, 284, H2288-H2294. doi:10.1152/ajpheart.00721.2002

Greene, M. E., & Gilman, B. G. (1974). Intraocular Pressure Measurement with Instrumented Contact Lenses. Investigative Ophthalmology, 13, 299-302.

Grzybowski, D. M., Holman, D. W., Katz, S. E., & Lubow, M. (2006). In vitro model of cerebrospinal fluid outflow through human arachnoid granulations. Investigative Ophthalmology and Visual Science, 47, 3664-3672. doi:10.1167/iovs.05-0929

Harris, C., Pearson, K., Hadley, K., & Zhu, S. (2015). Fabrication of three-dimensional hydrogel scaffolds for modeling shunt failure by tissue obstruction in hydrocephalus. Fluids and Barriers of …, 12, 1-15. doi:10.1186/s12987-015-0023-9

Harrison, D. J., Fluri, K., Seiler, K., Fan, Z., Effenhauser, C. S., & Manz, A. (1993). Micromachining a Miniaturized Capillary Electrophoresis-Based Chemical Analysis System on a Chip Published by : American Association for the Advancement of Science Stable URL : http://www.jstor.org/stable/2882118 Micromachining a Miniaturized Capillary El. Science (New York, N.Y.), 261, 895-897.

Harrison, D. J., Manz, A., Fan, Z., & Widmer, H. M. (1992). Capillary Electrophoresis and Sample Injection Systems. Analytical Chemistry, 64, 1926-1932. doi:10.1021/ac00041a030

Hastie, A. R., Dong, L., Smith, A., Finklestein, J., Lam, E. T., Huo, N., . . . Xiao, M. (2013). Rapid Genome Mapping in Nanochannel Arrays for Highly Complete and Accurate De Novo Sequence Assembly of the Complex Aegilops tauschii Genome. PLoS ONE, 8, e55864. doi:10.1371/journal.pone.0055864

Huh, D., Matthews, B. D., Mammoto, A., Montoya-Zavala, M., Hsin, H. Y., & Ingber, D. E. (2010). Reconstituting Organ-Level Lung Functions of a Chip. Science (New York, N.Y.), 328, 1662-1669.

Jain, M., Koren, S., Miga, K. H., Quick, J., Rand, A. C., Sasani, T. A., . . . Loose, M. (2018). Nanopore sequencing and assembly of a human genome with ultra-long reads. Nature Biotechnology. doi:10.1038/nbt.4060

Jiang, W., Kim, B. Y. S., Rutka, J. T., & Chan, W. C. W. (2008). Nanoparticle-mediated cellular response is size-dependent. Nature nanotechnology, 3, 145-150. doi:10.1038/nnano.2008.30

Khamlichi, A. E. (1998). African neurosurgery Part 1 Historical Outline. Surgical Neurology, 49, 222-227.

Kim, B. J., Jin, W., Baldwin, A., Yu, L., Christian, E., Krieger, M. D., . . . Meng, E. (2016). Parylene MEMS patency sensor for assessment of hydrocephalus shunt obstruction. Biomedical Microdevices, 18, 87. doi:10.1007/s10544-016-0112-9

Ko, W. H. (2007). Trends and frontiers of MEMS. Sensors and Actuators A, 136, 62-67. doi:10.1016/j.sna.2007.02.001

Lechler, K., & Lilja, M. (2008). Lower extremity leg amputation: an advantage in running ? Sports Technology, 1, 229-234. doi:10.1002/jst.57

Lee, W. R. (1968). The History of the Statutory Control of Mercury Poisoning in Great Britain. British Journal of Industrial Medicine, 25, 52-62.

Lekka, M., Gil, D., Pogoda, K., Dulińska-Litewka, J., Jach, R., Gostek, J., . . . Laidler, P. (2012). Cancer cell detection in tissue sections using AFM. Archives of biochemistry and biophysics, 518, 151-156. doi:10.1016/j.abb.2011.12.013

Leonardi, M., Leuenberger, P., Bertrand, D., Bertsch, A., & Renaud, P. (2003). A soft contact lens with a MEMS Strain Gage Embedded for Intraocular Pressure Monitoring. IEEE International Conference on Solid State Sensors, Actuators and Microsystems.

Leonardi, M., Pitchon, E. M., Bertsch, A., & Renaud, P. (2009). Wireless contact lens sensor for intraocular pressure monitoring : assessment on enucleated pig eyes. acta ophthalmologica, 87, 433-437. doi:10.1111/j.1755-3768.2008.01404.x

Liao, K.-h., Lin, Y.-s., Macosko, C. W., & Haynes, C. L. (2011). Cytotoxicity of Graphene Oxide and Graphene in Human Erythrocytes and Skin Fibroblasts. ACS Applied Materials and Interfaces, 3, 2607-2615. doi:10.1021/am200428v

Linninger, A. A., Sweetman, B., & Penn, R. (2009). Normal and hydrocephalic brain dynamics: The role of reduced cerebrospinal fluid reabsorption in ventricular enlargement. Annals of Biomedical Engineering, 37, 1434-1447. doi:10.1007/s10439-009-9691-4

Linninger, A. A., Tsakiris, C., Zhu, D. C., Xenos, M., Roycewicz, P., Danziger, Z., & Penn, R. (2005). Pulsatile cerebrospinal fluid dynamics in the human brain. IEEE transactions on bio-medical engineering, 52, 557-565. doi:10.1109/TBME.2005.844021

Lucisano, J. Y., Routh, T. L., Lin, J. T., & Gough, D. A. (2017). Glucose Monitoring in Individuals with Diabetes using a Long- Term Implanted Sensor/Telemetry System and Model. IEEE Transactions on Biomedical Engineering, 64, 1982-1993. doi:10.1109/TBME.2016.2619333.Glucose

Marx, K. A. (2003). Quartz Crystal Microbalance: A Useful Tool for Studying Thin Polymer Films and Complex Biomolecular Systems at the Solution - Surface Interface. biomacromolecules, 4. doi:10.1021/bm020116i

Mata, A., Fleischman, A. J., & Roy, S. (2005). Characterization of Polydimethylsiloxane (PDMS) Properties for Biomedical Micro / Nanosystems. Biomedical Microdevices, 7, 281-293.

McDonald, J. C., Duffy, D. C., Anderson, J. R., Chiu, D. T., Wu, H., Schueller, O. J. A., & Whitesides, G. M. (2000). Review General Fabrication of microfluidic systems in poly(dimethylsiloxane). Electrophoresis, 21, 27-40.

Meng, E., & Sheybani, R. (2014). Micro- and nano- fabricated implantable drug delivery systems: current state and future perspectives. Therapeutic Delivery, 5, 1167-1170.

Millikan, G. A. (1942). The Oximeter, an Instrument for Measuring Continuously the Oxygen Saturation of Arterial Blood in Man. Review of Scientific Instruments, 13, 434-444. doi:10.1063/1.1769941

Navarro, M., Michiardi, A., Castan, O., & Planell, J. A. (2008). Biomaterials in orthopaedics. Journal of the Royal Society, Interface, 5, 1137-1158. doi:10.1098/rsif.2008.0151

Nowack, B., Krug, H. F., & Height, M. (2011). 120 Years of Nanosilver History : Implications for Policy Makers. Environmental Science and Technology, 45, 1177-1183. doi:10.1021/es103316q

Pan, Y., Leifert, A., Ruau, D., Neuss, S., Brandau, W., Simon, U., & Jahnen-dechent, W. (2009). Gold Nanoparticles of Diameter 1.4 nm Trigger Necrosis by Oxidative Stress and Mitochondrial Damage. Small, 5, 2067-2076. doi:10.1002/smll.200900466

Pardo, M., Shuster-Meiseles, T., Levin-Zaidman, S., Rudich, A., & Rudich, Y. (2014). Low cytotoxicity of inorganic nanotubes and fullerene-like nanostructures in human bronchial epithelial cells: Relation to inflammatory gene induction and antioxidant response. Environmental Science and Technology, 48, 3457-3466. doi:10.1021/es500065z

Perestrelo, A. R., Águas, A. C. P., Rainer, A., & Forte, G. (2015). Microfluidic Organ / Body-on-a-Chip Devices at the Convergence of Biology and Microengineering. Sensors, 15, 31142-31170. doi:10.3390/s151229848

Petersen, K. E. (1982). Silicon as a Mechanical Material. Proceedings of the IEEE, 70.

Potkay, J. A. (2008). Long term, implantable blood pressure monitoring systems. Biomedical Microdevices, 10, 379-392. doi:10.1007/s10544-007-9146-3

Qin, D., Xia, Y., & Whitesides, G. M. (1996). Rapid Prototyping of Complex Structures with Feature Sizes Larger than 20 micrometers. Advanced Materials, 8, 917-919.

Qu, L., Xia, S., Bian, C., Sun, J., & Han, J. (2009). A micro-potentiometric hemoglobin immunosensor based on electropolymerized polypyrrole – gold nanoparticles composite. Biosensors and Bioelectronics, 24, 3419-3424. doi:10.1016/j.bios.2008.07.077

Roepke, C. L., & Schaff, E. A. (2014). Long Tail Strings : Impact of the Dalkon Shield 40 Years Later. Journal of Obstetrics and Gynecology, 4, 996-1005.

Simpson, P. C., Roach, D., Woolley, A. T., Thorsen, T., Johnston, R., Sensabauch, G. F., & Mathies, R. A. (1998). High-throughput genetic analysis using microfabricated 96-sample capillary array electrophoresis microplates. Proceedings of the National Academy of Sciences of the United States of America, 95, 2256-2261.

Sun, X., Fan, J., Fu, C., Yao, L., Zhao, S., Wang, J., & Xiao, J. (2017). WS2 and MoS2 biosensing platforms using peptides as probe biomolecules. Scientific Reports, 10290. doi:10.1038/s41598-017-10221-4

Sun, Z., Liu, Z., Meng, J., Meng, J., Duan, J., Xie, S., . . . Yang, X.-d. (2011). Carbon Nanotubes Enhance Cytotoxicity Mediated by Human Lymphocytes In Vitro. PLoS ONE, 6, e21073. doi:10.1371/journal.pone.0021073

Sweetman, B., & Xenos, M. (2011). Three-dimensional computational prediction of cerebrospinal fluid flow in the human brain. Computers in biology and …, 41, 67-75. doi:10.1016/j.compbiomed.2010.12.001.Three-dimensional

Takaki, Y., Takenaka, H., Morimoto, Y., Konuma, O., & Hirabayashi, K. (2012). Multi-view display module employing MEMS projector array. optics express, 20, 494-500.

Tan, J. L., Tien, J., Pirone, D. M., Gray, D. S., Bhadriraju, K., & Chen, C. S. (2003). Cells lying on a bed of microneedles : An approach to isolate mechanical force. Proceedings of the National Academy of Sciences of the United States of America, 100, 1484-1489.

Tegenfeldt, J. O., Prinz, C., Cao, H., Huang, R. L., Austin, R. H., Chou, S. Y., . . . Sturm, J. C. (2004). Micro- and nanofluidics for DNA analysis. Analytical and Bioanalytical Chemistry, 378, 1678-1692. doi:10.1007/s00216-004-2526-0

Teo, W. Z., Chng, E. L. K., Sofer, Z., & Pumera, M. (2014). Cytotoxicity of exfoliated transition-metal dichalcogenides (MoS 2, WS2, and WSe2) is lower than that of graphene and its analogues. Chemistry - A European Journal, 20, 9627-9632. doi:10.1002/chem.201402680

Terry, S. C., Jerman, J. H., & Angell, J. B. (1979). A Gas Chromatographic Air Analyzer Fabricated on a Silicon Wafer. IEEE Transactions on Electronic Devices, 26, 1880-1886.

Theodor, M., Ruh, D., Subramanian, S., Katharina, F., Heilmann, C., Beyersdorf, F., . . . Seifert, A. (2014). Implantable Pulse Oximetry on Subcutaneous Tissue. IEEE Conference on Engineering in Medicine and Biology Society.

Tsatalis, J. P., Aldahan, A. S., Hsu, V. M., Tsatalis, A. E., Brah, T. K., & Nouri, K. (2017). Narcissus' reflection : toxic ingredients in cosmetics through the ages. International Journal of Dermatology, 56, 239-241. doi:10.1111/ijd.13477

Voiculescu, I., & Nurashikin, A. (2012). Acoustic wave based MEMS devices for biosensing applications. Biosensors and Bioelectronics, 33, 1-9. doi:10.1016/j.bios.2011.12.041

Wang, J., Chatrathi, M. P., Tian, B., & Polsky, R. (2000). Microfabricated Electrophoresis Chips for Simultaneous Bioassays of Glucose , Uric Acid , Ascorbic Acid , and Acetaminophen. Analytical Chemistry, 72, 2514-2518. doi:10.1021/ac991489l

Wilmer, M. J., Ng, C. P., Lanz, H. L., Vulto, P., Suter-dick, L., & Masereeuw, R. (2016). Kidney-on-a-Chip Technology for Drug-Induced Nephrotoxicity Screening. Trends in Biotechnology, 34, 156-170. doi:10.1016/j.tibtech.2015.11.001

Xu, W., Appel, J., Chae, J., & Member, S. (2012). Real-Time Monitoring of Whole Blood Coagulation Using a Microfabricated Contour-Mode Film Bulk Acoustic Resonator. Journal of Microelectromechanical Systems, 21, 302-307.

Yasotharan, S., Pinto, S., Sled, J. G., Bolz, S.-s., & Günther, A. (2015). Artery-on-a-chip platform for automated, multimodal assessment of cerebral blood vessel structure and function. Lab on a Chip, 15, 2660-2669. doi:10.1039/C5LC00021A

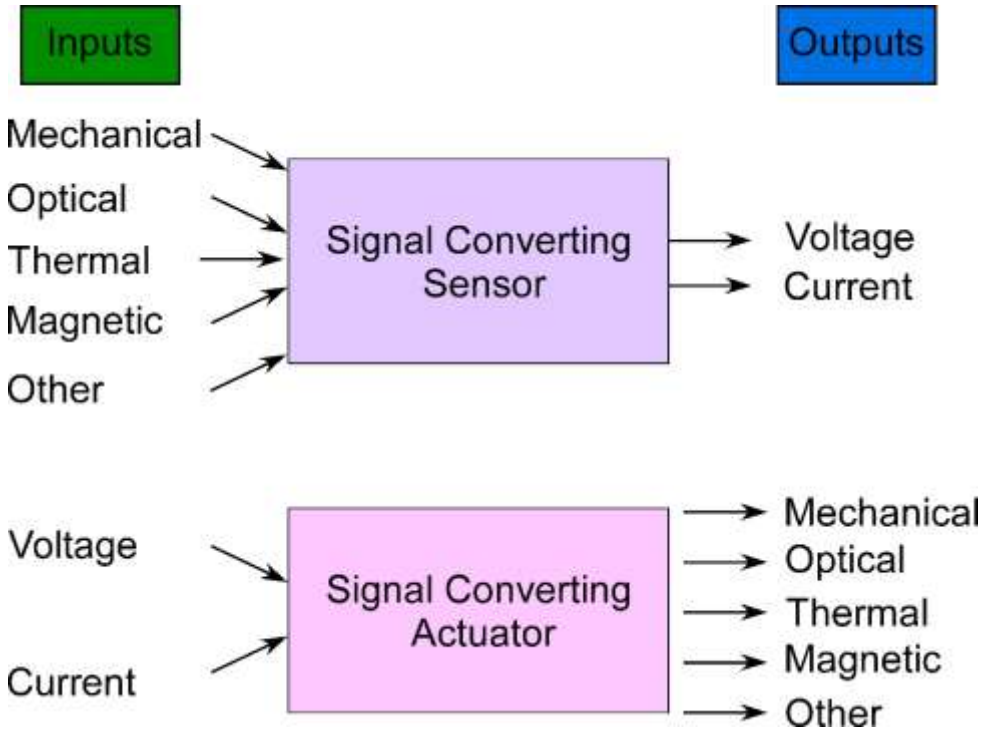

Figure 1.1. Schematic diagram of sensing and actuating concepts. MEMS devices are generally in the form of either sensors or actuators and can be integrated into systems which feature both sensing and actuating components. A physical action results in an electrical output—a sensor—while an electrical input results in a physical action—actuator.

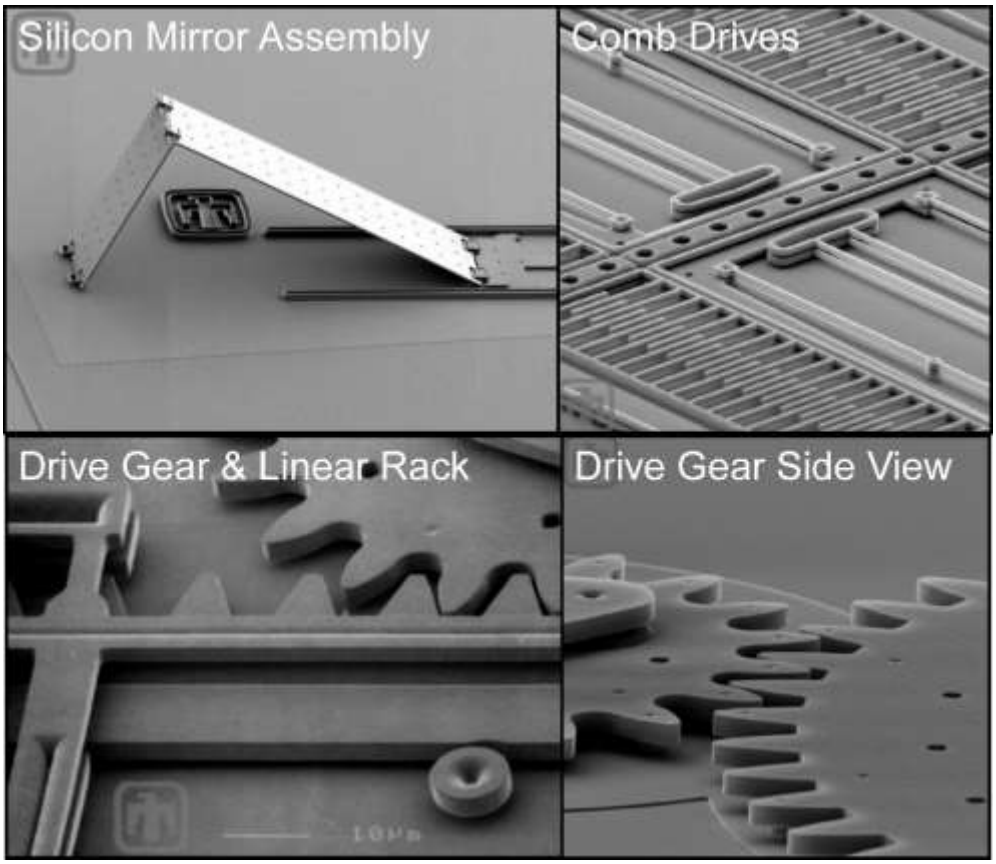

Figure 1.2. Scanning electron microscopy images of a variety of MEMS devices fabricated at Sandia National Laboratories. These MEMS devices exemplify the complex structures that can be achieved using MEMS fabrication techniques.

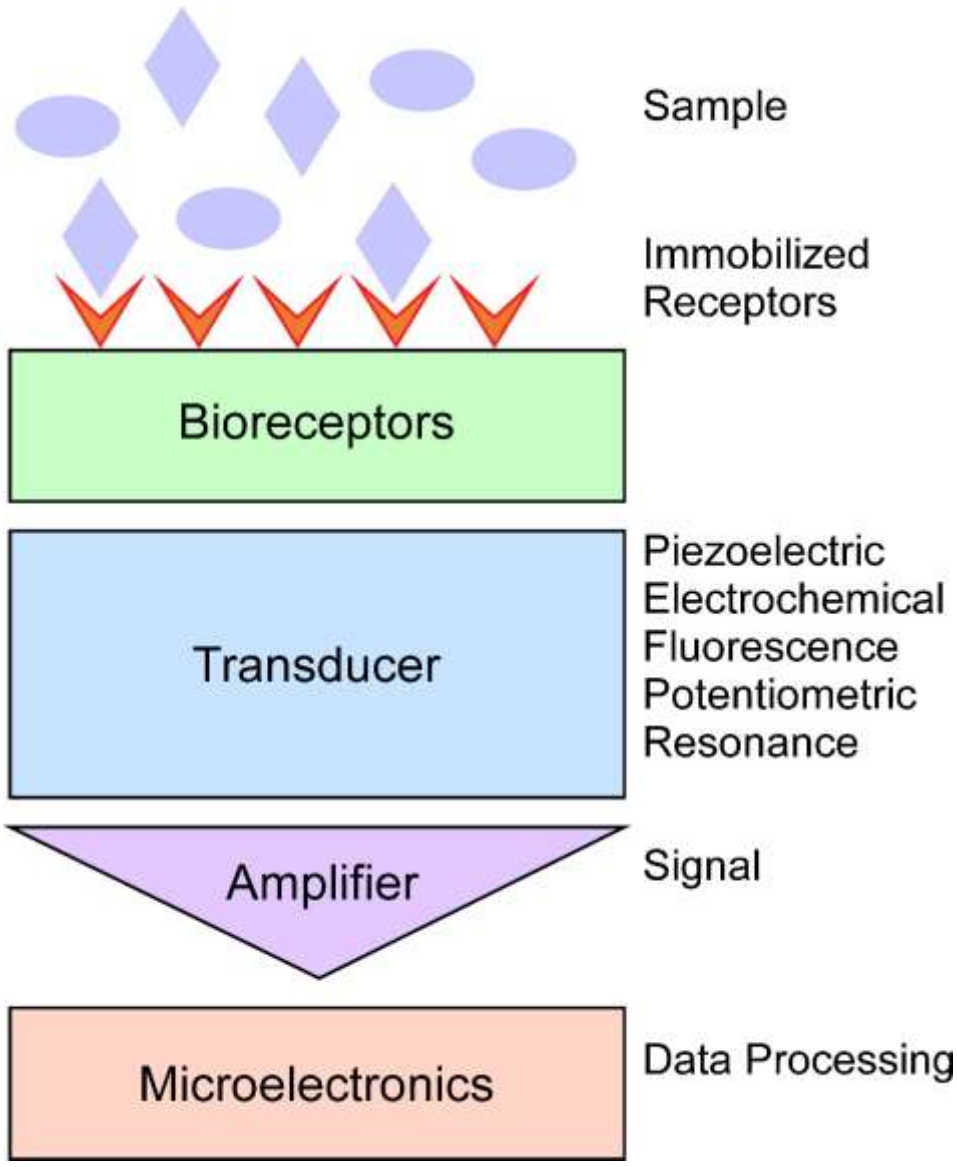

Figure 1.3. Schematic of biosensing concepts. Many biosensors have a similar overall concept. A receptors for specific disease indicating biomarkers are immobilized on the surface of a transducer. When a patient sample which contains the targeted biomarkers is placed on the transducer a change in the device parameters occurs. This change is then amplified and processed.

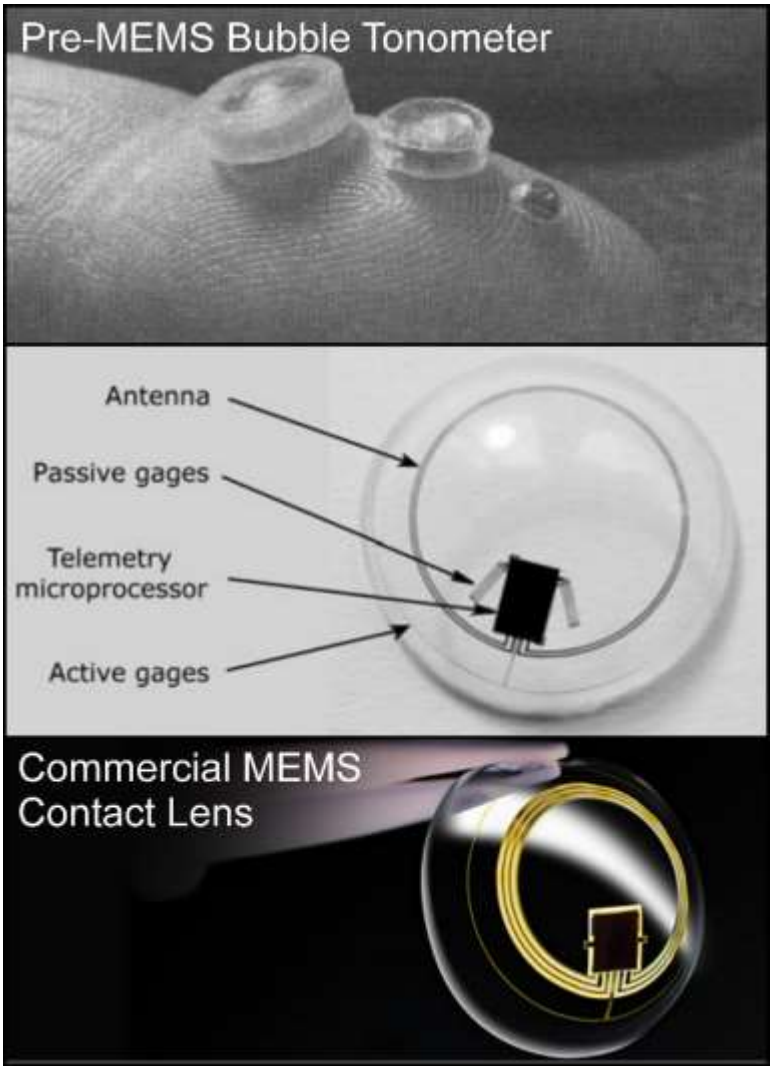

Figure 1.4. Advancement of Intraocular Pressure Sensing. In 1967 Collins published a bubble tonometer as a wireless passive implantable intraocular pressure sensor with the smallest device having a diameter of 2 mm. These devices were fabricated without silicon processing techniques and implanted in rabbits for up to 1 year with issue (Collins, 1967). With the advent of MEMS technology intraocular pressure measurement were refined leading to soft contact lenses with passive and active strain gauges and wireless powering and communication capable through the antenna (Matteo Leonardi et al., 2009). In 2016, the FDA announced device approval for SENSIMED Inc. Triggerfish contact lenses with embedded sensing capabilities(Dunbar et al., 2017).

CHAPTER 2

RAPID BLADDER CANCER CELL DETECTION FROM CLINICAL URINE SAMPLES USING AN ULTRA-THIN SILICONE MEMBRANE

Reproduced with permission from Royal Society of Chemistry. Appel J.H., Ren H., Sin M.L., Liao J.C., Chae J. “Rapid bladder cancer cell detection from clinical urine samples using an ultra-thin silicone membrane” Analyst. ePub 2015 Nov 9, DOI: 10.1039/C5AN01616A

2.1. Abstract

Early detection of initial onset, as well as recurrence, of cancer is paramount for improved patient prognosis and human health. Cancer screening is enhanced by rapid differentiation of cancerous from noncancerous cells which employs the inherent differences in biophysical properties. Our preliminary testing demonstrates that cell-line derived bladder cancer cells deform our <30 nm silicone membrane within an hour and induce visually distinct wrinkle patterns while cell-line derived non-cancerous cells fail to induce these wrinkle patterns. Herein, we report a platform for the rapid detection of cancerous cells from human clinical urine samples. We performed a blinded study with cells extracted from the urine of human patients suspected to have bladder cancer alongside healthy controls. Wrinkle patterns were induced specifically by the five cancer patient samples within 12 hours and not by the healthy controls. These results were independently validated by the standard diagnostic techniques cystoscopy and cytology. Thus, our ultra-thin membrane approach for cancer diagnosis appears as accurate as standard diagnostic methods while vastly more rapid, less invasive, and requiring limited expertise.

2.2. Introduction

Bladder cancer is the fifth most common cancer in the United States with estimated 74,000 new cases in 2015 (Society, 2015). Since bladder cancer has a high rate of new tumor formation, a recurrence rate of up to 70%, lifelong surveillance is necessary as often as every 3 months which incurs significant expense and time commitment (Aldousari & Kassouf, 2010). Current bladder cancer diagnosis is based on an invasive endoscopy procedure called cystoscopy followed by biopsy of suspect lesions for histological examination. To compensate for cystoscopy which lacks sensitivity for low grade flat carcinoma (Aldousari & Kassouf, 2010) urine cytology—the microscopic examination of naturally exfoliated and expelled urothelial cells in the urine—is widely employed alongside cystoscopy. While highly specific (>95%), urine cytology has low (~20%) and moderate (~60%) sensitivity for low and high grade cancers, respectively (Tomasini & Konety, 2013). As a consequence of this low sensitivity for early cancer detection, there are strong interests to develop urine-based diagnostics to complement and overcome shortcomings of cytology and cystoscopy. The majority of efforts have focused on developing molecular diagnostics based on cancer-associated genetic changes, as well as alterations in RNA and protein expression (Cheung, Sahai, Billia, Dasgupta, & Khan, 2013). While several molecular assays are commercially available, significant shortcomings remain, which include diagnostic sensitivity and excessive cost, precluding widespread adaptation (Cheung et al., 2013).

Quantitative measurement of cellular biophysical properties of cancerous and non-cancerous cells represents a promising alternative strategy for cancer diagnosis, given the intrinsic difference in cytoskeleton flexibility, morphology and stiffness of

cancerous from non-cancerous cells. Young's modulus, a measurement of cellular stiffness, is particularly promising for cancerous cell detection (Y. Chen et al., 2014; P. Li et al., 2015). For bladder cancer, Lekka *et al.* determined that cancerous cell lines HU456, T24, and BC3726 had an average Young's modulus of 0.8 kPa compared with 10.0 kPa for non-cancerous cell lines HU609 and HCU29 (M Lekka et al., 1999). For oral cancer, cells extracted from patients with oral squamous cell carcinoma were three-fold more flexible than non-cancerous cells from healthy donors (Remmerbach et al., 2009). Tan *et al*. also compared the translocation time, related to cytoskeleton flexibility of T24, cell-line derived human bladder cancer cells, and immortalized non-cancerous human urothelial cells (Tan et al., 2003). These cell types were passed through a micro pore via an applied electric field. The non-cancerous urothelial cells had an order of magnitude increase in translocation time when compared to their cancerous counterparts (M Lekka et al., 1999). Thus scanning force microscopy, optical stretching and translocation via applied electric field have all shown significant differences in the biophysical properties of cancerous and non-cancerous cells. The differences in Young's modulus and cytoskeleton flexibility between cancerous and non-cancerous cells are in part due to another biophysical property, the cellular traction forces applied to an in vitro surface. Cell traction forces can be visualized using micro-pillar structures (Tan et al., 2003) or silicone membranes (A. Harris, Wild, & Stopak, 1980; Ilyas et al., 2014). Li *et al*. employed a silicon nano-pillar structure to determine that cancerous human Hela cells exerted 20% greater cell traction force when compared to non-cancerous fibroblasts harvested from neonatal rat liver (Z. Li et al., 2009). The application of micro-pillars as a diagnostic device requires highly-optimized fabrication techniques and sophisticated

analytical methodologies. Although these methods all show distinct differences between the biophysical properties of cancerous and non-cancerous cells, they have not been employed for cancer cell detection.

Here we report a high-throughput strategy capable of differentiating bladder cancer cells from non-cancerous cells based on their respective cellular traction forces. Our method requires minimal sample preparation, does not demand highly-trained personnel for data interpretation, and only involves an inexpensive low-power microscope. Our approach leverages an ultra-thin, <30 nm, silicone membrane to visualize the distinct cell traction forces of bladder cancer cells. Our ultra-thin silicone membrane is deformed exclusively by cancerous cells, producing distinct wrinkle patterns compared to non-cancerous cells (J. Appel, Sin, Liao, & Chae, 2014). In this study, we examined the underlying mechanism for ultra-thin membrane deformation exclusively by cancerous bladder cells by manipulation and visualization of focal adhesion proteins. Furthermore, clinical validation of our cancer detection strategy was performed. A double-blind study was performed using urine collected from five individuals presenting cancer-like symptoms. And within 12 hours, of sample collection cancer cells present in all five patient urine samples generated wrinkle patterns. Our technique circumvents traditionally complex, costly, and invasive instrumentation for bladder cancer screening and detection as well as may be applied for the detection of additional cancers.

2.3. Materials and Methods

Device fabrication. Ultra-thin silicone membranes were formed by adding ~45μL of 12,500 cP viscosity liquid silicone (Brookfield Engineering Laboratories) to a 15 mm by 0.5 mm glass depression slide (Ted Pella, Inc.). The uppermost layer of silicone was cross-linked by inverting the slide over a flame for 5 to 10 seconds. The cell culture chamber was formed by attaching a 1.9 cm diameter by 2.54 cm height section of sterile PVC with vacuum grease to the glass slide (figure 2.1.(a)) (A. Harris et al., 1980). In some experiments, ultra-thin silicone membrane surfaces were modified by the addition of 10 μg fibronectin (BD Biosciences) in 1X PBS, incubated at room temperature for 1 hour, aspirated and membranes washed three times with 1X PBS.

Cell culture. RT4 is an established bladder cell-line derived from low grade human transitional cell papilloma. T24 is derived from high grade human transitional cell carcinoma. HEK293f is a transformed human embryonic kidney cell-line that served as non-cancerous controls to simulate epithelial cells found in non-cancerous urine samples. RT4 and T24 cells were grown in McCoy's 5A modified media (Life Technologies) and HEK293f cells were grown in Eagle's minimum essential medium (ATCC). Media was supplemented with 10% fetal bovine serum (FBS, Life Technologies), and 1X penicillin/streptomycin (Sigma-Aldrich). Cells were maintained in a 5% CO2 environment at 37˚C.

Cell-line sample preparation. Cells at 80% confluency were trypsinized (Invitrogen) or incubated with cell dissociation buffer (Life Technologies) for 5 min at 37˚C and washed with media supplemented with 10% FBS. Approximately $5x10^5$ cells were applied to each device and incubated in culture media with at 5% CO_2 at 37˚C at various time

intervals and then inspected via microscopy (figure 2.2.). For simulating clinical samples with hematuria, $5x10^5$ white blood cells from buffy coat (Innovative Research) were applied to the ultra-thin membrane prior to applying RT4 or HEK293f. For urine pH effect, artificial urine (Spectrum Laboratories Inc.) or clarified aggregated donor urine samples were supplemented with 10% FBS and the pH adjusted with hydrochloric acid.

Patient and healthy donor sample preparation. Five patient urine samples were obtained from men ages 53 to 89 undergoing trans-urethral resection of bladder tumor (TURBT) (Babjuk, 2009) at VA Palo Alto Health Care System and a sixth urine sample was collected from a healthy female donor control with no family history of bladder cancer and only a single grandparent with lung cancer likely linked to smoking, age 26. Informed consent was obtained from all patients. Cells present in the urine were pelleted by centrifugation at 300 x gravity, washed twice with 1X PBS and re-suspended in McCoy's 5A modified media supplemented with 10% FBS prior to application to the ultra-thin silicone membrane.

Data analysis. The pattern generated when a cluster or individual cell deforms the ultra-thin membrane is defined as a wrinkle pattern. Wrinkle patterns consist of a number of wrinkles which have various lengths. In addition, wrinkle patterns were quantified by measuring the number and length of each wrinkle following addition of cells to ultra-thin silicone membrane.

Fluorescent imaging. F-actin was fluorescently labeled with Alexa Fluor 488 Phalloidin phallotoxin (Life Technologies) following the manufacturer's instructions. Briefly,T24 and HEK293f cells were pre-incubated on the ultra-thin silicone membrane for 24 hours were fixed with 4% paraformaldehyde in 1X PBS for 10 min at 37˚C, washed twice with

1X PBS, permeabilized with 0.1% Triton X-100 in 1X PBS for 10 min at 37˚C and washed twice with 1X PBS. The permeabilized cells were incubated with fluorescent Alexa Fluor 488 Phalloidin phallotoxin for 20 min at room temperature, washed twice with 1X PBS and visualized under a confocal microscope (Nikon Eclipse TE2000-U). Fluorescent intensity traces were measured using Image J and the data was binned for every 4 values.

2.4. Results and Discussion

Ultra-thin membrane characterization. Previous reports have focused on the visualization of cell locomotion with cancerous cells on uncharacterized silicone membranes of various thicknesses (A. Harris et al., 1980; Ilyas et al., 2014; Pelham & Wang, 1999). We characterized our silicone membrane by applying a minute droplet of water to the surface (J. Appel et al., 2014; Huang et al., 2007). The approximately 0.5 μL of water on the surface of membrane induced a radial wrinkle pattern (figure 2.1. (b)). From the wrinkle pattern, the thickness of the membrane was calculated to be approximately 28 nm. A predictive estimation of the wavelength, amplitude and number of wrinkles is included in the supplemental materials (Cerda & Mahadevan, 2003).

Wrinkle pattern from cell-line derived cancerous cells. We compared the time and extent of membrane wrinkle formation generated by cell-line derived low grade bladder papillary carcinoma RT4 cells, used as a control (figure 2.3. (a)). In this study, we evaluated and compared RT4 cells to a cell-line derived high grade bladder carcinoma T24 cells. Cancer grades represent tumor severity and the likelihood of metastasis within human patients. Approximately $5x10^5$ RT4 or T24 cells were applied to our silicone membrane, and distinct wrinkles were generated by both within 4 hours (figure 2.3. (a) &

(b)). To elucidate the onset of wrinkle pattern formation for cancerous RT4 and T24 cells, a time-lapse experiment was performed for 4-, 6-, and 8-hour incubation periods; as opposed to a time-lapse experiment using only RT4 cells at 18-, 20-, and 22-hour incubation periods. Both the RT4 cells (figure 2.4. (a)-(d)) and the T24 cells (figure 2.4. (e)-(h)) induced wrinkle patterns after 4 hours of incubation. By examining the aggregate number of wrinkle patterns generated at various time intervals, we found a positive correlation between the number of wrinkles patterns and the time of incubation (figure 2.3. (c)). In contrast, the number of individual wrinkles and the length of these wrinkles, which comprise individual wrinkle patterns, showed little direct correlation with the incubation time (figure 2.3. (d)). For example, RT4 cells generated on average 5.7 individual wrinkles after 8 hours, while T24 cells generate 2.3 individual wrinkles. Our representative cancerous cells generated wrinkle patterns as early as four hours and the wrinkle patterns formed persisted over the entire length of observation.

To ensure that selectively cancerous cells induce wrinkle pattern formation on our ultra-thin silicone membrane, we used a non-cancerous healthy control of cell-line human kidney epithelial (HEK293f) cells. HEK293f cells were chosen due to the high degree of similarity between the epithelial cells found in the kidney and the bladder cavity. Approximately $5x10^5$ HEK293f cells were applied to our membrane. HEK293f cells failed to generate discernable wrinkle patterns or individual wrinkles (figure 2.4. (i)-(l)) after extended incubation period of 24 hours. Thus cell-induced wrinkle pattern formation was specific to the cancerous cell-line derived cells we tested and not shared with non-cancerous cell-line derived cells.

To better replicate potential clinical testing of human patient samples, we placed cell-line derived cancerous cells in modified urine environments. This simulates the conditions in which cells could not be readily extracted from human urine by centrifugation and instead whole urine samples would be applied to the membrane, such as in developing nations. We incubated cancerous RT4 or T24 cells on ultra-thin membranes in human (figure 2.5. (b)) or artificial (figure 2.5. (a)) urine at pH varying from 5 to 7, within the typical range of human urine (Wright et al., 2005). To sustain the cancerous cell-line derived RT4 or T24 cells for extended device testing, we supplemented the clarified—by centrifugation—human or artificial urine with 10 % fetal bovine serum. As expected, the cancerous RT4 and T24 cells retained the ability to induce membrane deformation and generated wrinkle patterns in both human and artificial urine, across all tested pH values. The aggregate number of wrinkle patterns was not a function of the type of urine, human or artificial, or the pH value (figure 2.5.). Thus the inherent biophysical properties differences responsible for cancer-specific wrinkle formation is not affected by the urine or changes in pH.

Wrinkle patterns from a mixture of cancerous and non-cancerous cells. First we examined the capacity of cancerous RT4 cells to generate wrinkle patterns in the presence of non-cancerous cells HEK293f and buffy coat cells. Buffy coat is the fraction of blood that is comprised principally of white blood cells. White blood cells are often found in clinical patient urine, as one of the primary symptoms of bladder cancer is hematuria or blood within the urine. We examined the attributes of the present wrinkle patterns, i.e. number and length of wrinkles within each wrinkle pattern. Quantitation of the number of wrinkles within a wrinkle pattern was performed by serially counting the

number of wrinkles generated by each cluster of cancerous cells or an individual cancerous cell. The length of each wrinkle within a wrinkle pattern was measured relative to the diameter of a cell, approximated as 20 μm. No apparent correlation was observed between mixture ratio and these wrinkle pattern attributes. However, a strong inverse trend was found between the overall number of wrinkle patterns and mixture ratio (figure 2.6. (a) & (b)). Wrinkle patterns are defined as the culmination of wrinkles generated by a cluster or individual cell within a discrete span separate from other cells and induced membrane deformations of the ultra-thin membrane. Therefore by examining the overall number of wrinkle patterns we can better represent clinical use of the ultra-thin membrane diagnosis platform, because a clinician would only need to determine if wrinkle patterns are present. Clinical patient urine samples are composed of a very small population of cancerous cells in the presence of an overwhelmingly non-cancerous cell population. Therefore increasing the number of non-cancerous cells better simulates clinical samples. Additional experimentation by varying mixture ratios to deplete the population of cancerous cells is necessary to define a true threshold for detection. However, in clinical applications approximations of the actual number of cancer cells present in a urine sample could be determined based on the number of wrinkle patterns present.

Clinical urine sample testing. To validate the ultra-thin membrane as a detection tool of human patient bladder cancer, we obtained urine samples from five individuals presenting cancer-like symptoms. All patients were male ages 53 to 89. And four of the five patients were being treated for a recurrence of bladder cancer. Additionally, two of the five patients reported a history of smoking. Urine samples were collected during a

trans-urethral resection of bladder tumor (TURBT) procedure, which is the current standard for bladder cancer diagnosis (Cheung et al., 2013). Also a control urine sample was collected via urination from a female healthy donor, age 26, with no family history of bladder cancer and only a single grandparent with lung cancer likely linked to smoking. Cells were extracted from all urine samples, washed and applied to the ultra-thin membrane.

Following 12 hours of incubation, wrinkle patterns were observed in the five bladder cancer patient samples (figure 2.7.). Additionally, the healthy donor control cells failed to generate wrinkle patterns even after an extended incubation period of 24 hours (figure 2.4. (m)-(p)). The actual number of wrinkle patterns observed (table 2.1.), ranging from 1 to 5, corresponds to less than a wrinkle pattern per ultra-thin membrane. This indicates that despite the low concentration of cancer cells, practical use of the ultra-thin membrane for cancer detection is well within the membrane detection limit which is dependent on the concentration of cancer cells in the urine sample.

Standard diagnosis method, TURBT confirmed the five patients had bladder cancer. TURBT is performed by an endoscopic examination of the bladder interior and upon finding abnormal tissue extracting a small biopsy. This biopsy is then sent for examination by an experienced cytopathologist. As a complementary diagnosis method urine cytology is performed. This method is also dependent on an experienced cytopathologist to extract cells from urine and examine for abnormal cellular structure. For the purposes of this experiment patients had previously undergone either cytology, cystoscopy or both before TURBT (table 2.1.). However, the patient prognosis was unknown until after analysis of the biopsy collected during TURBT. Interestingly, of the

five patient samples, two—patient #2 and #3—demonstrated false negative results, i.e. negative for malignancy, by standard urine cytology, while generating an accurate positive result on our ultra-thin silicone membrane. Thus, initial validation of our ultra-thing silicone membrane demonstrates that this platform is highly sensitive and accurate for the detection of human patient bladder cancer from urine samples.

Validation of cell traction forces that generate wrinkle patterns. To further characterize and identify the working mechanism of wrinkle pattern formation, we varied the cell transfer method. T24 cells were removed from culture dishes by the addition of the protease trypsin or a cell dissociation buffer applied to our ultra-thin silicone membranes and imaged at 1 hour intervals for a total of four hours. While the T24 cells treated with the protease trypsin required three hours for initial wrinkle pattern formation, the T24 cells treated with the cell dissociation buffer generated wrinkles within a single hour (figure 2.8. (a)). The initial transfer method relied on trypsin which physically severs the focal adhesion proteins on the surface of the cell which must be regrown prior to cell-induced wrinkle formation. By shifting to a cell dissociation buffer, the focal adhesion proteins remain intact which dramatically reduces the time for wrinkle pattern formation, by negating regeneration of the adhesion protein. Therefore, we were able to decrease the time for cancerous cell wrinkle formation to one hour post cell addition to our membrane by changing the cell transfer method.

In an effort to make wrinkle patterns generated by RT4 cells more distinctive, we investigated a means of increasing the individual attributes of wrinkle patterns. We attempted to increase the individual number and length of wrinkles within a wrinkle pattern by coating the membrane with fibronectin, a cellular adhesion promoting protein.

However, the average number and average length of wrinkles did not significantly vary with the addition of fibronectin (figure 2.8. (b)). Treatment of our ultra-thin silicone membrane surface with fibronectin failed to significantly affect the induction of membrane wrinkles measured by the number or length of individual wrinkles within wrinkle patterns.

To validate that cancerous cells are mechanically capable of generating sufficient strain, to induce deformation of our ultra-thin silicone membrane to produce wrinkle patterns. The observed strain induced deformation of our membrane by cancerous RT4 cells was compared to previously reported strain generated by cancerous cells (Z. Li et al., 2009). Water droplet calibration of the membrane approximated 0.1% to 0.4% lumped strain (figure 2.1. (b)). This correlates well with lump strain we derived from a study of cell traction forces of on a polydimethylsiloxane micro-pillar structure, which was estimated to be 0.5% lump strain (Z. Li et al., 2009). We derived this lump strain by averaging the strain generated by the displacement of each micro-pillar. This averaged strain was then normalized by the ratio between the surface area of each pillar in contact with the cell over the total area of the cell (Z. Li et al., 2009). Additionally, a positive correlation between cellular traction force and metastatic potential of cancerous cells has been reported (Koch, Munster, Bonakdar, Butler, & Fabry, 2012; Kraning-rush, Califano, & Reinhart-king, 2012). Thus the strain, as measured by cell traction forces, visualized by the number of wrinkles within a wrinkle pattern could be applied for discerning the grade of a cancer cell.

Cell traction forces are responsible for inducing strain in the ultra-thin membrane; these forces are dependent on focal adhesion proteins. Filamentous-actin (f-actin), a focal

adhesion protein integral for cell shape, relocates to the edges of the cell for cell locomotion and spreading upon a surface (D.-h. Kim et al., 2012). Thus a focus of f-actin indicates that a force is being applied by the cell to an external surface (D.-h. Kim et al., 2012). To verify that the cytoskeleton of cancerous cells induces membrane deformation and generates wrinkle patterns in our ultra-thin silicone membrane, we fluorescently stained the f-actin with philotoxin. Philotoxin specifically binds to f-actin and the co-localization of philotoxin adjacent to wrinkle patterns would strongly support cellular adhesion being responsible for the membrane deformation. Following 24 hours of incubation of on the membrane, we fixed and stained T24 or HEK293f cells to visualize the localization of f-actin relative to wrinkle formation. Individual (figure 2.9. (a) – (c)) and clusters (figure 2.9. (d) – (f)) of T24 cells both generated two wrinkles, and more importantly the fluorescently stained f-actin co–localized with these wrinkles. Within an individual T24 cell, a locus of f-actin co-localized with the origins of wrinkles produced by the cell (figure 2.9. (c)). An intensity trace of fluorescence adjacent to the wrinkle showed a dramatic increase in fluorescence, and thus and increased presence f-actin at this location (figure 2.10. (a) & (c)). In contrast, individual and clusters of HEK293f cells failed to generate wrinkles (figure 2.9. (g) – (l)), did not have any discernable locus of f-actin, and the fluorescent intensity trace showed homogeneous intensity within the cell (figure 2.10. (b) & (d)). The co-localization of an f-actin locus immediately adjacent to the origin of the wrinkle patterns generated by cancerous T24 cells, along with the lack an f-actin locus in non-cancerous HEK293f cells, which fail to induce wrinkling, supports the cytoskeleton of cancerous cells inducing the deformation of the membrane and ultimately for wrinkle pattern formation. This indicates that the cytoskeleton of the T24

cell is exerting a force on the ultra-thin membrane which does induce wrinkle pattern formation. Thus the underlying mechanism for membrane wrinkle formation appears dependent on f-actin foci and thus the cytoskeleton. While ancillary for clinical evaluation of patient samples, examining the underlying mechanism for wrinkle pattern formation gives insight into the inherent biophysical differences behind wrinkle pattern formation.

2.5. Conclusion

Results from our double-blind study on human patients with bladder cancer-like symptoms show that cells extracted from clinical urine samples can selectively deform our ultra-thin silicone membrane and generate wrinkle patterns. While cells extracted from the urine of healthy donors fail to sufficiently induce wrinkle formation. We confirm via manipulation and labeling of cellular adhesion proteins that this innate difference in the ability to generate wrinkle patterns in our membrane is in part due to the unique biophysical properties of cancerous cells from healthy counter parts. Thus, our ultra-thin silicone membrane has the potential to be developed into a simple, yet cost effective tool to discern the presence of bladder cancer from cells present in urine samples. Furthermore, our methodology can be applied toward the diagnosis of additional cancers where cells are easily obtained or naturally expelled, e.g. lung cancer detection through analysis of sputum. Moreover, our cancer diagnosis approach is highly amenable to developing nations where conventional diagnosis is cost-prohibitive and impedes continuous monitoring for initial onset and recurrences of cancer. Our device leverages inherent biophysical properties of cancerous cells for non-invasive, improved early detection and continuous surveillance for the recurrence of cancer.

Aldousari, S., & Kassouf, W. (2010). Update on the management of non-muscle invasive bladder cancer. Canadian Urological Association Journal, 4, 56-64.

Appel, J., Sin, M. L. Y., Liao, J. C., & Chae, J. (2014). Wrinkle Cellomics: Screening Bladder Cancer Cells Using an Ultra-Thin Silicone Membrane. IEEE International Conference on Micro Electro Mechanical Systems, 889-892.

Babjuk, M. (2009). Transurethral Resection of Non – muscle-invasive Bladder Cancer. European Urology Supplements, 8, 542-548. doi:10.1016/j.eursup.2009.06.003

Cerda, E., & Mahadevan, L. (2003). Geometry and Physics of Wrinkling. Physical Review Letters, 90, 1-4. doi:10.1103/PhysRevLett.90.074302

Chen, Y., Li, P., Huang, P.-H., Xie, Y., Mai, J. D., Wang, L., . . . Huang, T. J. (2014). Rare Cell Isolation and Analysis in Microfluidics. Lab on a Chip, 14, 626-645. doi:10.1039/c3lc90136j

Cheung, G., Sahai, A., Billia, M., Dasgupta, P., & Khan, M. S. (2013). Recent advances in the diagnosis and treatment of bladder cancer. BMC medicine, 11, 13. doi:10.1186/1741-7015-11-13

Harris, A., Wild, P., & Stopak, D. (1980). Silicone Rubber Substrata : A New Wrinkle in the Study of Cell Locomotion Author (s): Albert K . Harris , Patricia Wild and David Stopak Reviewed work (s): Source : Science , New Series , Vol . 208 , No . 4440 (Apr . 11 , 1980), pp . 177-179 Publish. Science (New York, N.Y.), 208, 177-179.

Huang, J., Juszkiewicz, M., de Jeu, W. H., Cerda, E., Emrick, T., Menon, N., & Russell, T. P. (2007). Capillary wrinkling of floating thin polymer films. Science (New York, N.Y.), 317, 650-653. doi:10.1126/science.1144616

Ilyas, A., Asghar, W., Ahmed, S., Lotan, Y., Hsienh, J.-T., Kim, Y.-t., & Iqbal, S. M. (2014). Electrophysiological analysis of biopsy samples using elasticity as an inherent cell marker for cancer detection. Analytical Methods, 6, 7166-7174. doi:10.1039/C4AY00781F

Kim, D.-h., Khatau, S. B., Feng, Y., Walcott, S., Sun, S. X., Longmore, G. D., & Wirtz, D. (2012). Actin cap associated focal adhesions and their distinct role in cellular mechanosensing. Scientific Reports, 2. doi:10.1038/srep00555

Koch, T. M., Munster, S., Bonakdar, N., Butler, J. P., & Fabry, B. (2012). 3D Traction Forces in Cancer Cell Invasion. PLoS ONE, 7. doi:10.1371/Citation

Kraning-rush, C. M., Califano, J. P., & Reinhart-king, C. A. (2012). Cellular Traction Stresses Increase with Increasing Metastatic Potential. PLoS ONE, 7. doi:10.1371/journal.pone.0032572

Lekka, M., Laidler, P., Gil, D., Lekki, J., Stachura, Z., & Hrynkiewicz, a. Z. (1999). Elasticity of normal and cancerous human bladder cells studied by scanning force microscopy. European biophysics journal : EBJ, 28, 312-316.

Li, P., Mao, Z., Peng, Z., Zhou, L., Chen, Y., Huang, P.-h., . . . Huang, T. J. (2015). Acoustic separation of circulating tumor cells. Proceedings of the National Academy of Sciences of the United States of America, 112, 4970-4975. doi:10.1073/pnas.1504484112

Li, Z., Song, J., Mantini, G., Lu, M.-Y., Fang, H., Falconi, C., . . . Wang, Z. L. (2009). Quantifying the traction force of a single cell by aligned silicon nanowire array. Nano letters, 9, 3575-3580. doi:10.1021/nl901774m

Pelham, R. J., & Wang, Y. L. (1999). High resolution detection of mechanical forces exerted by locomoting fibroblasts on the substrate. Molecular biology of the cell, 10, 935-945.

Remmerbach, T. W., Wottawah, F., Dietrich, J., Lincoln, B., Wittekind, C., & Guck, J. (2009). Oral cancer diagnosis by mechanical phenotyping. Cancer Research, 69, 1728-1732. doi:10.1158/0008-5472.CAN-08-4073

Society, A. C. (2015).

Tan, J. L., Tien, J., Pirone, D. M., Gray, D. S., Bhadriraju, K., & Chen, C. S. (2003). Cells lying on a bed of microneedles : An approach to isolate mechanical force. Proceedings of the National Academy of Sciences of the United States of America, 100, 1484-1489.

Tomasini, J. M., & Konety, B. R. (2013). Urinary Markers/Cytology: What and When Should a Urologist Use. Urologic Clinics of North America, 40(2), 165-173.

Wright, M. E., Michaud, D. S., Pietinen, P., Taylor, P. R., Virtamo, J., & Albanes, D. (2005). Estimated urine pH and bladder cancer risk in a cohort of male smokers. Cancer Causes and Control, 16, 1117-1123. doi:10.1007/s10552-005-0348-9

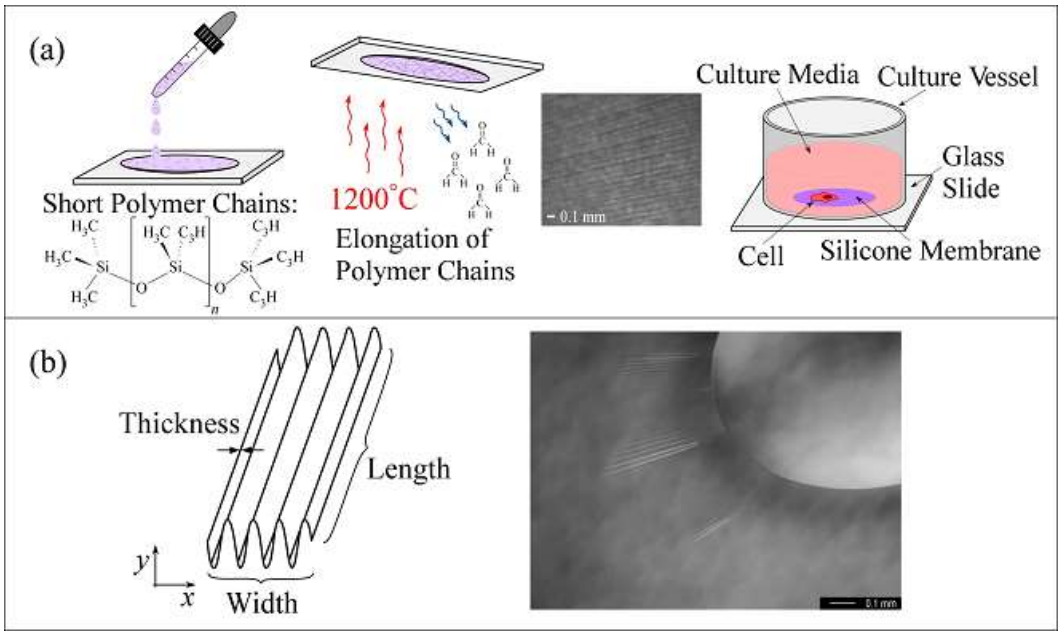

Figure 2.1. Membrane Characterization and Fabrication (a) Membrane fabrication method, beginning with high viscosity liquid silicone in a concave glass slide, then the top layer of the liquid silicone is cross-linked via heat forming the ultra-thin membrane; a culture vessel is then applied creating a water-tight seal with the glass slide. (b) Membrane characterization method, using water droplets to determine membrane thickness.

Figure 2.2. Overall imaging set-up for the observation of wrinkle patterns generated by cancerous cells. Inset shows 6 devices which each contain ultra-thin membranes, culture media and cells.

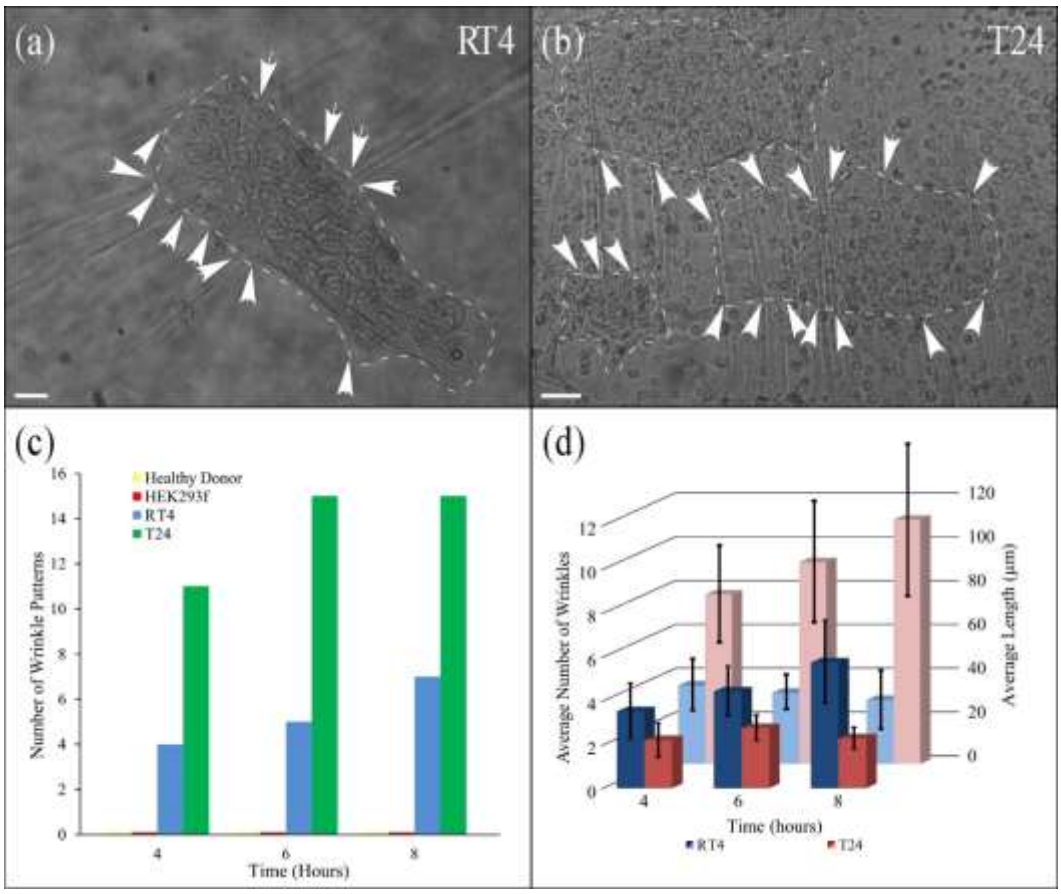

Figure 2.3. Wrinkle Pattern Formation and Analysis (a) Approximately 75 RT4 cells generating a wrinkle pattern which consists of 12 wrinkles with an average length of 75 μm, after more than 24 hours. (b) Approximately 150 T24 cells generating 3 wrinkle patterns, the top pattern consists of 5 wrinkles with an average length of 50 μm, the middle pattern consists of 13 wrinkles with an average length of 60 μm, and the bottom pattern consists of 3 wrinkles with an average length of 80 μm, after more than 24 hours. (c) Plot of the total number of wrinkle patterns generated by each cell type: RT4, T24, HEK293f, and Healthy Donor, at each time interval. (d) Plot showing the average attributes of a wrinkle pattern generated by either RT4 or T24 cells at each time interval, n=4. All scale bars are 20 μm.

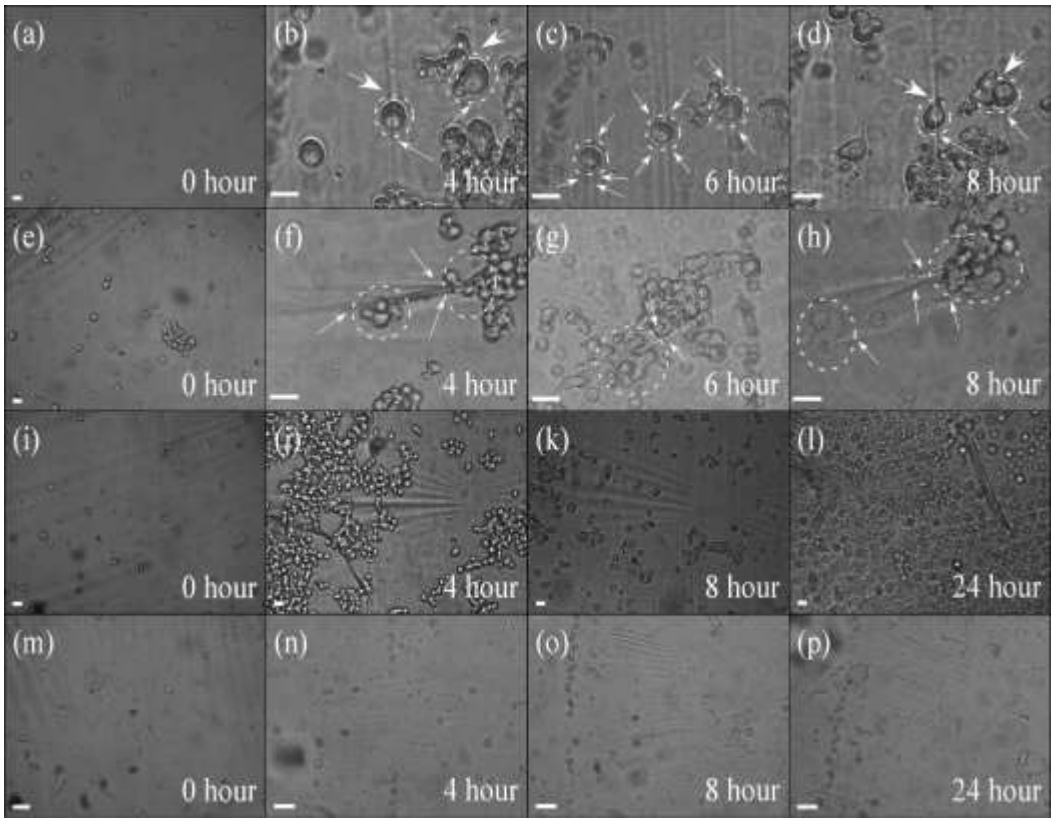

Figure 2.4. Time Lapse of Wrinkle Pattern Formation in All Cell Types (a) – (d) RT4 cells at 0, 4, 6, & 8 hours, generating 3 wrinkle patterns after 4 hours, (e) – (h) T24 cells at 0, 4, 6, & 8 hours, generating 2 wrinkle patterns after 4 hours, (i) – (l) HEK293f cells at 0, 4, 8, & 24 hours, no wrinkle patterns are present, (m) – (p) healthy donor epithelial cells at 0, 4, 8, & 24 hours, no wrinkle patterns are present. All scale bars are 20 μm.

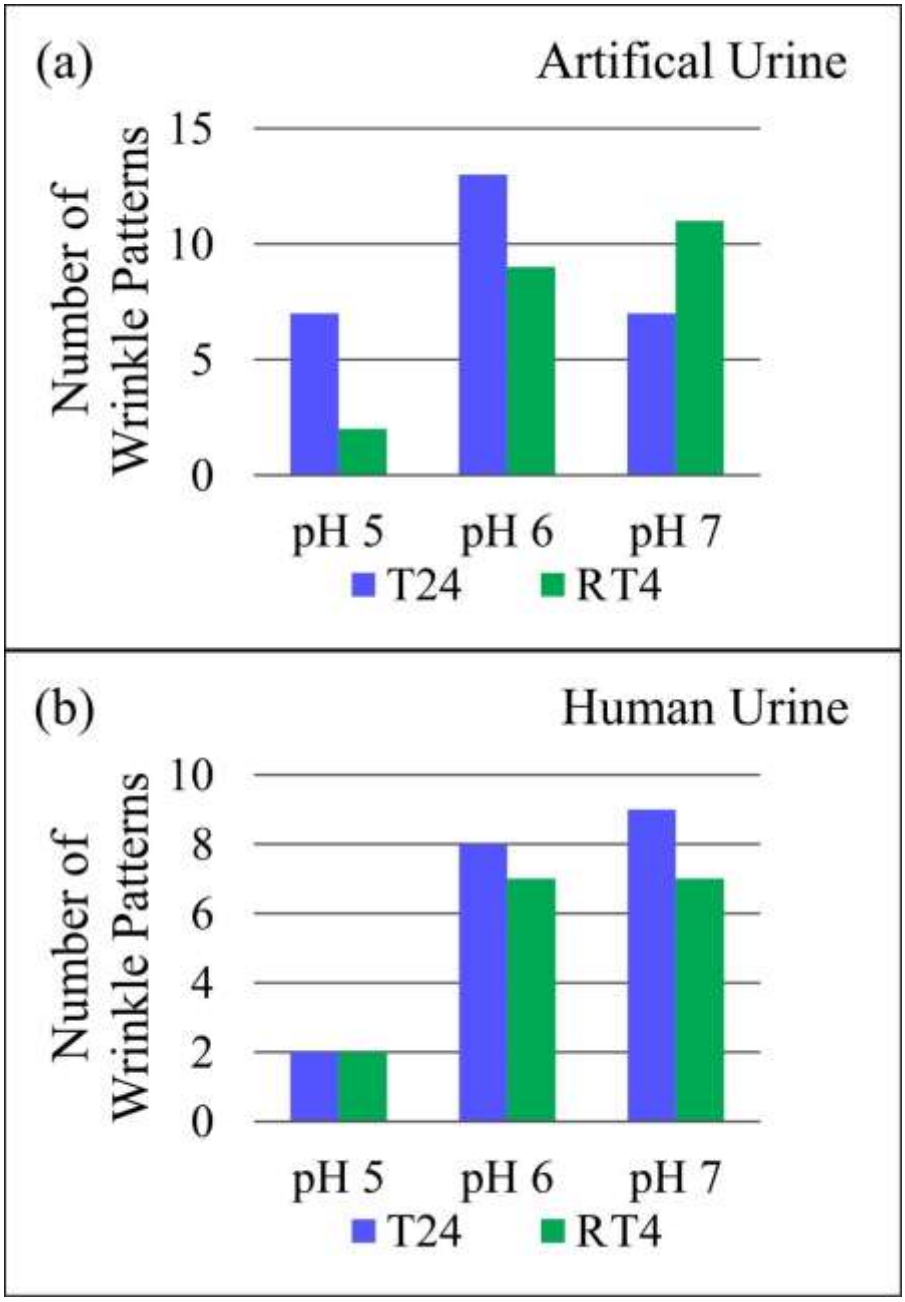

Figure 2.5. Analysis of Wrinkle Patterns in Urine of Varying pH Levels (a) Plot of the number of wrinkle patterns generated by either RT4 or T24 cells in artificial urine at various pH levels. (b) Plot of the number of wrinkle patterns generated by either RT4 or T24 cells in a mix of purified healthy donor urine at various pH levels.

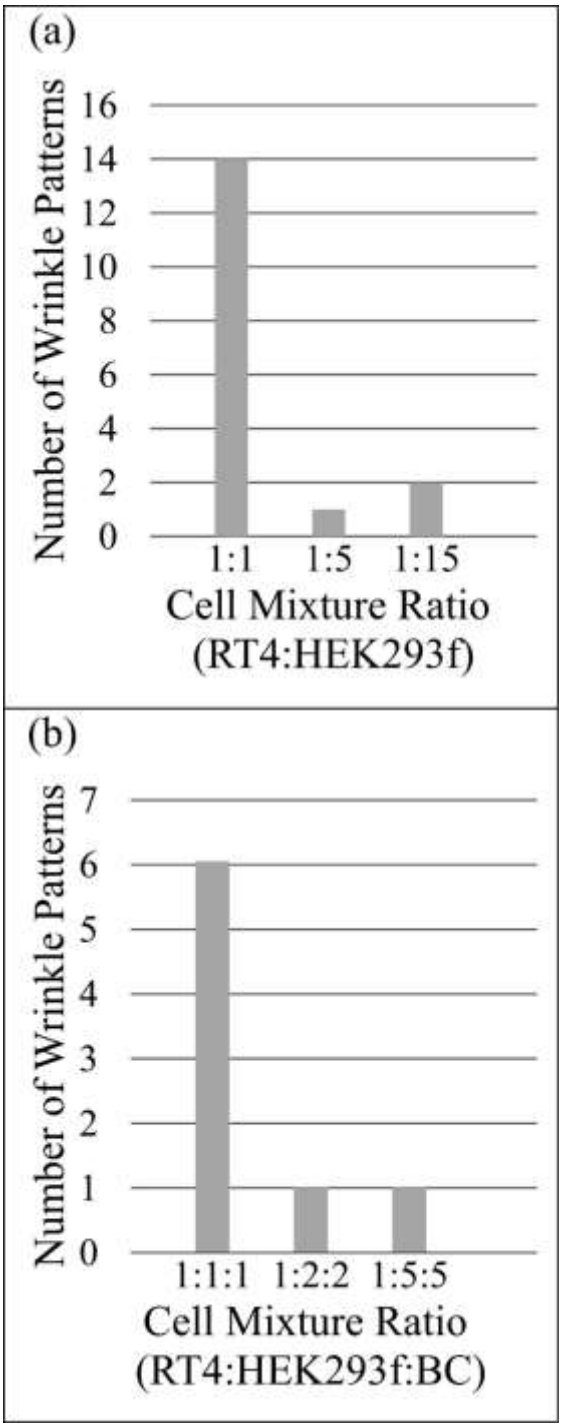

Figure 2.6. Wrinkle Patterns in Mixed Cell Populations (a)Plot of the number of wrinkle patterns generated by cancerous cells in each mixture ratio (RT4:HEK293f) (b) Plot of the number of wrinkle patterns generated by cancerous cells in each mixture ratio (RT4:HEK293f:buffy coat).

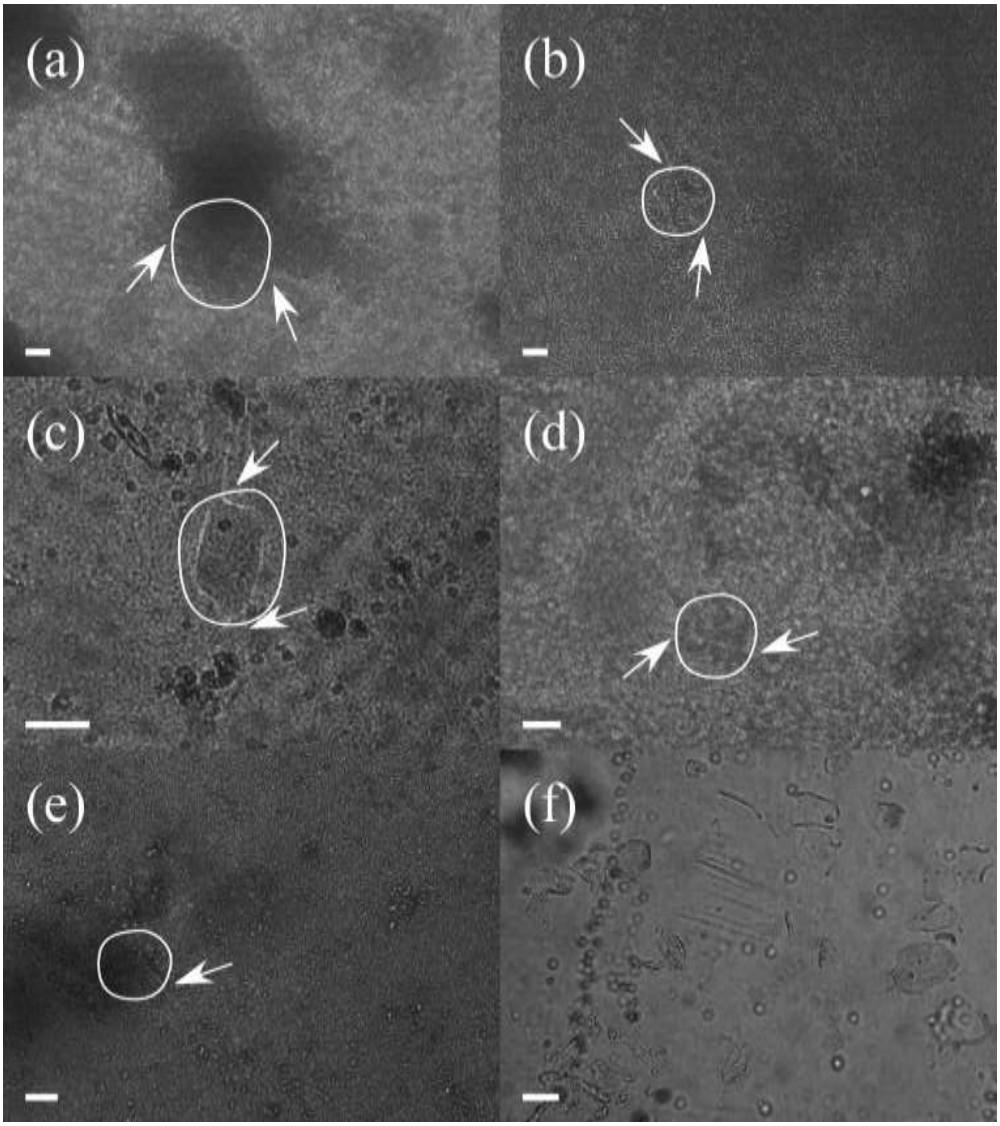

Figure 2.7. Wrinkle Patterns Formed by Clinical Patient Samples (a) wrinkle pattern generated by patient 1 after 24 hours (b) wrinkle pattern generated by patient 2 after 24 hours (c) wrinkle pattern generated by patient 5 after 12 hours (d) wrinkle pattern generated by patient 3 after 24 hours (e) wrinkle pattern generated by patient 4 after 12 hours (f) no wrinkle patterns generated by healthy donor control. All scale bars are 20 μm.

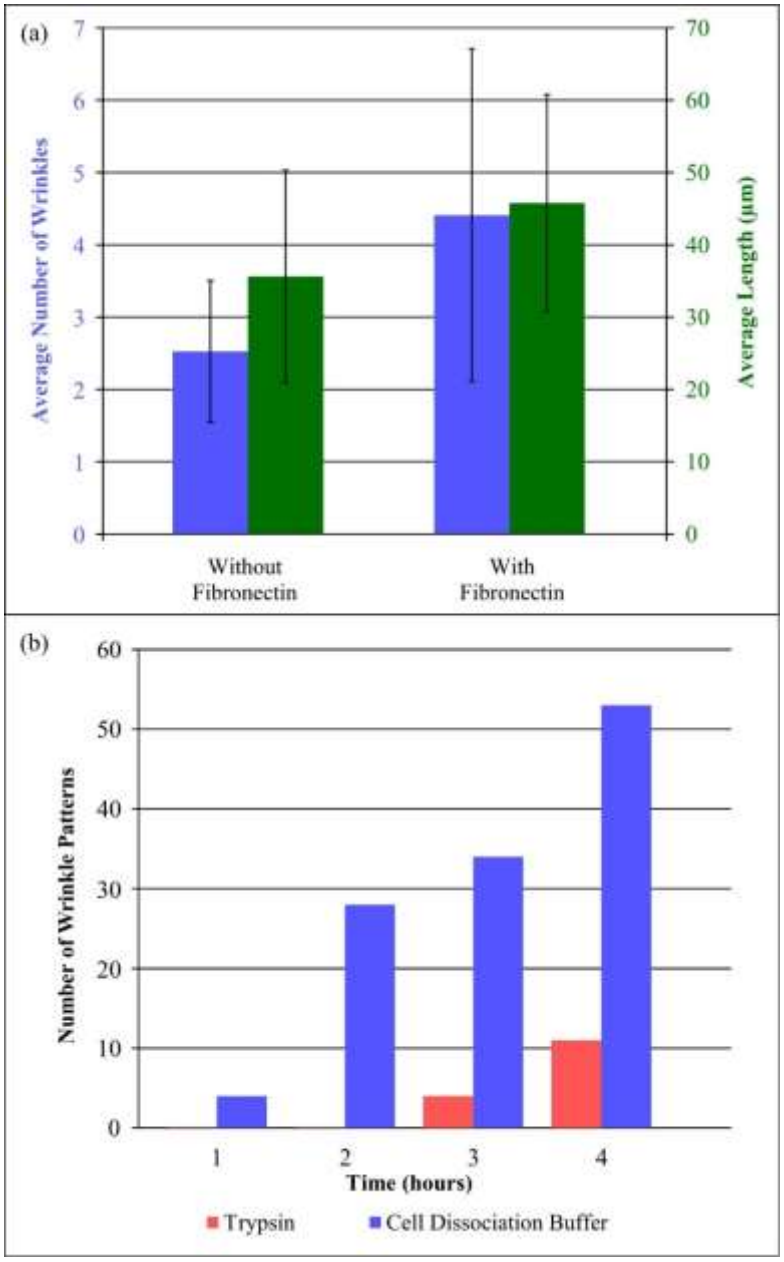

Figure 2.8. Comparing Cell Transfer Methods and Adhesion Promoting Proteins
(a) Plot of the total number of wrinkle patterns generated over time after being transferred using either trypsin or a cell dissociation buffer, n=3. (b) Plot of the average attributes of a wrinkle pattern generated by RT4 cells after 12 hours in either unmodified devices or devices coated with fibronectin.

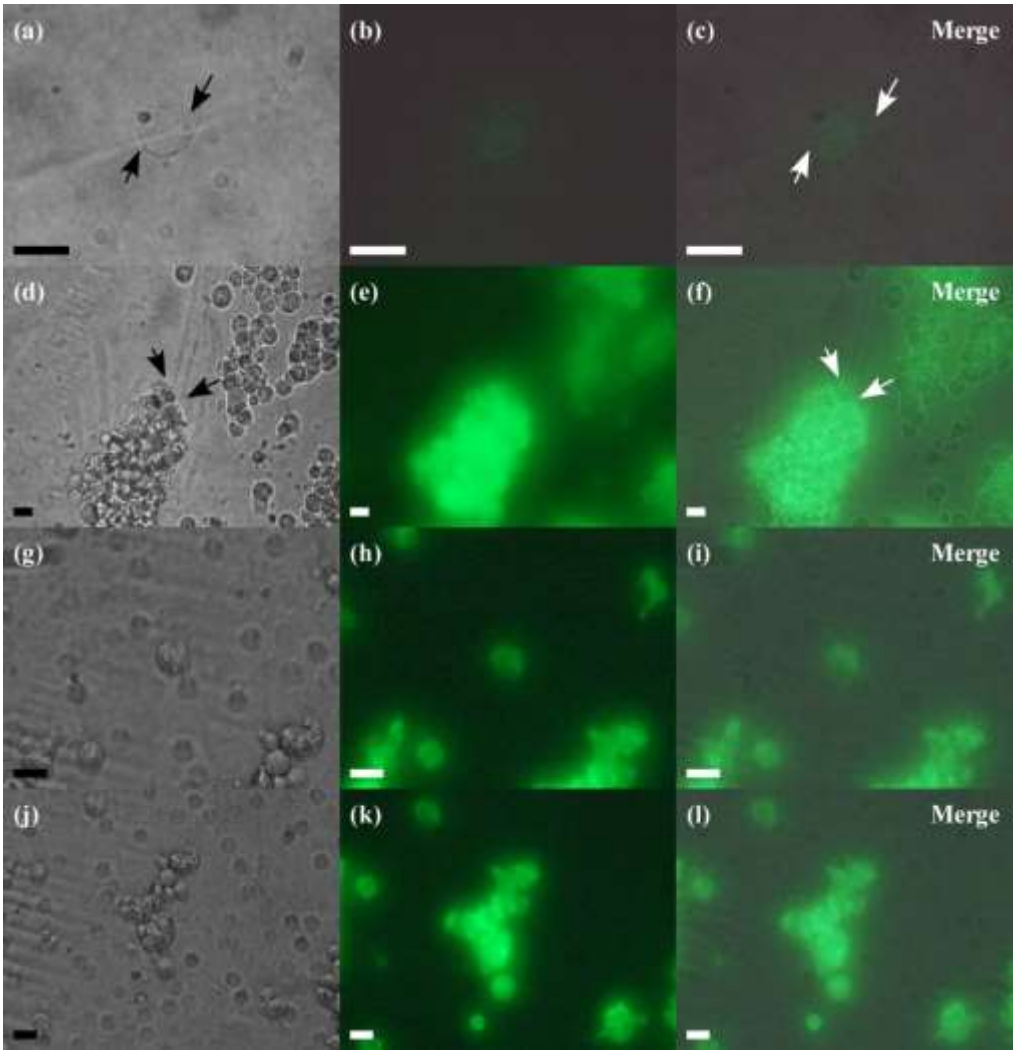

Figure 2.9. Fluorescent Staining of F-Actin in Cells Which Generate Wrinkle Patterns (a) A fixed individual T24 cell generating a wrinkle pattern consisting of 2 wrinkles with an average length of 40 μm. (b) Fluorescently stained F-actin in the T24 cell from (a). (c) Merge of (a) & (b) where both images are 60% opaque. (d) A fixed cluster of T24 cells generating a wrinkle pattern consisting of 2 wrinkles with an average length of 60 μm. (e) Fluorescently stained F-actin in the T24 cell cluster from (d). (f) Merge of (d) & (e) where both images are 60% opaque. (g) A fixed individual HEK293f cell. (h) Fluorescently stained F-actin in the HEK293f cell from (g). (i) Merge of (g) & (h) where both images are 60% opaque. (j) A fixed cluster of HEK293f cells. (k) Fluorescently stained F-actin in the cluster of HEK293f cells from (j). (l) Merge of (j) & (k) where both images are 60% opaque. All cells were fixed after more than 12 hours. All scale bars are 20 μm.

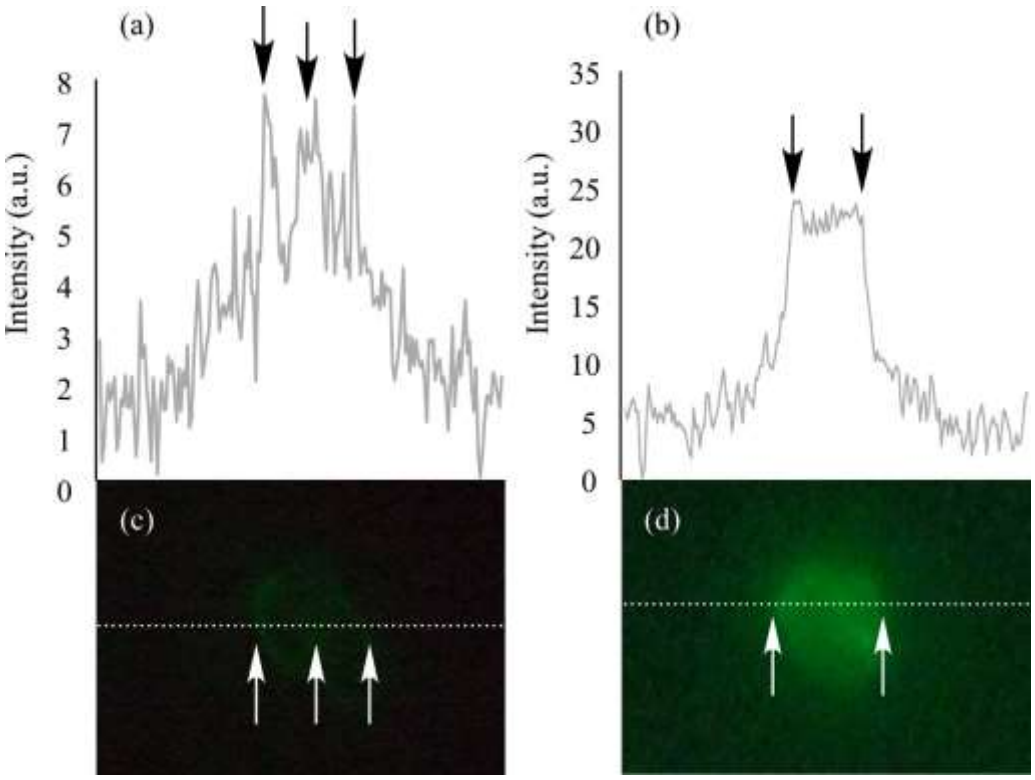

Figure 2.10. Fluorescent Intensity Traces Comparing F-Actin in T24 & HEK293f Cells (a) & (b) are intensity traces which follow the dashed white lines in (c) and (d) respectively, (c) is a fluorescently stained T24 cell and (d) is a fluorescently stained HEK293f cell. Arrows indicate spikes the corresponding areas responsible for spikes in the intensity traces. All scale bars are 20 μm.

Patient	Sex / Age	Urine Collection Method	Cystoscopy	Cytology	Diagnosis	Wrinkle Patterns	Number of Wrinkle Patterns
1	M / 53	TURBT	(10/23/2014) recurrence of bladder tumor at right UO, possibly involving distal right ureter	(10/23/2014) few atypical papillary-like structures are seen associated with bland appearing urothelial cells. The findings are atypical.	non-invasive papillary carcinoma low grade	Yes	2
2	M / 71	TURBT	small papillary recurrence at bladder neck on recent surveillance cysto	(11/05/2014) Negative for malignancy	non-invasive papillary carcinoma low grade	Yes	2
3	M / 89	TURBT	(11/6/2014) recurrent small bladder tumor near L UO	(11/05/2014) Negative for malignancy	non-invasive papillary urothelial carcinoma low grade	Yes	1
4	M / 80	TURBT	Not Available	(11/6/2014) atypical, there are cells with hyperchromatic nuclei, irregular nuclear contour and prominent nucleoli. Differential diagnosis includes reactive changes and neoplasia.	non-invasive papillary urothelial carcinoma high grade	Yes	1
5	M / 67	TURBT	Not Available	cytology (11/3/2014) suscipicious for malignancy (urothelial cells with enlarged nuclei, high N:C ratios and irregular nuclear contours.)	non-invasive papillary carcinoma high grade	Yes	5
6	F / 26	Urination	Not Applicable	Not Applicable	No Cancer	No	NA

Table 2.1. Comparison of Clinical Patient Diagnosis Methods and Wrinkle Pattern Detection. Relevant patient information including sex, age, prior cystoscopy and cytology results as well as the observation of wrinkle pattern formation and the aggregate number of wrinkle patterns for each patient sample if applicable.

CHAPTER 3

ULTRA-THIN ELASTOMER MEMBRANE ARRAY WRINKLING FOR BLADDER CANCER DIAGNOSIS

Reproduced with permission from IEEE. Appel, J.H., Sin, M.L.Y., Liao, J.C., Chae, J. "Ultra-thin elastomer membrane array wrinkling for bladder cancer diagnosis" Micro Electro Mechanical Systems (MEMS), 2016 IEEE 29th International Conference, 24-28 Jan. 2016

3.1. Abstract

We report an ultra-thin silicone membrane array to simultaneously discern the presence of cancerous cells in as many as 16 samples from multiple individuals. This high throughput parallel array relies on the intrinsic and specific biophysical properties of cancerous cells to induce deformation, or 'wrinkling' on the arrayed membrane. In contrast, non-cancerous cells fail to generate these membrane wrinkles. We evaluated an initial pilot study to test clinical urine samples from patients at a high risk for bladder cancer. We also expanded the functionality of the ultra-thin membrane array beyond bladder cancer toward the screening of cervical cancer. This screening array has the potential to be deployed at the point-of-care to improve throughput compared to sequential analysis by individual membranes and may be able to enhance reliability and accuracy by coordinating controls for false results concurrently.

3.2. Introduction

There are 17,986 active cytopathologists in the United States of America as of 2010 (Robboy et al., 2009). These experts must sequentially and tediously examine a myriad of patient samples, looking for cellular morphological features which may

indicate the presence of cancer or other diseases. While the workflow has been partially automated through the use of image assisted screening (Biscotti et al., 2005), full automation is challenged by the complex nature of the samples and the reliance upon these experts for interpretation of patient samples.

Cytopathogists exclusively examine the morphology of cells extracted from patient samples. However the inherent biophysical properties of cells may in fact aid cytopathologists in process of discerning cancerous cells from non-cancerous cells. It has been found that cancerous cells are in general more flexible, malleable, and stretchable. This was as shown by significant differences in cytoskeletal Young's modulus, fluidity, and cell traction forces (Coughlin et al., 2013; M Lekka et al., 1999; Z. Li et al., 2009). Various methods were used to analyze these differences. For example, Lekka *et al*. measured Young's modulus using scanning force microscopy. They found that the Young's modulus of bladder cancer cells were approximately an order of magnitude smaller, 0.4 ± 0.3 to 1.4 ± 0.7 Pa, compared to normal, non-cancerous cells, 10 ± 4.6 to 12.9 ± 4.8 Pa (M Lekka et al., 1999). Cellular fluidity was measured by Coughlin et al. using cellular adhesion to magnetic beads. They found a correlation between metastatic capabilities and cellular fluidity, where the more "fluid-like" a cell is the greater the likelihood of metastasis (Coughlin et al., 2013). Cell traction forces were measured by Li *et al*. using a silicon nanowire array. Three cell types were applied to the array such that cell traction forces could be compared between non-cancerous and cancerous cells. They found that cancerous cells generate between 22 and 50 % more cell traction force, 2.8 to 3.5 μN, than non-cancerous cells, 2.25 μN (Z. Li et al., 2009). These findings support the observation that cancerous cells have significantly different biophysical properties from

non-cancerous cells. Along with standard techniques the differences in biophysical properties can be used to assist cytopathologists in identifying cancerous cells. Additionally these differences may allow for, and even aid in the development of additional automation techniques within the field of cytopathology.

Cell adhesion and migration upon a surface generates traction forces, which induce easily indefinable localized deformation on a sufficiently thin membrane. Harris *et al*. reported a silicone membrane that visualized the traction forces generated by chick heart fibroblast cells during cellular locomotion. They approximated these forces, using a flexible weighted probe, to be in the range of 10 nN/μm of leading cell edge (A. Harris et al., 1980). Further refinement of this approach has included embedding fluorescent beads within the membrane to aid in tracking cell locomotion (Oliver, Dembo, & Jacobson, 1995) and modeling to extract the magnitude and direction of cellular traction forces (Dembo, Oliver, Ishihara, & Jacobson, 1996).

We presented a proof of concept study on a visualization platform to distinguish the presence of cancerous cells in mixed cell populations based on the inherent biophysical differences between cancerous and non-cancerous cells (J. H. Appel, Ren, Sin, Liao, & Chae, 2016). This visualization platform consisted of an ultra-thin silicone membrane which both cancerous and non-cancerous cells adhered to however cancerous cells exclusively deformed the membrane generating wrinkle patterns. This preliminary work established the working mechanisms of the visualization platform and determined its effectiveness; however a substantial challenge remains unsolved: only one patient sample could be evaluated at a time.

Herein, we present an ultra-thin membrane array for use within the field of cytopathology for the simultaneous analysis of clinical urine samples extracted from individuals with a history of bladder cancer. Additionally we expand beyond screening for bladder cancer into applications for cervical cancer, where cytopathology is the cornerstone of the screening protocol. By capitalizing on the inherent biophysical differences between cancerous and non-cancerous cells our ultra-thin membrane array offers cytopathogists a highly paralleled, high throughput screening tool for bladder cancer and potentially cervical cancer.

3.3. Materials and Methods

Visualization array platform – fabrication. Fabrication of the ultra-thin silicone membrane begins by coating a glass slide with high viscosity (12,500 cP) liquid silicone, as shown in figure 3.1. (a). Then we invert the slide over a low flame (Bunsen burner) effectively cross-linking the polymer chains in the liquid silicone forming a thin crust or membrane. After sanitizing (20% ethanol) the
microtiter insert, i.e. array structure, we apply a layer of vacuum grease to it and press it onto the glass slide creating a water tight seal in the area surrounding the membrane, figure 3.1. (b).

Visualization array platform – characterization. The physical properties of our ultra-thin silicone membrane were characterized with the addition of minute water droplets to its surface (J. H. Appel et al., 2016). Briefly, water droplets applied to a sufficiently thin membrane induce deformation in that membrane which results in a sinusoidal wrinkle pattern. Using the equations derived by Cerda *et al*. (Cerda & Mahadevan, 2003) we can derive the thickness of the membrane based on the number of individual wrinkles present

in each wrinkle pattern. The thickness of each membrane was determined from the observed number of wrinkles caused by the addition of water droplets to the membrane (figure 3.2. (a)). Due to inconsistences in the fabrication of the large scale membrane and the application of the microtiter insert, membrane thickness varies (figure 3.2. (b)). However the average thickness is 89 nm with a standard deviation of 30. Despite this inherent variation, membranes were still well within an acceptable thickness range.

Cell culture. T24 transitional bladder cancer cells were grown in McCoy's 5A modified media (Life Technologies Corp. 16600-082) supplemented with 10% fetal bovine serum (FBS Life Technologies Corp. 10082-139) and 1X penicillin/ streptomycin (Sigma-Aldrich Co. P4333-20ML) and incubated at 37 ˚C in humidity and 5% CO_2. Human embryonic kidney cells, HEK293f and cervical cancer cells, HeLa, were grown in eagle's minimum essential medium (ATCC 30-2003) supplemented with 10% FBS and 1X penicillin/streptomycin incubated at 37˚C in humidity and 5% CO_2.

Sample preparation – cell-line derived. Cells at 80% confluency were trypsinized for 5 min at 37˚C, inactivated with 10% FBS, pelted by centrifugation at 300 times gravity for 5 min, re-suspended in culture media and approximately $3x10^4$ cells, at a concentration of 150 cells/µL, were applied to each sub-section of the array. Cells were imaged after 24 hours exposure to the ultra-thin membrane array using a confocal microscope (Nikon Eclipse TE2000-U).

Sample preparation – patient samples. Clinical samples were collected via urination from 3 individuals undergoing routine screening for bladder cancer due to a history of bladder cancer. These samples were spun at 300 times gravity, washed twice with 1X PBS and re-suspended in culture media prior to application to the ultra-thin silicone membrane

array. After 24 hours exposure to the ultra-thin membrane wells were examined using a standard inverted microscope for the presence of wrinkle patterns.

3.4. Results and Discussion

Following the characterization of our ultra-thin silicone membrane array, we explored our device for discerning the presence of cancerous cells. We separately incubated $3x10^4$ T24 bladder cancer cells, HeLa cells derived from cervical cancer, and human embryonic kidney epithelial HEK293f cells on our membranes. After 24 hours of incubation on the ultra-thin membrane array T24 cells (figure 3.3. (a)), and HeLa cells (figure 3.3. (b)) both generate easily discernable wrinkle patterns, which each consist of 4 and 5 individual wrinkles and an average wrinkle length of 62.5 μm and 48 μm, respectively. However, 24 hours following adhesion to the membrane, HEK293f cells failed to induce any wrinkles (figure 3.3. (c)). Both bladder and cervical cancerous cells exerted significantly stronger adhesion forces on the membrane array when compared to non-cancerous cells.

Consistency within the array structure is vital to discerning capabilities particularly in the field of cytopathology, where each cell must be examined individually for the presence of cancer. Therefore we evaluate the ultra-thin silicone membrane array in terms of individual wells and the full array. We evaluated a full array using T24 bladder cancer cells and found that 50% of the wells identified the presence of cancerous cells via wrinkle pattern generation. This inconsistency directly justifies having an array of ultra-thin membranes to incorporate redundancy, and consequently reduce the potential for false negatives. There are two distinguishing features of wrinkle patterns, the number of wrinkles and the length of those wrinkles. Within this array an average

number and length of wrinkles of 2.88 and 39.88 μm, respectively, demonstrating consistent wrinkle pattern formation in the array (figure 3.4. (a)).

Additionally we aim to expand beyond the exclusive discerning of bladder cancer, such that we can screen patients for many varieties of cancers using the ultra-thin membrane array. Therefore we have examined the adhesion of cervical cancer cells on the ultra-thin silicone membrane array and found that 81% of wells identified the presence of cervical cancer via wrinkle pattern formation. Within this array an average number and length of wrinkles of 3.08 and 68 μm, respectively, demonstrating consistent wrinkle pattern formation in the array (figure 3.4. (b)).

The number and length of wrinkles are allow us to approximate the forces generated by the cell to form wrinkle patterns. However these parameters are of little significance in application because the mere presence of a single wrinkle pattern indicates that a cancerous cell has been discerned and that further investigation should be undertaken. Therefore the ultra-thin membrane theoretically has the potential to complement and improve the field of cytopathology. Specifically the arrayed version of the ultra-thin membrane can greatly enhance the through-put of cytopathology, due to the simplification of cancer cell screening and the multiplexing of patient samples.

With institutional review board approval, urine samples were collected from three patients with a history of bladder cancer, who were undergoing routine surveillance, bladder endoscopy (cystoscopy) and cytology (Cheung et al., 2013) at the VA Palo Alto Health Care System (table 3.1.). These patient urine samples were introduced to and analyzed on a single membrane array, occupying 2, 2, and 4 wells, respectively based on sample volume and the concentration of cells in each sample. After 24 hours exposure to

the ultra-thin membrane array the cells extracted from these patient samples failed to generate membrane wrinkles. The absence of wrinkle pattern formation suggests that cancerous cells were not present in the urine samples. Indeed, our membrane array results were confirmed by cystoscopy which was normal in two patients and the third individual had an insignificant, benign lesion. Our membrane array has simultaneously screened three patients and has the potential to concurrently screen 16 patients.

This demonstrates that our ultra-thin membrane array putatively does not generate false positive results. With further testing of patient samples we can continue to verify this trend and insure that true positives are indeed detected. Most importantly this initial clinical testing shows that non-cancerous cells extracted from patient urine samples, which included fragmented cells and bacteria do not interfere with the screening for bladder cancer. This implies that the ultra-thin membrane array truly has the potential to successfully screen patient samples in cytopathologic situations and with further adaption, such as robotic microscopy and image recognition, the potential to fully automate the field of cytopathology.

3.5. Conclusions

We present that an ultra-thin silicone membrane array which can serve as a cytopathology tool, i.e. a visualization platform to differentiate between cancerous and non-cancerous cells based on membrane wrinkle patterns. Our system exploits a fundamental difference in cell biophysical properties, ensuring the accuracy and sensitivity for cancer detection. It also vastly improves throughput as up to 16 patient samples can be tested and analyzed concurrently. With further development this high through-put ultra-thin membrane array has the potential to automate the field of

cytopathology reducing the time and cost associated with cancer screening and vastly improving patient prognosis through rapid screening and early diagnosis.

Appel, J. H., Ren, H., Sin, M. L. Y., Liao, J. C., & Chae, J. (2016). Rapid bladder cancer cell detection from clinical urine samples using an ultra-thin silicone membrane. Analyst, 141, 652-660. doi:10.1039/c5an01616a

Biscotti, C. V., Dawson, A. E., Dziura, B., Galup, L., Darragh, T., Rahemtulla, A., & Wills-Frank, L. (2005). Assisted primary screening using the automated ThinPrep Imaging System. American Journal of Clinical Pathology, 123, 281-287.

Cerda, E., & Mahadevan, L. (2003). Geometry and Physics of Wrinkling. Physical Review Letters, 90, 1-4. doi:10.1103/PhysRevLett.90.074302

Cheung, G., Sahai, A., Billia, M., Dasgupta, P., & Khan, M. S. (2013). Recent advances in the diagnosis and treatment of bladder cancer. BMC medicine, 11, 13. doi:10.1186/1741-7015-11-13

Coughlin, M. F., Bielenberg, D. R., Lenormand, G., Marinkovic, M., Waghorne, C. G., Zetter, B. R., & Fredberg, J. J. (2013). Cytoskeletal stiffness, friction, and fluidity of cancer cell lines with different metastatic potential. Clinical & experimental metastasis, 30, 237-250. doi:10.1007/s10585-012-9531-z

Dembo, M., Oliver, T., Ishihara, a., & Jacobson, K. (1996). Imaging the traction stresses exerted by locomoting cells with the elastic substratum method. Biophysical journal, 70, 2008-2022. doi:10.1016/S0006-3495(96)79767-9

Harris, A., Wild, P., & Stopak, D. (1980). Silicone Rubber Substrata : A New Wrinkle in the Study of Cell Locomotion Author (s): Albert K . Harris , Patricia Wild and David Stopak Reviewed work (s): Source : Science , New Series , Vol . 208 , No . 4440 (Apr . 11 , 1980), pp . 177-179 Publish. Science (New York, N.Y.), 208, 177-179.

Lekka, M., Laidler, P., Gil, D., Lekki, J., Stachura, Z., & Hrynkiewicz, a. Z. (1999). Elasticity of normal and cancerous human bladder cells studied by scanning force microscopy. European biophysics journal : EBJ, 28, 312-316.

Li, Z., Song, J., Mantini, G., Lu, M.-Y., Fang, H., Falconi, C., . . . Wang, Z. L. (2009). Quantifying the traction force of a single cell by aligned silicon nanowire array. Nano letters, 9, 3575-3580. doi:10.1021/nl901774m

Oliver, T., Dembo, M., & Jacobson, K. (1995). Traction forces in locomoting cells. Cell motility and the cytoskeleton, 31, 225-240. doi:10.1002/cm.970310306

Robboy, S. J., Weintraub, S., Horvath, A. E., Jensen, B. W., Alexander, B., Fody, E. P., . . . Black-Schaffer, S. (2009). Pathologist Workforce in the United States I . Development of a Predictive Model to Examine Factors Influencing Supply. Archives of Pathology and Laboratory Medicine, 137, 1723-1732. doi:10.5858/arpa.2013-0200-OA

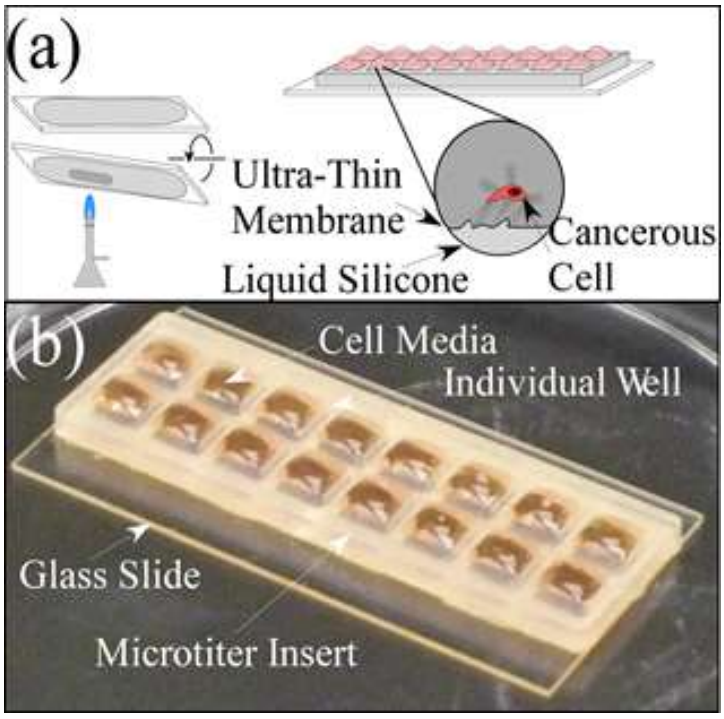

Figure 3.1. Schematic and photo of the visualization array platform. (a) Coat a glass slide with 12,500 cps liquid silicone. Cross-link the polymer using heat to form the ultra-thin membrane. Using vacuum grease adhere the array structure, i.e. microtiter insert, to the glass slide and fill wells with culture media and cells. (b) The completed ultra-thin silicone membrane 8x2 array, with a well footprint of 6.5 x 6.5 x 3.2 mm^3.

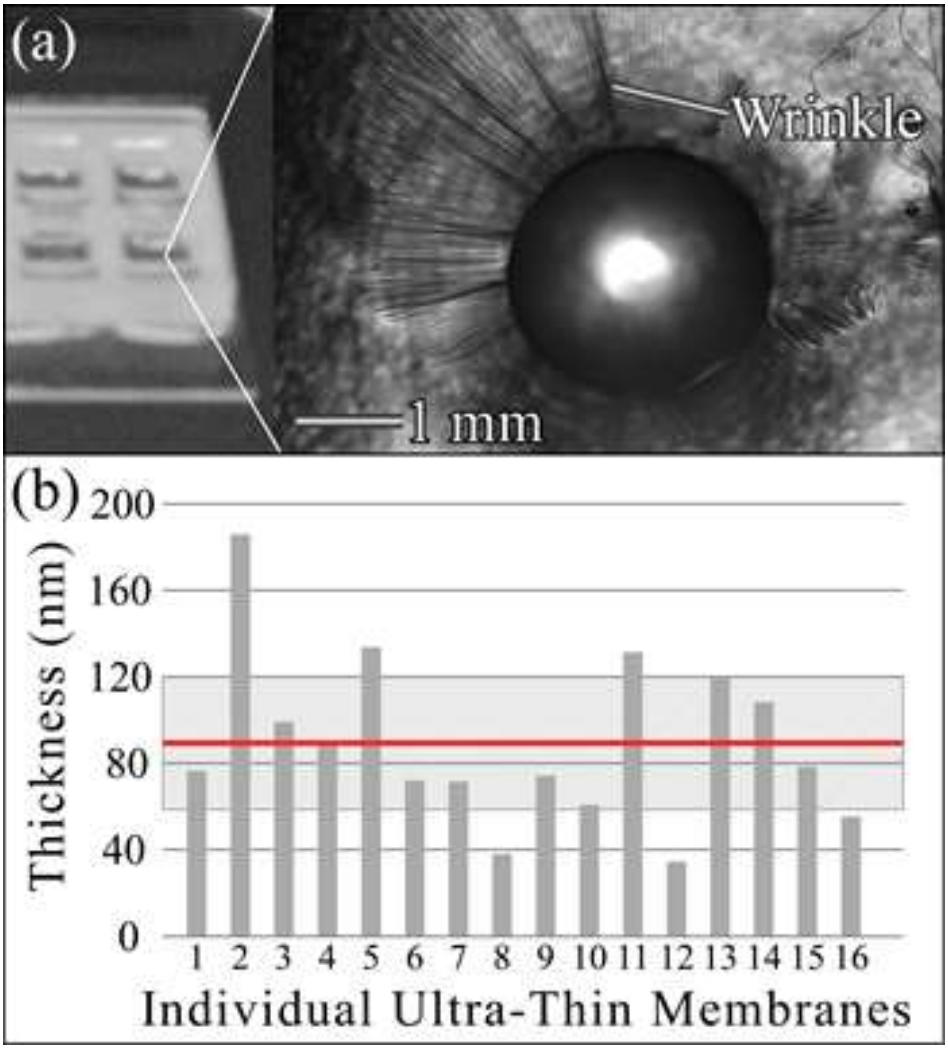

Figure 3.2. Characterization of the visualization array platform. (a) Exemplary ultra-thin membrane well during characterization via water droplet. (b) Variation in membrane thickness, average thickness delineated by the red line and standard deviation by the gray rectangle.

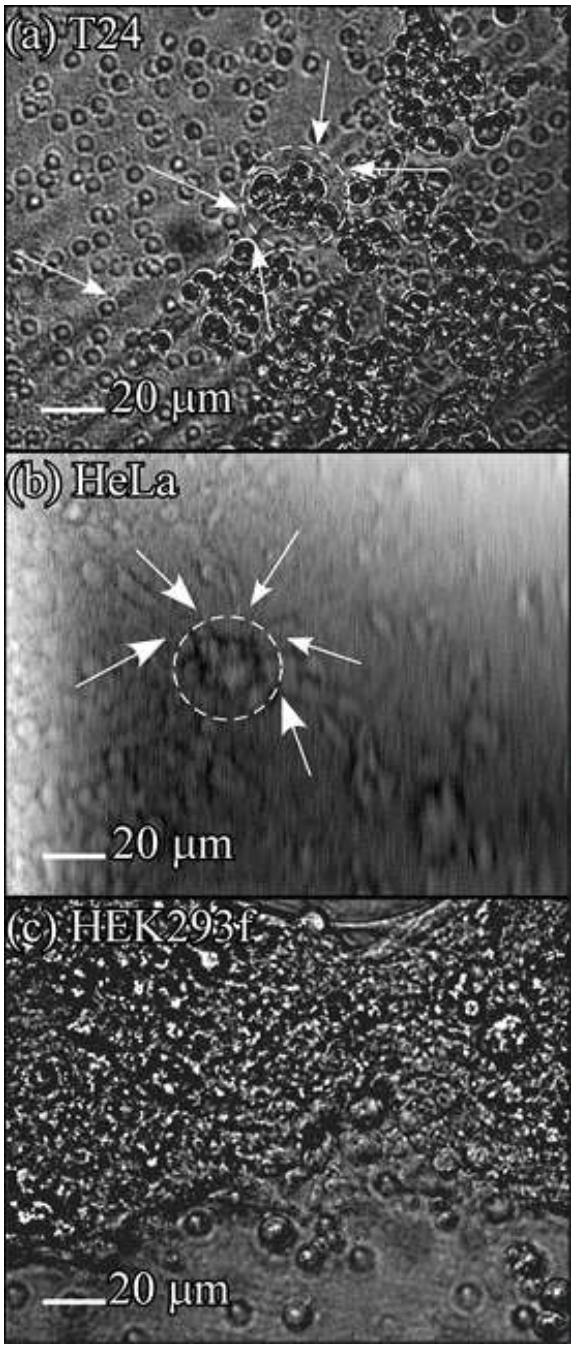

Figure 3.3. Various wrinkle patterns or lack thereof generated by cell-line derived samples. (a) Wrinkle pattern generated by bladder cancer cells. (b) Wrinkle pattern generated by cervical cancer cells, (dashed enclosures indicate the cluster of cells which generate each wrinkle pattern and arrows indicate the individual wrinkles). (c) Non-cancerous (HEK293f) cells after 24 hours of incubation: Pre-existing wrinkles formed during membrane fabrication are NOT distorted by the adhesion of HEK293f.

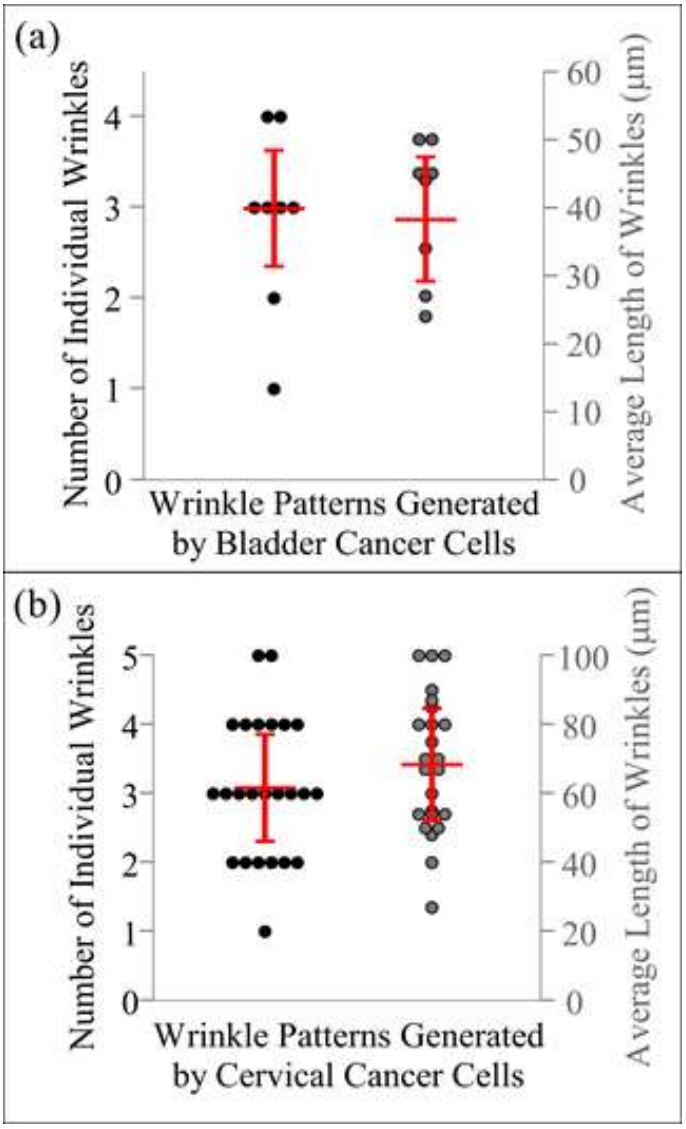

Figure 3.4. Characterization of wrinkle patterns within an array. (a) Characterizing wrinkle patterns generated in a single array by T24 cancerous bladder cells after 24 hours in contact with the ultra-thin membrane, 8 wrinkle patterns were observed. (b) Characterizing wrinkle patterns generated in a single array by HeLa cancerous cervical cells after 24 hours in contact with the ultra-thin membrane, 24 wrinkle patterns were observed.

Sex/Age	Endoscopy	Cytology	Diagnosis	Wrinkle Patterns
M/57	Normal	Negative	Normal	No
M/82	Normal	Negative	Normal	No
M/68	Insignificant lesion	Negative	Normal	No

Table 3.1. Comparison of clinical diagnosis methods and wrinkle pattern detection. Relevant patient information including sex, age, prior cystoscopy and cytology results as well as array-based ultra-thin membrane diagnosis via observation of wrinkle pattern formation.

CHAPTER 4

LOW CYTOTOXICITY AND GENOTOXICITY OF TWO-DIMENSIONAL MOS_2 AND WS_2

Reproduced with permission from American Chemical Society. Appel, J.H., Li, D.O., Podlevsky, J.D., Green, A.A., Wang Q.H., Chae J., "Low Cytotoxicity and Genotoxicity of Two-Dimensional MoS2 and WS2" ACS Biomaterials Science and Engineering, 2016, 2 (3) 361-367 DOI 10.1021/acsbiomaterials.5b00467

4.1. Abstract

Atomically thin transition-metal dichalcogenides (TMDs) have attracted considerable interest because of their unique combination of properties, including photoluminescence, high lubricity, flexibility, and catalytic activity. These unique properties suggest future uses for TMDs in medical applications such as orthodontics, endoscopy, and optogenetics. However, few studies thus far have investigated the biocompatibility of mechanically exfoliated and chemical vapor deposition (CVD)-grown pristine two-dimensional TMDs. Here, we evaluate pristine molybdenum disulfide (MoS_2) and tungsten disulfide (WS_2) in a series of biocompatibility tests, including live-dead cell assays, reactive oxygen species (ROS) generation assays, and direct assessment of cellular morphology of TMD-exposed human epithelial kidney cells (HEK293f). Genotoxicity and genetic mutagenesis were also evaluated for these materials via the Ames-Fluctuation test with the bacterial strain S. typhimurium TA100. Scanning electron microscopy of cultured HEK293f cells in direct contact with MoS_2 and WS_2 showed no impact on cell morphology. HEK293f cell viability, evaluated by both live-dead fluorescence labeling to detect acute toxicity and ROS to monitor for apoptosis, was

unaffected by these materials. Exposure of bacterial cells to these TMDs failed to generate genetic mutation. Together, these findings demonstrate that neither mechanically exfoliated nor CVD-grown TMDs are deleterious to cellular viability or induce genetic defects. Thus these TMDs appear biocompatible for future application in medical devices.

4.2. Introduction

Transition metal dichalcogenides (TMDs) are a class of layered materials with the general formula MX_2, where M represents a transition metal (Mo, W, Ta, Nb, etc.) and X represents a chalcogen (S, Se, Te). In the past few years, studies of atomically-thin 2D TMDs have expanded rapidly due to their impressive electrical, optical, and structural properties (Neto & Novoselov, 2011; M. Xu, Liang, Shi, & Chen, 2013). Semiconducting TMDs like MoS_2 and WS_2, have band gaps that transition from indirect to direct when their thicknesses are reduced from bulk to monolayer (Mak, Lee, Hone, Shan, & Heinz, 2010; Song, Hu, & Zeng, 2013). Monolayer TMDs have been integrated into field-effect transistors which possess both high on/off current ratios and reasonable carrier mobilities (Q. H. Wang, Kalantar-Zadeh, Kis, Coleman, & Strano, 2012), good photoluminescence at room temperature (He et al., 2015), and high elastic strength (Castellanos-Gomez et al., 2012). In the biomedical fields, fullerene-like TMD nanoparticles have been used for their tribological properties to reduce friction in numerous applications (R Tenne, 2003; Reshef Tenne, 2013; R. Tenne & Seifert, 2009). Solid lubricants containing fullerene-like WS_2 were commercialized in 2008 (Reshef Tenne & Redlich, 2010). In orthodontia, WS_2 nanoparticles have been embedded in the stainless steel wires used to manipulate teeth, and Redlich *et al*. reported that incorporation of WS_2 reduced overall frictional force in

this application by 54% (Redlich et al., 2008). Additional tribological applications include gels impregnated with WS_2 or MoS_2 nanoparticles to reduce friction in endoscopic procedures9 and bone tissue engineering (Lalwani et al., 2013).

Despite existing biomedical applications using TMDs and the still-emerging applications of 2D TMDs, few investigations into the biocompatibility and toxicity of TMDs have been performed. So far, initial in vivo toxicology tests of fullerene-like WS_2 nanoparticles on mammals found no toxic effects (Redlich et al., 2008). Cytotoxicity examinations of fullerene-like MoS_2 and WS_2 on human cell-lines, salivary gland cells (Goldman et al., 2015) and A549 (Wu et al., 2011), found that they are non-toxic to cells as cell viability remained high after prolonged exposure to TMDs (Goldman et al., 2015; Wu et al., 2011). Recently, Teo *et al*. reported the varying cytotoxicity of lithiated forms of WS_2, MoS_2 and WSe_2, which are chemically and electronically different from their pristine forms. In that study, human lung carcinoma epithelial cells (A549) were used to show that lithiated WS_2 and MoS_2 are extremely biocompatible while lithiated WSe_2 caused dose-dependent toxicological effects (Teo et al., 2014). Although lithiated TMDs are being explored as vectors for drug delivery and photothermal therapy (Liu et al., 2014), these chemically treated TMDs possess metallic conductivity and thus lack the highly desirable photoluminescent properties of pristine TMDs. These fundamental differences in the electronic and optical properties of lithiated and pristine TMDs suggest that these phases may also interact with biological systems in very different ways. Moreover, future medical application of TMDs in areas like optogenetics will require pristine materials that retain their fluorescence. Consequently, there is an urgent need for

systematic and in-depth biocompatibility and toxicity studies on pristine, unfunctionalized TMDs.

Here we report a detailed study examining the biocompatibility of pristine two-dimensional WS_2 and MoS_2 toward human epithelial kidney cells, HEK293f. Studying the impact of fine particulates on HEK293f is particularly relevant because particulates of this kind have the tendency to accumulate in the kidneys (Ballestri et al., 2001; Takenaka et al., 2001). We examine the effects of culturing HEK293f cells directly in contact with large flakes, or sheets, of thin TMDs using a fluorescent calcein-AM/ethidium homodimer-1 live/dead assay and a fluorogenic probe designed to measure reactive oxygen species (ROS) in live cells. We also examined the potential bacterial mutagenicity of these 2D nanoparticulates by performing an Ames-Fluctuation assay using S. typhimurium TA100. Our comprehensive set of experiments show that 2D and particulate forms of TMDs exhibit very low cytotoxicity and genotoxicity effects and are thus attractive materials for future biomedical applications.

4.3. Materials and Methods

TMD synthesis – flakes and sheets. Crystalline flakes of TMDs were exfoliated from bulk crystals of WS_2 (2D Semiconductors) and MoS_2 (SPI Supplies) using the scotch tape method onto substrates (silicon wafers with 300 nm SiO_2 and oxygen plasma treated PDMS). Large area sheets of MoS_2 were synthesized using chemical vapor deposition onto SiO_2/Si substrates that were cleaned by sonication in acetone for 5 min, in isopropanol for 5 min, and oxygen plasma for 10 min. The precursors were 15 mg molybdenum trioxide, MoO_3 (≥99.5%, Sigma-Aldrich) and 100 mg sulfur, S (99.5%, Alfa Aesar). Growth occurred in a 1-inch diameter tube furnace (Lindberg). The MoO_3

precursor was placed in the center of the heating zone in a quartz boat with the SiO_2/Si substrate placed above it, face down. The S was placed at the edge of the heating zone. The CVD growth occurred at vacuum pressure (1.37 Torr) with 300 sccm Ar gas flow. The furnace was first heated to 650°C at a rate of 16°C/min, held at 650°C for 30 min, and rapidly cooled to room temperature. The mechanically exfoliated and CVD-grown samples were used for the live-dead assay and the SEM assay.

TMD synthesis – particulates. TMD particulates were prepared from bulk WS_2, bulk MoS_2, and CVD-grown MoS_2 by ultrasonic bath sonication. Fragments of bulk MoS_2 and WS_2 weighed, placed in sterile water or tissue culture media and submerged in an ultrasonic bath until only the ultra-fine particulates remain. CVD particulates were prepared by sonicating the MoS_2-covered SiO_2/Si substrates until all traces of MoS_2 were removed from substrates. The concentrated particulate suspensions were then diluted to obtain the various concentrations used in the assays.

TMD characterization - Raman spectroscopy, scanning electron microscopy, surface charge and fluorescence. Mechanically exfoliated WS_2, mechanically exfoliated MoS_2, and CVD-grown MoS_2 were all deposited on Si wafers with a 300 nm SiO_2 capping layer. Raman spectroscopy was conducted using a WITec Alpha300R Confocal Raman Imaging System with 532 nm excitation, 300 μW laser power and a 100X objective lens.

TMD particulates were analyzed using SEM. A small amount of the liquid containing each type of fragment was placed onto a glass slide and left until completely evaporated. Then the glass slide was sputter coated with a layer of gold, approximately 10 nm thick, and imaged with a scanning electron microscope (Hitachi S-4700-II).

TMD particulates were evaluated for surface charges using a Zetasizer Nano ZS to evaluate zeta potential with a mechanically exfoliated MoS_2 particulate sample at a concentration of 1 mg/mL. TMD particulates were also evaluated for fluorescence (Horiba Nanolog) using a range of excitation wavelengths (400 nm to 600 nm) and emission wavelengths (600 nm to 800 nm). These measurements did not reveal any photoluminescence peaks attributable to MoS_2.

Cell culture. HEK293f cells (Invitrogen) were grown in Eagle's minimum essential medium (EMEM) (ATCC). Media was supplemented with 10% fetal bovine serum (FBS, Life Technologies), and 1X penicillin/streptomycin (Sigma-Aldrich). Cells were maintained in a 5% CO_2 environment at 37˚C. Cells at 80% confluency were trypsinized (Invitrogen) for 1 min at 37˚C and washed with media supplemented with 10% FBS. Approximately 10^5 cells were applied to each device and incubated in culture media with at 5% CO_2 at 37˚C.

Live-dead assay. Mechanically exfoliated tungsten disulfide, mechanically exfoliated molybdenum disulfide, CVD-grown molybdenum disulfide, silver, epoxy, graphite, and plain PDMS were prepared for the live / dead assay and all were placed on oxygen plasma cleaned PDMS substrates. Gold and silver were sputter coated onto the PDMS substrate and epoxy was mixed then spread onto the PDMS. HEK293f cells were cultured on 24 subsections of each material and incubated at 37˚C in a 5% CO_2 environment for 4, 12, 24 and 48 hours. After the desired time interval, samples were placed in a solution containing 2 μM calcein AM and 4 μM ethidium homodimer-1 (Life Technologies, viability/cytotoxicity kit for mammalian cells) and incubated at room temperature for 30

minutes, without exposure to light, then imaged under a fluorescent confocal microscope (Nikon Eclipse TE2000-U).

For the live-dead assay a minimum of 10 technical replicates of each material were examined at every time interval. The numbers of live and dead cells in direct contact with the material was tallied, and then the average percent of live cells was quantified from all samples. The standard error was also quantified for each time and material.

Cell morphology scanning electron microscopy preparation and imaging. Large flakes and sheets of each TMD was used for SEM imaging, all control materials from the live-dead assay were also imaged. HEK293f cells were cultured in direct contact with the all materials for 24 hours. Then cells were washed 3 times in PBS, fixed in 4% paraformaldehyde in 1X PBS for 10 min at 37˚C, and washed twice with 1X PBS. Samples were then dehydrated serially, 10 minute transfers through 50, 60, 70, 80, 90, and 100 % ethanol. Then devices were sputter coated with a layer of gold, approximately 10 nm thick, and imaged using a scanning electron microscope (Hitachi S-4700-II).

Reactive oxygen species (ROS) assay. TMD particulates and copper particulates were used for the ROS assay. Solid copper (8.33 mg) was placed in 1 mL of EMEM supplemented with 10 % FBS, then placed in an ultrasonic bath for seven minutes to degrade the copper into particles. HEK293f cells were cultured to 80% confluency then exposed to various concentrations of each TMD particulate (100, 10, 1, 0.1 μg/mL) and copper (8.33 mg/mL) for 1, 8 and 24 hours. After each time interval the proprietary ROS fluorogenic probe (Molecular Probes, CellROX) was added to a concentration of 5 μg/mL to the culture well and incubated for 30 minutes at 37 ˚C, then the culture well

was washed 3 times with 1X PBS to remove any unbound ROS fluorogenic probe and visualized under a fluorescent confocal microscope (Nikon Eclipse TE2000-U) using 485/520 (nm) excitation/emission.

For the ROS assay a minimum of 8 technical replicates of each TMD concentration, the positive copper control and the untreated negative control were examined at each exposure time. Fluorescence intensity was measured using ImageJ software, and then intensity was averaged over the full area of the image. Standard error was calculated by determining the standard deviation between each technical replicate and dividing by the square root of the number of technical replicates. Significance was calculated by determining the chi-squared value, in comparison to the copper-positive control, and then using a standard chi-squared distribution table to determine p-value.

Ames-fluctuation test – reverse mutation. TMD particulates were used for the Ames-Fluctuation test of reverse mutation. Particulates were sterilized using heat and 70% ethanol. The Ames-Fluctuation assay (Environmental Bio-Detection Products Inc.) was performed according to the manufacturer's instructions. Briefly, the reaction mixture containing Davis-Mingioli salts, D-glucose, bromocresol purple, D-Biotin and L-histidine was mixed with the particulates and purified water to concentrations of 100, 10, 1 and 0.1 μg/mL. TA100 bacteria, grown overnight to turbidity, was added to each concentration of TMD particulates. Each mixture was then distributed into 20 wells of a 96 well plate, along with the positive control: mutation generating sodium azide and negative control: untreated bacteria. All plates were placed in a sealed bag, to prevent evaporation, and incubated at 37˚C for 3 to 6 days. Results were read by visual inspection of each well,

with yellow or turbid wells considered positive for bacterial mutation and purple wells considered negative for mutation.

For the Ames-Fluctuation reverse mutation assay 20 wells of each sample and the controls were prepared. The number of yellow and purple wells, meaning positive and negative for mutation, respectively, were tallied and the percentage of revertants was calculated. Significance was calculated by determining the chi squared value, in comparison to the sodium azide-positive control, and then using a standard chi squared distribution table to determine p-value.

4.4. Results

Synthesis and characterization of WS_2 and MoS_2. Thin flakes of WS_2 and MoS_2 were prepared from bulk crystalline samples by mechanical exfoliation using adhesive tape. We examined mechanically exfoliated WS_2 (ME-WS_2) and MoS_2 (ME-MoS_2) flakes that were around 8 – 10 μm in diameter (Figure 4.1. (a)-(b)). Large area, continuous, thin films of bilayer, trilayer and few-layer MoS_2 were also synthesized using CVD (CVD-MoS_2) (Figure 4.1. (c)). Material size is of particular concern for cell viability because HEK293f cells are known to take up foreign materials via endocytosis (Osman et al., 2012). However, it is unlikely that the flakes or sheets of WS_2 and MoS_2 will permeate a cell membrane because they are of similar size to that of the cell (typically 20 μm in diameter). Additionally materials larger than 100 nm in diameter typically do not undergo endocytosis by HEK293f cells (Jiang et al., 2008; Osman et al., 2012).

We characterized these TMD samples using Raman spectroscopy to estimate their thicknesses, as shown in Figures 4.1. (d), 4.1. (e), and 4.1. (f). Characteristic peaks corresponding to the A1g and E12g phonons for MoS_2 and WS_2 are observed, and the

difference between them are used to identify the layer numbers. For our ME-WS_2 flakes the observed peak difference of 70.2 cm-1 corresponds to 5 to 8 atomic layers (Gutierrez et al., 2013; J. G. Song et al., 2013); for our ME-MoS_2 the difference of 21.9 cm-1 corresponds to 3 to 4 atomic layers (C. Lee et al., 2010); for our CVD-MoS_2 the difference of 20.7 cm-1 corresponds to 2 to 3 atomic layers (C. Lee et al., 2010). Material thickness is of particular concern for cell viability: if that material becomes "free floating" it may slice the cell membrane and induce death, as shown by Liao *et al*. for monolayer graphene and graphene oxide which slice red blood cells (K. H. Liao, Y. S. Lin, C. W. MacOsko, & C. L. Haynes, 2011). We avoid this issue by placing each material onto an inert substrate like polydimethylsiloxane (PDMS) or glass, where we can exclusively examine the interaction between the material surface and the cells.

Cellular viability and acute toxicity screening. To determine human cell viability following exposure to TMDs, we performed a fluorescence-based live-dead assay. HEK293f cells were exposed to ME-WS_2, ME-MoS_2 and CVD-MoS_2 for various time intervals. Then cells were fluorescently labeled as live using calcein-acetoxymethyl (calcein AM) or dead using ethidium homodimer-1. Calcein AM passively crosses the cell membrane where it is converted into green fluorescent calcein by intracellular esterases in live cells (Bratosin, Mitrofan, Palii, Estaquier, & Montreuil, 2005). Ethidium homodimer-1 exclusively enters cells via damaged cell membranes and undergoes a 40-fold enhancement of fluorescence when bound to nucleic acids in the nucleus of dead or dying cells (Skala et al., 2005). In Figure 4.2. (a)-(c), the green regions indicate living cells, while the red spots indicate the nuclei of dead cells. These images clearly show that the majority of HEK293f cells exposed to ME-WS_2, ME-MoS_2, and CVD-MoS_2 after 24

hours are alive (green) and only a few cells have died (red), indicating that these TMDs in the mechanically exfoliated and CVD-grown forms are not acutely toxic to HEK293f cells. Over time, the percentage of surviving HEK293f cells increases if those cells are in contact with ME-WS_2, ME-MoS_2, CVD MoS_2, PDMS, or graphite. In contrast, the percentage of surviving cells decreases when in contact with silver and remains low (~10%) when in contact with acutely toxic epoxy (Figure 4.2. (d)). HEK293f cells undergo mitosis at a rate of approximately once every 23 to 24 hours (Graham, Smiley, Russell, & Nairn, 1977), thus over a 48 hour time period cells should double twice. Due to the doubling rate, cells in contact with a biocompatible material show an increase in percentage of survivability. This result indicates that MoS_2 and WS_2 in these thin, large-area forms are non-toxic.

Cellular adhesion to transition-metal dichalcogenides. We investigated the nature of the interaction between cells and each material by scanning electron microscopy (SEM) imaging of HEK293f cells cultured for 24 hours in direct contact with either TMDs or epoxy as shown in Figure 4.3. The images on the left side (Figure 4.3. (a), (c), (e)) provide an overview of cells interacting with large surface areas of each material. The images on the right side (Figure 4.3. (b), (d), (f)) show a magnified view of HEK293f interaction with each material. In the case of ME-WS_2, ME-MoS_2, and CVD-MoS_2, filopodia spread upon the surface of each respective material indicating good cellular adhesion and healthy cell morphology. Additionally, cells interact directly with each respective material, as observed directly by the presence and arrangement of filopodia. In contrast, in Figure 4.3. (g)-(h) cells up to 300 μm away from epoxy and in direct contact show the same rounded morphology, which indicates cellular toxicity. Observations

based on control materials, PDMS, graphite, and silver are provided in Figure 4.4. These comparison materials were chosen due to their range of biocompatibilities, from the very biocompatible graphite (G. Y. Chen et al., 2012) and PDMS (Łopacińska, Emnéus, & Dufva, 2013) to cytotoxic silver (de Lima, Seabra, & Durán, 2012) and acutely toxic epoxy. The observed interaction between HEK293f cells and TMDs indicates that not only cells are viable when exposed to TMDs but they thrive in contact with them.

Oxidative stress assays. In biomedical implants, particulates are generated as the body breaks down implanted materials (Anderson, Rodriguez, & Chang, 2008), which can then infiltrate cells and interfere with basic cellular function. This process occurs by exposing the implant to a harsh, low pH environment; encapsulating it in proteins and eventually fibrous tissue; and surrounding it with macrophage cells that combine to form foreign body giant cells (Anderson et al., 2008). To investigate the potential for TMD-based particulates to influence cellular activities in the body, we produced micro- to nano-scale TMD particulates and measured their influence on HEK293f cells. We produced TMD particulates by applying ultrasonic agitation to crystals of WS_2 and MoS_2, and CVD-grown MoS_2. Histograms of particulate dimensions and representative SEM images of the particulates are shown in Figure 4.5. These particulates have average diameters of about 200-300 nm. As endocytosis typically occurs in particles that are smaller than 100 nm (Jiang et al., 2008; Osman et al., 2012), the sizes of these particulates should prevent endocytosis. Additionally we evaluated ME-MoS_2 particulates for surface charges using zeta potential. This allows us to evaluate cell viability risks due to surfaces charges. We found a surface charge of -22.87 ± 0.17 mV for ME-MoS_2. Based on a previous study by Ayala *et al*., a negative surface charge should not interfere with either internal or external

cellular mechanisms (Ayala, Herrera, Latorre-Esteves, Toores-Lugo, & Rinaldi, 2013). By varying the volume of the solution-phase TMDs we added to the cell growth media, we were able to examine cellular viability after exposure to various concentrations of particulate TMDs.

Materials that are not acutely toxic can still compromise cell viability by triggering oxidative stress, which commonly induces programmed cell death (apoptosis) (Circu & Aw, 2010). We exposed cells to particulates of TMDs and looked for an elevation in the amount of reactive oxygen species (ROS) using a proprietary cell-permeable fluorogenic probe (Figure 4.6.). The fluorogenic probe is oxidized when interacting with ROS and then the oxidized form of the reagent binds to DNA and fluoresces (Elahi, Kong, & Matata, 2009). Therefore, the fluorescent intensity directly corresponds to the amount of ROS generated by the cells. We determined the fluorescence intensity as a measure of ROS level at various concentrations of particulate TMDs for multiple exposure times (Figure 4.7.) as well as for the flake/sheet forms of TMDs after 12 hours of exposure (Figure 4.8.). For comparison, we also used copper, a known generator of ROS, as a positive control (Alarifi, Ali, Verma, Alakhtani, & Ali, 2013). A CVD MoS_2 concentration of 100 µg/mL was not tested due to the difficulty in fabricating sufficient amounts of MoS_2 via CVD to achieve that concentration. Additionally we attempted to track the TMD particulates via optical microscopy, but we did not detect any photoluminescence signals even in the TMD particulate samples before cellular exposure. This is likely because we have primarily multilayer particulates that have an indirect bandgap and do not emit photoluminescence (Splendiani et al., 2010). After, one hour of exposure to TMDs, there was no significant difference in fluorescence

intensity between the untreated cells, the cells exposed to TMD particulates, and the cells exposed to copper (Figure 4.7. (a)). However, after 8 hours of exposure to TMD particulates all concentrations and the untreated cells showed a significantly lower in fluorescence intensity from the ROS-generating copper control (Figure 4.7. (b)). Corresponding p-values in Figure 4.7. of these measurements are marked with * if they are less than 0.1 or ** if they are less than 0.05. After 12 hours of exposure to TMD flakes/sheets and PDMS cells showed significantly lower fluorescence intensity from the ROS-generating copper control (Figure 4.8.). After 24 hours of exposure to TMD particulates at all concentrations and untreated cells show a significant difference in fluorescence intensity from the ROS-generating copper control (Figure 4.7. (c)). Additionally we evaluated the viability of HEK293f cells after 48 hours exposure to particulates of ME-MoS_2, and found that 98% of cells remained viable during this time period (Figure 4.9.). Measurements of ROS level show that particulates generated from ME-WS_2, ME-MoS_2 and CVD-MoS_2 do not induce ROS, even in concentrations as high as 100 μg/mL, 100 μg/mL, and 10 μg/mL, respectively. Hence, the solution phase TMD particulates do not activate this pathway to programmed cell death, even after 24 hours exposure.

Mutagenicity assays. We evaluated the effect of TMD particulates on mutagenicity using Ames-fluctuation assays. The Ames assay employs strains of Salmonella typhimurium with loss-of-function mutations in the genes for histidine synthesis. When these strains gain the ability to grow in histidine-free environments, they must do so by acquiring compensatory mutations that enable them to regain histidine synthesis capability. Consequently, when the bacteria are exposed to a mutagen, a greater fraction of them will

acquire beneficial mutations and thrive without histidine. For this study, we used S. typhimurium tester strain TA100, which has a base-pair mutation, the most common type of genetic mutation. After 3 days exposure to various concentrations of TMD particulates, the TA100 bacterial strain showed no significant mutation as shown in Figure 4.10. A significantly lower percentage of revertants was observed in untreated and TMD particulate treated samples. Significance was determined using p-values (** if they are less than 0.1 or * if they are less than 0.05) calculated referencing the positive highly mutagenic control, sodium azide. This mutation assay yields a color change triggered by the growth of bacteria, in a non-histidine environment. Although, there was a low level of mutation that occurred for each TMD concentration, ranging from 5 to 25 % of the total replicates. This was anticipated because random mutation easily occurs in this bacterial strain, as 10 to 15% of untreated negative control samples regained histidine synthesis, as shown in Figure 4.11. Thus we can extrapolate that particulate TMDs are not a mutagenic agent for TA100, and therefore do not introduce base-pair substitutions.

4.5. Discussion

The results of the wide variety of assays we have conducted all point to the excellent biocompatibility of 2D TMDs towards mammalian tissue cells and bacteria. First, our live-dead assays showed no acute toxicity. Cells touching or in close proximity to the 2D TMDs show excellent survival, as shown in Figure 4.2. In contrast to other cell viability tests that rely on the conversion of extracellular dehydrogenases (Y. Li et al., 2012), which can be influenced by the presence of nanoparticles (Woodruff et al., 2012), these fluorescence tests do not have that complication and are thus more suitable for evaluating nanostructured materials. In a previous study by Teo *et al*., lithiated forms of

WS_2 and MoS_2 are evaluated for biocompatibility, but these lithiated forms are fundamentally different than pristine TMDs in that they are metallic rather than semiconducting, and chemically quite different (Teo et al., 2014). In many potential biomedical applications for TMDs, we anticipate that the structural integrity, semiconducting electronic properties, and optical properties of pristine TMDs will be preferred over lithiated forms.

Our evaluation of cell morphology with SEM imaging of HEK293f cells showed that the cells have excellent adhesion and interaction with the TMDs as indicated by the presence of multiple filopodia In contrast, known toxic materials yielded weak adhesion and rounded cells. The only other related study to our knowledge, Goldman *et al*., examined fullerene-like WS_2 nanoparticles (Goldman et al., 2015), rather than 2D forms as we show here, which have very different physical properties.

The ROS generation tests using nano-particulates showed that TMDs have far lower levels of ROS compared to copper, a known ROS generator, for several exposure times, as shown in Figure 4.7. We observed time-dependent changes in fluorescence due to ROS that likely indicate the time necessary for HEK293f cells to undergo apoptosis, which ranges from 6 to 9 hours (Mao et al., 2007). A previous study by Kou *et al*. using lithiated nanosheets of MoS_2 also showed no significant generation of ROS (Kou et al., 2014).

Finally, since genetic modifications can lead to long-term health risks, we evaluated genotoxicity of TMD particulates using the Ames-fluctuation assay. If particulates are to induce genetic mutations, they are likely to do so by two mechanisms: (1) smaller particles can enter the cell and directly disrupt cellular activity, and (2) larger

particles can block and disrupt the function of porins, which are important for the transfer of materials into the cell. Since we have a range of particle sizes in our dispersions, it is conceivable to have both modes of genotoxicity. However, our results showed no significant genotoxicity for any of our 2D TMD preparations, as shown in Figure 4.10. Thus, we believe that the smaller particles are likely not being taken up into the cells at a significant rate, and that the larger particles are ineffective at blocking porins.

4.6. Conclusions

We have performed an extensive study of the biocompatibility of different pristine forms of the TMDs MoS_2 and WS_2. Our fluorescence-based live-dead assay, reactive oxygen species assay and mutagenic assay all strongly suggest that both 2D sheets and quasi-2D nano-particulates of WS_2 and MoS_2 are biocompatible and non-mutagenic towards HEK293f human kidney cells and S. typhimurium TA100 bacteria, respectively. We found that the TMD materials did not trigger the generation of high levels of ROS that accompanies cell death. Even after prolonged exposure to concentrations as high as 100 μg/mL of TMDs, S. typhimurium bacteria did not significantly mutate. The results of our investigation pave the way for the use of 2D ME-WS_2, ME-MoS_2, and CVD MoS_2 in medical implantations, and highlights areas where additional investigations of biocompatibility will be important for adoption into implants and other biological systems.

Alarifi, S., Ali, D., Verma, A., Alakhtani, S., & Ali, B. A. (2013). Cytotoxicity and genotoxicity of copper oxide nanoparticles in human skin keratinocytes cells. International journal of toxicology, 32, 296-307. doi:10.1177/1091581813487563

Anderson, J. M., Rodriguez, A., & Chang, D. T. (2008). Foreign Body Reaction to Biomaterials. Seminars in Immunology, 20, 86-100.

Ayala, V., Herrera, A. P., Latorre-Esteves, M., Toores-Lugo, M., & Rinaldi, C. (2013). Effect of surface charge on the colloidal stability and in vitro uptake of carboxymethyl dextran-coated iron oxide nanoparticles. Journal of nanoparticle research, 15, 1874. doi:10.1007/s11051-013-1874-0

Ballestri, M., Baraldi, A., Gatti, A. M., Furci, L., Bagni, A., Loria, P., . . . Albertazzi, A. (2001). Liver and kidney foreign bodies granulomatosis in a patient with malocclusion, bruxism, and worn dental prostheses. Gastroenterology, 121, 1234-1238. doi:10.1053/gast.2001.29333

Bratosin, D., Mitrofan, L., Palii, C., Estaquier, J., & Montreuil, J. (2005). Novel fluorescence assay using calcein-AM for the determination of human erythrocyte viability and aging. Cytometry Part A, 66, 78-84. doi:10.1002/cyto.a.20152

Castellanos-Gomez, A., Poot, M., Steele, G. a., Van Der Zant, H. S. J., Agraït, N., & Rubio-Bollinger, G. (2012). Elastic properties of freely suspended MoS 2 nanosheets. Advanced Materials, 24, 772-775. doi:10.1002/adma.201103965

Chen, G. Y., Pang, D. W. P., Hwang, S. M., Tuan, H. Y., & Hu, Y. C. (2012). A graphene-based platform for induced pluripotent stem cells culture and differentiation. Biomaterials, 33, 418-427. doi:10.1016/j.biomaterials.2011.09.071

Circu, M. L., & Aw, T. Y. (2010). Reactive oxygen species, cellular redox systems, and apoptosis. Free Radical Biology and Medicine, 48, 749-762. doi:10.1016/j.freeradbiomed.2009.12.022

de Lima, R., Seabra, A. B., & Durán, N. (2012). Silver nanoparticles: A brief review of cytotoxicity and genotoxicity of chemically and biogenically synthesized nanoparticles. Journal of Applied Toxicology, 32, 867-879. doi:10.1002/jat.2780

Elahi, M. M., Kong, Y. X., & Matata, B. M. (2009). Oxidative stress as a mediator of cardiovascular disease. Oxidative Medicine and Cellular Longevity, 259-269.

Goldman, E. B., Zak, A., Tenne, R., Kartvelishvily, E., Levin-Zaidman, S., Neumann, Y., . . . Aframian, D. J. (2015). Biocompatibility of tungsten disulfide inorganic nanotubes and fullerene-like nanoparticles with salivary gland cells. Tissue engineering. Part A, 21, 1013-1023. doi:10.1089/ten.TEA.2014.0163

Graham, F. L., Smiley, J., Russell, W. C., & Nairn, R. (1977). Characteristics of a Human Cell Line Transformed by DNA from Human Adenovirus Type 5. Journal of General Virology, 36, 59-74.

Gutierrez, H. R., Perea-Lopez, N., Elias, A. L., Berkdemir, A., Wang, B., Lv, R., . . . Terrones, M. (2013). Extraordinary room-temperature photoluminescence in triangular WS 2 monolayers. Nano Letters, 13, 3447-3454. doi:10.1021/nl3026357

He, Z., Sheng, Y., Rong, Y., Lee, G.-d., Li, J., & Warner, J. H. (2015). Layer-dependent modulation of tungsten disulfide photoluminescence by lateral electric fields. ACS nano, 9, 2740-2748. doi:10.1021/nn506594a

Jiang, W., Kim, B. Y. S., Rutka, J. T., & Chan, W. C. W. (2008). Nanoparticle-mediated cellular response is size-dependent. Nature nanotechnology, 3, 145-150. doi:10.1038/nnano.2008.30

Kou, Z., Wang, X., Yuan, R., Chen, H., Zhi, Q., Gao, L., . . . Guo, L. (2014). A promising gene delivery system developed from PEGylated MoS2 nanosheets for gene therapy. Nanoscale Research Letters, 9, 587. doi:10.1186/1556-276X-9-587

Lalwani, G., Henslee, A. M., Farshid, B., Parmar, P., Lin, L., Qin, Y. X., . . . Sitharaman, B. (2013). Tungsten disulfide nanotubes reinforced biodegradable polymers for bone tissue engineering. Acta Biomaterialia, 9, 8365-8373. doi:10.1016/j.actbio.2013.05.018

Lee, C., Yan, H., Brus, L. E., Heinz, T. F., Hone, Ḱ. J., & Ryu, S. (2010). Anomalous Lattice Vibrations of Single- and Few-Layer MoS2. ACS Nano, 4, 2695-2700.

Li, Y., Chen, D. H., Yan, J., Chen, Y., Mittelstaedt, R. A., Zhang, Y., . . . Chen, T. (2012). Mutation Research / Genetic Toxicology and Environmental Mutagenesis Genotoxicity of silver nanoparticles evaluated using the Ames test and in vitro micronucleus assay. Mutation Research - Genetic Toxicology and Environmental Mutagenesis, 745, 4-10. doi:10.1016/j.mrgentox.2011.11.010

Liao, K. H., Lin, Y. S., MacOsko, C. W., & Haynes, C. L. (2011). Cytotoxicity of graphene oxide and graphene in human erythrocytes and skin fibroblasts. ACS Applied Materials and Interfaces, 3, 2607-2615. doi:10.1021/am200428v

Liu, T., Wang, C., Gu, X., Gong, H., Cheng, L., Shi, X., . . . Liu, Z. (2014). Drug delivery with PEGylated MoS2 nano-sheets for combined photothermal and chemotherapy of cancer. Advanced Materials, 26, 3433-3440. doi:10.1002/adma.201305256

Łopacińska, J. M., Emnéus, J., & Dufva, M. (2013). Poly(Dimethylsiloxane) (PDMS) Affects Gene Expression in PC12 Cells Differentiating into Neuronal-Like Cells. PLoS ONE, 8, 1-11. doi:10.1371/journal.pone.0053107

Mak, K. F., Lee, C., Hone, J., Shan, J., & Heinz, T. F. (2010). Atomically thin MoS2: A new direct-gap semiconductor. Physical Review Letters, 105, 2-5. doi:10.1103/PhysRevLett.105.136805

Mao, W. P., Ye, J. L., Guan, Z. B., Zhao, J. M., Zhang, C., Zhang, N. N., . . . Tian, T. (2007). Cadmium induces apoptosis in human embryonic kidney (HEK) 293 cells by caspase-dependent and -independent pathways acting on mitochondria. Toxicology in Vitro, 21, 343-354. doi:10.1016/j.tiv.2006.09.004

Neto, a. H. C., & Novoselov, K. (2011). Two-Dimensional Crystals: Beyond Graphene. Materials Express, 1, 10-17. doi:10.1166/mex.2011.1002

Osman, O., Zanini, L. F., Frénéa-Robin, M., Dumas-Bouchiat, F., Dempsey, N. M., Reyne, G., . . . Haddour, N. (2012). Monitoring the endocytosis of magnetic nanoparticles by cells using permanent micro-flux sources. Biomedical Microdevices, 14, 947-954. doi:10.1007/s10544-012-9673-4

Redlich, M., Katz, A., Rapoport, L., Wagner, H. D., Feldman, Y., & Tenne, R. (2008). Improved orthodontic stainless steel wires coated with inorganic fullerene-like nanoparticles of WS2 impregnated in electroless nickel-phosphorous film. Dental Materials, 24, 1640-1646. doi:10.1016/j.dental.2008.03.030

Skala, M. C., Squirrell, J. M., Vrotsos, K. M., Eickhoff, J. C., Gendron-Fitzpatrick, A., Eliceiri, K. W., & Ramanujam, N. (2005). Multiphoton microscopy of endogenous fluorescence differentiates normal, precancerous, and cancerous squamous epithelial tissues. Cancer Research, 65, 1180-1186. doi:10.1158/0008-5472.CAN-04-3031

Song, J. G., Park, J., Lee, W., Choi, T., Jung, H., Lee, C. W., . . . Kim, H. (2013). Layer-controlled, wafer-scale, and conformal synthesis of tungsten disulfide nanosheets using atomic layer deposition. ACS Nano, 7, 11333-11340. doi:10.1021/nn405194e

Song, X., Hu, J., & Zeng, H. (2013). Two-dimensional semiconductors: recent progress and future perspectives. Journal of Materials Chemistry C, 1, 2952. doi:10.1039/c3tc00710c

Splendiani, A., Sun, L., Zhang, Y., Li, T., Kim, J., Chim, C.-y., . . . Wang, F. (2010). Emerging Photoluminescence in Monolayer MoS2. Nano letters, 10, 1271-1275. doi:10.1021/nl903868w

Takenaka, S., Karg, E., Roth, C., Schulz, H., Ziesenis, A., Heinzmann, U., . . . Heyder, J. (2001). Pulmonary and systemic distribution of inhaled ultrafine silver particles in rats. Environmental Health Perspectives, 109, 547-551. doi:10.2307/3454667

Tenne, R. (2003). Advances in the synthesis of inorganic nanotubes and fullerene- like nanoparticles. Angewandte Chemie-International Edition, 42, 5124-5132. doi:10.1002/anie.200301651

Tenne, R. (2013). Recent advances in the research of inorganic nanotubes and fullerene-like nanoparticles. Frontiers of Physics, 1-8. doi:10.1007/s11467-013-0326-8

Tenne, R., & Redlich, M. (2010). Recent advances in the research of inorganic nanotubes and fullerene-like nanoparticles. Chemical Society Reviews, 1423-1434. doi:10.1007/s11467-013-0326-8

Tenne, R., & Seifert, G. (2009). Recent Progress in the Study of Inorganic Nanotubes and Fullerene-Like Structures. Annual Review of Materials Research, 39, 387-413. doi:10.1146/annurev-matsci-082908-145429

Teo, W. Z., Chng, E. L. K., Sofer, Z., & Pumera, M. (2014). Cytotoxicity of exfoliated transition-metal dichalcogenides (MoS 2, WS2, and WSe2) is lower than that of graphene and its analogues. Chemistry - A European Journal, 20, 9627-9632. doi:10.1002/chem.201402680

Wang, Q. H., Kalantar-Zadeh, K., Kis, A., Coleman, J. N., & Strano, M. S. (2012). Electronics and optoelectronics of two-dimensional transition metal dichalcogenides. Nature nanotechnology, 7, 699-712. doi:10.1038/nnano.2012.193

Woodruff, R. S., Li, Y., Yan, J., Bishop, M., Jones, M. Y., Watanabe, F., . . . Chen, T. (2012). Genotoxicity evaluation of titanium dioxide nanoparticles using the Ames test and Comet assay. Journal of Applied Toxicology, 32, 934-943. doi:10.1002/jat.2781

Wu, H., Yang, R., Song, B., Han, Q., Li, J., Zhang, Y., . . . Wang, C. (2011). Biocompatible inorganic fullerene-like molybdenum disulfide nanoparticles produced by pulsed laser ablation in water. ACS Nano, 5, 1276-1281. doi:10.1021/nn102941b

Xu, M., Liang, T., Shi, M., & Chen, H. (2013). Graphene-like two-dimensional materials. Chemical Reviews, 113, 3766-3798. doi:10.1021/cr300263a

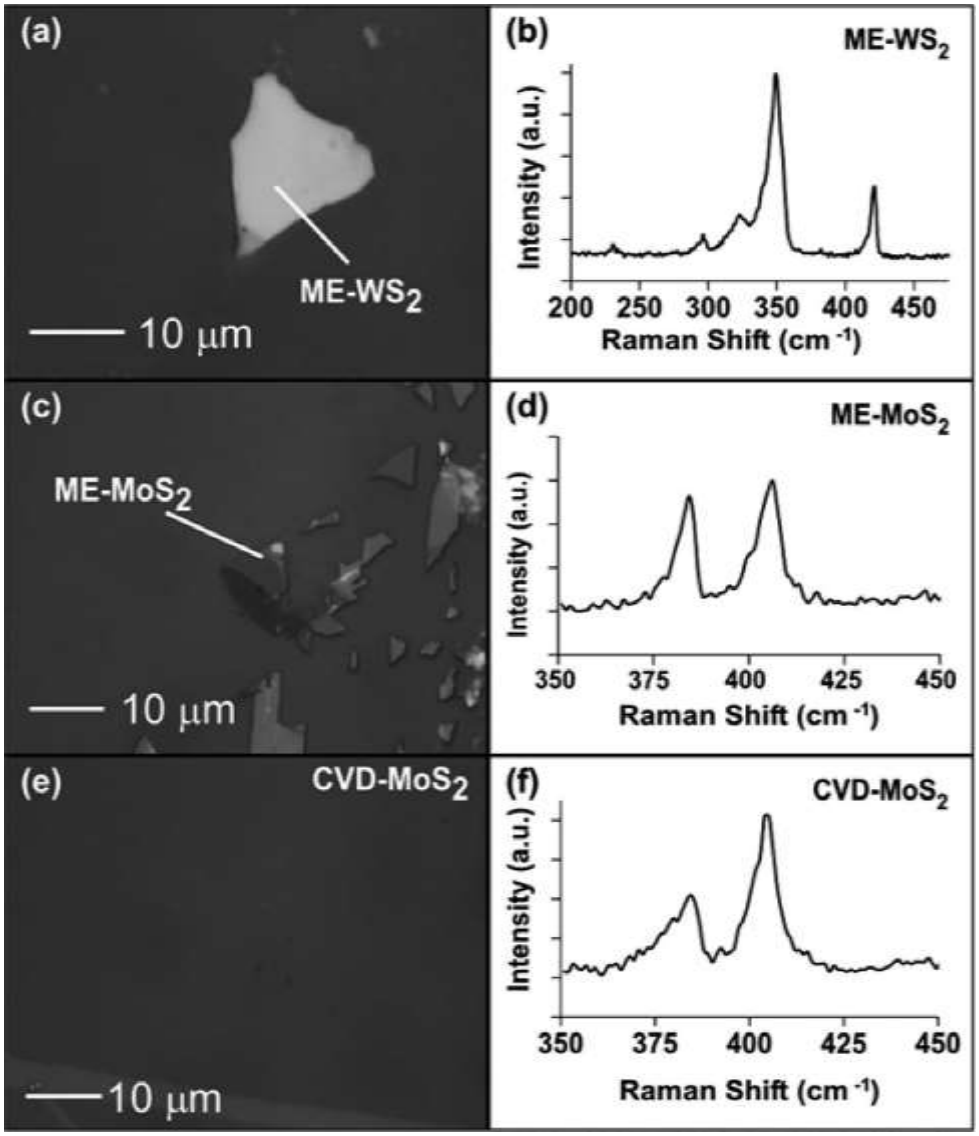

Figure 4.1 Scanning electron microscopy images and Raman spectra. SEM images on left and Raman spectra on right (a) & (b) mechanically exfoliated few-layer WS_2 (ME-WS_2), (c) & (d) few-layer ME-MoS_2, and (e)&(f) chemical vapor deposition grown (CVD)-MoS_2.

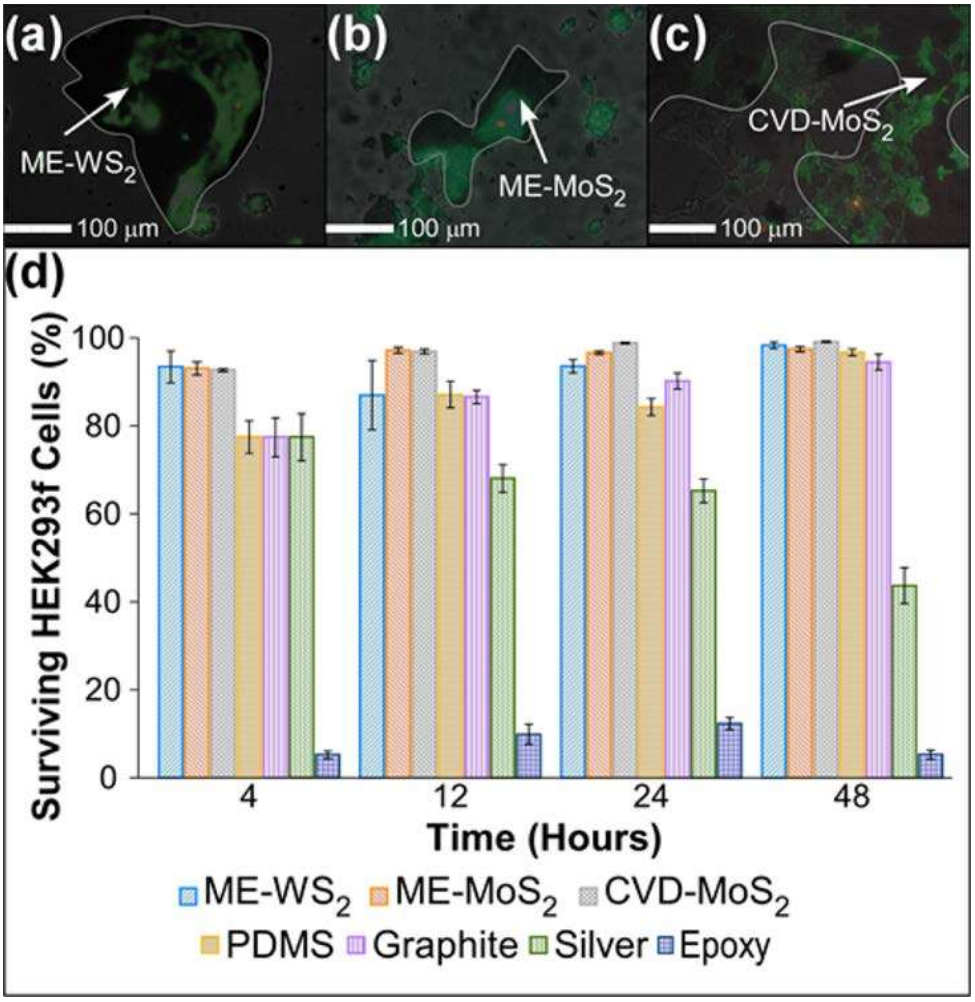

Figure 4.2. Cellular viability assay showing fluorescence images of HEK293f cells in direct contact with TMD flakes/sheets. (a−c) Green color shows live cells and red color show dead cells. The panels are for (a) ME-WS_2 (b) ME-MoS_2, and (c) CVD-MoS_2. (d) Overall cell viability of different control materials and different TMDs at as a function of time.

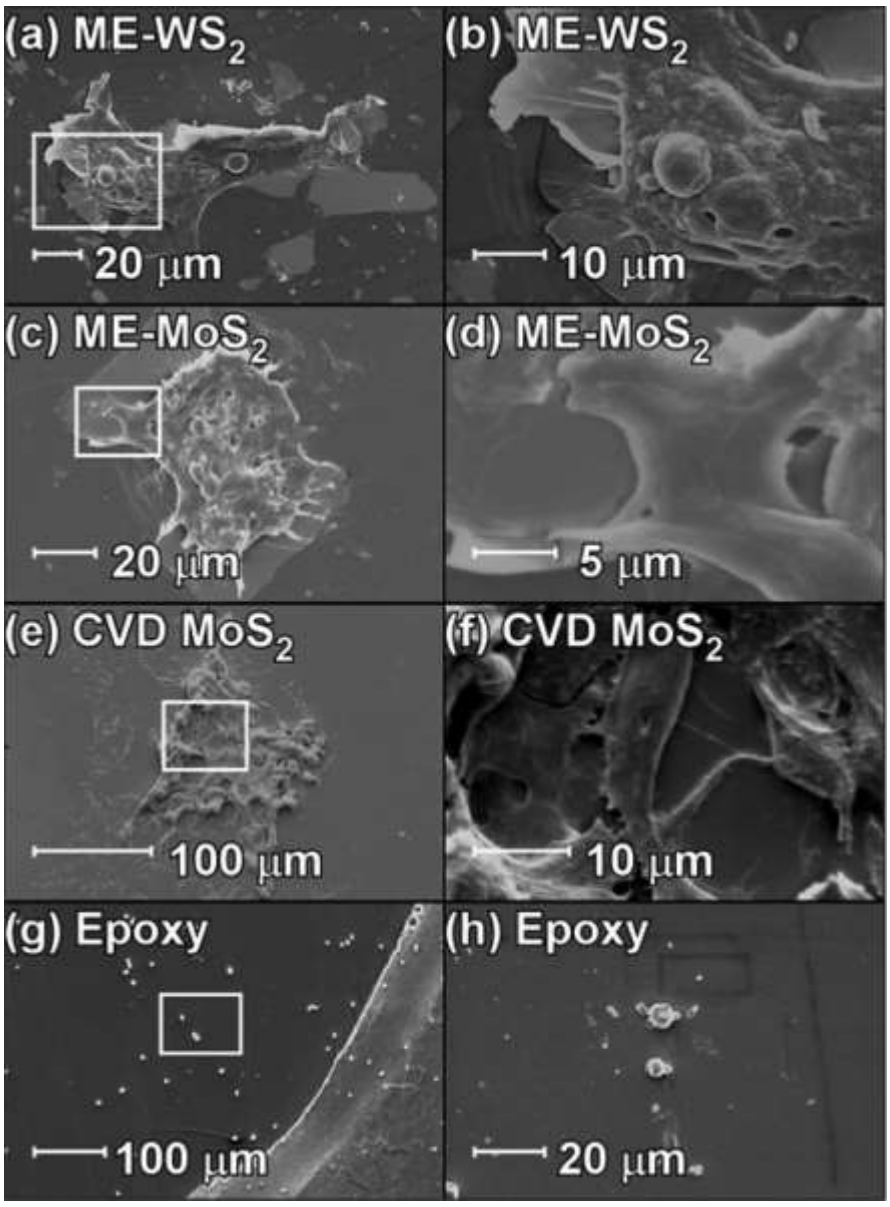

Figure 4.3. Scanning electron microscopy images showing viable HEK293f cells adhered to (a, b) ME-WS_2, (c, d) ME-MoS_2, (e, f) CVD-MoS_2, and (g, h) epoxy. The regions indicated by rectangles in the left panels are shown magnified in the right panels.

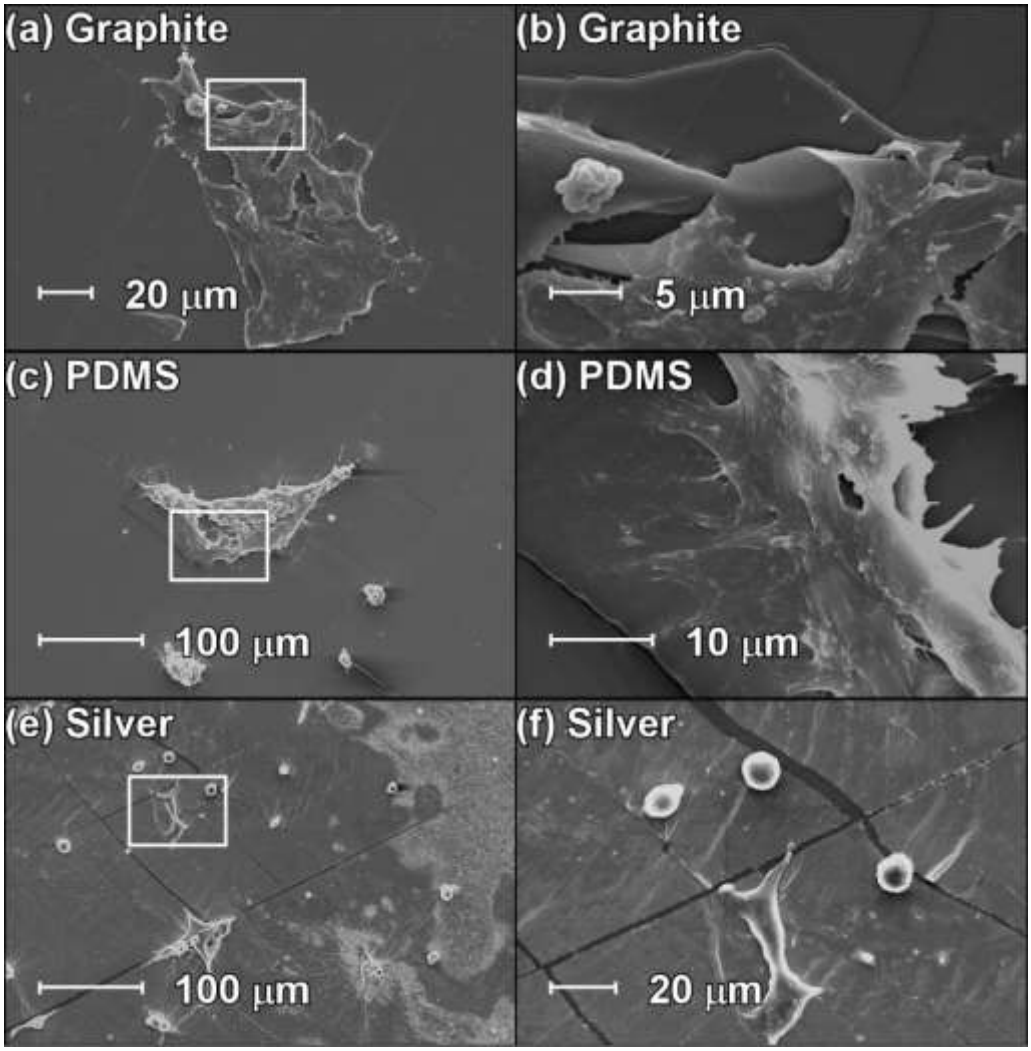

Figure 4.4. Scanning electron microscopic images of control materials showing healthy cell morphology in the cases of graphite and PDMS and poor cell morphology in the case of silver. (a) & (b) HEK293f cells adhere to graphite flakes, (c) and (d) HEK293f cells adhere to PDMS substrate, (e) and (f) HEK293f cells adhere to sputtered silver substrate.

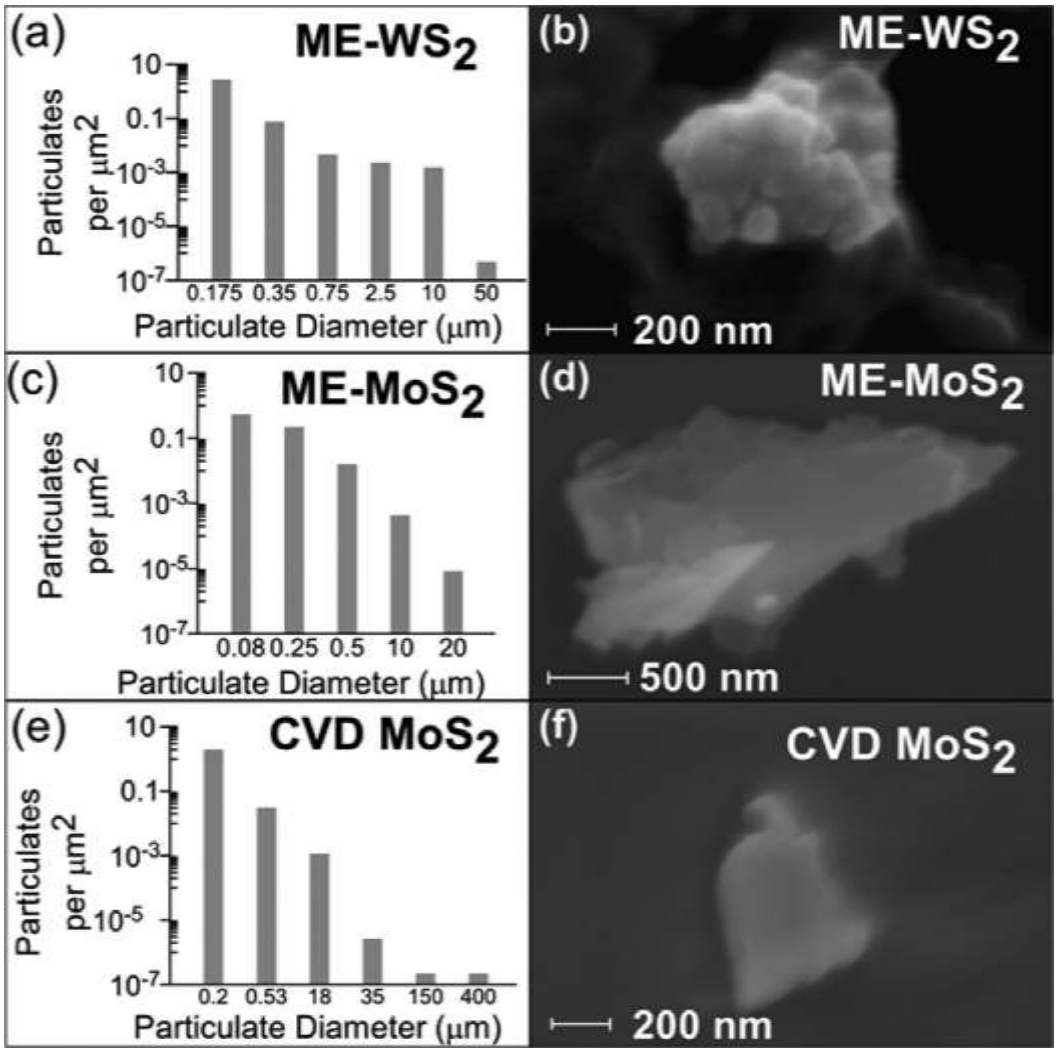

Figure 4.5. Transition metal dichalcoginide particulates. (a, c, e) Histograms showing particulate diameters and (b, d, f) SEM images of representative particulates for (a, b) ME-WS_2, (c, d) ME-MoS_2, and (e, f) CVD-MoS_2.

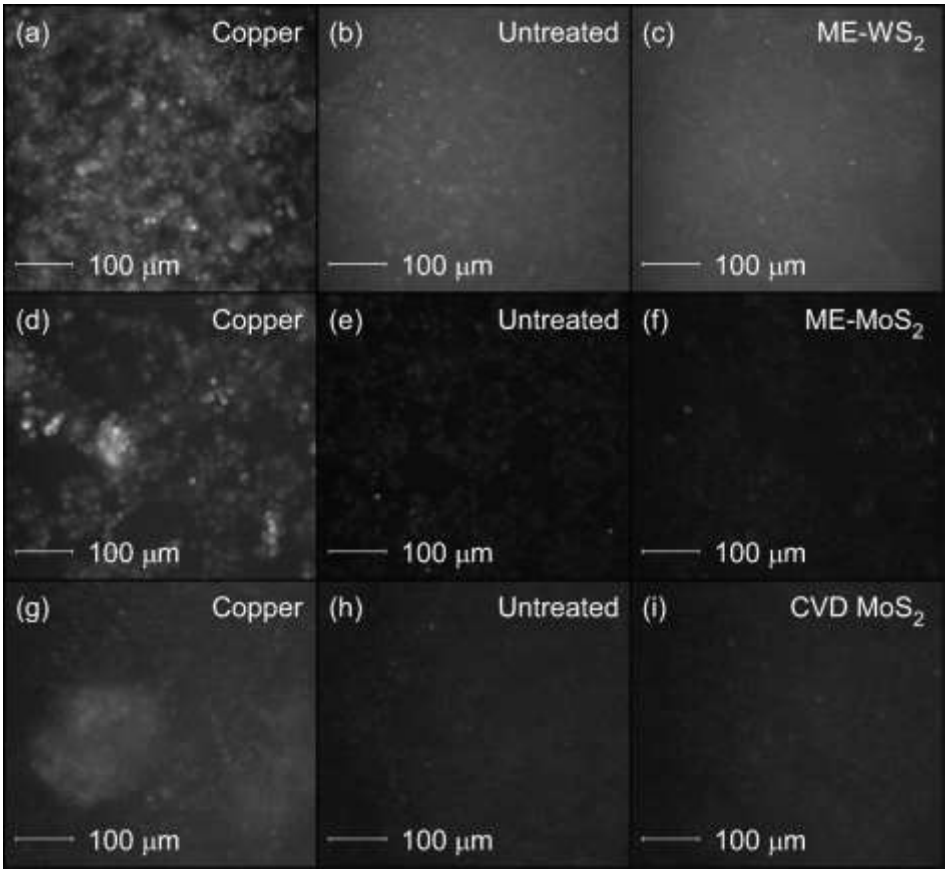

Figure 4.6. Fluorescent images of HEK293f after exposure to various materials, (a, d, g) positive ROS inducing copper, (b, e, h) untreated cells, (c) ME-WS_2, (f) ME-MoS_2, and (i) CVD-MoS_2.

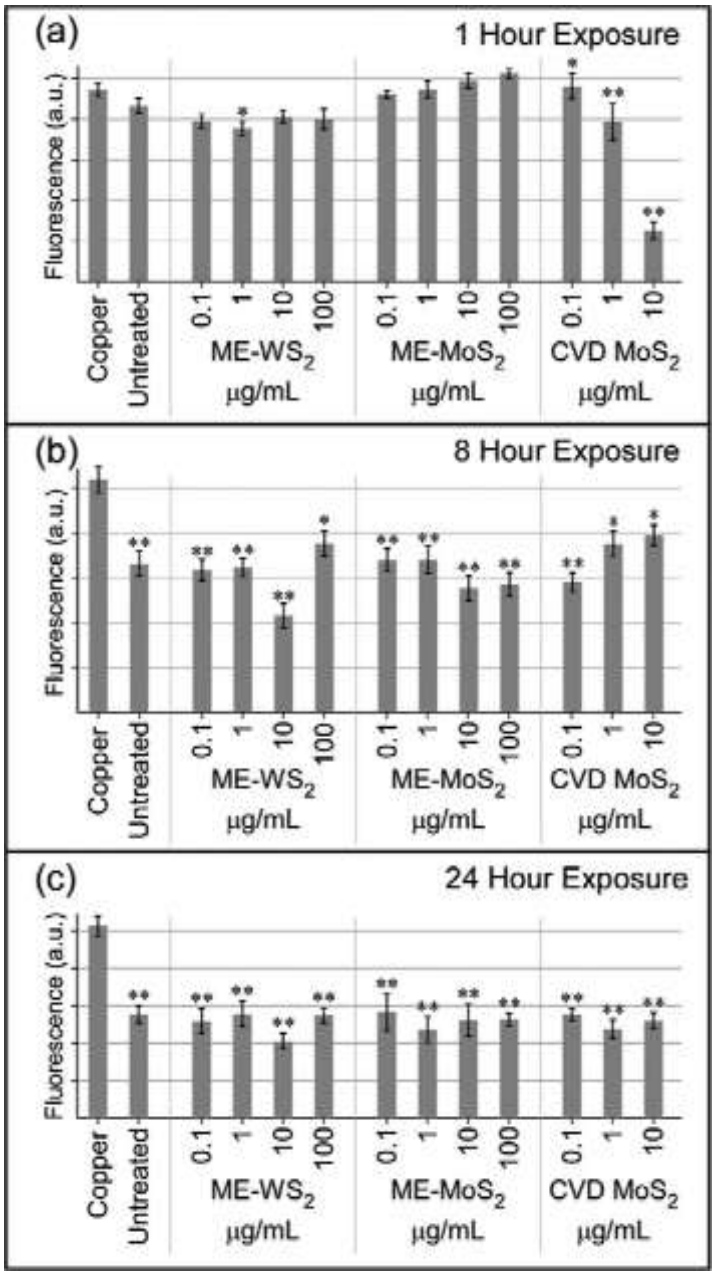

Figure 4.7. Fluorescence intensity plots measuring reactive oxygen species (ROS) generation for various TMD particulates and a copper positive control. TMD particulates do not generate significant levels of ROS after exposures of (a) 1, (b) 8, and (c) 24 hours.

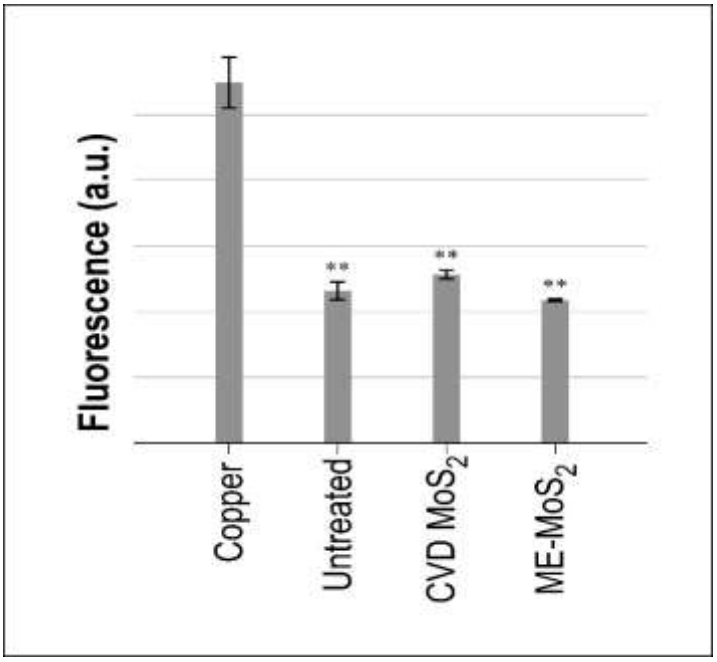

Figure 4.8. Fluorescence intensity plots measuring reactive oxygen species (ROS) generation for various TMD flakes/sheets, a copper positive control, and an untreated negative control. TMD flakes/sheets do not generate significant levels of ROS after 12 hours of exposure.

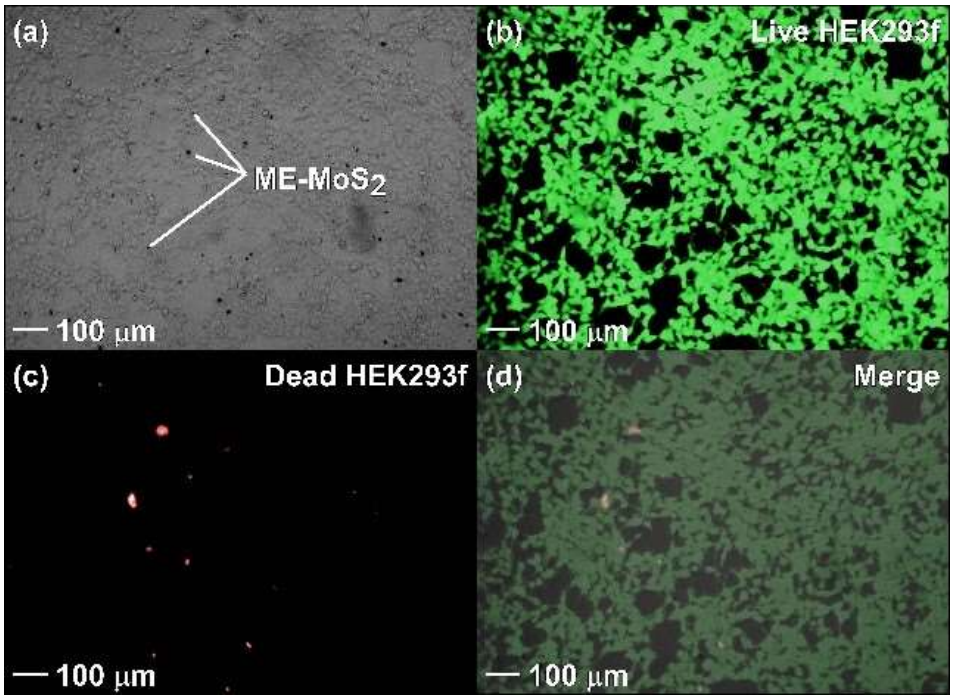

Figure 4.9. Cellular viability assay showing fluorescence images of HEK293f cells in direct contact with particulates of ME-MoS_2 (a) optical image of particulates in contact with HEK293f cells, (b) live cells stained with green fluorescent calcein AM, (c) dead cells stained with red fluorescent ethidium homodimer-1 and (d) merge of (a), (b) & (c) showing the overall viability of cells exposed to particulates of ME-MoS_2.

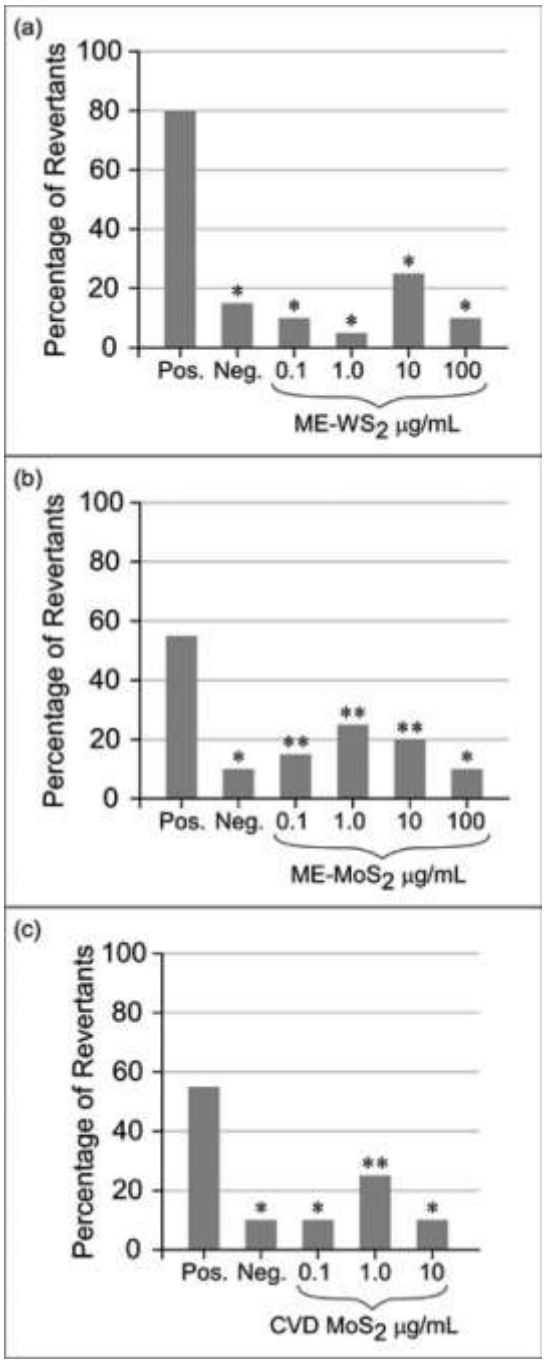

Figure 4.10. Mutagenicity measurement by Ames fluctuation test. The percentage of bacterial revertants after 3 days is calculated for positive controls of sodium azide, negative control of untreated bacteria, and varying concentrations of particulates of (a) ME-WS_2, (b) ME-MoS_2, and (c) CVD-MoS_2.

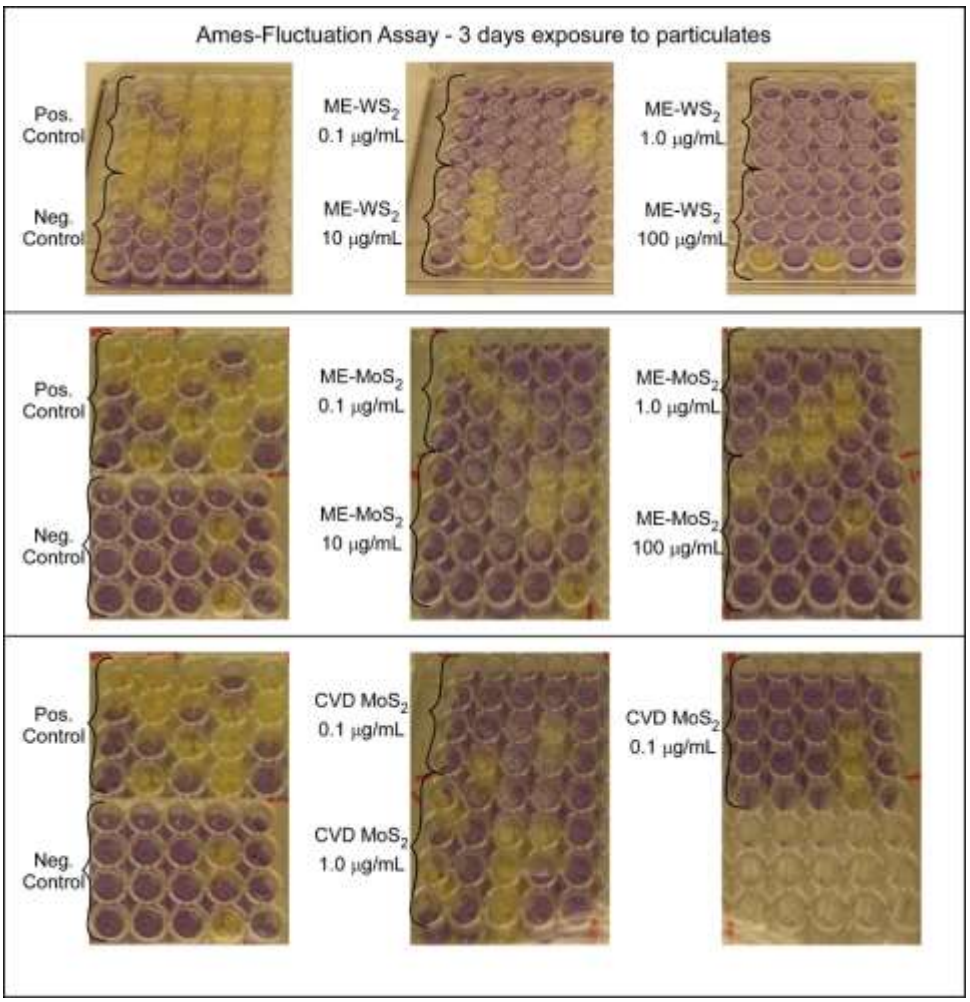

Figure 4.11. Ames-Fluctuation assay after exposure to controls and various concentrations of ME-WS_2, ME-MoS_2, and CVD-MoS_2 showing that TMD particulates are non-mutagenic towards S. typhimurium TA100.

CHAPTER 5
PHYSIOLOGICALLY AND BIOLOGICALLY REALISTIC EVALUATION OF AN ARTIFICIAL ARACHNOID GRANULATION COMPRISED OF HYDROGEL CHECK VALVES FOR THE TREATMENT OF HYDROCEPHALIC FLUID RETENTION

5.1. Abstract

Hydrocephalus is the leading cause of pediatric neurosurgery, as the current treatment requires the implantation of a shunt system to bypass cerebral spinal fluid (CSF) into the stomach. However, these shunt systems have a notoriously high failure rate, with 40 % of shunts failing within the first two years of implantation. Therefore, researchers have pursued alternate means of redirecting CSF flow within the cranium. Herein, is presented the evaluation of a fully realized, surgically friendly, passive implant to replace malfunctioning arachnoid granulations, the biological valves which naturally regulate the CSF flow pathway. Our artificial arachnoid granulation (aAG) is comprised of two hydrogel check valves encapsulated in a grommet structure. To aid in implantation and overall function aAG includes a removable puncture tool, a cone shape to wedge the dura mater apart, six suture points, and redundant hydrogel valves each with redundant CSF inlets. The hydrogel valves were individually evaluated in worst-case fluidic conditions emulating occlusion-modes in traditional shunts. Then the complete aAG was implanted in cadaver dura and evaluated in a cadaver bench-top model of hydrocephalus. Both individual valves and encapsulated valves remain within the design specifications for the relevant fluidic parameters, cracking pressure, hydraulic resistance, and reverse flow leakage. However, after prolonged evaluation an individual hydrogel check valve

failed to maintain the desired reverse flow leakage parameter. This provided a unique opportunity to investigate the potential failure modes for hydrogel check valves. After examining the valve via scanning electron microscopy, optical profilometry, and protein elution we determined that the failure mode was mechanical fatigue rather than occlusion, the most common failure mechanism for traditional shunts. This evaluation preliminarily validates the aAG as an alternative treatment for hydrocephalus paving the way for animal trials and subsequent human testing.

5.2. Introduction

Nearly 1 in every 500 infants born in the United States suffer from hydrocephalus (Pople, 2002). Hydrocephalus is characterized as a flaw in the cerebral spinal fluid (CSF) flow pathway (figure 5.1. (a)), which results in an accumulation of fluid in the brain. In healthy individuals, CSF is generated at a rate of 18 to 24 mL/hour by the ventricles (Zhu, Xenos, Linninger, & Penn, 2006). It then flows through and around the cerebral cortex providing nutrients and buoyancy and is drained through the arachnoid granulations, which act as one-way biological valves. In the case of hydrocephalic patients, this flow pathway is disrupted, either CSF cannot exit the ventricle—classified as non-communicating hydrocephalus—or CSF can exit the ventricle—communicating hydrocephalus—but is obstructed at a later point in the flow pathway, typically at the arachnoid granulations. Hydrocephalus affects brain development, can induce seizures, and if left untreated leads to death (Drake, Kestle, & Tuli, 2000).

The current standard of care is the implantation of a shunt system (figure 5.1. (b)). These are implanted such that a short catheter, ventricular catheter, directs CSF from the ventricle through the skull into a regulating mechanism that controls CSF flow into a

second, longer catheter, distal catheter, which then directs CSF into distal organs. Unfortunately, these shunts have a notoriously high failure rate, where 40 % of shunts fail within the first two years of implantation (Drake et al., 2000) and 80% within 15 years (Stone, Walker, Jacobson, Phillips, & Silberstein, 2013). In the United States these failures are voluntarily reported to and classified by the Food and Drug Administration. Figure 5.1. (c) shows the failure mechanisms reported within the last 5 years, with the largest percentile nearly 18 % being occlusion-based, then breakage and leakage, respectively. The shunt system in figure 5.1. (d) was explanted after 12 years due to both tissue infiltration and breakage/leakage of the distal catheter. Of the mechanisms reported the most preventable are catheter based-occlusion failures. Occlusion normally divides into two general groups, based on the lifespan of implant (Hanak, Ross, Harris, Browd, & Shain, 2016). The act of implantation requires the destruction of tissue and the blood brain barrier. This leaves the implanted shunt in the presence of blood and cellular debris (C. A. Harris & Mcallister, 2012), both contain proteins that bind to the shunt inducing macrophages and monocytes to produce growth factors. These in turn attract astrocytes and can potentiate an inflammatory response (Moshayedi et al., 2014). This has been a common issue with ventricular catheters as simulated by Harris et al. (C. Harris et al., 2015) and observed in explanted shunts (Hanak et al., 2016). While short term failure is generally more likely, long term failure can be equally devastating. While rare, cases of mineralization or calcification are often noted in long term studies of shunt failure. For example, Yamamoto et al. reported a small study with 12 patients, 3 of whom suffered from long term failure due to mineralization of the distal catheter (Yamamoto, Ohno, Aoyagi, Ichinose, & Hirakawa, 2002). They concluded that mechanical stress and the

addition of barium sulfate lead to catheter degradation and nucleation of mineral deposits, which ultimately induced a crack in the catheter (Yamamoto et al., 2002). Generally, occlusion-based shunt failures can be categorized based on implant lifespan with foreign body response, infection, and cellular growth resulting in short term failures and mechanical fatigue, mineralization, and calcification in long term ones.

Therefore, numerous studies have been pursued to reduce flaws in shunt design, such as changing the surface properties of catheters to reduce cellular adhesion (Anderson, 2001) or the integration of proposed sensing elements to the system (Clark, Malpas, Mccormick, Heppner, & Budgett, 2015; B. J. Kim et al., 2016). Unfortunately, these modifications fail to address some of the underlying causes of occlusion, specifically, the large surface area for debris to accumulate. Thus, researchers have developed artificial arachnoid granulations (aAGs) to treat communicating hydrocephalus. These devices are inspired by arachnoid granulations to replicate the fluid dynamic capabilities. In vitro studies of explanted arachnoid granulation tissue, found that the differential pressure across the explanted tissue, i.e. cracking pressure, was approximately 39.5 mmH2O and the resulting flow rate was 269 µL/min. However, when the flow was reversed, the differential pressure was 44 mmH2O and the flow rate was 0 µL/min, demonstrating the key fluid dynamic features of arachnoid granulations, a non-zero cracking pressure and one-way fluid flow into the superior sagittal sinus (SSS) (Holman, Kurtcuoglu, & Grzybowski, 2010).

Micro-electro-mechanical system (MEMS) based valves have been designed as aAGs, to establish and regulate one-way CSF flow from the subarachnoid space (SAS) into the SSS. In 2011, Oh et al. developed a 3-D dome petal perforated membrane based

aAG (Oh, Kim, Kralick, & Noh, 2011; Oh, Liu, Medina, Kralick, & Noh, 2014) and in 2014 Schwerdt et al. designed a hydrogel check-valve based aAG (Schwerdt et al., 2015; Schwerdt, Bristol, & Chae, 2014). These designs both utilize perforated membranes to achieve unidirectional flow. The 3-D dome petal valve, however, does not have a non-zero cracking pressure, i.e. the minimum differential pressure required to open the valve (Oh et al., 2011). The hydrogel check-valve design can vary cracking pressure based on the diameter of the inlet and range from 20 to 110 mmH2O which gives it a distinct advantage as healthy arachnoid granulations have a differential pressure of 39.5 mmH2O when fluid is passing through (Schwerdt et al., 2014). Additionally, the hydrogel check valve has been evaluated and found functionally equivalent to healthy arachnoid granulations and traditional shunts in terms of its transient hydrodynamic properties, lack of clogging and overtime performance (Schwerdt et al., 2015). However, the hydrogel check valve is only the functional component of the overall aAG, an encapsulating structure coined a grommet must be used to achieve a fully implantable device. The first iteration of this grommet was presented by Schwerdt et al. as a simple I-shape with a single hydrogel check valve enclosed (Schwerdt et al., 2015). This grommet was 12 mm in diameter, contained a single fluid inlet/outlet, and was evaluated for surgical viability. Unfortunately, it was found to be very difficult to place within the cadaver human brain and several potential failure points were identified.

Herein, we report a fully-realized, surgically friendly aAG (figure 5.1. (e)-(g)) and its evaluation in a cadaver bench-top model of hydrocephalus, as well as continued evaluation of the aAG, functional component: the hydrogel check valve in increasingly realistic physiological and biological conditions. The aAG is designed as a replacement

of malfunctioning arachnoid granulations, so the schematic in figure 5.1. (e) shows the designated implantation location, at the longitudinal fissure, i.e. where arachnoid granulations are naturally found. Figure 5.1. (f) & (g) shows the removable puncture tool to aid in the implantation, which is integrated into the aAG to slice the dura mater, wedge the dura mater apart to insert the aAG and hold the aAG in place during suturing. This final iteration of the grommet structure is larger than the preliminary design, however it encapsulates two hydrogel check valves, provides four CSF inlets, six suture points, and a conical structure to aid in implantation. These hydrogel check valves utilize the same operating principle as reported by Schwerdt et al. where a perforated hydrogel membrane swells to seal a through silicon via and if sufficient differential pressure is applied the membrane deflects out-of-plane to allow CSF flow (Schwerdt et al., 2014). These hydrogel check valves were individually evaluated in a physiologically realistic spherical bench-top model of hydrocephalus. This is composed of a multi-directional flow pathway emulating the radius of curvature of the implantation location, longitudinal fissure where the SAS meets the SSS. Additionally, as protein and cellular adhesion to traditional shunts easily leads to occlusion (Sgouros & Dipple, 2004) and aAGs could also be susceptible to occlusion, we tested the hydrogel check valve in fluidic conditions which provide physiologically realistic concentrations of calcium, blood, fibronectin, and a combination of all three, in CSF extracted from hydrocephalus patients and maintained at internal body temperature ~ 37 °C during evaluation. These evaluations showed that the hydrogel check valve maintains functionality in each condition, with the hydraulic resistance maintaining within the specifications of traditional shunt systems and the

reverse flow leakage maintaining well below the maximum allowable leakage flow rate of 50 µL/min (Czosnyka, Czosnyka, Whitehouse, & Pickard, 1997).

After valve functionality was established under these stringent conditions, a valve was encapsulated in the grommet structure and placed into a cadaver model of hydrocephalus. This cadaver model uses sheep cerebral cortex and dura mater to emulate the desired implant location, in the dura mater regulating CSF flow from the SAS to the SSS, while still allowing for the measurement of differential pressure across the aAG and flow out of the aAG. The aAG in the cadaver model shows near identical flow vs. differential pressure characteristics with an above zero cracking pressure and little to no reverse flow leakage. The cadaver model does not truly replicate the SSS, as there is no perpendicular blood flow at the outlets of the grommet, therefore we constructed a simulated SSS matching the dimensions, blood flow and viscosity to evaluate the flow around the grommet structure post-implantation. The blood-mimicking fluid spiked with both fluorescent and non-fluorescent 10 µm beads show flow evenly dividing at the cone structure and coming back together after the grommet. While the aAG maintained design specifications during cadaver testing, in valve testing after nearly 3 months the valve failed to maintain less than 50 µL/min reverse flow leakage. This gave us a unique opportunity to examine the failure mechanism of this hydrogel check valve and compare it to the commonly found failure modes in traditional shunts. We examined the valve using scanning electron microscopy, and optical profilometry and similar valves using protein elution. While we did observe adsorbed blood cells, cellular debris, biofilm formation, and were able to elute albumin from the valve, this did not contribute to overall valve failure. Instead this was attributed to mechanical fatigue of the hydrogel as

seen by a crack at the center of the hydrogel structure. This information provides valuable insights into improving the hydrogel check valve by optimizing the hydrogel layer for robustness and incorporating coatings to decrease cellular and protein adsorption. Ultimately, we have developed an aAG which is capable of accurately replicating the function of arachnoid granulations in a variety of in vitro models of hydrocephalus increasing in both biologically and physiologically realistic conditions.

5.3. Material and Methods

Fabrication of silicon-based hydrogel check valve. The fabrication of the silicon-based hydrogel check valve was performed using MEMS manufacturing technology, following the protocol developed by Schwerdt et al. (Schwerdt et al., 2015; Schwerdt et al., 2014). Briefly, we began with a clean silicon wafer, chemical vapor deposition is used to deposit ~100 nm of silicon dioxide and then parylene is thermally deposited, ~100 nm. This layer was then patterned using O2 plasma and submerged ~12 hours in a pH adjusted hydrogel adhesion promoting solution of γ-methacryloxypropyltrimethoxysilane then rinsed with water and baked at 100°C for at least 1 hour. The hydrogel solution was prepared; the base 2-hydroxyethyl methacrylate, crosslinker ethylene glycol dimethacrylate and photoinitiator 2,2-dimethoxy-2-phenylacetophenone mixed at a ratio of 1 to 0.04 to 0.1 respectively. This solution was poured onto the prepared wafer with the aid of a spacer to define the thickness of the resulting hydrogel layer which was simultaneously UV crosslinked and patterned at ~ 400 mJ/cm2. Backside alignment is then used to define the inlet dimensions and prepare for deep reactive ion etching. Through silicon etching is completed when the silicon dioxide is visible. Then the silicon dioxide and parylene are each etched using hydrofluoric acid and O2 plasma respectively. And the wafer is submerged in water for at least 12 hours to prepare for evaluation.

Fabrication of the artificial arachnoid granulation. The artificial arachnoid granulation (aAG) is comprised of three elements, two hydrogel check valves encapsulated within a grommet structure. After ascertaining valve functionality, two valves are then infilled with water soluble wax and placed within a custom steel mold. Uncured polydimethylsiloxane (PDMS) mixed with crosslinker at a ratio of 10:1 is poured into the

mold. The mold is then degassed for approximately two minutes until all air bubbles are removed from the structure and then left to cure at room temperature for 24 to 48 hours. When the PDMS has fully cured, the mold is cracked open and the resulting aAG structure is submerged in ~45°C water to remove the wax, re-hydrate the hydrogel membrane, and prepare for functional evaluation.

Construction of the spherical bench-top model of hydrocephalus. The bench top model of hydrocephalus was constructed using a two-piece spherical mold with an interior diameter of approximately 6.4 cm. This closely approximates the radius of curvature at the longitudinal fissure where SSS and SAS meet, as shown in figure 5.1. (e). Four short lengths of tubing, diameter 5 mm, was added to the spherical mold, 3 on piece A and the last on the piece B, and a water tight seal was formed using a combination of PDMS and epoxy, as shown in figure 5.2. To fill the spherical set up the tubing in part B was filled with the desired fluid and then the rest of part B was filled. Then a hydrogel check valve was inserted in the interior of the left section of tubing on part A and back filled with fluid and connected to part B. Using the remaining two tubing sections the sphere was filled with the desired fluid. After the tubing was filled with fluid a pressure sensor was connected to ~ cm away from the fluidic chamber and the rest was sealed. The tubing connected to part B was then connected to a syringe pump (Harvard Apparatus Pump 33). Finally, the section of tubing with the hydrogel was connected via a Y shaped tubing connector to the pressure sensor and a down stream flow sensor.

Calibration of sensors. Two pressure sensors (Omega PX26-005DV) were used in this set up, however one of them was configured as a flow sensor using different calibration methods. Calibrating the pressure sensor required a vertical column and data acquisition

board (National Instruments NI USB 6216), one side of the sensor was connected to the bottom of the vertical column and various amounts of water was added to it. The voltage at each water level was recorded as well as the height in mm of the water level. Minimum of five different water levels were recorded to draw a statistically viable trend line, the equation of which was used as the conversion from sensor voltage output to differential pressure. The flow sensor was calibrated in a similar manner, using a linear regression. The flow sensor was connected to a syringe pump, a data acquisition board, and connected across a 35 cm length of 500 µm diameter tubing such that the flow could be determined based on the differential pressure across a known fluidic resistance. Eight different flow rates were used to calibrate the sensor in both forward and reverse flow and the voltage at each flow rate was recorded giving a linear trend line, the equation of which was used as the conversion from sensor voltage output to flow rate.

Evaluation of hydrogel check valve in the spherical bench-top model of hydrocephalus. The hydrogel check valve was first evaluated for basic functionality in the spherical setup. This pass/fail test ensured two things, that the valve would open under forward flow and that the reverse flow leakage was less than 50 µL/min. Pass/fail testing was performed in the spherical setup with water. Initially, the syringe pump was set to forward flow at a rate of 100 µL/min. After the flow rate stabilized the syringe pump was stopped and stabilized. Then flow was reversed at a rate of -25 µL/min continuing to decrease flow in 25 µL/min intervals until a reverse flow of -200 µL/min was achieved. During this testing the absolute value of the differential pressure across the valve should continuously increase indicating that the valve is closed and not leaking. After a valve passes initial testing a full characterization is performed to establish valve characteristics

such as cracking pressure. Characterization is performed using the spherical set up and various fluids at either room temperature or internal body temperature ~37°C. Similar to the pass/fail testing, the syringe pump is initially set to forward flow at a rate of 100 µL/min and after the flow was stabilized it is decreased then stabilized in 25 µL/min intervals until zero flow. After flow is stopped it is then reversed at a rate of -25 µL/min continuing to decrease flow in 25 µL/min intervals until a reverse flow of -200 µL/min was achieved, then flow is set to -100 µL/min and then flow is stopped. Then a forward flow of 25 µL/min is set and increased in 25 µL/mi intervals until a forward flow of 100 µL/min is achieved. During characterization if flow leakage was observed and had a leakage rate of higher than 50 µL/min the valve was considered defective. The closing of the valve resulted in an increase of differential pressure between the interior of the spherical set up and the tubing representing the superior sagittal sinus. Additionally, a Medtronic PS Medical Strata II valve was obtained and tested under the same protocol as the hydrogel check valve in order to establish a comparison of fluidic characteristics in each fluid.

Cerebrospinal fluid preparation. CSF from male and female hydrocephalic patients was collected with institutional review board approval at Phoenix Children's Hospital. Samples were maintained in a 4°C environment when not in use. Five CSF solutions were generated from an aggregate of patient CSF, four of which were spiked with various additives known to generate occlusions in traditional shunts: final concentration of 1.1 mM calcium, 7.5 µg/mL fibronectin, 5% blood, and all three, calcium, fibronectin, and blood.

Construction of the cadaver bench-top model of hydrocephalus. The cadaver bench-top model was built from a clear union PVC fitting and sheep cadaver cerebral cortex and dura mater tissues (figure 5.3.). Dura mater was removed from the sheep brain and placed between the two sections of the PVC union fitting, a water tight seal was formed between the respective sides of the union with a differential pressure sensor measuring pressure across the dura mater. With the water tight seal confirmed, the structure was then disassembled and the aAG was sutured into the dura mater (figure 5.4.) and further secured using surgical glue as recommended. The structure was carefully reassembled with a cylindrical section of cerebral cortex tissue placed at the inlet of the aAG and filled with patient CSF making sure air was fully removed from the set up. The cerebral cortex side of the set-up was then connected to an unfilled water column while the other side was connected to a pre-calibrated flow sensor and a reservoir to maintain a pressure equilibrium during testing.

Evaluation of artificial arachnoid granulation in the cadaver bench-top model of hydrocephalus. As the valves within the aAG were established as functional via the previously described pass/fail testing. Testing the aAG began with a stable near zero differential pressure with the CSF level in the column matching the height of the aAG. CSF was added to the column in 5 mm height intervals with at least one minute of stabilization time before adding more CSF until a forward flow rate of at least 200-300 μL/min was achieved. CSF was then drained from the column and the cadaver bench-top model was reversed to evaluate reverse flow leakage. Again, we began with the CSF level in the column matching the height of the aAG and then increase it in 5 mm height

intervals until a differential pressure of 300 mmH2O was achieved. This was repeated at least two times.

Evaluation of flow around the artificial Arachnoid Granulation in a simulated superior sagittal sinus. We fabricated a simulated superior sagittal sinus setup reflecting the dimensions of the SSS. This was achieved using by curing PDMS in a custom 3D printed mold. The pre-fabricated aAG was inserted into the simulated superior sagittal sinus setup. This set up was then filled with a water/glycerol solution, at a ratio of 16:9, which matches the dynamic viscosity of blood with various concentrations of both fluorescent and non-fluorescent beads. Beads flowed at a rate of 0.3 L/min matching the anticipated flow rate in the superior sagittal sinus (Hirabuki et al., 2000) and were recorded. The 600 images taken during fluorescent testing were stacked and aggregated to show the flow pattern just below the tip of the grommet structure. And 100 of the images taken during non-fluorescent testing were divided into 5 columns with a width of 315 μm and beads were tallied within each column of the 4.4 mm2 field of view.

Scanning electron microscopy. After the hydrogel check valves failed, due to excessive reverse flow leakage they were dried and then prepared for scanning electron microscopy. The valve was sputter coated with a layer of gold, approximately 10 nm thick, and imaged using a scanning electron microscope (Hitachi S-4700-II).

Elution of the hydrogel check valve, protein identification via electrophoresis and Bradford protein concentration assay. CSF spiked with all three additives at realistic physiological concentrations was flowed through the hydrogel check valves at 200 μL/min for 72 hours at 37°C using a peristaltic pump (Harvard Apparatus). The valves were washed with TBS (50 mM Tris-HCl pH 7.4 and 150 mM NaCl) at a rate of 200

μL/min for 1 hour. Valves were fragmented, then incubated in 500 μL of 4X SDS loading buffer (40% v/v glycerol, 240 mM Tris-HC) pH 6.8, 8% wt/v sodium dodecyl sulfate (SDS), 0.04% bromophenol blue, 5% β-mercaptoethanol) at 75°C for 10 minutes, electrophoresed with multiple loadings *Sheen et al* on a 3% stacking/6% resolving SDS polyacrylamide gel and stained with coomassie (Bio-Rad).

5.4. Results

The aAG is composed of two components, i.e. hydrogel check valves, encapsulated by a passive grommet structure. The grommet structure is designed to aid surgeons with device implantation. Schwerdt et al. introduced a preliminary 12 mm I-shaped grommet (Schwerdt et al., 2015). Here, we present a 24 mm cone shaped grommet (figure 5.5. (a)), which encapsulates two hydrogel check valves, provides four CSF inlets, six suture points, and a conical structure to aid in implantation (figure 5.5. (b) & (c)). As demonstrated by Schwerdt et al. the hydrogel check valves capitalize on the "fully-passive" swelling of a perforated hydrogel membrane to achieve a non-zero cracking pressure and little to no reverse flow leakage. Swelling of the hydrogel effectively seals the inlet until sufficient differential pressure is applied, where the differential pressure becomes greater than the intrinsic cracking pressure, PT, of the valve (figure 5.5. (d)) (Schwerdt et al., 2014). Figure 5.5. (e) & (f) shows scanning electron microscopy images of the outlet, i.e. tethered hydrogel membrane (e) and the inlet, i.e. through silicon via (f). The inset image of the valve inlet shows the texture at the walls of the via, while this texture ranges from 2 to 5 microns it should not provide purchase for cellular growth.

Prior to evaluating the full aAG, we evaluated the hydrogel check valves, in physiologically realistic bench-top model of hydrocephalus. In order to more accurately evaluate valves, we developed a physiological representation of the implantation location, at the longitudinal fissure where the SAS meets the SSS. This spherical bench-top setup (figure 5.6. (a) and figure 5.2.) emulates the radius of curvature at the interface of the two hemispheres of the brain and generates the resulting multi-directional fluid flow anticipated at the inlet of the hydrogel check valve. By comparison the proof-of-concept testing model was a purely linear flow pathway into the valve inlet (Schwerdt et al., 2015). Similar valve fluidic parameters (figure 5.6. (b) & (c)) were found. However, the time to obtain stabile flow in the spherical set up was greater, >5 min, than in the linear flow setup. This difference in time was likely due to the larger fluid volume in the spherical set up, approximately 5 times greater at 200 mL, which would more slowly translate changes in the flow rate. Aside from this delay, the change from linear inlet flow to multi-directional inlet flow did not affect the functionality of the hydrogel check valve showing that under physiologically realistic flow patterns the valve operated within the design specifications.

To further emulate realistic patient conditions, we developed a series of biologically realistic fluids all based on CSF with various additives known to generate occlusion-based failures in traditional shunts (figure 5.7.). The hydrogel check valve maintained functionality, without a reverse flow leakage greater than 50 μL/min, for a total of 89 days, while being testing under six fluid conditions: CSF at room temperature ~23°C, CSF at internal body temperature ~ 37°C, CSF at 37°C spiked with calcium (1.1mM), CSF at 37°C spiked with blood (5% v/v), CSF at 37°C spiked with fibronectin

(7.5μg/mL) and CSF at 37°C spiked with all three additives. The respective concentrations for each additive was based on concentrations from studies analyzing CSF of patients (Jones & Keep, 1988; Rutter & Smales, 1976; Schutzer et al., 2010; Torre et al., 1991). These fluid conditions were chosen to replicate surgical, foreign body, and long-term implantation conditions. An FDA approved Medtronic PS Medical Strata II shunt was tested in identical conditions to the hydrogel check valve. Both show very similar fluidic characteristics. As shown in figure 5.6. (b), the hydrogel check valve performs within the same parameters, namely cracking pressure ~40 mmH2O (figure 5.6. (b) inset), as the Medtronic Strata II shunt in the worst-case condition of CSF at 37°C spiked with all three additives. Showing that in the spherical bench-top model of hydrocephalus the hydrogel check valve has nearly identical fluidic characteristics as a FDA approved traditional shunt system. Furthermore, the average hydraulic resistance, 169.8 ± 47 mmH2O/mL/min, and reverse flow leakage, 6.97 ± 3.7 μL/min, under all fluidic conditions remained within or below, respectively, the establish parameter for traditional shunt systems (figure 5.6. (c)) (Czosnyka et al., 1997).

After establishing valve functionality in both a physiologically and biologically realistic environment we encapsulated the valve into a grommet structure. This was then sutured into cadaver dura mater and inserted into a second bench-top model of hydrocephalus, which employs cadaver cerebral cortex in addition to dura mater and allows for measurement of both differential pressure across the aAG and the flow out of the aAG (figure 5.3. and figure 5.8. (a)). The fluidic characteristics of the aAG were measured using CSF maintained at ~37 °C (figure 5.8. (b)). The inset of figure 5.8. (b) shows a cracking pressure of ~15 mmH2O for the overall aAG in the cadaver setup.

In order to evaluate the impact of implanting the aAG in the designated location, we also developed a bench-top model of the SSS (figure 5.8. (c)). This model matches the interior dimensions of the SSS space as well as the blood viscosity and flow. The blood emulating fluid was spiked with both fluorescent and non-fluorescent 10 μm diameter particles to evaluate the resulting SSS blood flow pattern post-implantation of the aAG. Figure 5.8. (d) shows a stacked and aggregated image of fluorescent particles over time, where particles initially impact one side of the cone fluid then bifurcates at the tip and reconnects after the structure. This pattern is confirmed by tallying the number of non-fluorescent particles in regions B-F for 100 images taken during a physiologically realistic flow rate of 0.3 L/min (Hirabuki et al., 2000).

After ensuring a viable implantation location, long term valve testing was performed in various fluidic conditions (figure 5.6. (c)). After 89 days the valve failed to remain within design specifications by having an above 50 μL/min reverse flow leakage. This provided us with a unique opportunity to explore the failure mechanisms of this valve and extrapolate methods to counter these failure modes. Scanning electron microscopy was performed (figure 5.9. (a) & (b)) to establish gross analysis. Two observations prompted further investigation, as shown in (a) at the dashed line there appears to be a change in the hydrogel structure and the dashed box indicated the region in (b) at the base of the hydrogel tethers showing the accumulation of biological debris or the growth of a biofilm. Therefore, we exposed a valve to continuous worst-case fluidic conditions for 72 hours and then eluted the proteins which adsorbed to the valve surface (figure 5.10.). Proteins from the eluent were isolated using SDS-PAGE and found to be below the threshold for detection, 50 ng of protein. This was then repeated using the

eluent from 5 valves (figure 5.9. (c)) and a single band appeared at approximately 67 kD, which corresponds to albumin. However, the aggregation of debris would not necessarily account for the increase in reverse flow leakage. Therefore, we investigated the abnormal surface feature found in figure 5.9. (a) using optical profilometry to determine if the structure could be a crack in the hydrogel (figure 5.9. (d)). We determined that this feature was indeed a crack that could be associated with mechanical fatigue of the hydrogel layer. This crack would permit reverse flow leakage under elevated reverse pressures.

5.5. Discussion

Despite the recent improvements in traditional shunt systems, with the augmentation of internal surfaces (Anderson, 2001) as well as the proposed integration of sensing elements (Clark et al., 2015; B. J. Kim et al., 2016). Commercial shunts still suffer from a notoriously high failure rate where 40% of implanted shunts fail within the first two years of use (Drake et al., 2000) and 80% within the first 15 years (Stone et al., 2013). There are numerous failure modes that have been identified and tracked by the FDA, with the leading causes of shunt explanation being occlusion, breakage, and leakage (figure 5.1. (c)). As these shunt systems artificially bypass the natural, brain-contained CSF flow pathway to redirect CSF into the stomach, researchers have long sought ways to reintegrate CSF flow within the brain (Aschoff et al., 1999). One such concept, a ventriculosinus shunt also known as the el-shafei shunt, redirects CSF from the ventricle into the SSS. While this has been attempted in human hydrocephalus patients, it is more effective for a niche subset of patients i.e. non-congenital adult hydrocephalus patients. Infant growth has been shown to interfere with ventriculosinus shunts overtime

(Toma, Tarnaris, Kitchen, & Watkins, 2010). MEMS researchers have further refined this concept for a greater subset of patients, those who suffer from communicating hydrocephalus. Employing micro-scale valves to regulate flow directly from the SAS to the SSS, acting as aAGs.

In healthy individuals, the arachnoid granulations act as one-way biological valves to regulate CSF flow from the SAS to the SSS (figure 5.1. (a)). Arachnoid granulations have two key fluidic characteristics, a one-way fluid flow and a non-zero cracking pressure. Explanted healthy arachnoid granulation tissue, shows a forward flow rate of up to 269 µL/min and a cracking pressure of approximately 39.5 mmH2O (Holman et al., 2010). These parameters give a baseline for the design of micro-scale valves, which act as aAGs. Traditional shunt systems also provide a guideline for these characteristics having a cracking pressure range of 10 to 230 mmH2O (Hirabuki et al., 2000). Two micro-scale valve concepts have been pursued as aAGs, a 3D dome petal valve (Oh et al., 2011) and a hydrogel check valve (Schwerdt et al., 2014). The 3D dome petal concept achieved little to no reverse flow leakage under a differential pressure of ~ 200 mmH2O, however it was unable to achieve a non-zero cracking pressure, as the valve opened under approximately zero applied pressure (Oh et al., 2011). The hydrogel check valve capitalized on the inherent swelling of a perforated hydrogel membrane to achieve both a non-zero cracking pressure, 20-110 mmH2O, and little to no reverse flow leakage with an applied differential pressure of greater than 800 mmH2O (Schwerdt et al., 2014). Neither of these first iterations concepts were implantable designs rather valves which approximated the function of arachnoid granulations.

Subsequently, the 3D dome petal concept was integrated into a micro-needle array for ease of implantation in the dura mater, to regulate flow from the SAS to the SSS (Oh et al., 2014). Preliminary evaluation of the implantable micro-needle array showed its ability to puncture cadaver dura mater and the short-term adhesion of blood platelets (Oh et al., 2014). However, the valve fluidic characteristics, i.e. cracking pressure and reverse flow leakage, were not evaluated in this secondary containment vessel and the preliminary evaluations were only performed for a duration of one hour despite the intended long-term use of the device. The hydrogel check valve was also integrated into a containment vessel, i.e. an I-shaped PDMS grommet structure, with a single hydrogel valve encapsulated within it (Schwerdt et al., 2015). As with the 3D dome petal valve integrated into a micro-needle array, the hydrogel valve was not functionally evaluated after encapsulation within the grommet structure.

Both the micro-needle array and the I-shaped grommet have distinct advantages as implants. The micro-needle array is easily placed in the dura mater, as titanium coated needles can puncture the dura without deformation. However, methods of long-term fixation of the micro-needle array such as suturing or surgical glue were not discussed, as the array is tapered this may allow for loosening of the fixation over time. Additionally, mechanical compliance between the implant and the dura mater is also a concern. The Young's modulus of SU8 is in the range of 4 GPa (T. Xu et al., 2016), and the modulus of PDMS is 0.548 to 3.728 MPa depending on crosslinking ratios (Z. Wang, Volinsky, & Gallant, 2014), while the modulus of human dura mater is in the range of 65 to 105 MPa (Runza et al., 1999). Often, drastic differences in implant stiffness or implant density (SU8 1,200, Ti 4,506, PDMS 965, and cerebral cortex 1,045 kg/m3) can lead to glial scar

formation (Lind, Linsmeier, & Schouenborg, 2013). Despite the mechanical compliance of the I-shaped PDMS grommet being closer to that of dura mater, the implantation protocol for the I-shaped grommet is significantly more complex, requiring an incision of the dura mater before the inserting the grommet and affixing it via suturing (Schwerdt et al., 2015). Our iteration of the grommet structure, the aAG, (figure 5.5. (a)-(c)) incorporates concepts from both the micro-needle array and the I-shaped grommet. The aAG incorporates redundancy, similar to micro-needle array, by having two hydrogel check valves encapsulated within one structure, additionally redundancy is achieved by having two CSF inlets per valve. Additionally, the aAG is designed to be surgically friendly with the cone shape and inclusion of a puncture tool, (figure 5.1. (f) & (g), to easily puncture the dura mater and wedge it open to insert the aAG. Also, the puncture tool aids in affixing the aAG by holding it in place during suturing and the application of surgical glue. Furthermore, the aAG is made of mechanically compliant PDMS to match the stiffness of the dura mater.

To evaluate the effects of implanting the aAG into the SSS, we developed a simulated SSS setup based on the interior SSS. Blood emulating water spiked with fluorescent and non-fluorescent microbeads flowed around the tip of the grommet generating the flow pattern shown in figure 5.8. (a). Images were aggregated to demonstrate the flow over time and non-fluorescent beads were quantified by tallying the number of beads per column to show the symmetry of flow at the tip of the implanted aAG, where bead bifurcate around the grommet tip. While the concept of an artificial device which mimics the cracking pressure and flow parameters of arachnoid granulations is relatively novel, the desire to directly drain CSF into the SSS was

presented as early as 1896 (Aschoff et al., 1999). In practice the closest device to realize this goal is the El-Shafei shunt, a non-regulated flow pathway artificially generated between the ventricle and SSS (Toma et al., 2010). Both our proposed aAG and the El-Shafei shunt intrude into the SSS, with respective protruding volumes of 176 mm3 and 171 mm3 and surface areas of 256 mm2 and 528 mm2. As the El-Shafei concept with a similar protruding volume and surface area has not lead to cases of thrombosis we can hypothesize that the aAG would also follow this trend.

The aAG is not simple a grommet structure, it contains two functional components, hydrogel check valves, which replicate the fluid dynamic characteristics of arachnoid granulations. Therefore, these must also be evaluated individually. Throughout testing in a physiologically realistic bench-top model of hydrocephalus (figure 5.6. (a)), these devices remained within design specifications over the course of 89 days of testing using a wide range of fluidic conditions known to induce failure in traditional shunt systems. Traditional shunt systems have a cracking pressure range of 10 to 230 mmH2O, a fluidic resistance range of 13.5 to 340 mmH2O/mL/min and a maximum reverse flow leakage of 50 µL/min (Hirabuki et al., 2000). The hydrogel check valve tested in the wide range of fluidic conditions has an average cracking pressure of 24.1 ± 3.4 mmH2O, fluidic resistance of 169.7 ± 47 mmH2O/mL/min and a reverse flow leakage of 6.9 ± 3.7 µL/min (figure 5.6. (c) and figure 5.11.). These three valve fluidic characteristics are all well aligned and within the specifications for traditional shunt systems. Additionally, industry standards such as ISO 7197 and ASTM F647 designate specific pressure and flow characteristics for example an acceptable shunt is evaluated in terms of reverse flow leakage by applying a differential pressure of at least 300 mmH2O and monitoring the

resulting leakage of less than 100 µL/min, ASTM F647 6.2.3.2. The hydrogel check valve is placed under similar differential pressures and achieves a reverse flow leakage of less than 50 µL/min indicating that the valve leakage rate is lower even than the allowable range for traditional shunts.

Furthermore, when the valve is encapsulated into the grommet structure it further maintains design specifications. This testing was performed using the cadaver-based bench-top model of hydrocephalus (figure 5.3. and figure 5.8. (a)). This second bench-top model was designed to not only allow for functional testing of the hydrogel check valves encapsulated by the grommet but to test the validity of the redundant CSF inlets. Comparing pre- and post-encapsulation the cracking pressure of the valve decreased from 70 mmH2O to 19.5 mmH2O, however this remains within the desired cracking pressure range and pre-encapsulation testing was performed at room temperature with water, while post-encapsulation testing was performed at internal body temperature ~ 37°C with patient CSF. The cadaver bench-top model also included cadaver cerebral cortex material (figure 5.8. (a)) to represent the SAS. Often in patients with hydrocephalus the cerebral cortex tissue swells placing it directly in contact with the dura mater. To avoid aAG blockage due to cerebral cortex swelling, alternate CSF inlets were incorporated parallel to the cerebral cortex tissue (figure 5.5. (c)). In functional testing of the aAG CSF flow was unobstructed by the presence of free-floating cadaver cerebral cortex tissues. Therefore, the aAG maintained functionality within a realistic cadaver bench-top model of hydrocephalus.

While the valve did remain within design specifications while encapsulated by the grommet structure, however, in individual testing it eventually failed by exceeding a

reverse flow rate of 50 µL/min. This provided a unique opportunity to isolate, understand, and compare failure modes between the hydrogel check valves and traditional shunt systems. As previous studies have found with conventional shunts, bio-films and cellular debris tend to adsorb to the surface of hydrocephalus shunts and can induce failure (Brydon et al., 1998). The amount and identity of these proteins and cellular debris indicate foreign body response or sensitization. Specific proteins, such as fibronectin, are known to attract astrocyte and glial cells to the surface of shunts inducing and proliferating foreign body response (Brydon et al., 1998; VandeVord et al., 2004). Therefore, we performed scanning electron microscopy to investigate the valve surface looking for cellular debris, material accumulation or other features which could indicate a valve failure mode (figure 5.9.). Gross SEM imagery identified the accumulation of debris and a hydrogel surface feature which could both have caused the increase in reverse flow leakage.

Therefore, we performed two assessments to isolate the failure mechanism. First, we emulated the testing conditions by continuously flowing worst-case CSF at ~37°C for 72 hours, eluted the proteins adsorbed on the surface of the hydrogel check valve, and performed a standard SDS- polyacrylamide gel electrophoresis assay, as shown in figure 5.10. While CSF is a protein-rich solution, examination of the CSF solution spiked with all three additives had an expected band at 220 kDa corresponding to the molecular mass of fibronectin. However, the most prominent band in the CSF sample corresponds to the highly abundant albumin protein, 67 kDa. Protein eluted from a single hydrogel check valve incubated for 72 hours in CSF spiked with all three additives was below our threshold for detection, approximately 100 ng of protein (figure 5.10.). To overcome this,

we increased the number of devices to five hydrogel check valves, figure 5.9. (c). The eluted protein from the combined five devices had a single band at 67 kDa, corresponding to the overwhelming abundant albumin protein from the CSF solution (Schutzer et al., 2010). Albumin protein has been previously reported to adsorb to hydrocephalus shunts (Brydon et al., 1998). With a total mass of merely 1 μg adsorbed to 5 devices, as found using a Bradford protein concentration assay, 200 ng per a device on average, few proteins appear to have adsorbed to the surface of the hydrogel. This further supports that protein adsorption to the surface of the hydrogel check valve did not significantly contribute to device failure.

Therefore, we further investigated the abnormal surface feature of the hydrogel (figure 5.12.). This was further investigated in detail using optical profilometry, figure 5.9. (d) and found that this deformation was at two different heights indicating a crack in the hydrogel. This crack would permit reverse flow leakage under elevated reverse pressures. This may have resulted from structural weakness in the relatively thin hydrogel layer of merely 100 μm after prolonged testing. Repeated testing of at least 8 replicates where the applied force on the hydrogel is at least 0.577 mN forcing the malleable hydrogel into sharp edge of the significantly stiffer silicon substrate beneath the hydrogel may have caused this crack formation. There are numerous ways to address this mechanical fatigue-based failure mode, increasing the thickness of the hydrogel, optimizing the structural properties of the hydrogel, or exchanging the silicon substrate for a more compliant, yet, biocompatible polymer. These are all promising avenues to pursue. As each new iteration of the aAG is developed modes of failure must also be considered, it is reassuring that the traditional shunt failure mode of occlusion was not

present, likely due the significantly reduced surface area of the aAG when compared to traditional shunts.

Anderson, J. M. (2001). Biological Responses to Materials. Annual Review of Materials Research, 31, 81-110.

Aschoff, A., Kremer, P., Hashemi, B., & Kunze, S. (1999). The scientific history of hydrocephalus and its treatment. neurosurgical Review, 22, 67-93.

Brydon, H. L., Keir, G., Thompson, E. J., Bayston, R., Harkness, W., Keir, G., & Hayward, R. (1998). Protein adsorption to hydrocephalus shunt catheters : CSF protein adsorption Protein adsorption to hydrocephalus shunt catheters : CSF protein adsorption. Electrophoresis, 643-647.

Clark, T. M., Malpas, S. C., Mccormick, D., Heppner, P., & Budgett, D. M. (2015). Implantable Multi-Modal Sensor to Improve Outcomes in Hydrocephalus Management. IEEE Sensors Journal, 15, 6027-6035.

Czosnyka, M., Czosnyka, Z., Whitehouse, H., & Pickard, J. D. (1997). Hydrodynamic properties of hydrocephalus shunts: United Kingdom Shunt Evaluation Laboratory. Journal of neurology, neurosurgery, and psychiatry, 62, 43-50. doi: 10.1136/jnnp.62.1.43

Drake, J. M., Kestle, J. R. W., & Tuli, S. (2000). CSF shunts 50 years on – past, present and future. Child's Nervous System, 16, 800-804.

Hanak, B. W., Ross, E. F., Harris, C. A., Browd, S. R., & Shain, W. (2016). Toward a better understanding of the cellular basis for cerebrospinal fluid shunt obstruction: report on the construction of a bank of explanted hydrocephalus devices. Journal of Neurosurgery: Pediatrics, 18, 213-223. doi: 10.3171/2016.2.PEDS15531

Harris, C., Pearson, K., Hadley, K., & Zhu, S. (2015). Fabrication of three-dimensional hydrogel scaffolds for modeling shunt failure by tissue obstruction in hydrocephalus. Fluids and Barriers of …, 12, 1-15. doi: 10.1186/s12987-015-0023-9

Harris, C. A., & Mcallister, J. P. (2012). What We Should Know About the Cellular and Tissue Response Causing Catheter Obstruction in the Treatment of Hydrocephalus. Neurosurgery, 70, 1589-1602. doi: 10.1227/NEU.0b013e318244695f

Hirabuki, N., Watanabe, Y., Mano, T., Fujita, N., Tanaka, H., Ueguchi, T., & Nakamura, H. (2000). Quantitation of Flow in the Superior Sagittal Sinus Performed with Cine Phase-contrast MR Imaging of Healthy and Achondroplastic Children. American Journal of Neuroradiology, 21, 1497-1501.

Holman, D. W., Kurtcuoglu, V., & Grzybowski, D. M. (2010). Cerebrospinal fluid dynamics in the human cranial subarachnoid space: an overlooked mediator of

cerebral disease. II. In vitro arachnoid outflow model. Journal of the Royal Society, Interface / the Royal Society, 7, 1205-1218. doi: 10.1098/rsif.2010.0032

Jones, H., & Keep, R. (1988). Brain Fluid Calcium Concentration and Response To Acute Hypercalcaemia During Development in the Rat. J Physiol., 402, 579-593.

Kim, B. J., Jin, W., Baldwin, A., Yu, L., Christian, E., Krieger, M. D., . . . Meng, E. (2016). Parylene MEMS patency sensor for assessment of hydrocephalus shunt obstruction. Biomedical Microdevices, 18, 87. doi: 10.1007/s10544-016-0112-9

Lind, G., Linsmeier, C. E., & Schouenborg, J. (2013). The density difference between tissue and neural probes is a key factor for glial scarring. Scientific Reports, 3, 1-7. doi: 10.1038/srep02942

Moshayedi, P., Ng, G., Kwok, J. C. F., Yeo, G. S. H., Bryant, C. E., Fawcett, J. W., Guck, J. (2014). The relationship between glial cell mechanosensitivity and foreign body reactions in the central nervous system. Biomaterials, 35, 3919-3925. doi: 10.1016/j.biomaterials.2014.01.038

Oh, J., Kim, G., Kralick, F., & Noh, H. (2011). Design and Fabrication of a PDMS / Parylene Microvalve for the Treatment of Hydrocephalus. Journal of Microelectromechanical Systems, 20, 811-818.

Oh, J., Liu, K., Medina, T., Kralick, F., & Noh, H. (2014). A novel microneedle array for the treatment of hydrocephalus. Microsystem Technologies, 20, 1169-1179. doi: 10.1007/s00542-013-1988-4

Pople, I. K. (2002). Hydrocephalus And Shunts: What The Neurologist Should Know. Journal of neurology, neurosurgery, and psychiatry, 73, i17-i22.

Runza, M., Pietrabissa, R., Mantero, S., Albani, A., Quaglini, V., & Contro, R. (1999). Lumbar Dura Mater Biomechanics: Experimental Characterization and Scanning Electron Microscopy Observatios. Anesthesia & Analgesia, 88, 1317-1321. doi: 10.1097/00000539-199906000-00022

Rutter, N., & Smales, O. R. (1976). Calcium, magnesium, and glucose levels in blood and CSF of children with febrile convulsions. Archives of disease in childhood, 51, 141-143. doi: 10.1136/adc.51.2.141

Schutzer, S. E., Liu, T., Natelson, B. H., Angel, T. E., Schepmoes, A. A., Purvine, S. O., . . . Bergquist, J. (2010). Establishing the proteome of normal human cerebrospinal fluid. PLoS ONE, 5, 1-7. doi: 10.1371/journal.pone.0010980

Schwerdt, H. N., Amjad, U., Appel, J., Elhadi, A. M., Lei, T., Preul, M. C., Chae, J. (2015). In Vitro Hydrodynamic, Transient, and Overtime Performance of a Miniaturized Valve for Hydrocephalus. Annals of biomedical engineering, 43, 603-615. doi: 10.1007/s10439-015-1291-x

Schwerdt, H. N., Bristol, R. E., & Chae, J. (2014). Miniaturized Passive Hydrogel Check Valve for Hydrocephalus Treatment. IEEE Transactions on Biomedical Engineering, 61, 814-820.

Sgouros, S., & Dipple, S. J. (2004). an investigation of structural degradation of CSF shunt valves performed using SEM and energy dispersive x ray microanalysis. Journal of neurosurgery, 100, 534-540.

Stone, J. J., Walker, C. T., Jacobson, M., Phillips, V., & Silberstein, H. J. (2013). Revision rate of pediatric ventriculoperitoneal shunts after 15 years. Journal of Neurosurgery: Pediatrics, 11, 15-19.

Toma, A. K., Tarnaris, A., Kitchen, N. D., & Watkins, L. D. (2010). Ventriculosinus shunt. Neurosurgical Review, 33, 147-152. doi: 10.1007/s10143-010-0242-0

Torre, D., Zeroli, C., Issi, M., Fiori, G. P., Ferraro, G., & Speranza, F. (1991). Cerebrospinal fluid concentration of fibronectin in meningitis. Journal of clinical pathology, 44, 783-784.

VandeVord, P. J., Gupta, N., Wilson, R. B., Vinuya, R. Z., Schaefer, C. J., Canady, A. I., & Wooley, P. H. (2004). Immune reactions associated with silicone-based ventriculo-peritoneal shunt malfunctions in children. Biomaterials, 25, 3853-3860. doi: 10.1016/j.biomaterials.2003.10.024

Wang, Z., Volinsky, A. A., & Gallant, N. D. (2014). Crosslinking effect on polydimethylsiloxane elastic modulus measured by custom-built compression instrument. Journal of Applied Polymer Science, 131, 1-4. doi: 10.1002/app.41050

Xu, T., Yoo, J. H., Babu, S., Roy, S., Lee, J. B., & Lu, H. (2016). Characterization of the mechanical behavior of SU-8 at microscale by viscoelastic analysis. Journal of Micromechanics and Microengineering, 26. doi: 10.1088/0960-1317/26/10/105001

Yamamoto, S., Ohno, K., Aoyagi, M., Ichinose, S., & Hirakawa, K. (2002). Calcific deposits on degraded shunt catheters: long-term follow-up of V-P shunts and late complications in three cases. Child's Nervous System, 18, 19-25. doi: 10.1007/s00381-001-0532-5

Zhu, D. C., Xenos, M., Linninger, A. A., & Penn, R. D. (2006). Dynamics of lateral ventricle and cerebrospinal fluid in normal and hydrocephalic brains. Journal of Magnetic Resonance Imaging, 24, 756-770. doi: 10.1002/jmri.2067

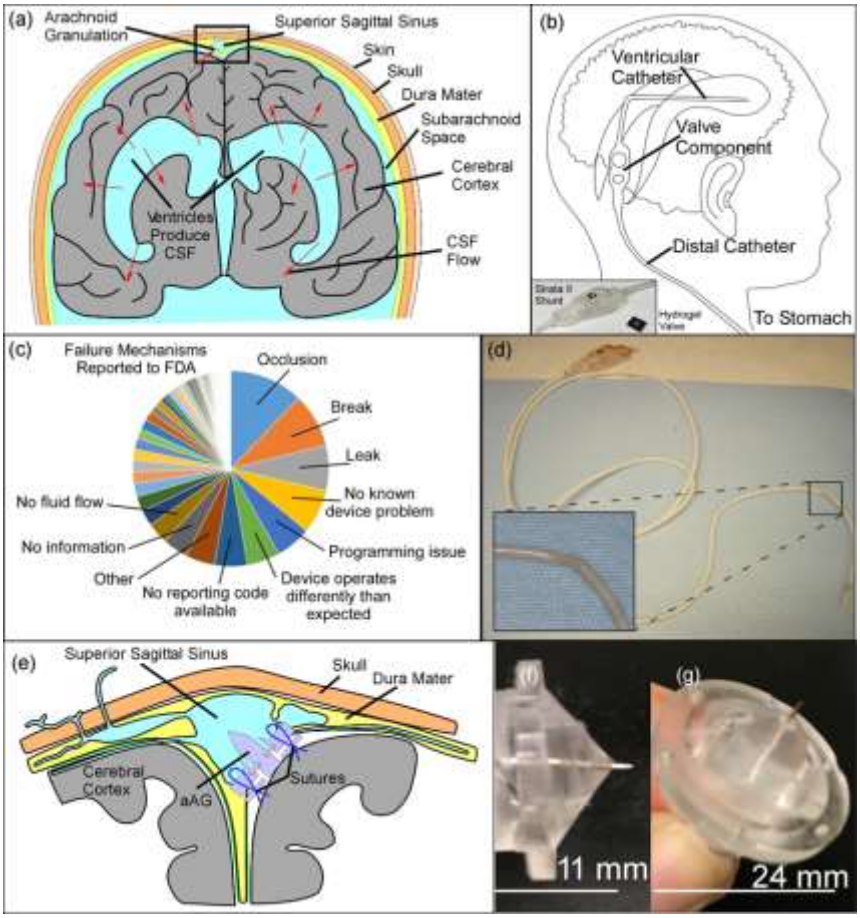

Figure 5.1. Cerebrospinal fluid flow and hydrocephalus, including current and proposed treatments. (a) Schematic of cerebrospinal fluid flow (CSF) in normal brains, where CSF is produced at the ventricles (~18-24 mL/hour) it flows through and around the cerebral cortex and is drained out of the arachnoid granulations into the superior sagittal sinus. (b) In hydrocephalus this pathway is obstructed, the current treatment is the implantation of a shunt system (inset). Shunts are highly prone to failure, a breakdown of failure mode as reported to the FDA within the last 5 years is shown (c). (d) Explanted shunt after 12 years of use with breakage of the distal catheter and occlusion on the valve mechanism. (e-g) Proposed implantation location and images of an artificial arachnoid granulation (aAG) designed to replace shunt systems.

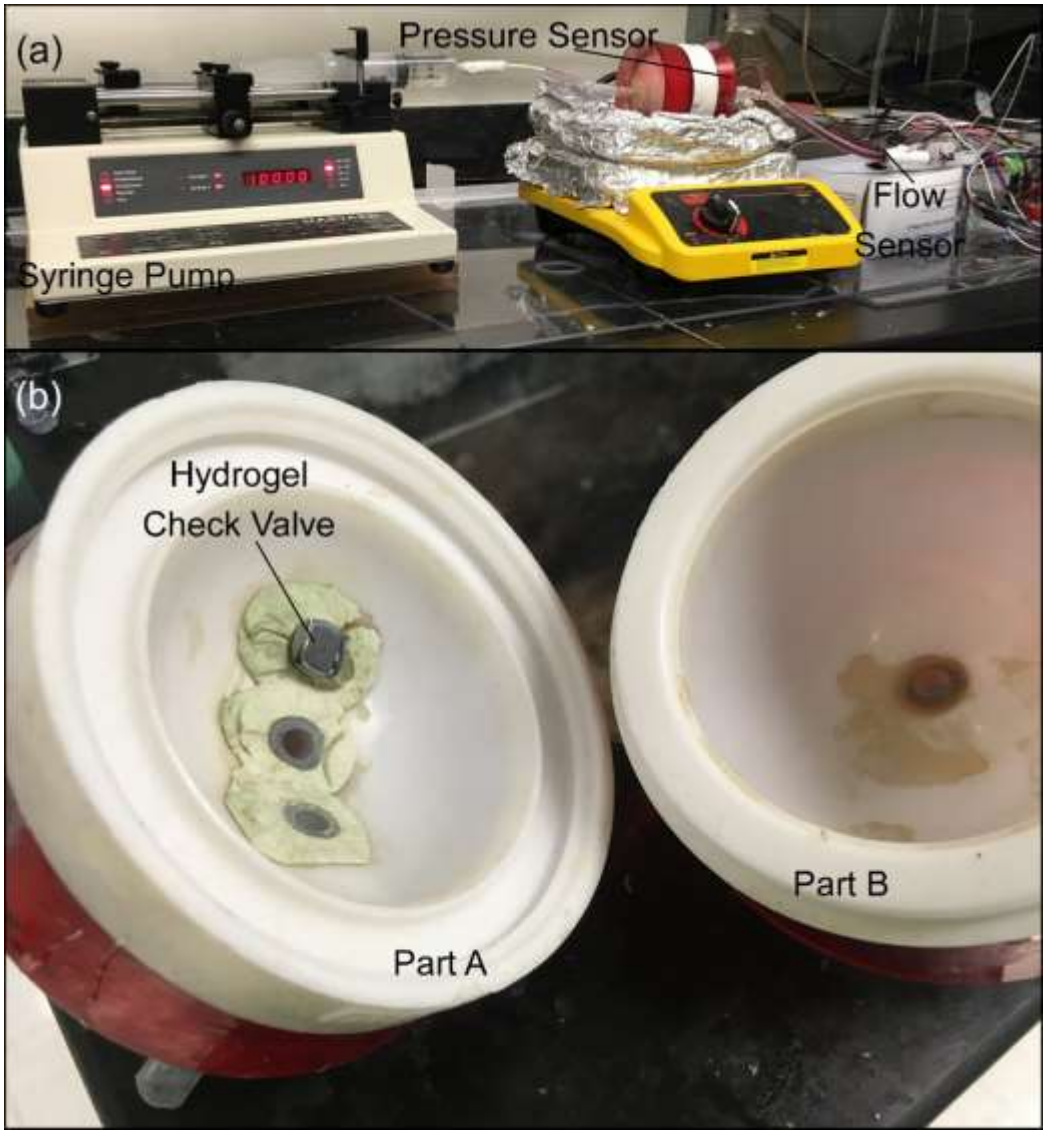

Figure 5.2. The spherical testing setup to mimic the desired implant location. (a) Image of the overall testing setup where a syringe pump flows CSF into a sphere (b) maintained at body temperature ~37°C and the differential pressure across the valve and the flow rate out of the valve are monitored.

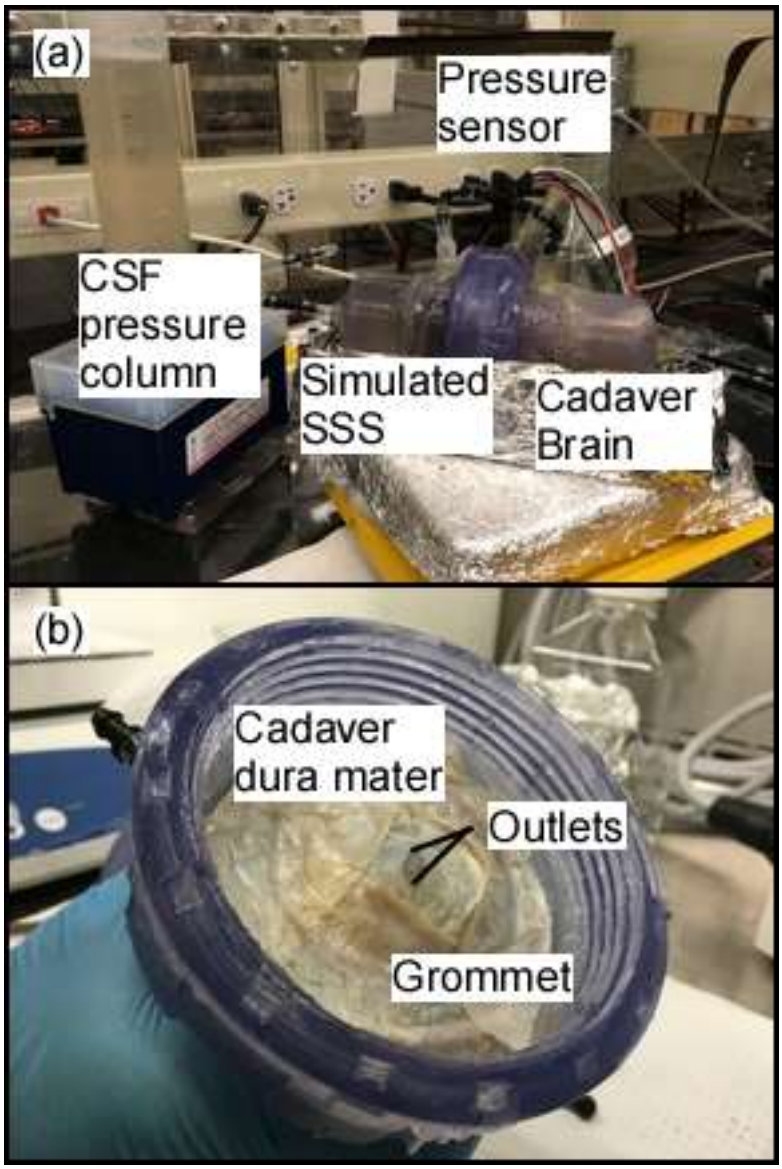

Figure 5.3. Cadaver bench-top model of hydrocephalus. (a) overall image of cadaver bench top model testing for reverse flow leakage with the simulated superior sagittal sinus (SSS) towards the CSF pressure column. (b) artificial arachnoid granulation sutured into cadaver dura mater for testing.

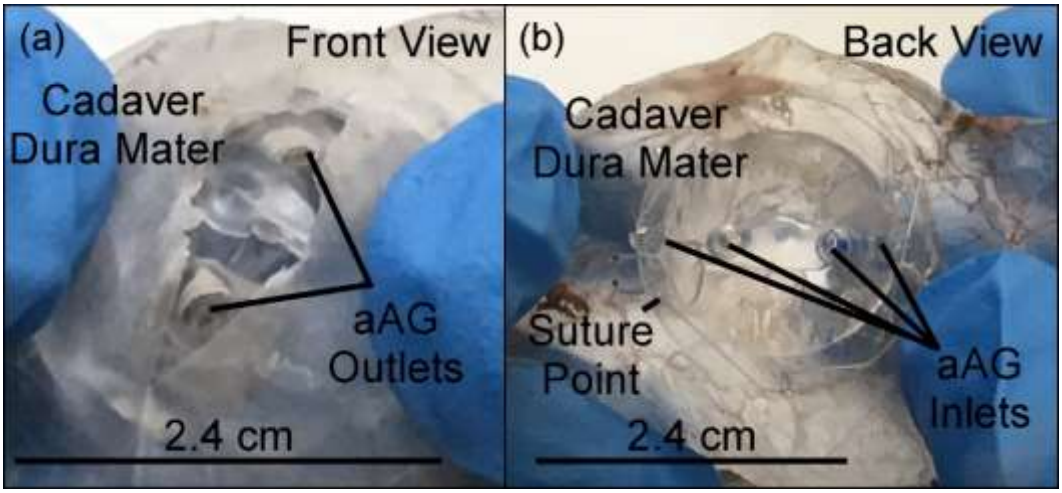

Figure 5.4. Artificial arachnoid granulation sutured into cadaver dura mater. (a) front view, i.e. SSS side of the aAG sutured into dura mater with both outlets unobstructed. (b) back view, i.e. SAS side of the aAG sutured into dura mater with 6 suture points and 4 CSF inlets.

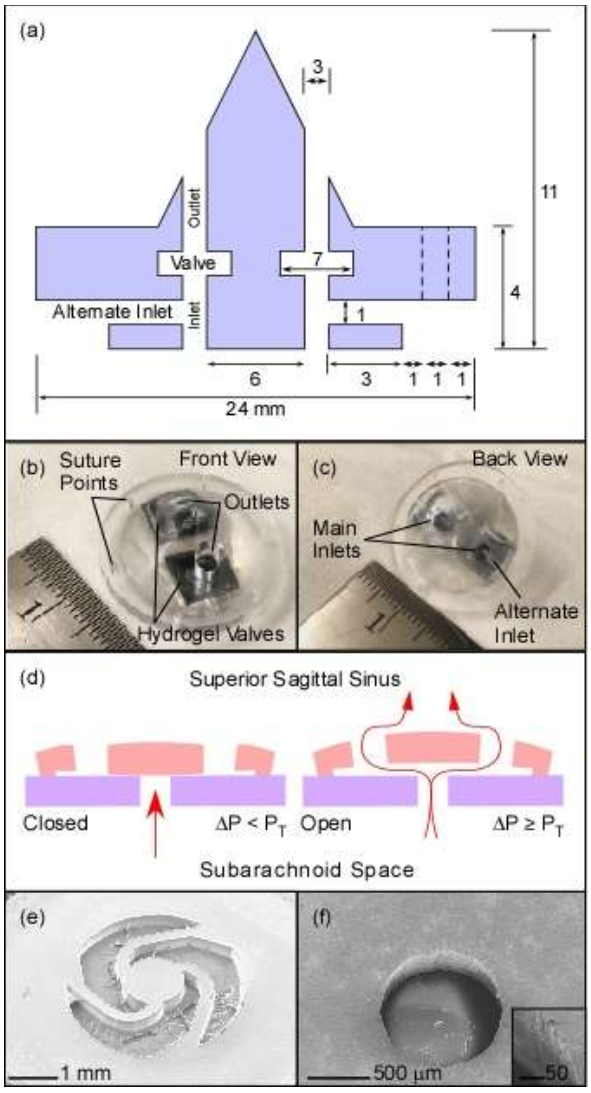

Figure 5.5. Artificial arachnoid granulation overall dimensions and implementation with hydrogel check valve operating principle and scanning electron microscopy. (a) Dimensions of the artificial arachnoid granulation (aAG). (b) front view, i.e. SSS side of the aAG showing the outlets, suture points and hydrogel check valves. (c) back view, i.e. SAS side of the aAG showing main and alternate CSF inlets. (d) Schematic demonstrating the operating principle of the hydrogel check valve, where the valve remains closed until the differential pressure ΔP becomes greater than the cracking pressure P_T it then opens allowing fluid to flow exclusively from the subarachnoid space to the superior sagittal sinus. (e)&(f) scanning electron microscopy images of (e) hydrogel valve outlet and (f) through silicon via inlet, with inset image showing the texture of the through silicon via.

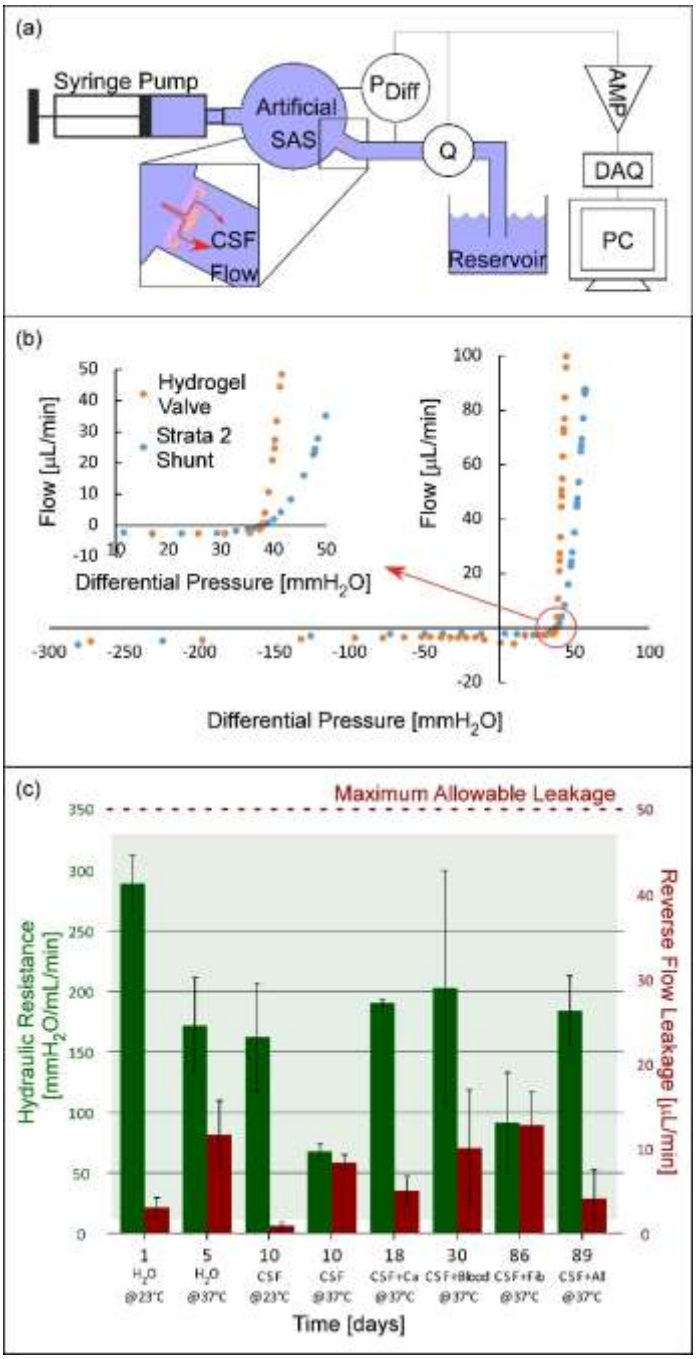

Figure 5.6. Hydrogel check valve operation in the spherical bench-top model of hydrocephalus. (a) Schematic of the spherical bench-top model. (b) Differential pressure vs. flow characteristics of the hydrogel check valve and a traditional shunt in the worst case fluidic condition, CSF spiked with physiological concentrations of blood, fibronectin, and calcium and maintained at ~37°C. (c) Hydraulic resistance and reverse flow leakage of a single hydrogel check valve during 89 days of testing under various fluidic conditions.

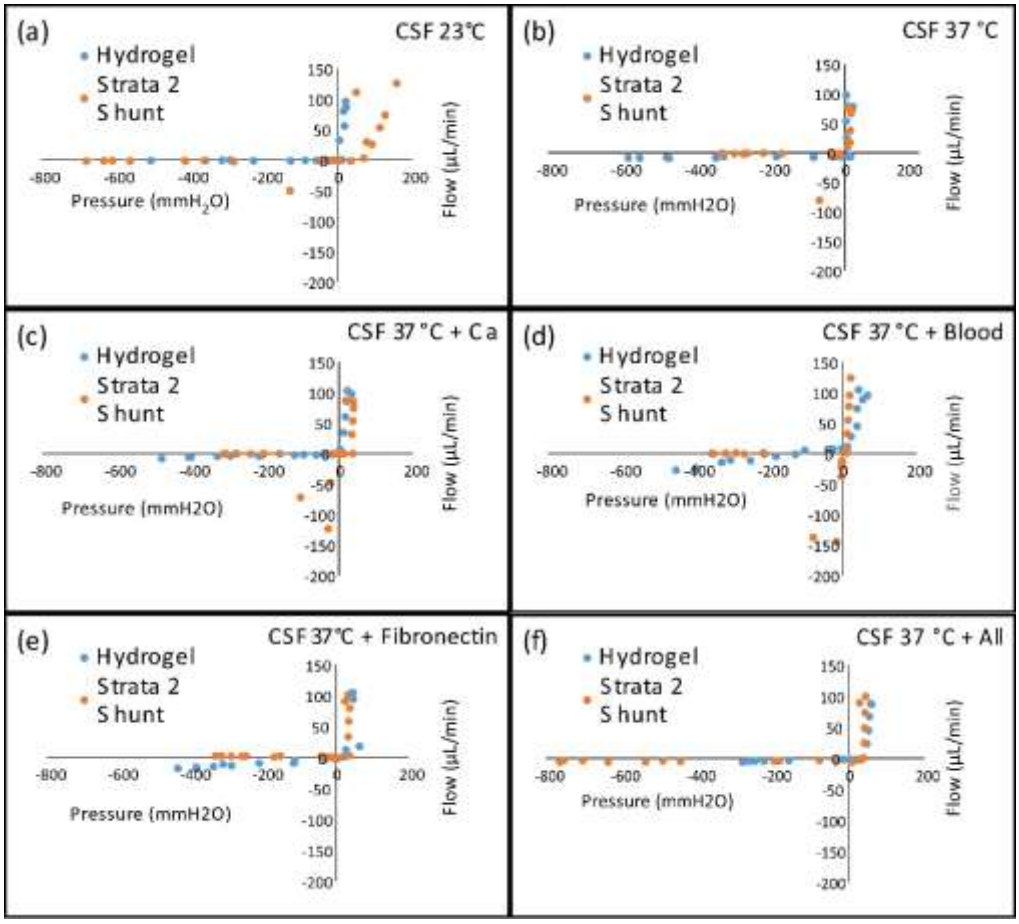

Figure 5.7. Differential pressure vs flow characteristics of a hydrogel check valve and a traditional shunt under various fluidic conditions. (a) CSF at room temperature, ~23°C. (b) CSF at body temperature, ~37°C. (c) CSF at body temperature, ~37°C, spiked with 1.1mM calcium. (d) CSF at body temperature, ~37°C, spiked with 5% blood. (e) CSF at body temperature, ~37°C, spiked with 7.5 µg/mL fibronectin. (f) CSF at body temperature, ~37°C, spiked with 1.1mM calcium, 5% blood, and 7.5 µg/mL fibronectin.

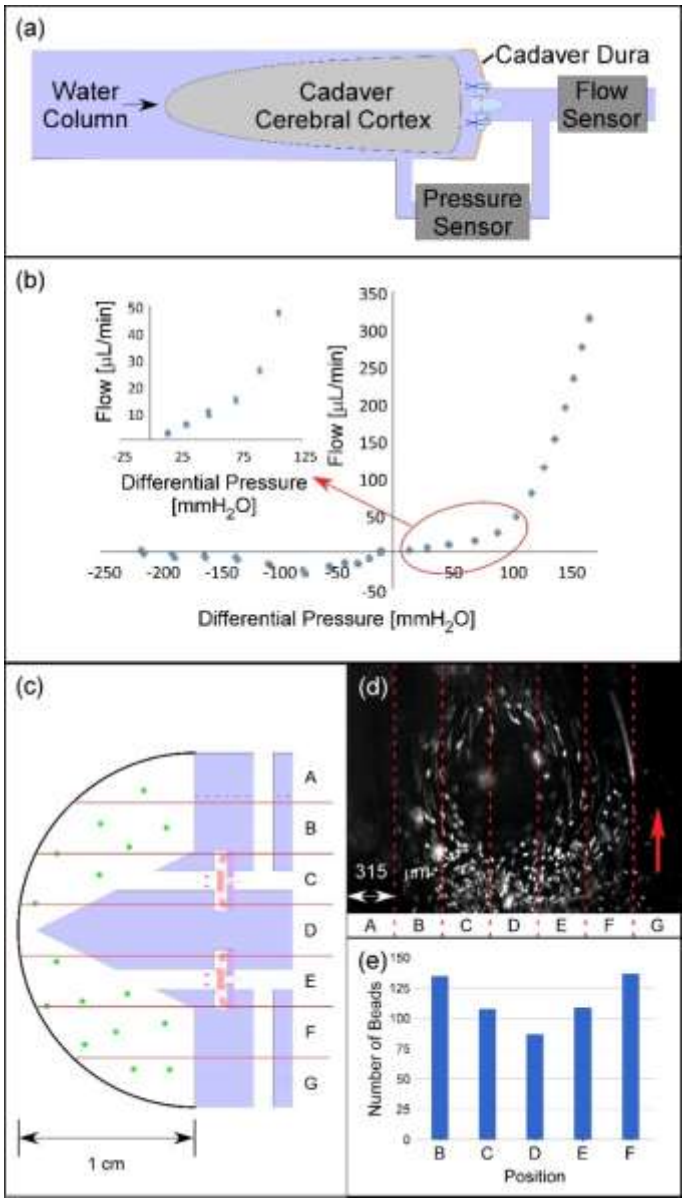

Figure 5.8. aAG testing in a cadaver bench-top model of hydrocephalus and a simulated SSS. (a) schematic of the cadaver bench-top model of hydrocephalus to monitor differential pressure and flow of the aAG. (b) fluidic characteristics of the overall aAG in the cadaver model with the inset showing the cracking pressure of the aAG. (c) schematic of the aAG inside the simulated SSS model. (d) Compilation of 600 images taken while fluid matching the viscosity of blood spiked with 10 µm fluorescent beads flows around the grommet structure at a rate of 0.3 L/min. (e) Quantification of the number of beads relative to grommet position over 100 images.

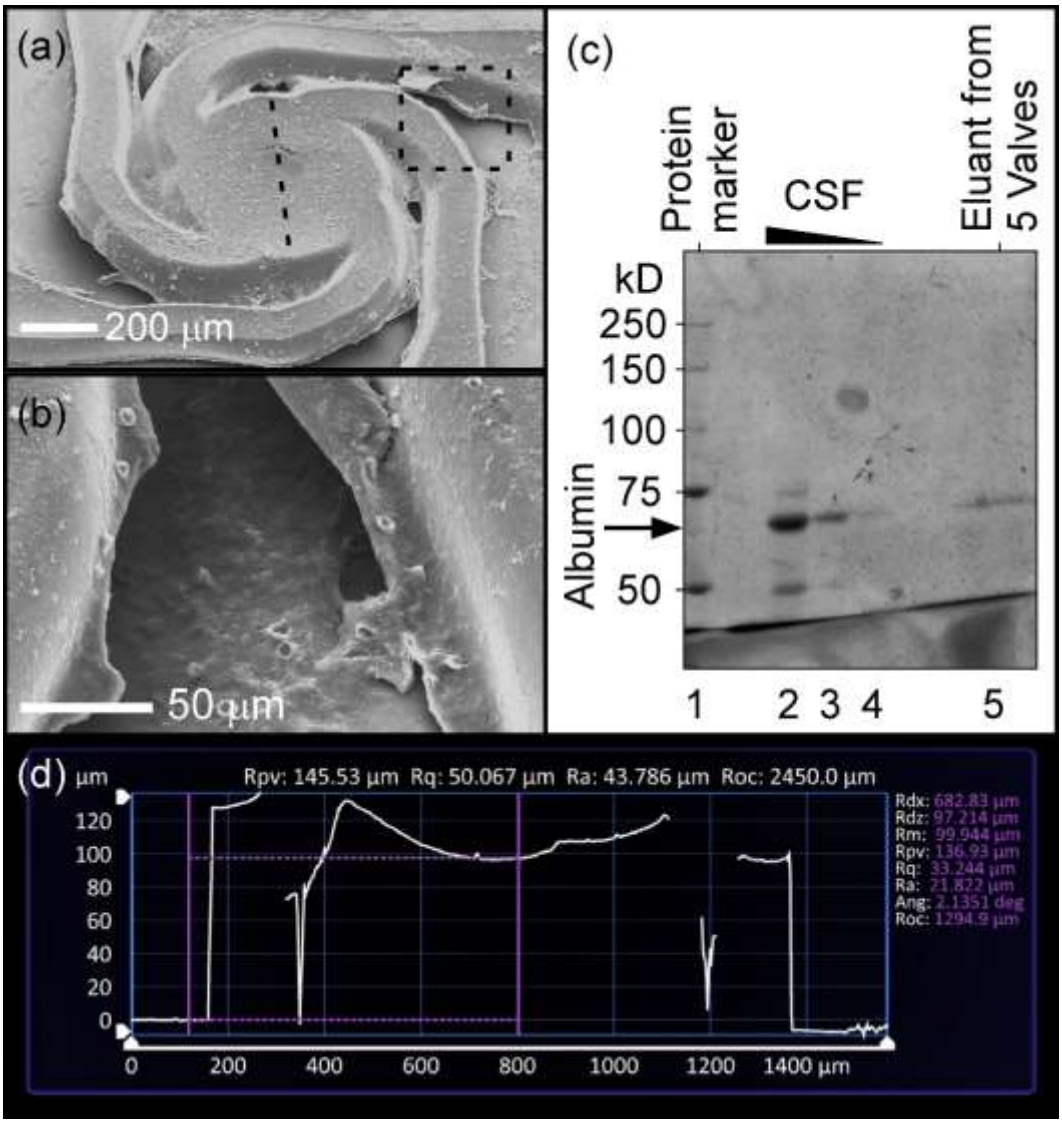

Figure 5.9. Failure mechanism exploration. Scanning electron microscopy of (a) the overall valve after 89 days of testing and (b) the area between two tethers indicated by a square in (a). (c) Electrophoresis of protein elution from an aggregate of 5 valves exposed to worst case fluidic conditions for 72 hours. (d) Optical profilometry of the line indicated in (a) showing a crack in the hydrogel.

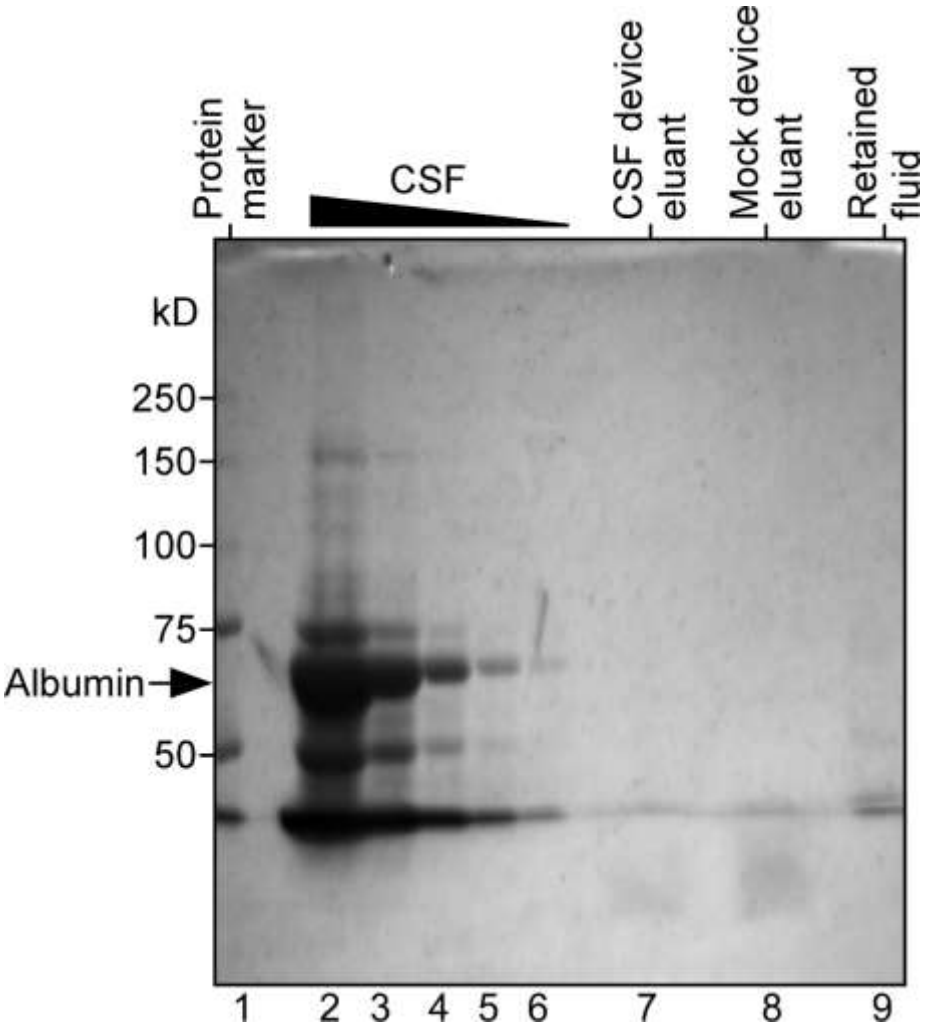

Figure 5.10. Electrophoresis of protein elution of a single hydrogel check valve. Protein aggregation after 72 hours of exposure to worst case fluidic conditions was not above the threshold for detection for sodium dodecyl sulfate polyacrylamide gel electrophoresis.

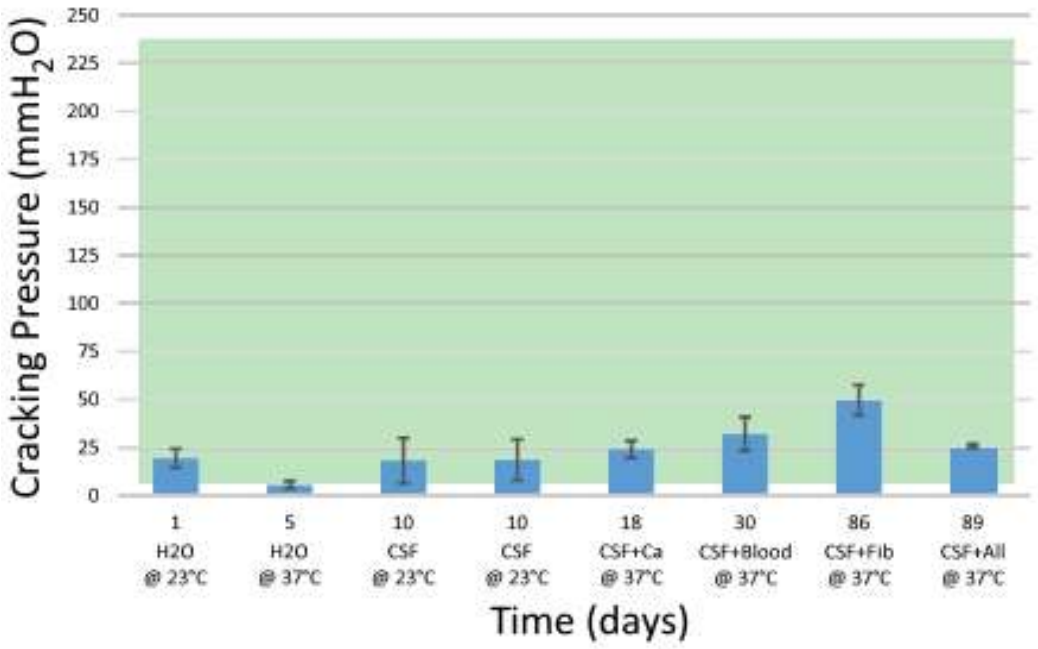

Figure 5.11. Cracking pressure under various conditions. Cracking pressure of a single hydrogel check valve under a wide variety of conditions known to induce occlusion in traditional shunt systems. Green box highlights the acceptable cracking pressure range for traditional shunt systems, 10 to 230 mmH_2O.

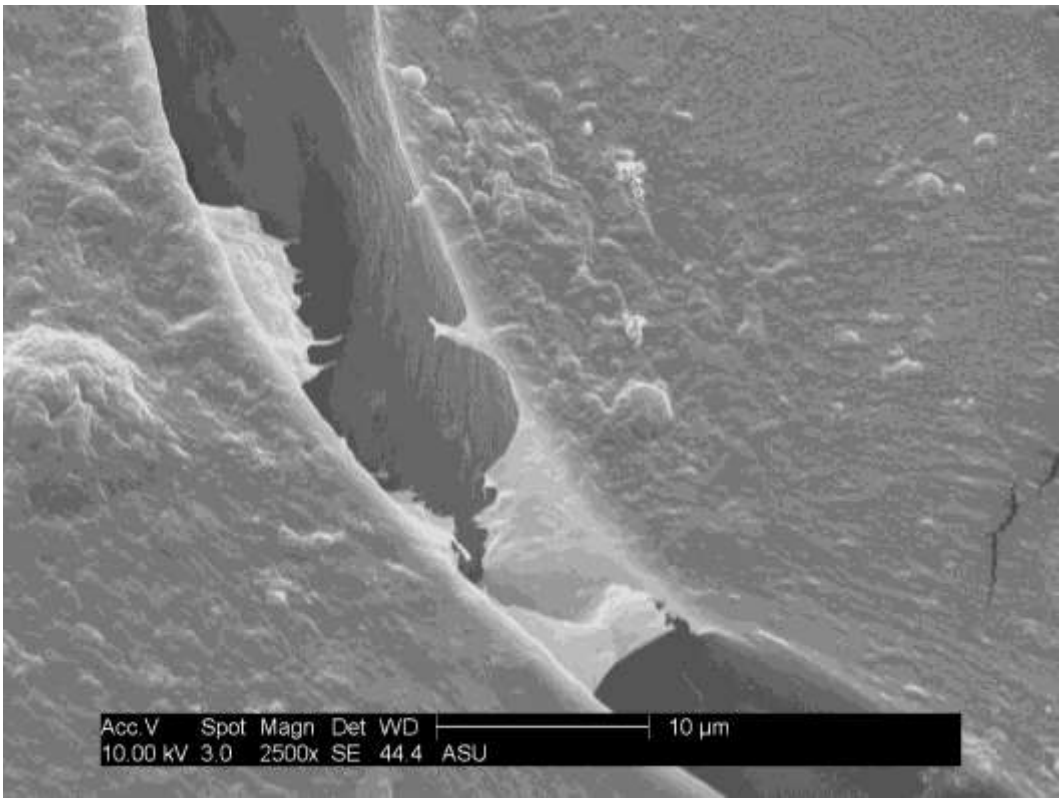

Figure 5.12. Detailed failure mechanism exploration. Scanning electron microscopy of the surface feature determined to be a crack in the hydrogel membrane.

REFERENCES

Abraham, W. T., Adamson, P. B., Bourge, R. C., Aaron, M. F., Costanzo, M. R., Stevenson, L. W., & Strickland, W. (2011). Wireless pulmonary artery haemodynamic monitoring in chronic heart failure: a randomised controlled trial. Lancet, 377, 658-666. doi: 10.1016/S0140-6736(11)60101-3

Abraham, W. T., Stevenson, L. W., Bourge, R. C., Lindenfeld, J. A., Bauman, J. G., & Adamson, P. B. (2016). Sustained efficacy of pulmonary artery pressure to guide adjustment of chronic heart failure therapy: complete follow-up results from the CHAMPION randomised trial. The Lancet, 387, 453-461. doi: 10.1016/S0140-6736(15)00723-0

Alarifi, S., Ali, D., Verma, A., Alakhtani, S., & Ali, B. A. (2013). Cytotoxicity and genotoxicity of copper oxide nanoparticles in human skin keratinocytes cells. International journal of toxicology, 32, 296-307. doi: 10.1177/1091581813487563

Alcendor, D. J., Block III, F. E., Cliff, D. E., Daniels, J. S., Ellacott, K. L. J., Goodwin, C. R., . . . Wikswo, J. P. (2013). Neurovascular unit on a chip : implications for translational applications. Stem Cell Research and Therapy, 4, 1-5.

Aldousari, S., & Kassouf, W. (2010). Update on the management of non-muscle invasive bladder cancer. Canadian Urological Association Journal, 4, 56-64.

Alkilany, A. M., & Murphy, C. J. (2010). Toxicity and cellular uptake of gold nanoparticles : what we have learned so far ? Journal of nanoparticle research, 12, 2313-2333. doi: 10.1007/s11051-010-9911-8

Amini, A. R., Wallace, J. S., & Nukavarapu, S. P. (2011). Short-Term and Long-Term Effects of Orthopedic Biodegradable Implants. Journal of Long Term Effects of Medical Implants, 21, 93-122.

Anderson, J. M. (2001). Biological Responses to Materials. Annual Review of Materials Research, 31, 81-110.

Anderson, J. M., Rodriguez, A., & Chang, D. T. (2008). Foreign Body Reaction to Biomaterials. Seminars in Immunology, 20, 86-100.

Appel, J., Sin, M. L. Y., Liao, J. C., & Chae, J. (2014). Wrinkle Cellomics: Screening Bladder Cancer Cells Using an Ultra-Thin Silicone Membrane. IEEE International Conference on Micro Electro Mechanical Systems, 889-892.

Appel, J. H., Ren, H., Sin, M. L. Y., Liao, J. C., & Chae, J. (2016). Rapid bladder cancer cell detection from clinical urine samples using an ultra-thin silicone membrane. Analyst, 141, 652-660. doi: 10.1039/c5an01616a

Aschoff, A., Kremer, P., Hashemi, B., & Kunze, S. (1999). The scientific history of hydrocephalus and its treatment. neurosurgical Review, 22, 67-93.

Ayala, V., Herrera, A. P., Latorre-Esteves, M., Toores-Lugo, M., & Rinaldi, C. (2013). Effect of surface charge on the colloidal stability and in vitro uptake of carboxymethyl dextran-coated iron oxide nanoparticles. Journal of nanoparticle research, 15, 1874. doi: 10.1007/s11051-013-1874-0

Babjuk, M. (2009). Transurethral Resection of Non – muscle-invasive Bladder Cancer. European Urology Supplements, 8, 542-548. doi: 10.1016/j.eursup.2009.06.003

Ballestri, M., Baraldi, A., Gatti, A. M., Furci, L., Bagni, A., Loria, P., . . . Albertazzi, A. (2001). Liver and kidney foreign bodies granulomatosis in a patient with malocclusion, bruxism, and worn dental prostheses. Gastroenterology, 121, 1234-1238. doi: 10.1053/gast.2001.29333

Biscotti, C. V., Dawson, A. E., Dziura, B., Galup, L., Darragh, T., Rahemtulla, A., & Wills-Frank, L. (2005). Assisted primary screening using the automated ThinPrep Imaging System. American Journal of Clinical Pathology, 123, 281-287.

Bottan, S., Poulikakos, D., & Kurtcuoglu, V. (2012). Phantom model of physiologic intracranial pressure and cerebrospinal fluid dynamics. IEEE Transactions on Biomedical Engineering, 59, 1532-1538. doi: 10.1109/TBME.2012.2187448

Bottan, S., Schmid Daners, M., de Zelicourt, D., Fellner, N., Poulikakos, D., & Kurtcuoglu, V. (2013). Assessment of intracranial dynamics in hydrocephalus: effects of viscoelasticity on the outcome of infusion tests. Journal of neurosurgery, 119, 1511-1519. doi: 10.3171/2013.8.JNS122497

Bratosin, D., Mitrofan, L., Palii, C., Estaquier, J., & Montreuil, J. (2005). Novel fluorescence assay using calcein-AM for the determination of human erythrocyte viability and aging. Cytometry Part A, 66, 78-84. doi: 10.1002/cyto.a.20152

Brunette, D. M. (1986). Fibroblasts on Micromachined Substrata Orient Hierarchically to Grooves of Different Dimensions. Experimental cell research, 164, 11-26.

Brydon, H. L., Keir, G., Thompson, E. J., Bayston, R., Harkness, W., Keir, G., & Hayward, R. (1998). Protein adsorption to hydrocephalus shunt catheters : CSF protein adsorption Protein adsorption to hydrocephalus shunt catheters : CSF protein adsorption. Electrophoresis, 643-647.

Buishas, J., Gould, I. G., & Linninger, A. A. (2014). A computational model of cerebrospinal fluid production and reabsorption driven by Starling forces. Croatian medical journal, 55, 481-497. doi: 10.3325/cmj.2014.55.481

Cao, H., Tegenfeldt, J. O., Austin, R. H., & Chou, S. Y. (2002). Gradient nanostructures for interfacing microfluidics and nanofluidics. Applied Physics Letters, 81, 3058-3060. doi: 10.1063/1.1515115

Cao, H., Yu, Z., Wang, J., Tegenfeldt, J. O., Austin, R. H., Chen, E., . . . Chou, S. Y. (2002). Fabrication of 10 nm enclosed nanofluidic channels. Applied Physics Letters, 81, 2002-2004. doi: 10.1063/1.1489102

Carter, S. B. (1967). A Method of Confining Single Cells to Study Individual Cell Reactions and Clone Formation. Experimental cell research, 48, 189-193.

Castellanos-Gomez, A., Poot, M., Steele, G. a., Van Der Zant, H. S. J., Agraït, N., & Rubio-Bollinger, G. (2012). Elastic properties of freely suspended MoS 2 nanosheets. Advanced Materials, 24, 772-775. doi: 10.1002/adma.201103965

Cerda, E., & Mahadevan, L. (2003). Geometry and Physics of Wrinkling. Physical Review Letters, 90, 1-4. doi: 10.1103/PhysRevLett.90.074302

Chen, G. Y., Pang, D. W. P., Hwang, S. M., Tuan, H. Y., & Hu, Y. C. (2012). A graphene-based platform for induced pluripotent stem cells culture and differentiation. Biomaterials, 33, 418-427. doi: 10.1016/j.biomaterials.2011.09.071

Chen, Y., Li, P., Huang, P.-H., Xie, Y., Mai, J. D., Wang, L., . . . Huang, T. J. (2014). Rare Cell Isolation and Analysis in Microfluidics. Lab on a Chip, 14, 626-645. doi: 10.1039/c3lc90136j

Cheung, G., Sahai, A., Billia, M., Dasgupta, P., & Khan, M. S. (2013). Recent advances in the diagnosis and treatment of bladder cancer. BMC medicine, 11, 13. doi: 10.1186/1741-7015-11-13

Circu, M. L., & Aw, T. Y. (2010). Reactive oxygen species, cellular redox systems, and apoptosis. Free Radical Biology and Medicine, 48, 749-762. doi: 10.1016/j.freeradbiomed.2009.12.022

Clark, T. M., Malpas, S. C., Mccormick, D., Heppner, P., & Budgett, D. M. (2015). Implantable Multi-Modal Sensor to Improve Outcomes in Hydrocephalus Management. IEEE Sensors Journal, 15, 6027-6035.

Collins, C. C. (1967). Miniature Passive Pressure Transensor for Implanting in the Eye. IEEE transactions on bio-medical engineering, 14, 74-83.

Cooper, R. L., Beale, D. G., & Constable, I. (1979). Passive radiotelemetry of intraocular pressure in vivo: calibration and validation of continual scleral guard-ring applanation transensors in the dog and rabbit. Investigative Ophthalmology and Visual Science, 18, 930-938.

Coughlin, M. F., Bielenberg, D. R., Lenormand, G., Marinkovic, M., Waghorne, C. G., Zetter, B. R., & Fredberg, J. J. (2013). Cytoskeletal stiffness, friction, and fluidity of cancer cell lines with different metastatic potential. Clinical & experimental metastasis, 30, 237-250. doi: 10.1007/s10585-012-9531-z

Couvreur, P., Tulkens, P., Roland, M., Trouet, A., & Speiser, P. (1977). Nanocapsules: A New Type of Lysosomotropic Carrier. Federation of European Biochemical Societies Letters, 84, 0-3.

Czosnyka, M., Czosnyka, Z., Whitehouse, H., & Pickard, J. D. (1997). Hydrodynamic properties of hydrocephalus shunts: United Kingdom Shunt Evaluation Laboratory. Journal of neurology, neurosurgery, and psychiatry, 62, 43-50. doi: 10.1136/jnnp.62.1.43

de Lima, R., Seabra, A. B., & Durán, N. (2012). Silver nanoparticles: A brief review of cytotoxicity and genotoxicity of chemically and biogenically synthesized nanoparticles. Journal of Applied Toxicology, 32, 867-879. doi: 10.1002/jat.2780

Dembo, M., Oliver, T., Ishihara, a., & Jacobson, K. (1996). Imaging the traction stresses exerted by locomoting cells with the elastic substratum method. Biophysical journal, 70, 2008-2022. doi: 10.1016/S0006-3495(96)79767-9

Dodson, K. H., Echevarria, F. D., Li, D., Sappington, R. M., & Edd, J. F. (2016). Retina-on-a-chip: a microfluidic platform for point access signaling studies. Biomedical Microdevices, 17. doi: 10.1007/s10544-015-0019-x.Retina-on-a-chip

Drake, J. M., Kestle, J. R. W., & Tuli, S. (2000). CSF shunts 50 years on – past, present and future. Child's Nervous System, 16, 800-804.

Duffy, D. C., Mcdonald, J. C., Schueller, O. J. A., & Whitesides, G. M. (1998). Rapid Prototyping of Microfluidic Systems in Poly(dimethylsiloxane). Analytical Chemistry, 70, 4974-4984.

Dunbar, G. E., Shen, B. Y., & Aref, A. A. (2017). The Sensimed Triggerfish contact lens sensor: efficacy, safety, and patient perspectives. Clinical Ophthalmology, 11, 875-882.

Eddy, D. S., & Sparks, D. R. (1998). Application of MEMS Technology in Automotive Sensors and Actuators. Proceedings of the IEEE.

Elahi, M. M., Kong, Y. X., & Matata, B. M. (2009). Oxidative stress as a mediator of cardiovascular disease. Oxidative Medicine and Cellular Longevity, 259-269.

Feynman, R. P. (1959). There's Plenty of Room at the Bottom: An Invitation to Enter a New World of Physics. American Physical Society.

Fiala, J., Bingger, P., Foerstert, K., Heilmann, C., & Beyersdorti, F. (2010). Implantable Sensor for Blood Pressure Determination via Pulse Transit Time. IEEE Sensors.

Galbraith, C. G., & Heetz, M. I. P. S. (1997). A micromachined device provides a new bend on fibroblast traction forces. Proceedings of the National Academy of Sciences of the United States of America, 94, 9114-9118.

Gehlen, M., Kurtcuoglu, V., & Daners, M. S. c. (2016). Patient Specific Hardware-in-the-Loop Testing of Cerebrospinal Fluid Shunt Systems. IEEE transactions on bio-medical engineering, 63, 348-358. doi: 10.1109/TBME.2015.2457681

Goldman, E. B., Zak, A., Tenne, R., Kartvelishvily, E., Levin-Zaidman, S., Neumann, Y., . . . Aframian, D. J. (2015). Biocompatibility of tungsten disulfide inorganic nanotubes and fullerene-like nanoparticles with salivary gland cells. Tissue engineering. Part A, 21, 1013-1023. doi: 10.1089/ten.TEA.2014.0163

Gough, D. A., Kumosa, L. S., Routh, T. L., Lin, J. T., & Lucisano, J. Y. (2010). Function of an Implanted Tissue Glucose Sensor for More than 1 Year in Animals. Science Translational Medicine, 2.

Gough, D. A., Makale, M. T., Lin, J. T., Calou, R. E., Tsai, A. G., Chen, P. C., . . . Gough, D. A. (2003). Tissue window chamber system for validation of implanted oxygen sensors of implanted oxygen sensors. American Journal of Physiology - Heart and Circulatory Physiology, 284, H2288-H2294. doi: 10.1152/ajpheart.00721.2002

Graham, F. L., Smiley, J., Russell, W. C., & Nairn, R. (1977). Characteristics of a Human Cell Line Transformed by DNA from Human Adenovirus Type 5. Journal of General Virology, 36, 59-74.

Greene, M. E., & Gilman, B. G. (1974). Intraocular Pressure Measurement with Instrumented Contact Lenses. Investigative Ophthalmology, 13, 299-302.

Grzybowski, D. M., Holman, D. W., Katz, S. E., & Lubow, M. (2006). In vitro model of cerebrospinal fluid outflow through human arachnoid granulations. Investigative Ophthalmology and Visual Science, 47, 3664-3672. doi: 10.1167/iovs.05-0929

Gutierrez, H. R., Perea-Lopez, N., Elias, A. L., Berkdemir, A., Wang, B., Lv, R., . . . Terrones, M. (2013). Extraordinary room-temperature photoluminescence in triangular WS 2 monolayers. Nano Letters, 13, 3447-3454. doi: 10.1021/nl3026357

Hanak, B. W., Ross, E. F., Harris, C. A., Browd, S. R., & Shain, W. (2016). Toward a better understanding of the cellular basis for cerebrospinal fluid shunt obstruction: report on the construction of a bank of explanted hydrocephalus devices. Journal of Neurosurgery: Pediatrics, 18, 213-223. doi: 10.3171/2016.2.PEDS15531

Harris, A., Wild, P., & Stopak, D. (1980). Silicone Rubber Substrata : A New Wrinkle in the Study of Cell Locomotion Author (s): Albert K . Harris , Patricia Wild and David Stopak Reviewed work (s): Source : Science , New Series , Vol . 208 , No . 4440 (Apr . 11 , 1980), pp . 177-179 Publish. Science (New York, N.Y.), 208, 177-179.

Harris, C., Pearson, K., Hadley, K., & Zhu, S. (2015). Fabrication of three-dimensional hydrogel scaffolds for modeling shunt failure by tissue obstruction in hydrocephalus. Fluids and Barriers of …, 12, 1-15. doi: 10.1186/s12987-015-0023-9

Harris, C. A., & Mcallister, J. P. (2012). What We Should Know About the Cellular and Tissue Response Causing Catheter Obstruction in the Treatment of Hydrocephalus. Neurosurgery, 70, 1589-1602. doi: 10.1227/NEU.0b013e318244695f

Harrison, D. J., Fluri, K., Seiler, K., Fan, Z., Effenhauser, C. S., & Manz, A. (1993). Micromachining a Miniaturized Capillary Electrophoresis-Based Chemical Analysis System on a Chip Published by : American Association for the Advancement of Science Stable URL : http://www.jstor.org/stable/2882118 Micromachining a Miniaturized Capillary El. Science (New York, N.Y.), 261, 895-897.

Harrison, D. J., Manz, A., Fan, Z., & Widmer, H. M. (1992). Capillary Electrophoresis and Sample Injection Systems. Analytical Chemistry, 64, 1926-1932. doi: 10.1021/ac00041a030

Hastie, A. R., Dong, L., Smith, A., Finklestein, J., Lam, E. T., Huo, N., . . . Xiao, M. (2013). Rapid Genome Mapping in Nanochannel Arrays for Highly Complete and Accurate De Novo Sequence Assembly of the Complex Aegilops tauschii Genome. PLoS ONE, 8, e55864. doi: 10.1371/journal.pone.0055864

He, Z., Sheng, Y., Rong, Y., Lee, G.-d., Li, J., & Warner, J. H. (2015). Layer-dependent modulation of tungsten disulfide photoluminescence by lateral electric fields. ACS nano, 9, 2740-2748. doi: 10.1021/nn506594a

Hirabuki, N., Watanabe, Y., Mano, T., Fujita, N., Tanaka, H., Ueguchi, T., & Nakamura, H. (2000). Quantitation of Flow in the Superior Sagittal Sinus Performed with Cine Phase-contrast MR Imaging of Healthy and Achondroplastic Children. American Journal of Neuroradiology, 21, 1497-1501.

Holman, D. W., Kurtcuoglu, V., & Grzybowski, D. M. (2010). Cerebrospinal fluid dynamics in the human cranial subarachnoid space: an overlooked mediator of cerebral disease. II. In vitro arachnoid outflow model. Journal of the Royal Society, Interface / the Royal Society, 7, 1205-1218. doi: 10.1098/rsif.2010.0032

Huang, J., Juszkiewicz, M., de Jeu, W. H., Cerda, E., Emrick, T., Menon, N., & Russell, T. P. (2007). Capillary wrinkling of floating thin polymer films. Science (New York, N.Y.), 317, 650-653. doi: 10.1126/science.1144616

Huh, D., Matthews, B. D., Mammoto, A., Montoya-Zavala, M., Hsin, H. Y., & Ingber, D. E. (2010). Reconstituting Organ-Level Lung Functions of a Chip. Science (New York, N.Y.), 328, 1662-1669.

Ilyas, A., Asghar, W., Ahmed, S., Lotan, Y., Hsienh, J.-T., Kim, Y.-t., & Iqbal, S. M. (2014). Electrophysiological analysis of biopsy samples using elasticity as an inherent cell marker for cancer detection. Analytical Methods, 6, 7166-7174. doi: 10.1039/C4AY00781F

Jain, M., Koren, S., Miga, K. H., Quick, J., Rand, A. C., Sasani, T. A., . . . Loose, M. (2018). Nanopore sequencing and assembly of a human genome with ultra-long reads. Nature Biotechnology. doi: 10.1038/nbt.4060

Jiang, W., Kim, B. Y. S., Rutka, J. T., & Chan, W. C. W. (2008). Nanoparticle-mediated cellular response is size-dependent. Nature nanotechnology, 3, 145-150. doi: 10.1038/nnano.2008.30

Jones, H., & Keep, R. (1988). Brain Fluid Calcium Concentration and Response To Acute Hypercalcaemia During Development in the Rat. J Physiol., 402, 579-593.

Khamlichi, A. E. (1998). African neurosurgery Part 1 Historical Outline. Surgical Neurology, 49, 222-227.

Kim, B. J., Jin, W., Baldwin, A., Yu, L., Christian, E., Krieger, M. D., . . . Meng, E. (2016). Parylene MEMS patency sensor for assessment of hydrocephalus shunt obstruction. Biomedical Microdevices, 18, 87. doi: 10.1007/s10544-016-0112-9

Kim, D.-h., Khatau, S. B., Feng, Y., Walcott, S., Sun, S. X., Longmore, G. D., & Wirtz, D. (2012). Actin cap associated focal adhesions and their distinct role in cellular mechanosensing. Scientific Reports, 2. doi: 10.1038/srep00555

Ko, W. H. (2007). Trends and frontiers of MEMS. Sensors and Actuators A, 136, 62-67. doi: 10.1016/j.sna.2007.02.001

Koch, T. M., Munster, S., Bonakdar, N., Butler, J. P., & Fabry, B. (2012). 3D Traction Forces in Cancer Cell Invasion. PLoS ONE, 7. doi: 10.1371/Citation

Kou, Z., Wang, X., Yuan, R., Chen, H., Zhi, Q., Gao, L., . . . Guo, L. (2014). A promising gene delivery system developed from PEGylated MoS2 nanosheets for gene therapy. Nanoscale Research Letters, 9, 587. doi: 10.1186/1556-276X-9-587

Kraning-rush, C. M., Califano, J. P., & Reinhart-king, C. A. (2012). Cellular Traction Stresses Increase with Increasing Metastatic Potential. PLoS ONE, 7. doi: 10.1371/journal.pone.0032572

Lalwani, G., Henslee, A. M., Farshid, B., Parmar, P., Lin, L., Qin, Y. X., . . . Sitharaman, B. (2013). Tungsten disulfide nanotubes reinforced biodegradable polymers for bone tissue engineering. Acta Biomaterialia, 9, 8365-8373. doi: 10.1016/j.actbio.2013.05.018

Lechler, K., & Lilja, M. (2008). Lower extremity leg amputation: an advantage in running ? Sports Technology, 1, 229-234. doi: 10.1002/jst.57

Lee, C., Yan, H., Brus, L. E., Heinz, T. F., Hone, Ḱ. J., & Ryu, S. (2010). Anomalous Lattice Vibrations of Single- and Few-Layer MoS2. ACS Nano, 4, 2695-2700.

Lee, W. R. (1968). The History of the Statutory Control of Mercury Poisoning in Great Britain. British Journal of Industrial Medicine, 25, 52-62.

Lekka, M., Gil, D., Pogoda, K., Dulińska-Litewka, J., Jach, R., Gostek, J., . . . Laidler, P. (2012). Cancer cell detection in tissue sections using AFM. Archives of biochemistry and biophysics, 518, 151-156. doi: 10.1016/j.abb.2011.12.013

Lekka, M., Laidler, P., Gil, D., Lekki, J., Stachura, Z., & Hrynkiewicz, a. Z. (1999). Elasticity of normal and cancerous human bladder cells studied by scanning force microscopy. European biophysics journal : EBJ, 28, 312-316.

Leonardi, M., Leuenberger, P., Bertrand, D., Bertsch, A., & Renaud, P. (2003). A soft contact lens with a MEMS Strain Gage Embedded for Intraocular Pressure Monitoring. IEEE International Conference on Solid State Sensors, Actuators and Microsystems.

Leonardi, M., Pitchon, E. M., Bertsch, A., & Renaud, P. (2009). Wireless contact lens sensor for intraocular pressure monitoring : assessment on enucleated pig eyes. acta ophthalmologica, 87, 433-437. doi: 10.1111/j.1755-3768.2008.01404.x

Li, P., Mao, Z., Peng, Z., Zhou, L., Chen, Y., Huang, P.-h., . . . Huang, T. J. (2015). Acoustic separation of circulating tumor cells. Proceedings of the National Academy of Sciences of the United States of America, 112, 4970-4975. doi: 10.1073/pnas.1504484112

Li, Y., Chen, D. H., Yan, J., Chen, Y., Mittelstaedt, R. A., Zhang, Y., . . . Chen, T. (2012). Mutation Research / Genetic Toxicology and Environmental Mutagenesis Genotoxicity of silver nanoparticles evaluated using the Ames test and in vitro micronucleus assay. Mutation Research - Genetic Toxicology and Environmental Mutagenesis, 745, 4-10. doi: 10.1016/j.mrgentox.2011.11.010

Li, Z., Song, J., Mantini, G., Lu, M.-Y., Fang, H., Falconi, C., . . . Wang, Z. L. (2009). Quantifying the traction force of a single cell by aligned silicon nanowire array. Nano letters, 9, 3575-3580. doi: 10.1021/nl901774m

Liao, K.-h., Lin, Y.-s., Macosko, C. W., & Haynes, C. L. (2011). Cytotoxicity of Graphene Oxide and Graphene in Human Erythrocytes and Skin Fibroblasts. ACS Applied Materials and Interfaces, 3, 2607-2615. doi: 10.1021/am200428v

Liao, K. H., Lin, Y. S., MacOsko, C. W., & Haynes, C. L. (2011). Cytotoxicity of graphene oxide and graphene in human erythrocytes and skin fibroblasts. ACS Applied Materials and Interfaces, 3, 2607-2615. doi: 10.1021/am200428v

Lind, G., Linsmeier, C. E., & Schouenborg, J. (2013). The density difference between tissue and neural probes is a key factor for glial scarring. Scientific Reports, 3, 1-7. doi: 10.1038/srep02942

Linninger, A. A., Sweetman, B., & Penn, R. (2009). Normal and hydrocephalic brain dynamics: The role of reduced cerebrospinal fluid reabsorption in ventricular enlargement. Annals of Biomedical Engineering, 37, 1434-1447. doi: 10.1007/s10439-009-9691-4

Linninger, A. A., Tsakiris, C., Zhu, D. C., Xenos, M., Roycewicz, P., Danziger, Z., & Penn, R. (2005). Pulsatile cerebrospinal fluid dynamics in the human brain. IEEE transactions on bio-medical engineering, 52, 557-565. doi: 10.1109/TBME.2005.844021

Liu, T., Wang, C., Gu, X., Gong, H., Cheng, L., Shi, X., . . . Liu, Z. (2014). Drug delivery with PEGylated MoS2 nano-sheets for combined photothermal and chemotherapy of cancer. Advanced Materials, 26, 3433-3440. doi: 10.1002/adma.201305256

Łopacińska, J. M., Emnéus, J., & Dufva, M. (2013). Poly(Dimethylsiloxane) (PDMS) Affects Gene Expression in PC12 Cells Differentiating into Neuronal-Like Cells. PLoS ONE, 8, 1-11. doi: 10.1371/journal.pone.0053107

Lucisano, J. Y., Routh, T. L., Lin, J. T., & Gough, D. A. (2017). Glucose Monitoring in Individuals with Diabetes using a Long- Term Implanted Sensor/Telemetry System and Model. IEEE Transactions on Biomedical Engineering, 64, 1982-1993. doi: 10.1109/TBME.2016.2619333.Glucose

Mak, K. F., Lee, C., Hone, J., Shan, J., & Heinz, T. F. (2010). Atomically thin MoS2: A new direct-gap semiconductor. Physical Review Letters, 105, 2-5. doi: 10.1103/PhysRevLett.105.136805

Mao, W. P., Ye, J. L., Guan, Z. B., Zhao, J. M., Zhang, C., Zhang, N. N., . . . Tian, T. (2007). Cadmium induces apoptosis in human embryonic kidney (HEK) 293 cells

by caspase-dependent and -independent pathways acting on mitochondria. Toxicology in Vitro, 21, 343-354. doi: 10.1016/j.tiv.2006.09.004

Marx, K. A. (2003). Quartz Crystal Microbalance: A Useful Tool for Studying Thin Polymer Films and Complex Biomolecular Systems at the Solution - Surface Interface. biomacromolecules, 4. doi: 10.1021/bm020116i

Mata, A., Fleischman, A. J., & Roy, S. (2005). Characterization of Polydimethylsiloxane (PDMS) Properties for Biomedical Micro / Nanosystems. Biomedical Microdevices, 7, 281-293.

McDonald, J. C., Duffy, D. C., Anderson, J. R., Chiu, D. T., Wu, H., Schueller, O. J. A., & Whitesides, G. M. (2000). Review General Fabrication of microfluidic systems in poly(dimethylsiloxane). Electrophoresis, 21, 27-40.

Meng, E., & Sheybani, R. (2014). Micro- and nano- fabricated implantable drug delivery systems: current state and future perspectives. Therapeutic Delivery, 5, 1167-1170.

Millikan, G. A. (1942). The Oximeter, an Instrument for Measuring Continuously the Oxygen Saturation of Arterial Blood in Man. Review of Scientific Instruments, 13, 434-444. doi: 10.1063/1.1769941

Moshayedi, P., Ng, G., Kwok, J. C. F., Yeo, G. S. H., Bryant, C. E., Fawcett, J. W., . . . Guck, J. (2014). The relationship between glial cell mechanosensitivity and foreign body reactions in the central nervous system. Biomaterials, 35, 3919-3925. doi: 10.1016/j.biomaterials.2014.01.038

Navarro, M., Michiardi, A., Castan, O., & Planell, J. A. (2008). Biomaterials in orthopaedics. Journal of the Royal Society, Interface, 5, 1137-1158. doi: 10.1098/rsif.2008.0151

Neto, a. H. C., & Novoselov, K. (2011). Two-Dimensional Crystals: Beyond Graphene. Materials Express, 1, 10-17. doi: 10.1166/mex.2011.1002

Nowack, B., Krug, H. F., & Height, M. (2011). 120 Years of Nanosilver History : Implications for Policy Makers. Environmental Science and Technology, 45, 1177-1183. doi: 10.1021/es103316q

Oh, J., Kim, G., Kralick, F., & Noh, H. (2011). Design and Fabrication of a PDMS / Parylene Microvalve for the Treatment of Hydrocephalus. Journal of Microelectromechanical Systems, 20, 811-818.

Oh, J., Liu, K., Medina, T., Kralick, F., & Noh, H. (2014). A novel microneedle array for the treatment of hydrocephalus. Microsystem Technologies, 20, 1169-1179. doi: 10.1007/s00542-013-1988-4

Oliver, T., Dembo, M., & Jacobson, K. (1995). Traction forces in locomoting cells. Cell motility and the cytoskeleton, 31, 225-240. doi: 10.1002/cm.970310306

Osman, O., Zanini, L. F., Frénéa-Robin, M., Dumas-Bouchiat, F., Dempsey, N. M., Reyne, G., . . . Haddour, N. (2012). Monitoring the endocytosis of magnetic nanoparticles by cells using permanent micro-flux sources. Biomedical Microdevices, 14, 947-954. doi: 10.1007/s10544-012-9673-4

Pan, Y., Leifert, A., Ruau, D., Neuss, S., Brandau, W., Simon, U., & Jahnen-dechent, W. (2009). Gold Nanoparticles of Diameter 1.4 nm Trigger Necrosis by Oxidative Stress and Mitochondrial Damage. Small, 5, 2067-2076. doi: 10.1002/smll.200900466

Pardo, M., Shuster-Meiseles, T., Levin-Zaidman, S., Rudich, A., & Rudich, Y. (2014). Low cytotoxicity of inorganic nanotubes and fullerene-like nanostructures in human bronchial epithelial cells: Relation to inflammatory gene induction and antioxidant response. Environmental Science and Technology, 48, 3457-3466. doi: 10.1021/es500065z

Pelham, R. J., & Wang, Y. L. (1999). High resolution detection of mechanical forces exerted by locomoting fibroblasts on the substrate. Molecular biology of the cell, 10, 935-945.

Perestrelo, A. R., Águas, A. C. P., Rainer, A., & Forte, G. (2015). Microfluidic Organ / Body-on-a-Chip Devices at the Convergence of Biology and Microengineering. Sensors, 15, 31142-31170. doi: 10.3390/s151229848

Petersen, K. E. (1982). Silicon as a Mechanical Material. Proceedings of the IEEE, 70.

Pople, I. K. (2002). Hydrocephalus And Shunts: What The Neurologist Should Know. Journal of neurology, neurosurgery, and psychiatry, 73, i17-i22.

Potkay, J. A. (2008). Long term, implantable blood pressure monitoring systems. Biomedical Microdevices, 10, 379-392. doi: 10.1007/s10544-007-9146-3

Qin, D., Xia, Y., & Whitesides, G. M. (1996). Rapid Prototyping of Complex Structures with Feature Sizes Larger than 20 micrometers. Advanced Materials, 8, 917-919.

Qu, L., Xia, S., Bian, C., Sun, J., & Han, J. (2009). A micro-potentiometric hemoglobin immunosensor based on electropolymerized polypyrrole – gold nanoparticles composite. Biosensors and Bioelectronics, 24, 3419-3424. doi: 10.1016/j.bios.2008.07.077

Redlich, M., Katz, A., Rapoport, L., Wagner, H. D., Feldman, Y., & Tenne, R. (2008). Improved orthodontic stainless steel wires coated with inorganic fullerene-like nanoparticles of WS2 impregnated in electroless nickel-phosphorous film. Dental Materials, 24, 1640-1646. doi: 10.1016/j.dental.2008.03.030

Remmerbach, T. W., Wottawah, F., Dietrich, J., Lincoln, B., Wittekind, C., & Guck, J. (2009). Oral cancer diagnosis by mechanical phenotyping. Cancer Research, 69, 1728-1732. doi: 10.1158/0008-5472.CAN-08-4073

Robboy, S. J., Weintraub, S., Horvath, A. E., Jensen, B. W., Alexander, B., Fody, E. P., . . . Black-Schaffer, S. (2009). Pathologist Workforce in the United States I . Development of a Predictive Model to Examine Factors Influencing Supply. Archives of Pathology and Laboratory Medicine, 137, 1723-1732. doi: 10.5858/arpa.2013-0200-OA

Roepke, C. L., & Schaff, E. A. (2014). Long Tail Strings : Impact of the Dalkon Shield 40 Years Later. Journal of Obstetrics and Gynecology, 4, 996-1005.

Runza, M., Pietrabissa, R., Mantero, S., Albani, A., Quaglini, V., & Contro, R. (1999). Lumbar Dura Mater Biomechanics: Experimental Characterization and Scanning Electron Microscopy Observatios. Anesthesia & Analgesia, 88, 1317-1321. doi: 10.1097/00000539-199906000-00022

Rutter, N., & Smales, O. R. (1976). Calcium, magnesium, and glucose levels in blood and CSF of children with febrile convulsions. Archives of disease in childhood, 51, 141-143. doi: 10.1136/adc.51.2.141

Schutzer, S. E., Liu, T., Natelson, B. H., Angel, T. E., Schepmoes, A. A., Purvine, S. O., . . . Bergquist, J. (2010). Establishing the proteome of normal human cerebrospinal fluid. PLoS ONE, 5, 1-7. doi: 10.1371/journal.pone.0010980

Schwerdt, H. N., Amjad, U., Appel, J., Elhadi, A. M., Lei, T., Preul, M. C., . . . Chae, J. (2015). In Vitro Hydrodynamic , Transient , and Overtime Performance of a Miniaturized Valve for Hydrocephalus. Annals of biomedical engineering, 43, 603-615. doi: 10.1007/s10439-015-1291-x

Schwerdt, H. N., Bristol, R. E., & Chae, J. (2014). Miniaturized Passive Hydrogel Check Valve for Hydrocephalus Treatment. IEEE Transactions on Biomedical Engineering, 61, 814-820.

Sgouros, S., & Dipple, S. J. (2004). an investigation of structural degradation of CSF shunt valves performed using SEM and energy dispersive x ray microanalysis. Journal of neurosurgery, 100, 534-540.

Simpson, P. C., Roach, D., Woolley, A. T., Thorsen, T., Johnston, R., Sensabauch, G. F., & Mathies, R. A. (1998). High-throughput genetic analysis using microfabricated 96-sample capillary array electrophoresis microplates. Proceedings of the National Academy of Sciences of the United States of America, 95, 2256-2261.

Skala, M. C., Squirrell, J. M., Vrotsos, K. M., Eickhoff, J. C., Gendron-Fitzpatrick, A., Eliceiri, K. W., & Ramanujam, N. (2005). Multiphoton microscopy of

endogenous fluorescence differentiates normal, precancerous, and cancerous squamous epithelial tissues. Cancer Research, 65, 1180-1186. doi: 10.1158/0008-5472.CAN-04-3031

Society, A. C. (2015).

Song, J. G., Park, J., Lee, W., Choi, T., Jung, H., Lee, C. W., . . . Kim, H. (2013). Layer-controlled, wafer-scale, and conformal synthesis of tungsten disulfide nanosheets using atomic layer deposition. ACS Nano, 7, 11333-11340. doi: 10.1021/nn405194e

Song, X., Hu, J., & Zeng, H. (2013). Two-dimensional semiconductors: recent progress and future perspectives. Journal of Materials Chemistry C, 1, 2952. doi: 10.1039/c3tc00710c

Splendiani, A., Sun, L., Zhang, Y., Li, T., Kim, J., Chim, C.-y., . . . Wang, F. (2010). Emerging Photoluminescence in Monolayer MoS2. Nano letters, 10, 1271-1275. doi: 10.1021/nl903868w

Stone, J. J., Walker, C. T., Jacobson, M., Phillips, V., & Silberstein, H. J. (2013). Revision rate of pediatric ventriculoperitoneal shunts after 15 years. Journal of Neurosurgery: Pediatrics, 11, 15-19.

Sun, X., Fan, J., Fu, C., Yao, L., Zhao, S., Wang, J., & Xiao, J. (2017). WS2 and MoS2 biosensing platforms using peptides as probe biomolecules. Scientific Reports, 10290. doi: 10.1038/s41598-017-10221-4

Sun, Z., Liu, Z., Meng, J., Meng, J., Duan, J., Xie, S., . . . Yang, X.-d. (2011). Carbon Nanotubes Enhance Cytotoxicity Mediated by Human Lymphocytes In Vitro. PLoS ONE, 6, e21073. doi: 10.1371/journal.pone.0021073

Sweetman, B., & Xenos, M. (2011). Three-dimensional computational prediction of cerebrospinal fluid flow in the human brain. Computers in biology and …, 41, 67-75. doi: 10.1016/j.compbiomed.2010.12.001.Three-dimensional

Takaki, Y., Takenaka, H., Morimoto, Y., Konuma, O., & Hirabayashi, K. (2012). Multi-view display module employing MEMS projector array. optics express, 20, 494-500.

Takenaka, S., Karg, E., Roth, C., Schulz, H., Ziesenis, A., Heinzmann, U., . . . Heyder, J. (2001). Pulmonary and systemic distribution of inhaled ultrafine silver particles in rats. Environmental Health Perspectives, 109, 547-551. doi: 10.2307/3454667

Tan, J. L., Tien, J., Pirone, D. M., Gray, D. S., Bhadriraju, K., & Chen, C. S. (2003). Cells lying on a bed of microneedles : An approach to isolate mechanical force. Proceedings of the National Academy of Sciences of the United States of America, 100, 1484-1489.

Tegenfeldt, J. O., Prinz, C., Cao, H., Huang, R. L., Austin, R. H., Chou, S. Y., . . . Sturm, J. C. (2004). Micro- and nanofluidics for DNA analysis. Analytical and Bioanalytical Chemistry, 378, 1678-1692. doi: 10.1007/s00216-004-2526-0

Tenne, R. (2003). Advances in the synthesis of inorganic nanotubes and fullerene- like nanoparticles. Angewandte Chemie-International Edition, 42, 5124-5132. doi: 10.1002/anie.200301651

Tenne, R. (2013). Recent advances in the research of inorganic nanotubes and fullerene-like nanoparticles. Frontiers of Physics, 1-8. doi: 10.1007/s11467-013-0326-8

Tenne, R., & Redlich, M. (2010). Recent advances in the research of inorganic nanotubes and fullerene-like nanoparticles. Chemical Society Reviews, 1423-1434. doi: 10.1007/s11467-013-0326-8

Tenne, R., & Seifert, G. (2009). Recent Progress in the Study of Inorganic Nanotubes and Fullerene-Like Structures. Annual Review of Materials Research, 39, 387-413. doi: 10.1146/annurev-matsci-082908-145429

Teo, W. Z., Chng, E. L. K., Sofer, Z., & Pumera, M. (2014). Cytotoxicity of exfoliated transition-metal dichalcogenides (MoS 2, WS2, and WSe2) is lower than that of graphene and its analogues. Chemistry - A European Journal, 20, 9627-9632. doi: 10.1002/chem.201402680

Terry, S. C., Jerman, J. H., & Angell, J. B. (1979). A Gas Chromatographic Air Analyzer Fabricated on a Silicon Wafer. IEEE Transactions on Electronic Devices, 26, 1880-1886.

Theodor, M., Ruh, D., Subramanian, S., Katharina, F., Heilmann, C., Beyersdorf, F., . . . Seifert, A. (2014). Implantable Pulse Oximetry on Subcutaneous Tissue. IEEE Conference on Engineering in Medicine and Biology Society.

Toma, A. K., Tarnaris, A., Kitchen, N. D., & Watkins, L. D. (2010). Ventriculosinus shunt. Neurosurgical Review, 33, 147-152. doi: 10.1007/s10143-010-0242-0

Tomasini, J. M., & Konety, B. R. (2013). Urinary Markers/Cytology: What and When Should a Urologist Use. Urologic Clinics of North America, 40(2), 165-173.

Torre, D., Zeroli, C., Issi, M., Fiori, G. P., Ferraro, G., & Speranza, F. (1991). Cerebrospinal fluid concentration of fibronectin in meningitis. Journal of clinical pathology, 44, 783-784.

Tsatalis, J. P., Aldahan, A. S., Hsu, V. M., Tsatalis, A. E., Brah, T. K., & Nouri, K. (2017). Narcissus' reflection : toxic ingredients in cosmetics through the ages. International Journal of Dermatology, 56, 239-241. doi: 10.1111/ijd.13477

VandeVord, P. J., Gupta, N., Wilson, R. B., Vinuya, R. Z., Schaefer, C. J., Canady, A. I., & Wooley, P. H. (2004). Immune reactions associated with silicone-based ventriculo-peritoneal shunt malfunctions in children. Biomaterials, 25, 3853-3860. doi: 10.1016/j.biomaterials.2003.10.024

Voiculescu, I., & Nurashikin, A. (2012). Acoustic wave based MEMS devices for biosensing applications. Biosensors and Bioelectronics, 33, 1-9. doi: 10.1016/j.bios.2011.12.041

Wang, J., Chatrathi, M. P., Tian, B., & Polsky, R. (2000). Microfabricated Electrophoresis Chips for Simultaneous Bioassays of Glucose , Uric Acid , Ascorbic Acid , and Acetaminophen. Analytical Chemistry, 72, 2514-2518. doi: 10.1021/ac991489l

Wang, Q. H., Kalantar-Zadeh, K., Kis, A., Coleman, J. N., & Strano, M. S. (2012). Electronics and optoelectronics of two-dimensional transition metal dichalcogenides. Nature nanotechnology, 7, 699-712. doi: 10.1038/nnano.2012.193

Wang, Z., Volinsky, A. A., & Gallant, N. D. (2014). Crosslinking effect on polydimethylsiloxane elastic modulus measured by custom-built compression instrument. Journal of Applied Polymer Science, 131, 1-4. doi: 10.1002/app.41050

Wilmer, M. J., Ng, C. P., Lanz, H. L., Vulto, P., Suter-dick, L., & Masereeuw, R. (2016). Kidney-on-a-Chip Technology for Drug-Induced Nephrotoxicity Screening. Trends in Biotechnology, 34, 156-170. doi: 10.1016/j.tibtech.2015.11.001

Woodruff, R. S., Li, Y., Yan, J., Bishop, M., Jones, M. Y., Watanabe, F., . . . Chen, T. (2012). Genotoxicity evaluation of titanium dioxide nanoparticles using the Ames test and Comet assay. Journal of Applied Toxicology, 32, 934-943. doi: 10.1002/jat.2781

Wright, M. E., Michaud, D. S., Pietinen, P., Taylor, P. R., Virtamo, J., & Albanes, D. (2005). Estimated urine pH and bladder cancer risk in a cohort of male smokers. Cancer Causes and Control, 16, 1117-1123. doi: 10.1007/s10552-005-0348-9

Wu, H., Yang, R., Song, B., Han, Q., Li, J., Zhang, Y., . . . Wang, C. (2011). Biocompatible inorganic fullerene-like molybdenum disulfide nanoparticles produced by pulsed laser ablation in water. ACS Nano, 5, 1276-1281. doi: 10.1021/nn102941b

Xu, M., Liang, T., Shi, M., & Chen, H. (2013). Graphene-like two-dimensional materials. Chemical Reviews, 113, 3766-3798. doi: 10.1021/cr300263a

Xu, T., Yoo, J. H., Babu, S., Roy, S., Lee, J. B., & Lu, H. (2016). Characterization of the mechanical behavior of SU-8 at microscale by viscoelastic analysis. Journal of Micromechanics and Microengineering, 26. doi: 10.1088/0960-1317/26/10/105001

Xu, W., Appel, J., Chae, J., & Member, S. (2012). Real-Time Monitoring of Whole Blood Coagulation Using a Microfabricated Contour-Mode Film Bulk Acoustic Resonator. Journal of Microelectromechanical Systems, 21, 302-307.

Yamamoto, S., Ohno, K., Aoyagi, M., Ichinose, S., & Hirakawa, K. (2002). Calcific deposits on degraded shunt catheters : long-term follow-up of V-P shunts and late complications in three cases. Child's Nervous System, 18, 19-25. doi: 10.1007/s00381-001-0532-5

Yasotharan, S., Pinto, S., Sled, J. G., Bolz, S.-s., & Günther, A. (2015). Artery-on-a-chip platform for automated, multimodal assessment of cerebral blood vessel structure and function. Lab on a Chip, 15, 2660-2669. doi: 10.1039/C5LC00021A

Zhu, D. C., Xenos, M., Linninger, A. A., & Penn, R. D. (2006). Dynamics of lateral ventricle and cerebrospinal fluid in normal and hydrocephalic brains. Journal of Magnetic Resonance Imaging, 24, 756-770. doi: 10.1002/jmri.20679

APPENDIX A

INITIAL TRIAL WRINKLE CELLOMICS MEMBRANE

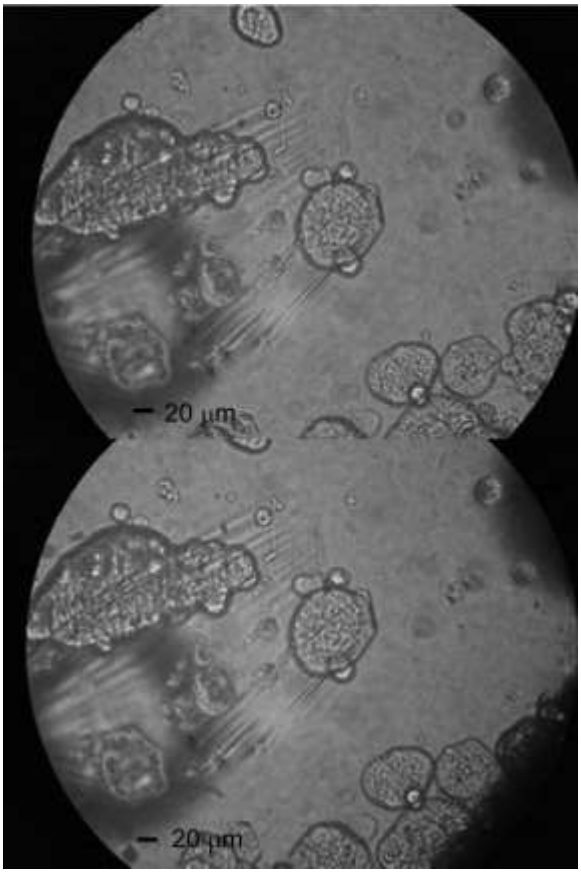

24 hour incubation of RT4 cells

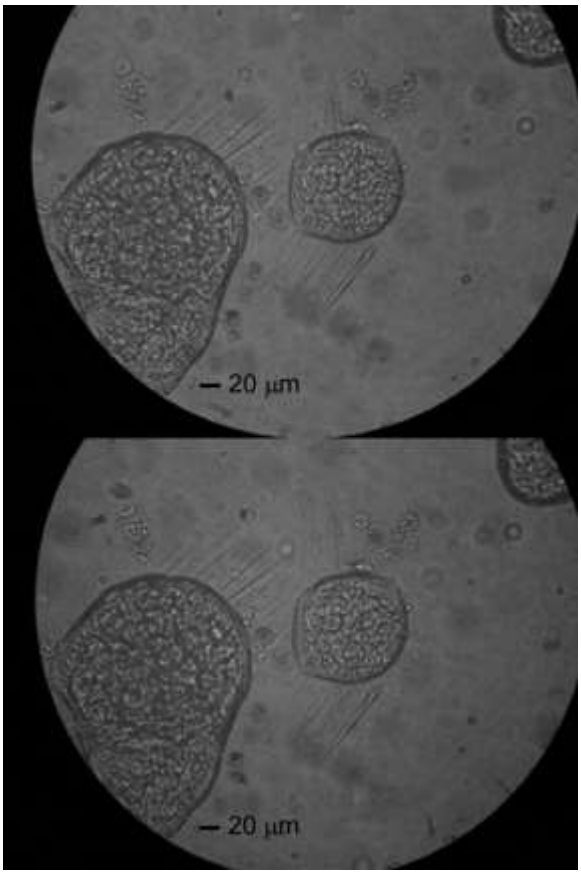

72 hour incubation of RT4 cells

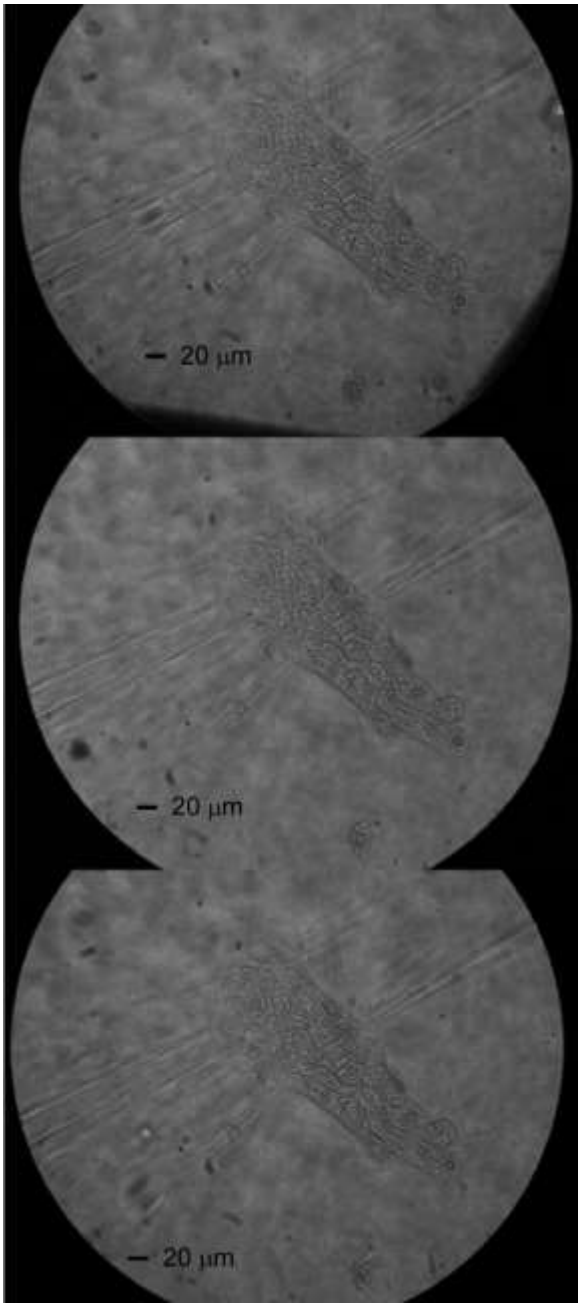

5 day incubation of RT4 cells

APPENDIX B

WRINKLE CELLOMICS MEMBRANE COATED WITH FIBRONECTIN RT4 CELLS WITH 12 HOUR INCUBATION PERIOD

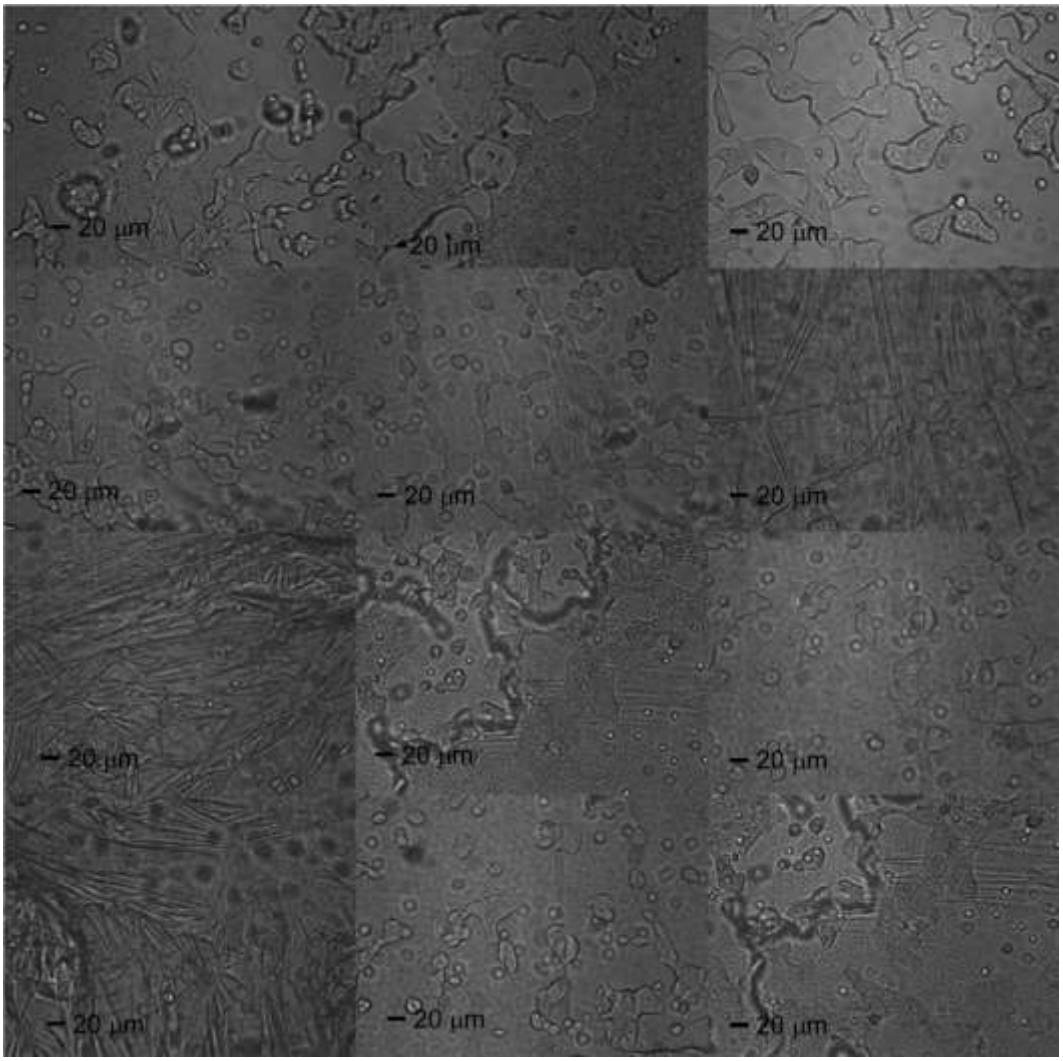
20 µm
20 µm
20 µm
20 µm
20 µm
20 µm
20 µm
20 µm
20 µm
20 µm
20 µm

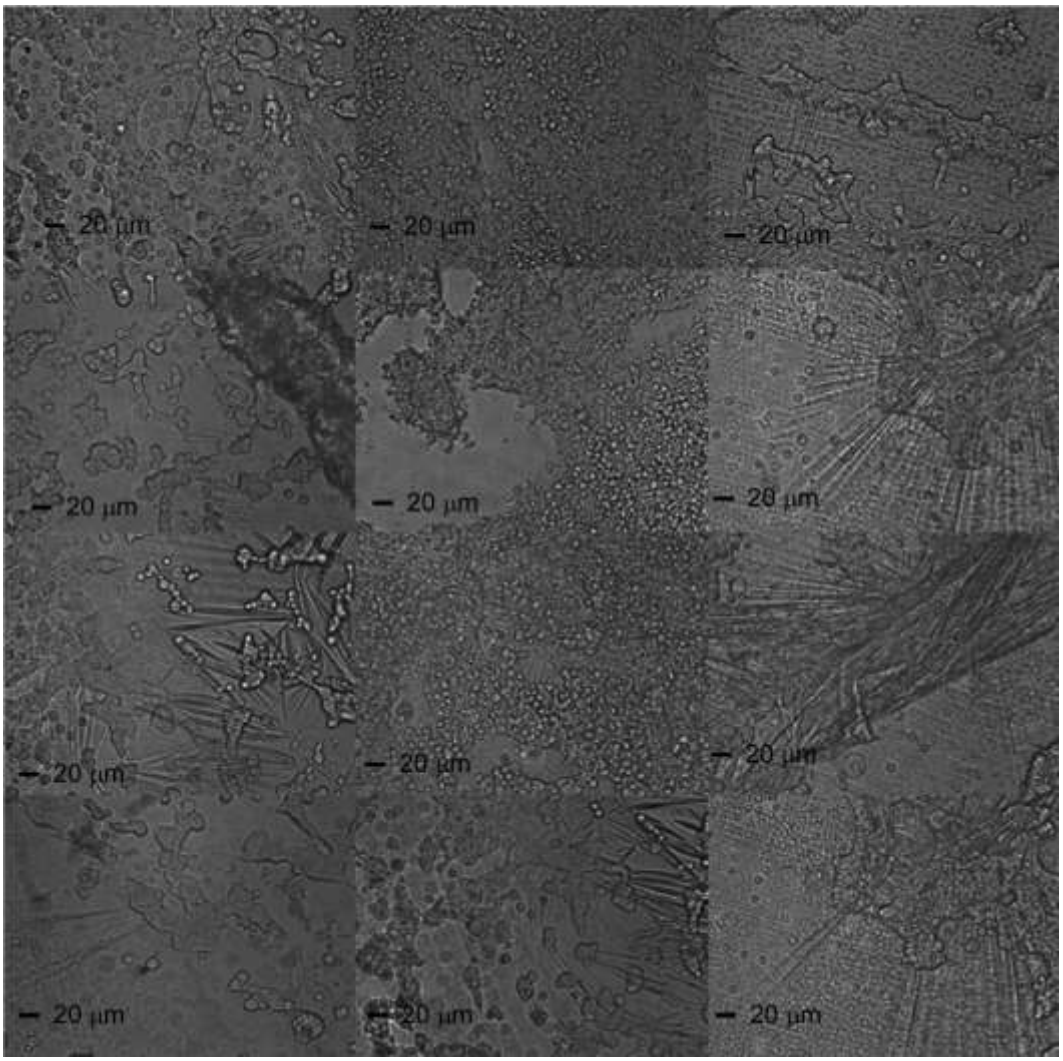
20 µm
20 µm
20 µm
20 µm
20 µm
20 µm
20 µm
20 µm
20 µm
20 µm
20 µm
20 µm

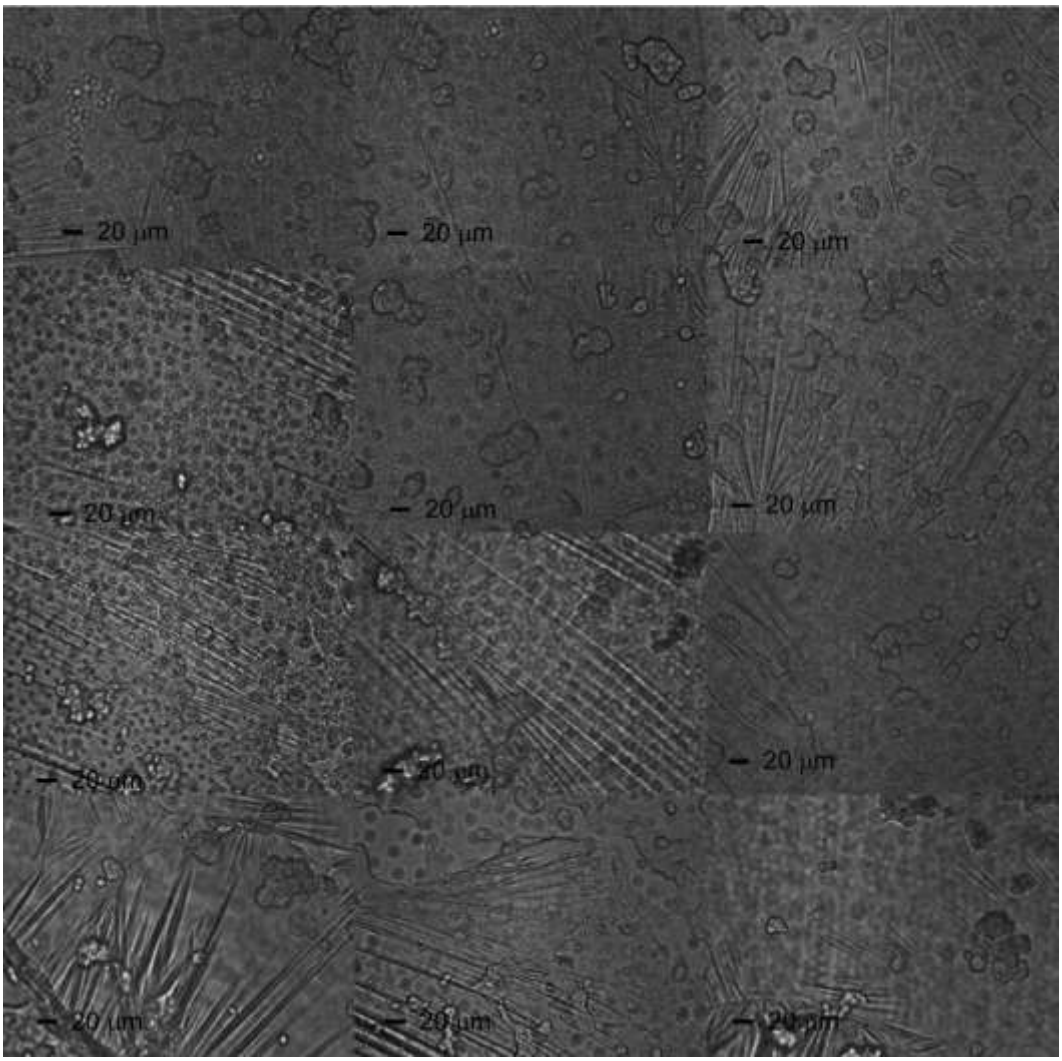
20 µm
20 µm
20 µm
20 µm
20 µm
20 µm
20 µm
20 µm
20 µm
20 µm
20 µm
20 µm

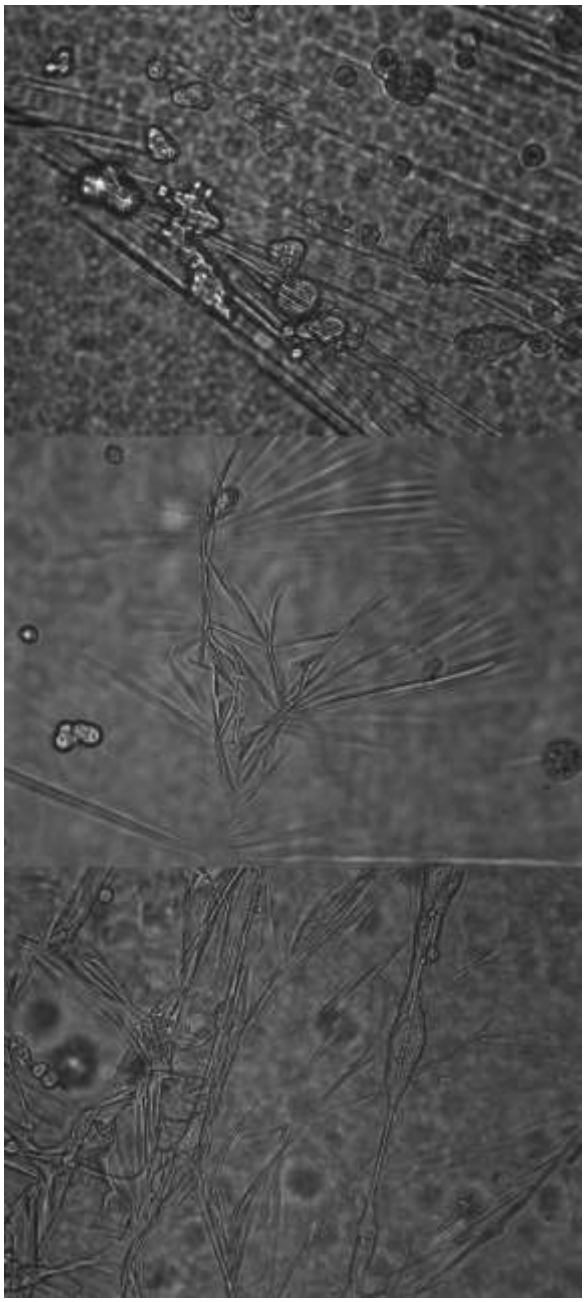

APPENDIX C

WRINKLE CELLOMICS MEMBRANE WITHOUT FIBRONECTIN COATING RT4 CELLS WITH 12 HOUR INCUBATION PERIOD

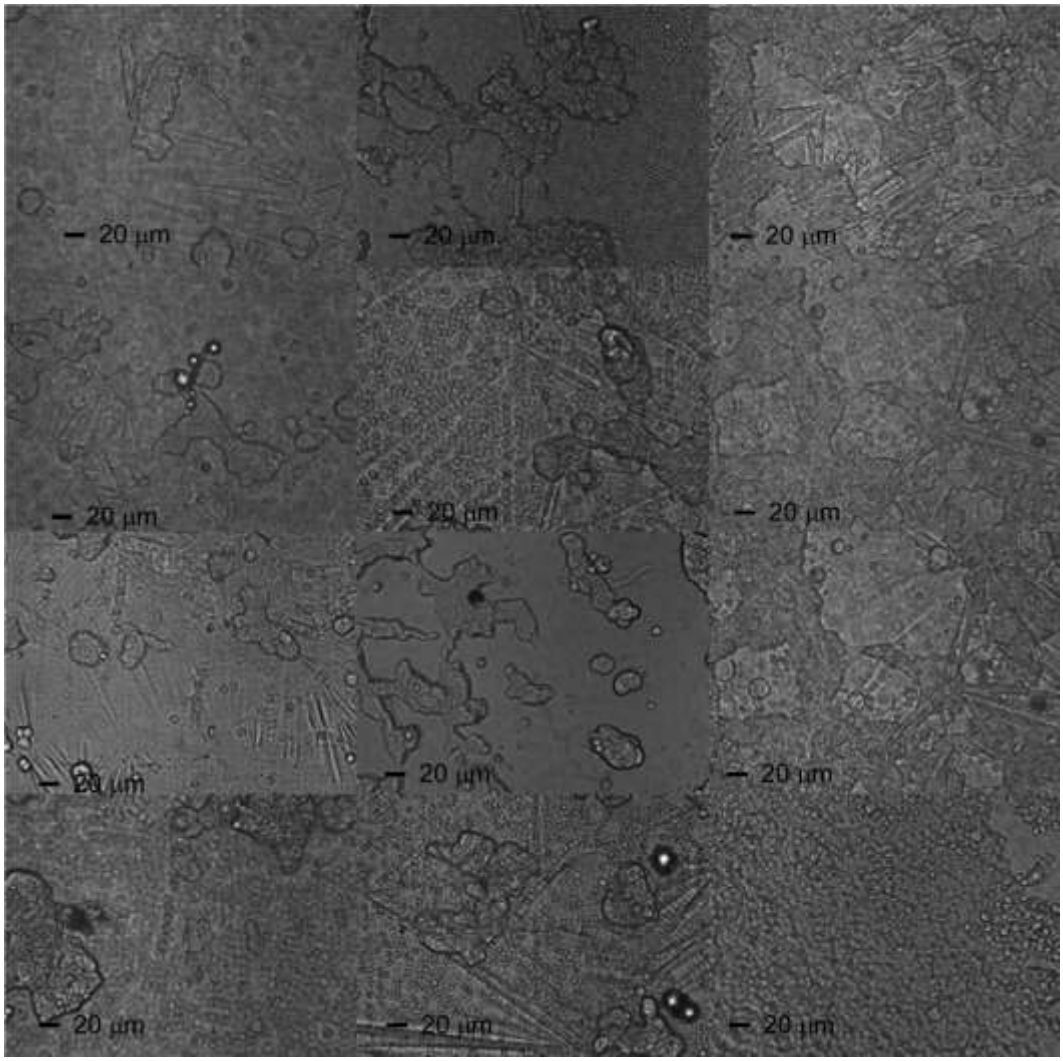
20 µm
20 µm
20 µm
20 µm
20 µm
20 µm
20 µm
20 µm
20 µm
20 µm
20 µm
20 µm

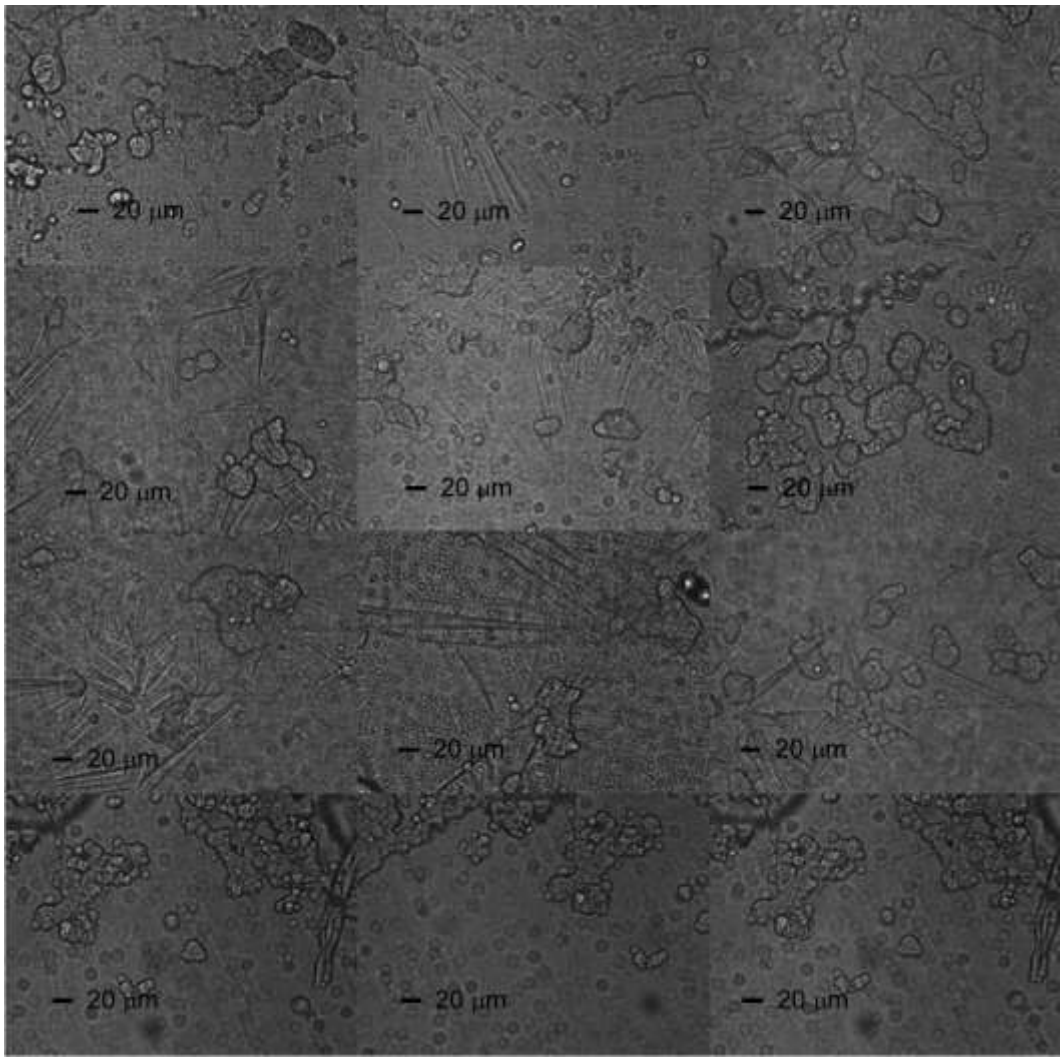
20 µm
20 µm
20 µm
20 µm
20 µm
20 µm
20 µm
20 µm
20 µm
20 µm
20 µm
20 µm

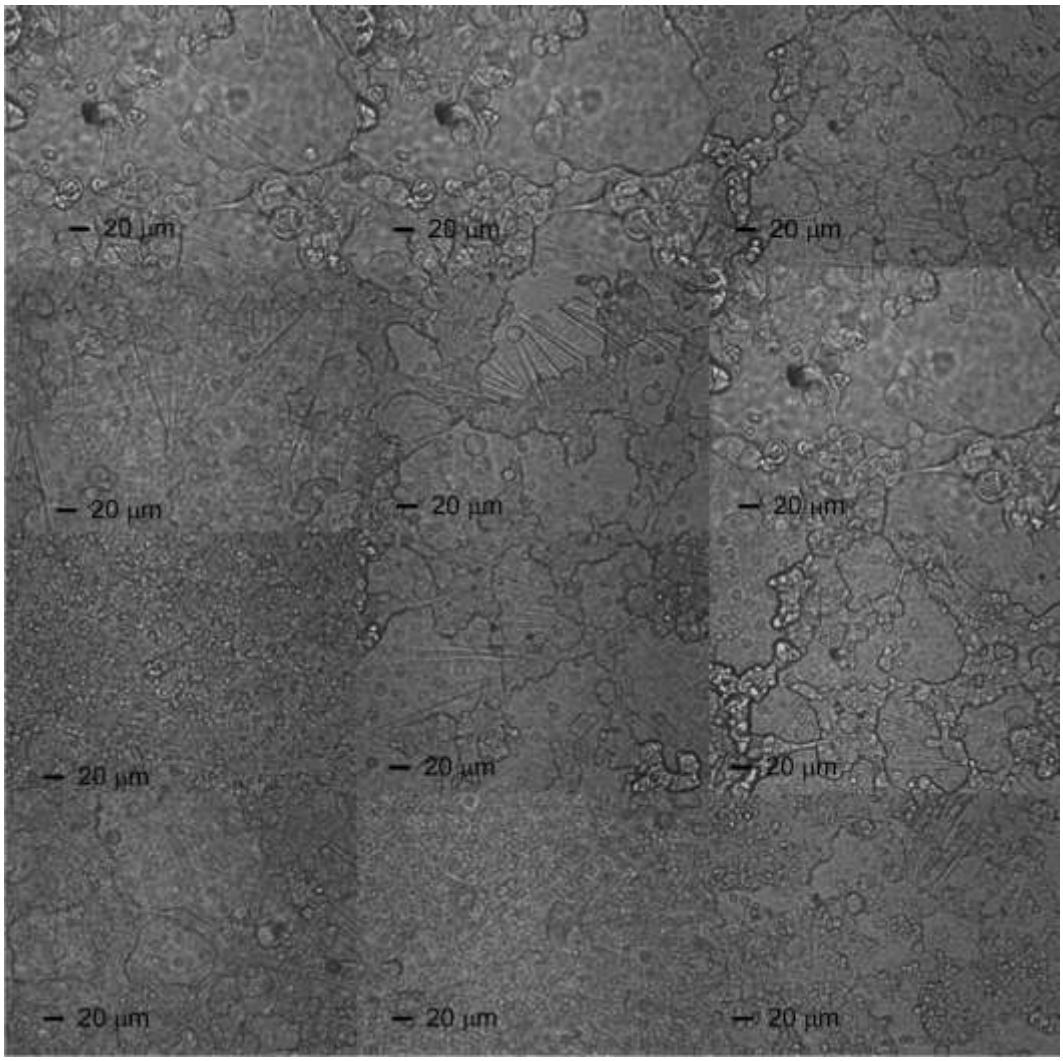
20 µm
20 µm
20 µm
20 µm
20 µm
20 µm
20 µm
20 µm
20 µm
20 µm
20 µm

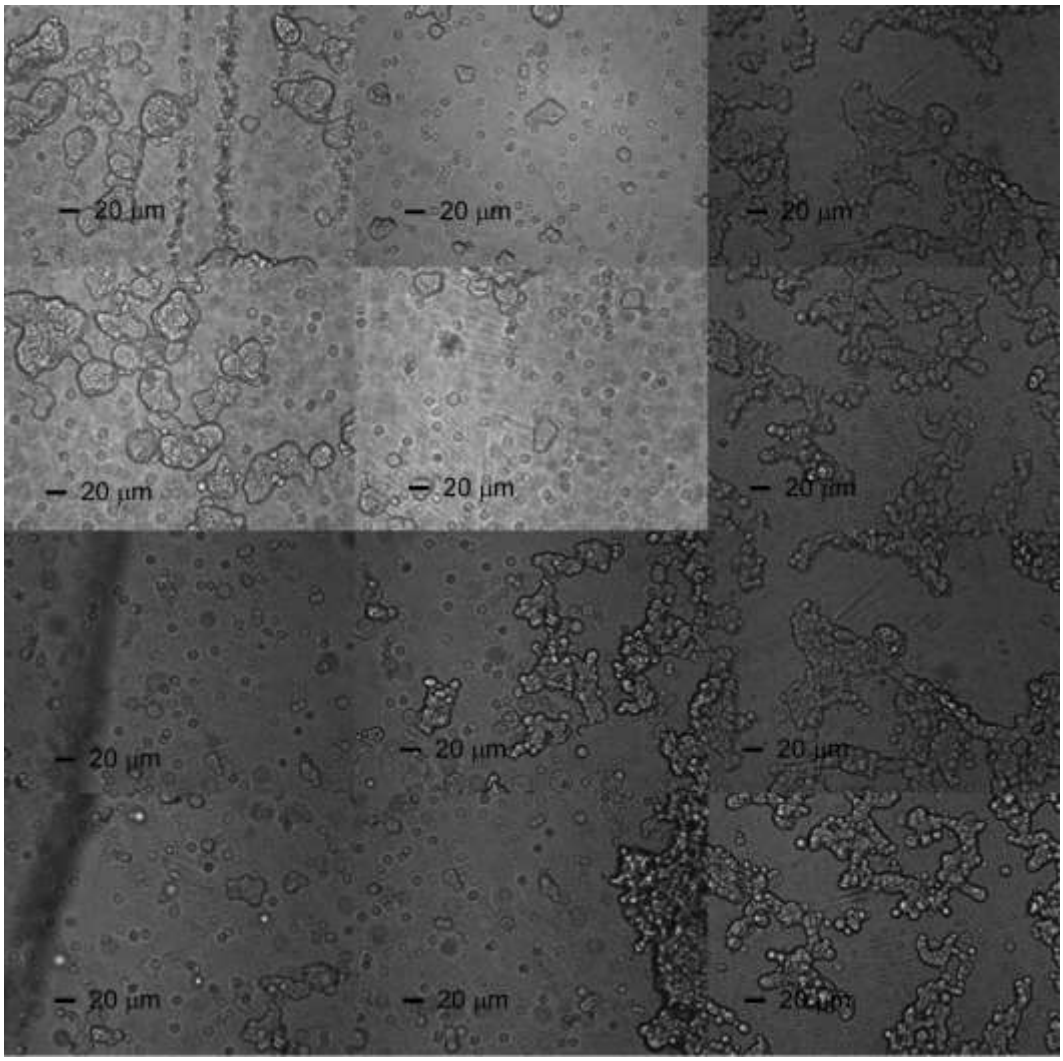
20 µm
20 µm
20 µm
20 µm
20 µm
20 µm
20 µm
20 µm
20 µm
20 µm
20 µm
20 µm

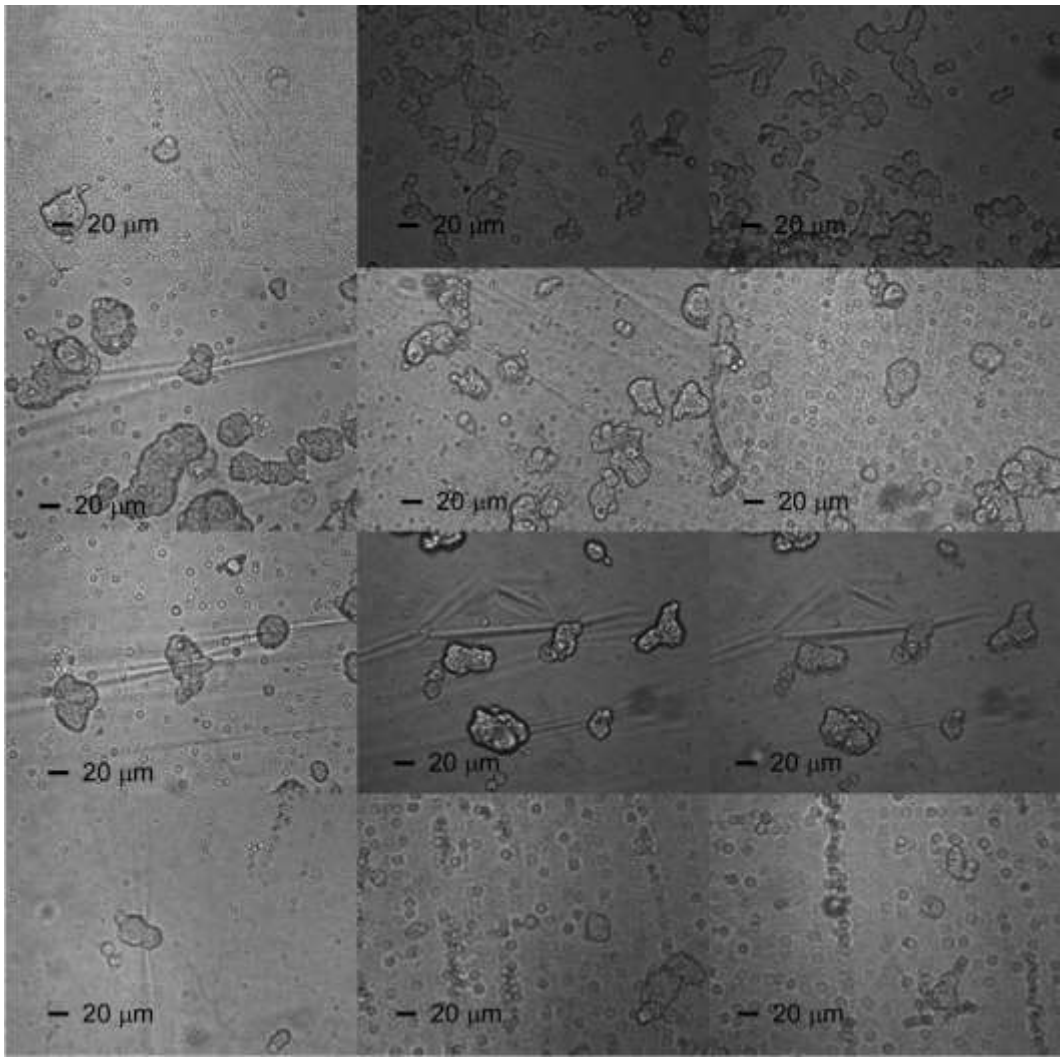
20 µm
20 µm
20 µm
20 µm
20 µm
20 µm
20 µm
20 µm
20 µm
20 µm
20 µm
20 µm

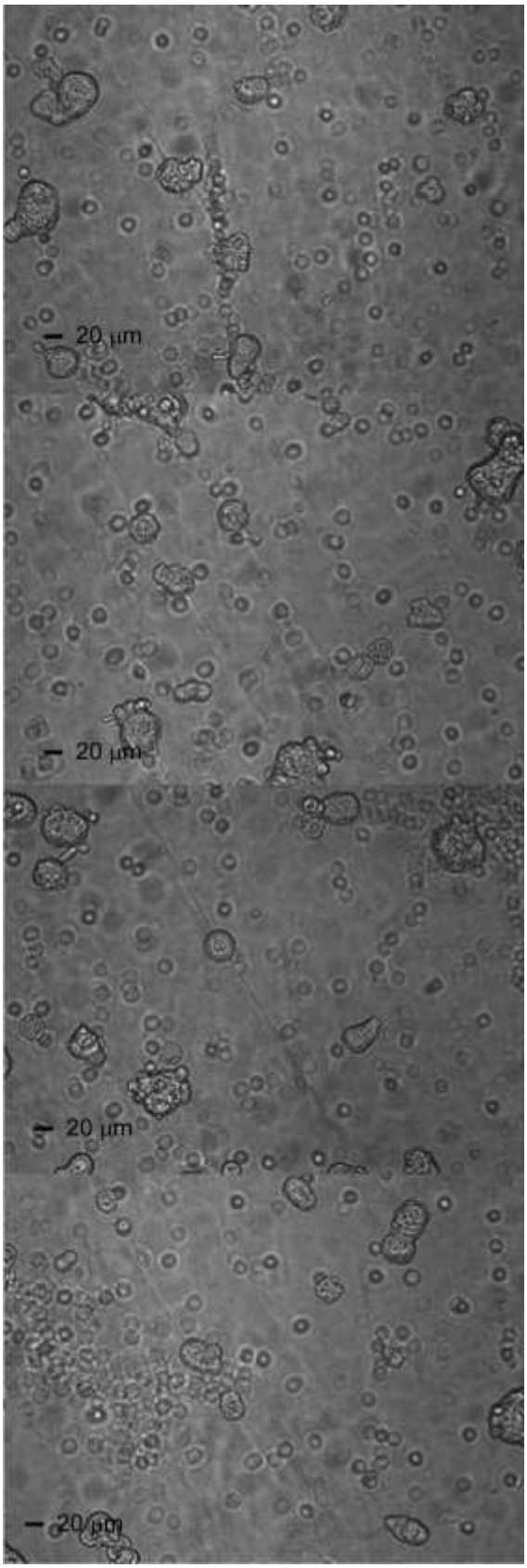
20 µm
20 µm
20 µm
20 µm

APPENDIX D

CELLOMICS MEMBRANE CANCEROUS CELLS WITH 12 HOUR INCUBATION PERIOD IN ARTIFICAL URINE AT VARIOUS PH LEVELS

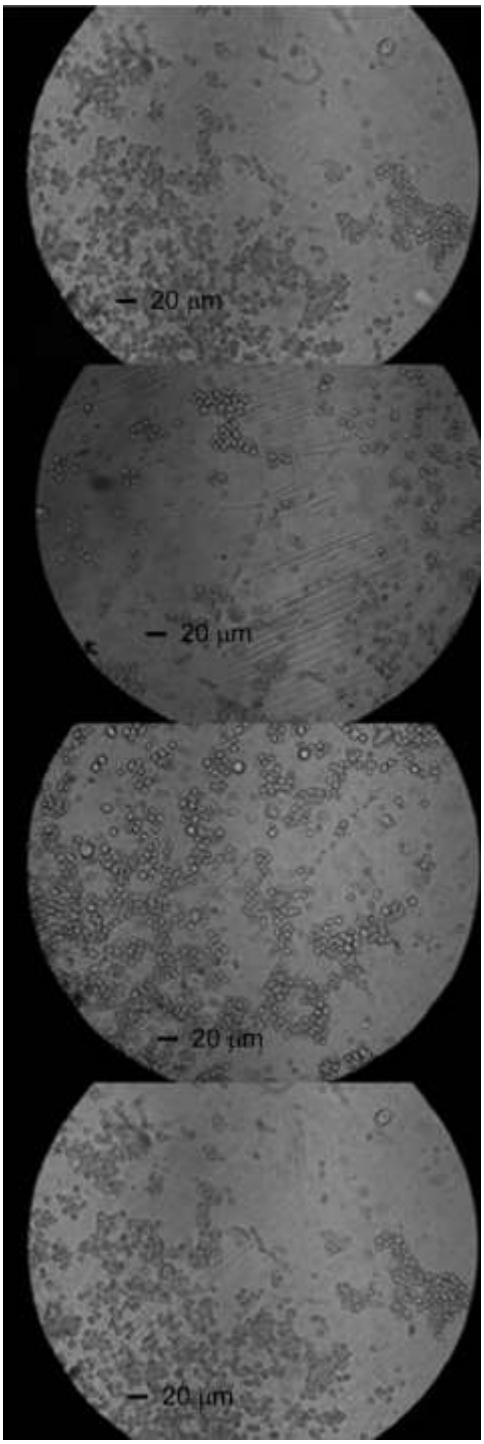

RT4 cells after 12 hours of incubation on the ultra-thin membrane in artificial urine at a pH level of 5

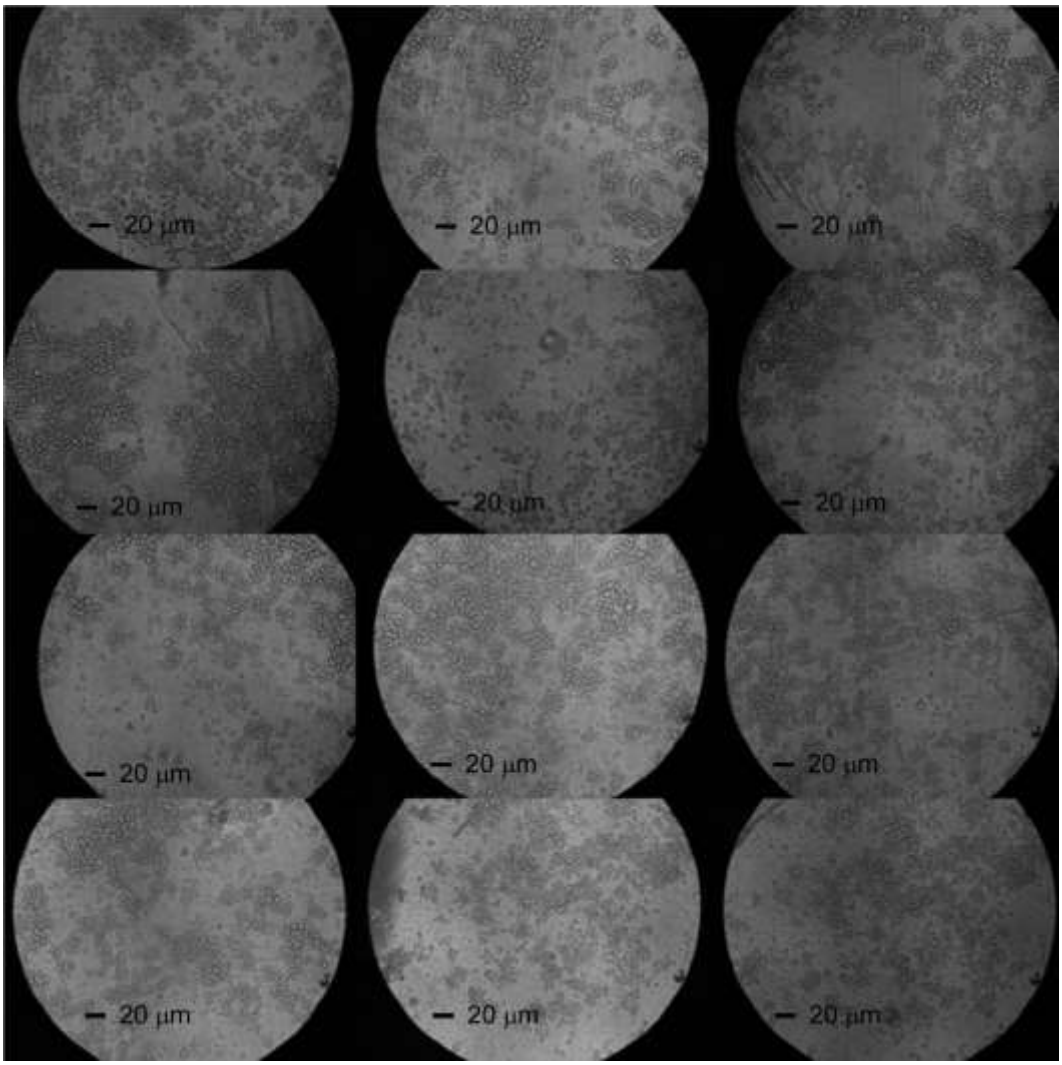

RT4 cells after 12 hours of incubation on the ultra-thin membrane in artificial urine at a pH level of 6

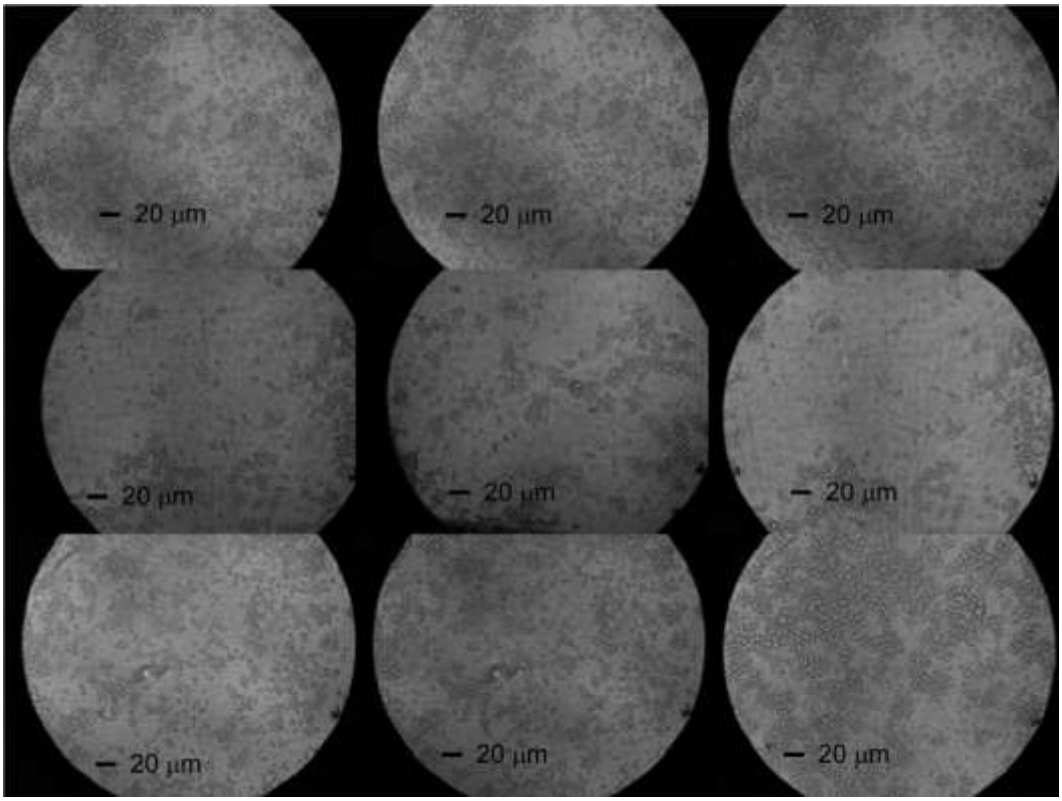

RT4 cells after 12 hours of incubation on the ultra-thin membrane in artificial urine at a pH level of 6

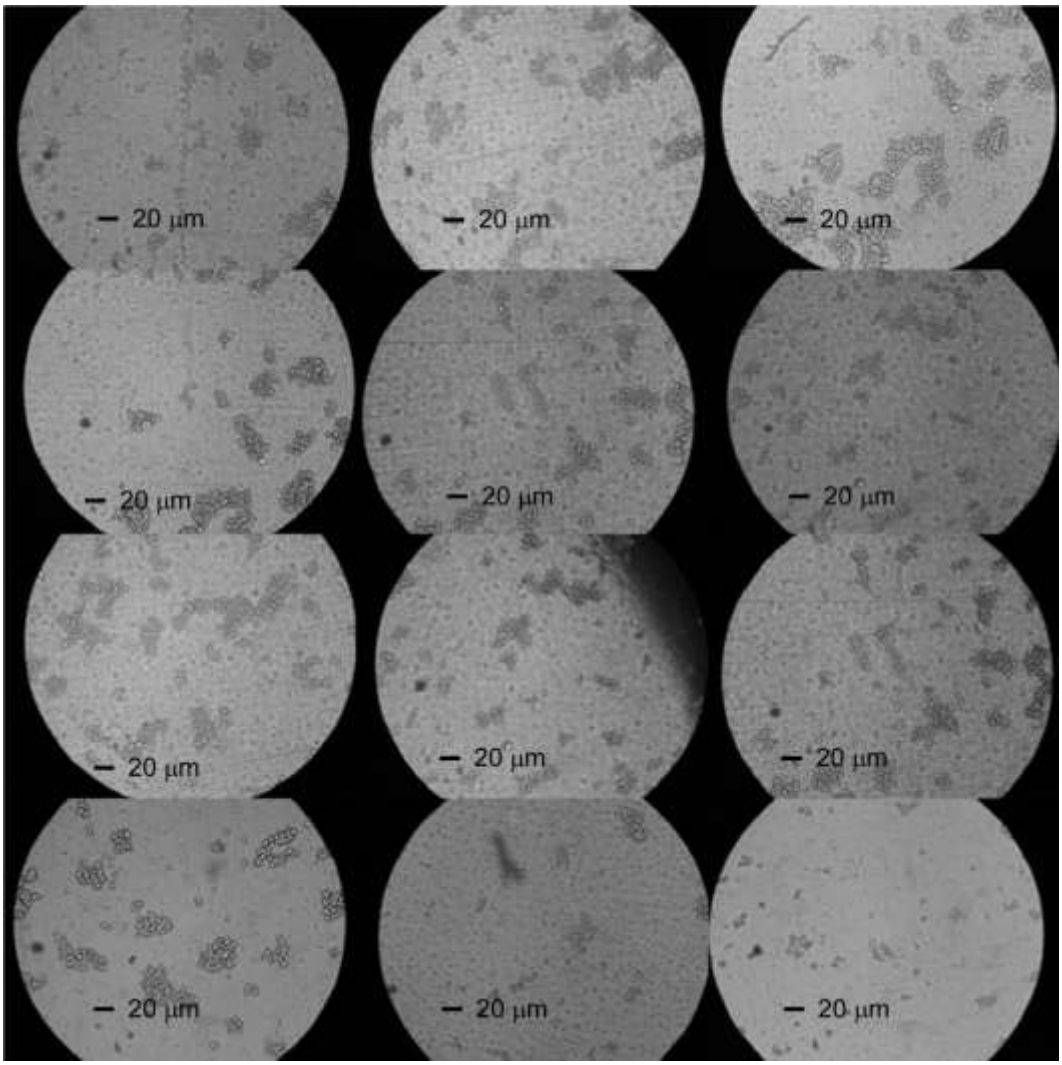

RT4 cells after 12 hours of incubation on the ultra-thin membrane in artificial urine at a pH level of 7

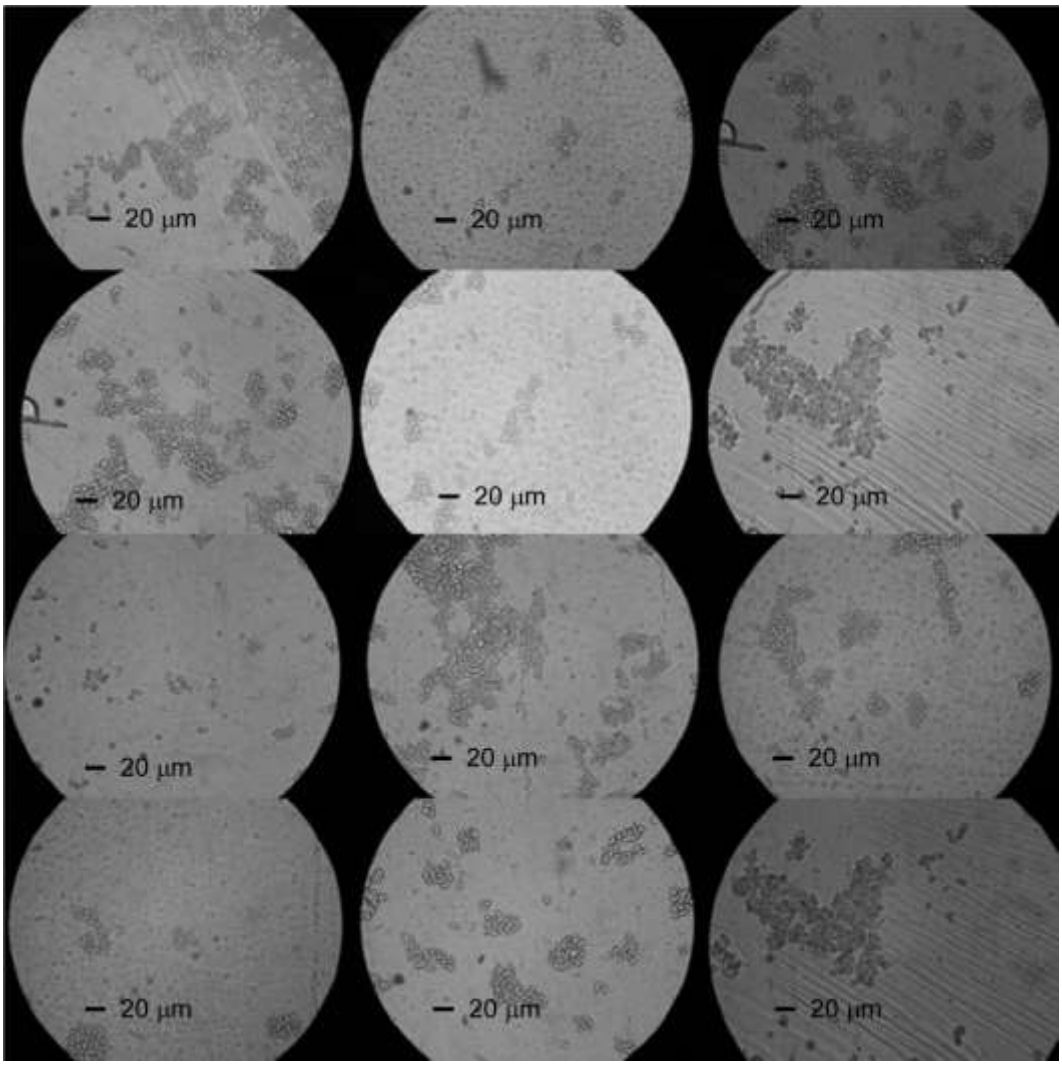

RT4 cells after 12 hours of incubation on the ultra-thin membrane in artificial urine at a pH level of 7

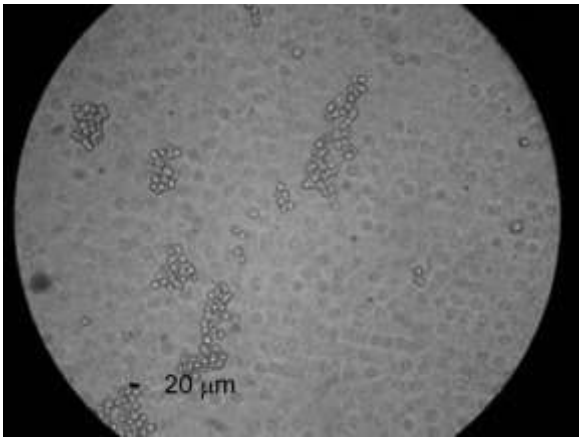

RT4 cells after 12 hours of incubation on the ultra-thin membrane in artificial urine at a pH level of 7

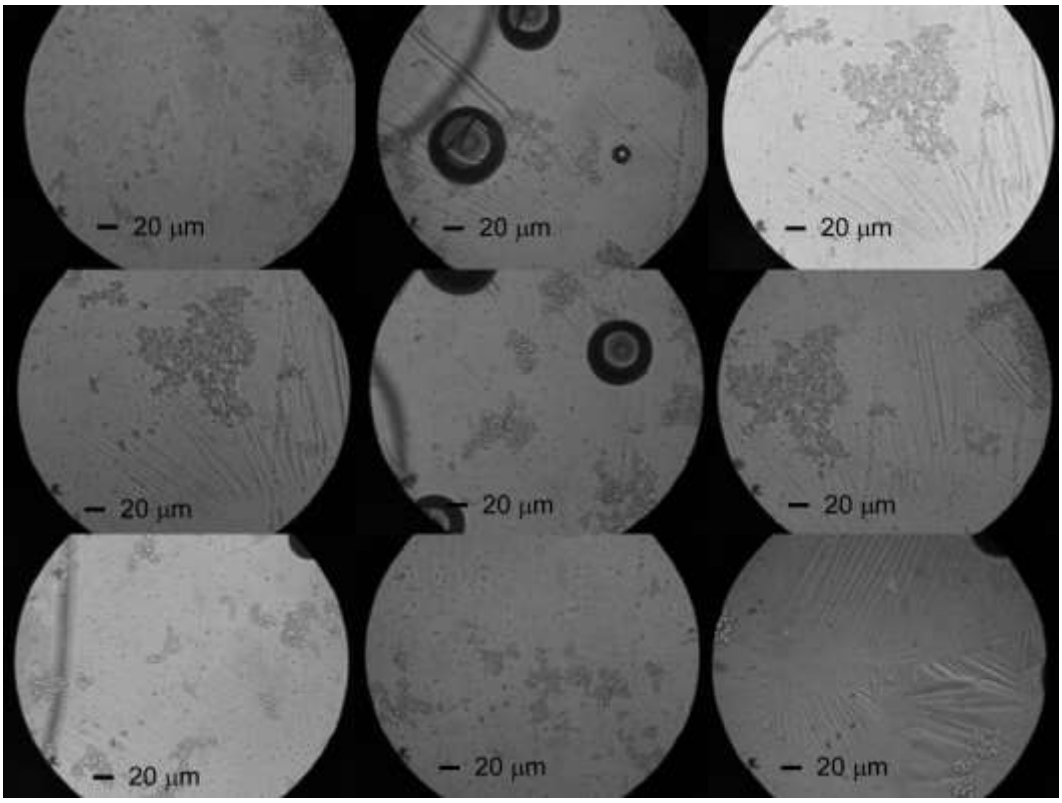

T24 cells after 12 hours of incubation on the ultra-thin membrane in artificial urine at a pH level of 5

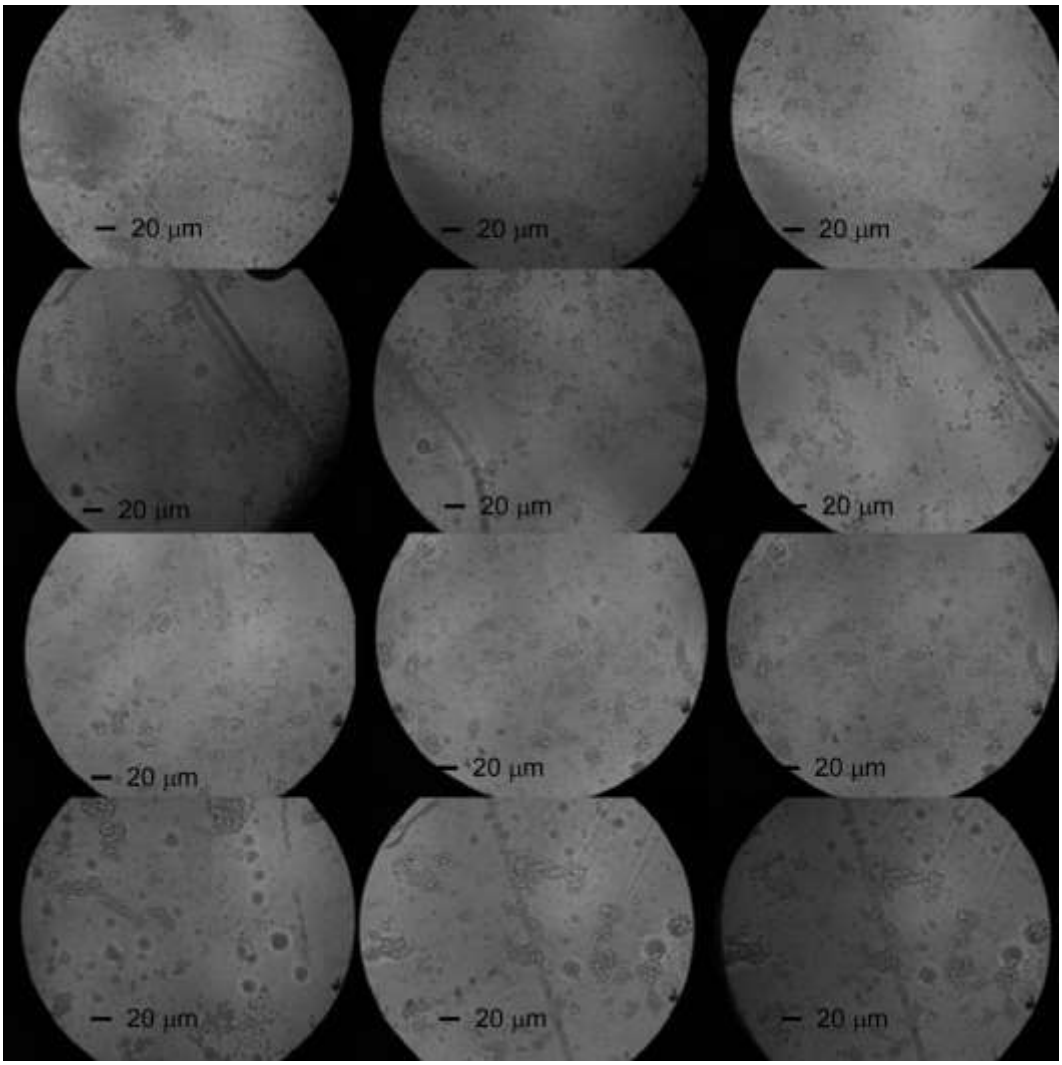

T24 cells after 12 hours of incubation on the ultra-thin membrane in artificial urine at a pH level of 6

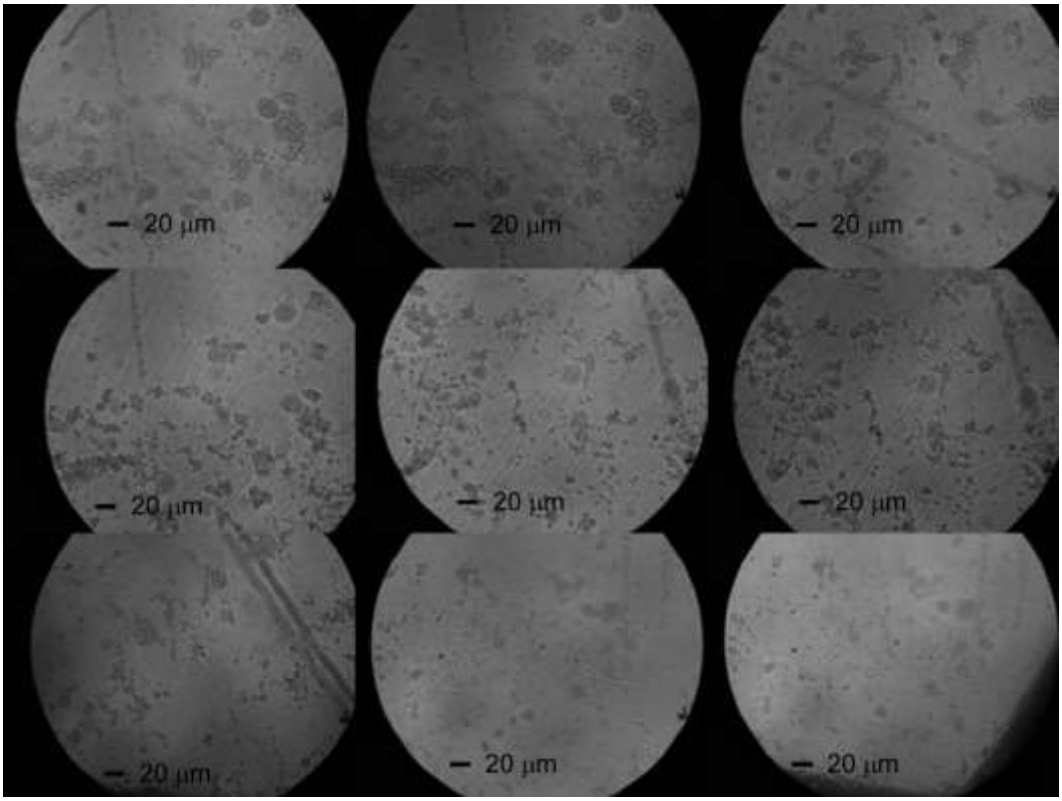

T24 cells after 12 hours of incubation on the ultra-thin membrane in artificial urine at a pH level of 6

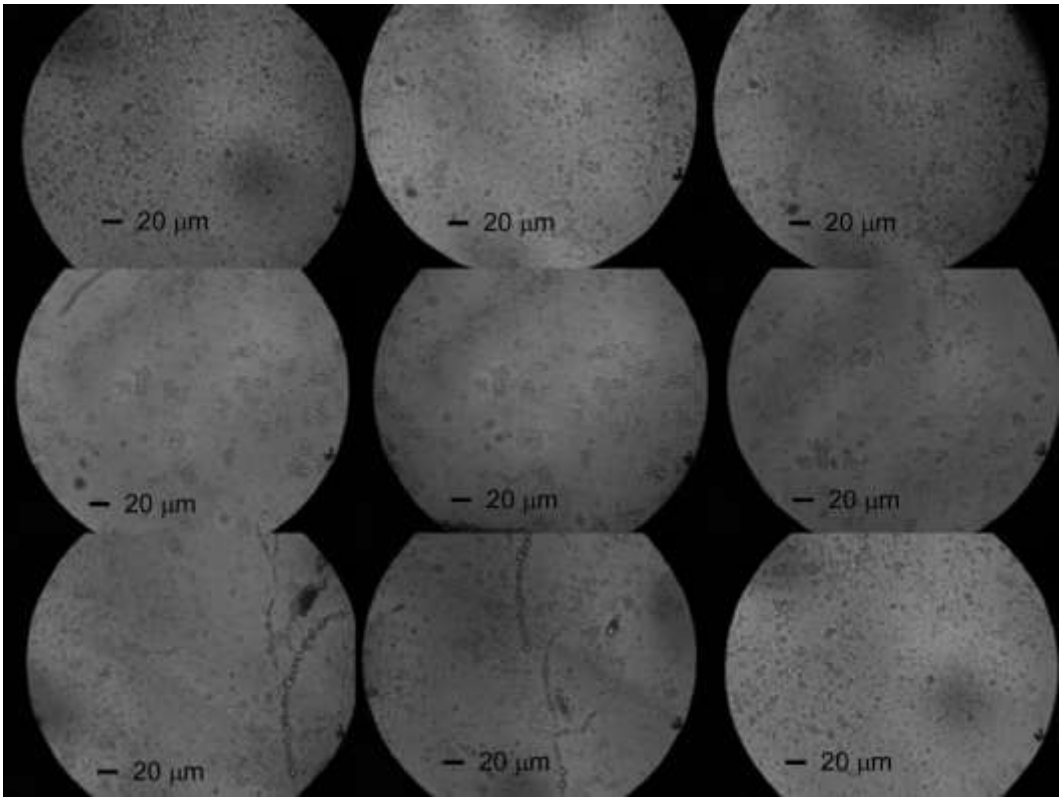

T24 cells after 12 hours of incubation on the ultra-thin membrane in artificial urine at a pH level of 6

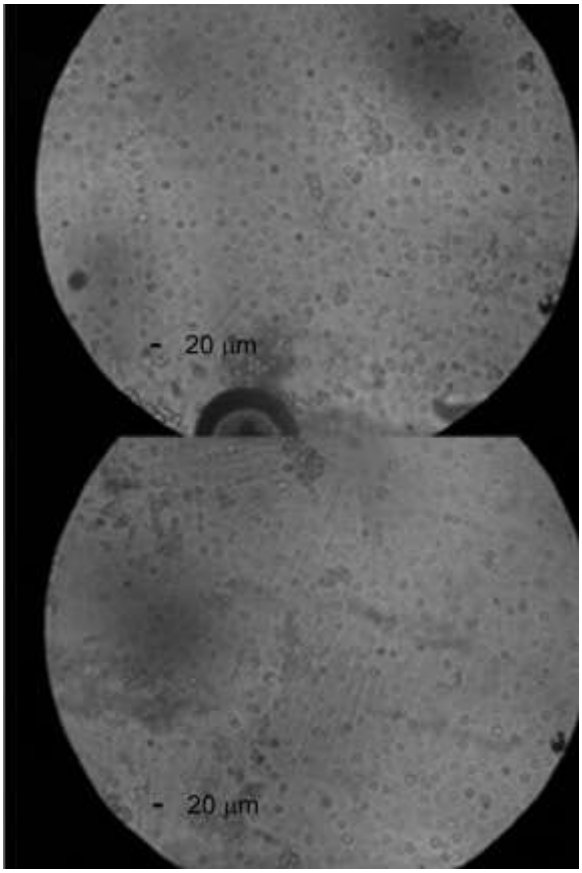

T24 cells after 12 hours of incubation on the ultra-thin membrane in artificial urine at a pH level of 6

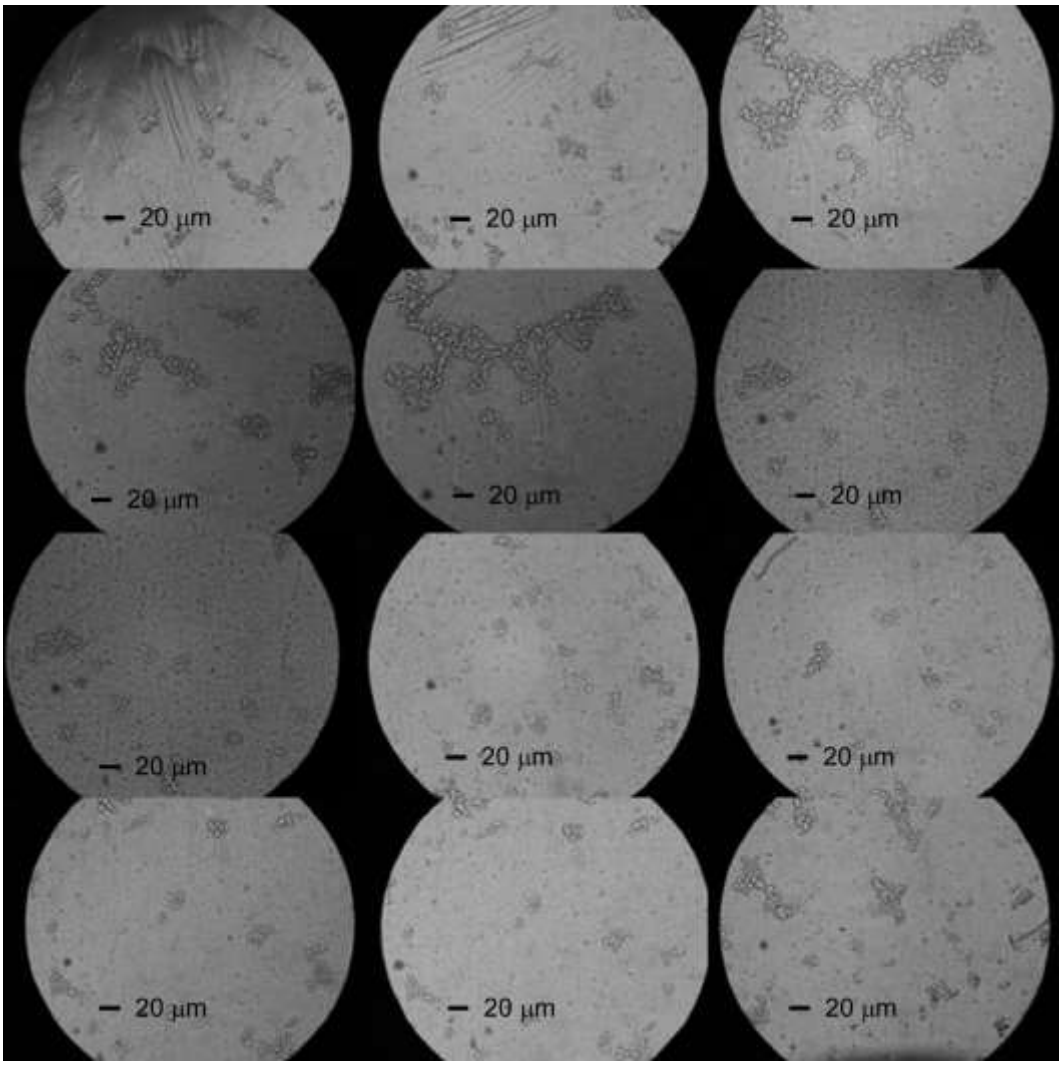

T24 cells after 12 hours of incubation on the ultra-thin membrane in artificial urine at a pH level of 7

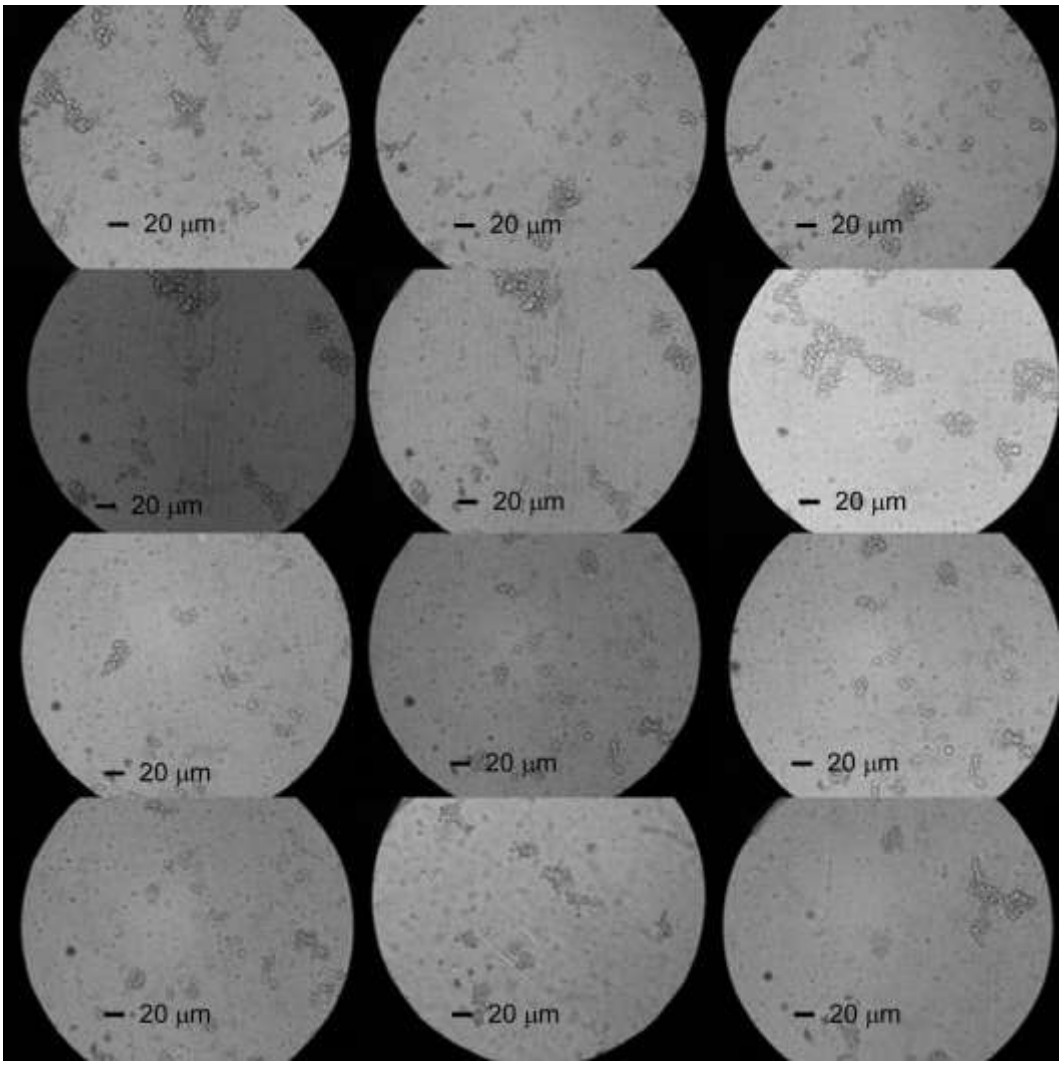

T24 cells after 12 hours of incubation on the ultra-thin membrane in artificial urine at a pH level of 7

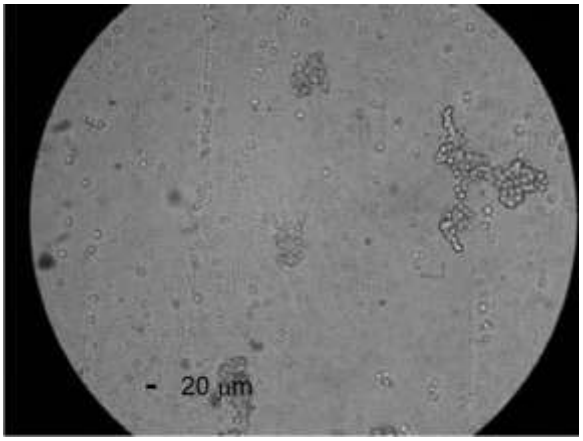

T24 cells after 12 hours of incubation on the ultra-thin membrane in artificial urine at a pH level of 7

APPENDIX E

CELLOMICS MEMBRANE CANCEROUS CELLS WITH 12 HOUR INCUBATION PERIOD IN HUMAN URINE AT VARIOUS PH LEVELS

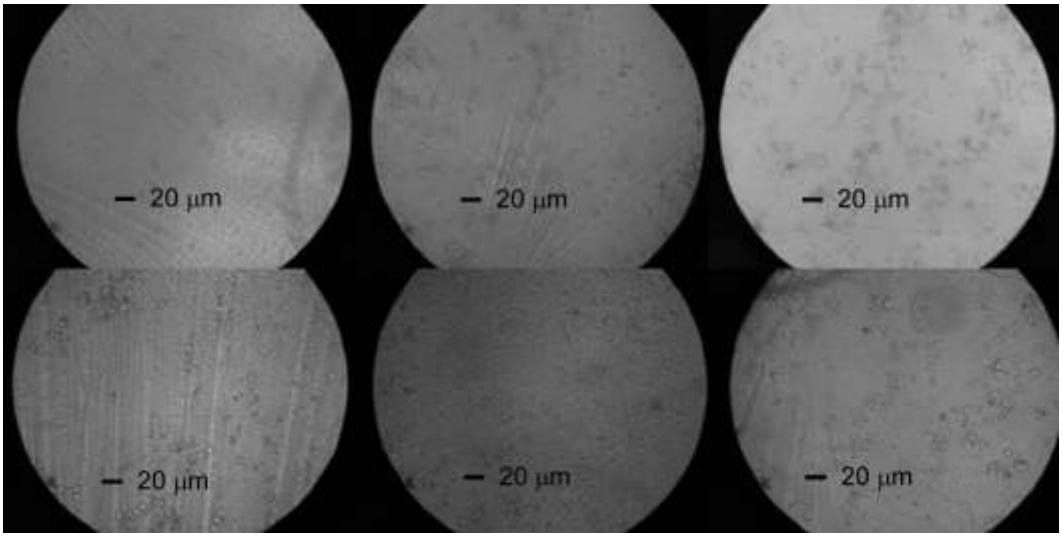

RT4 cells after 12 hours of incubation on the ultra-thin membrane in human urine at a pH level of 5

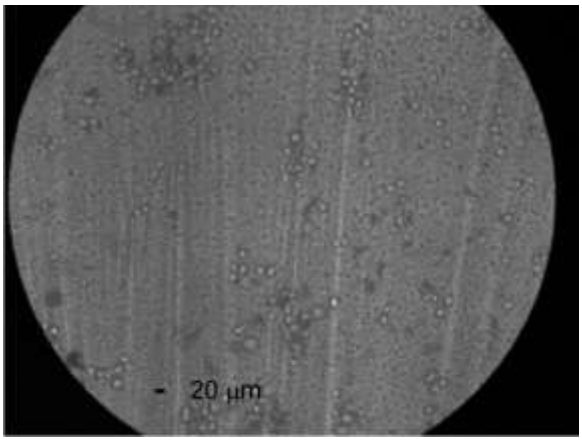

RT4 cells after 12 hours of incubation on the ultra-thin membrane in human urine at a pH level of 5

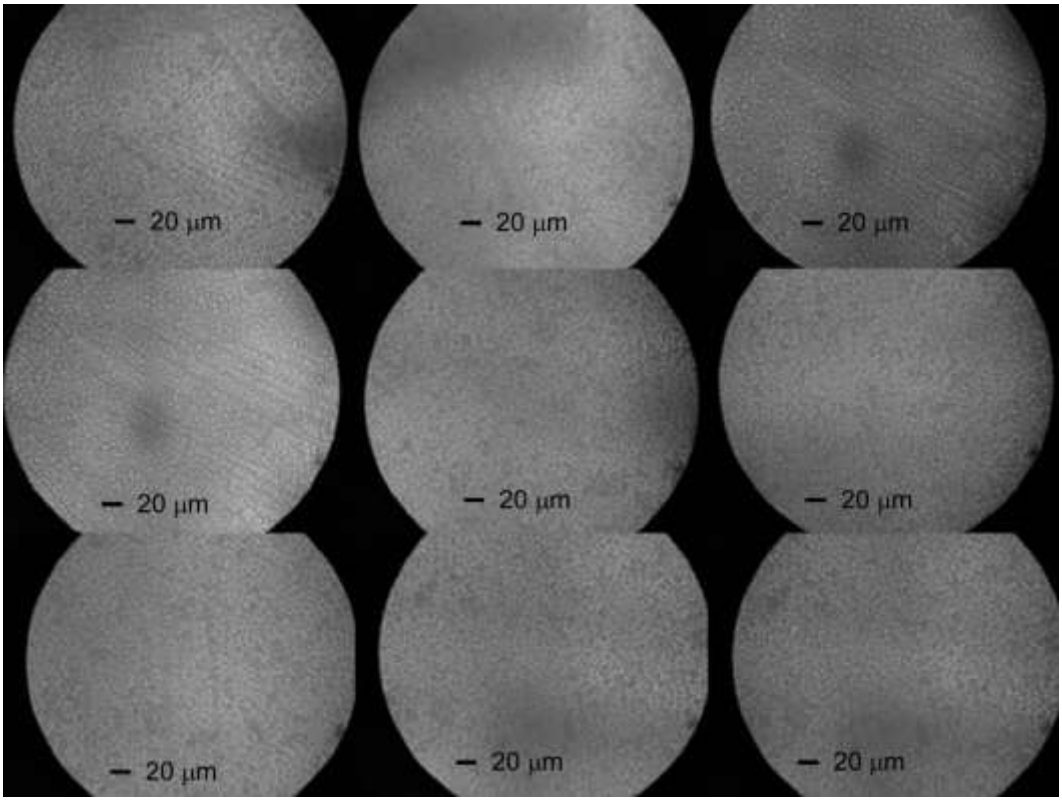

RT4 cells after 12 hours of incubation on the ultra-thin membrane in human urine at a pH level of 6

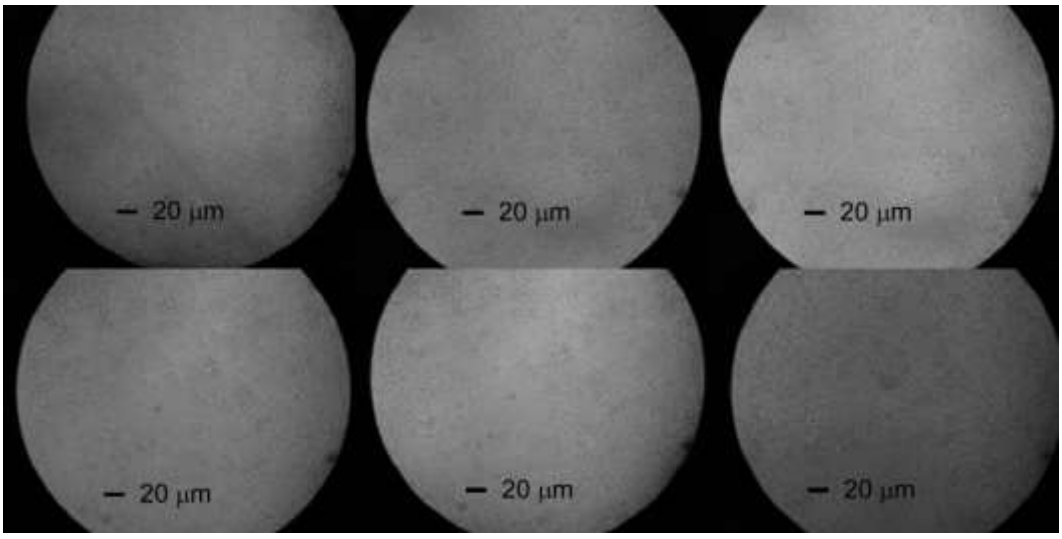

RT4 cells after 12 hours of incubation on the ultra-thin membrane in human urine at a pH level of 6

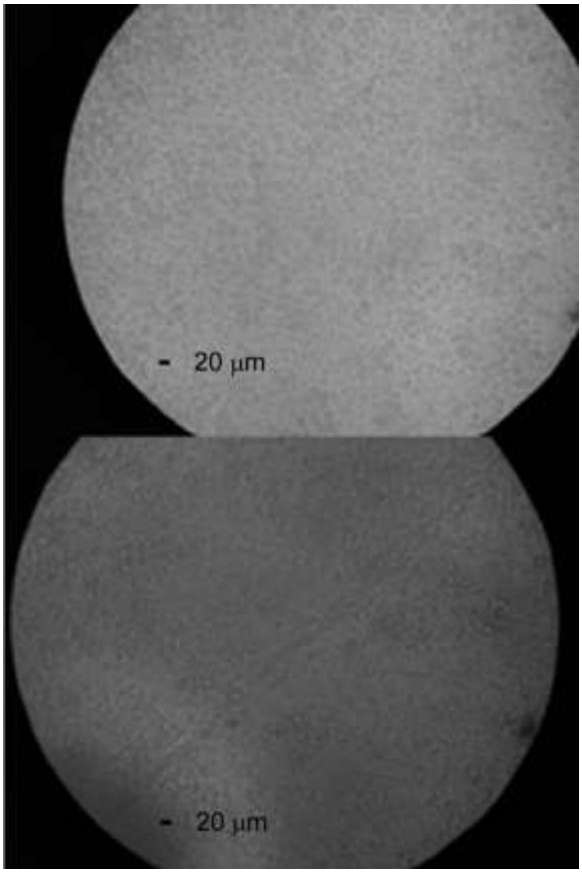

RT4 cells after 12 hours of incubation on the ultra-thin membrane in human urine at a pH level of 6

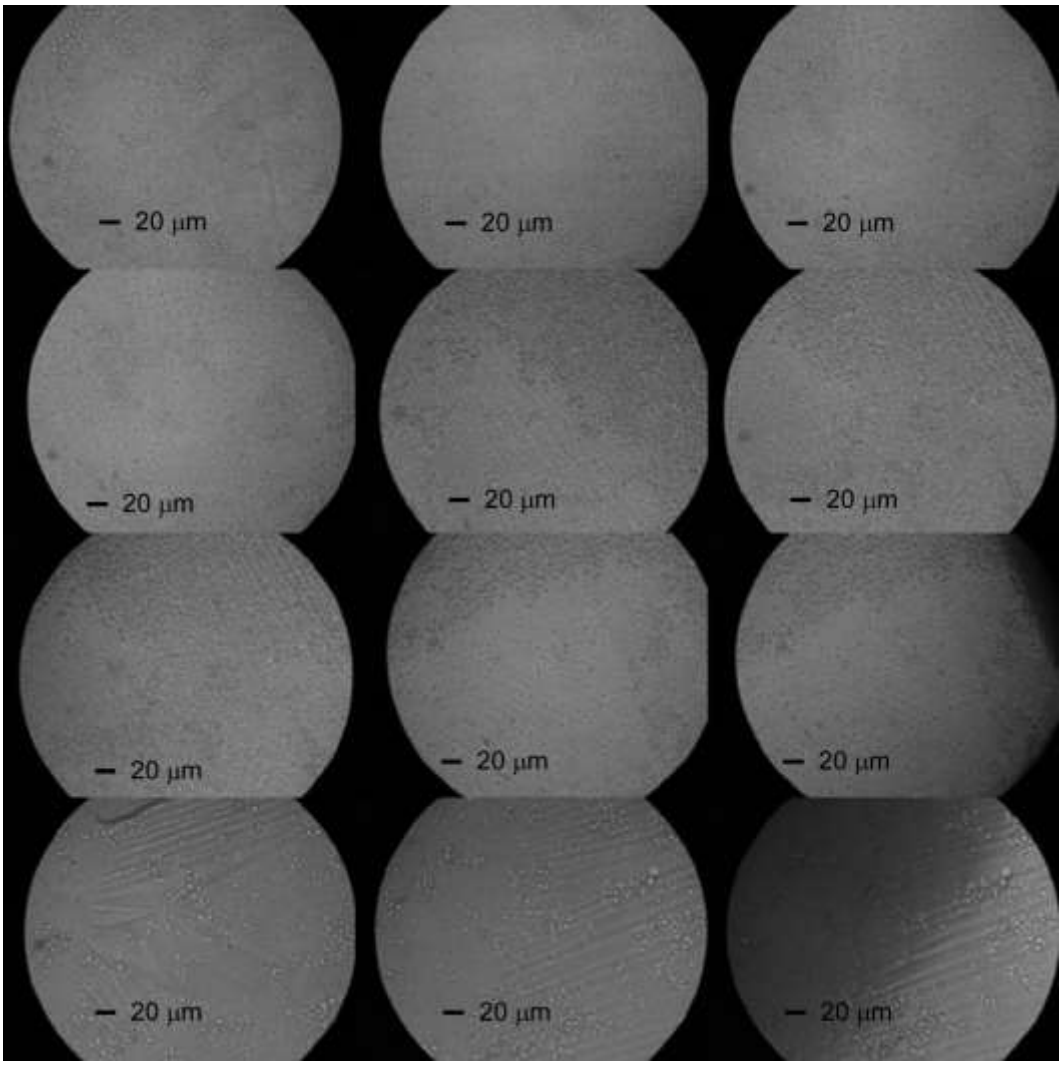

RT4 cells after 12 hours of incubation on the ultra-thin membrane in human urine at a pH level of 7

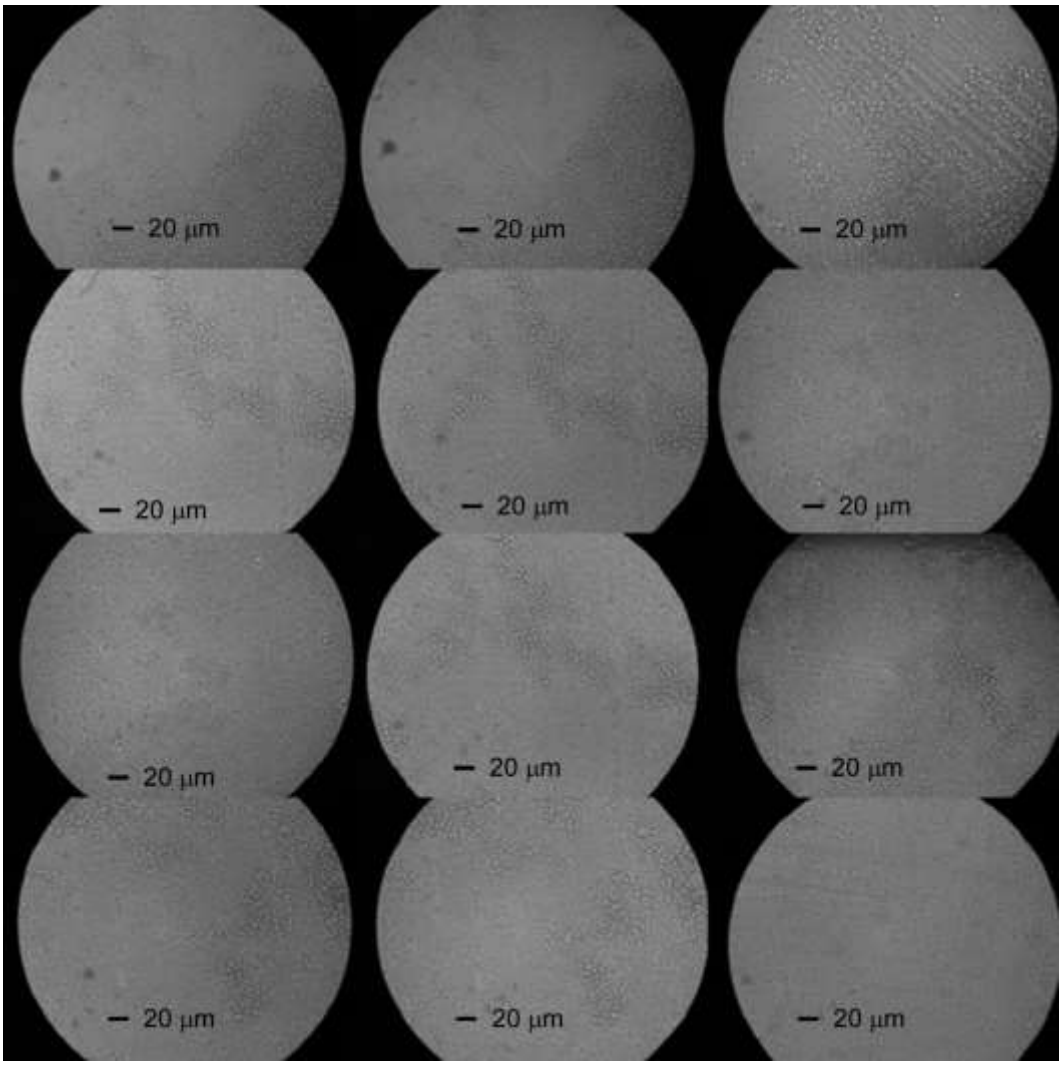

RT4 cells after 12 hours of incubation on the ultra-thin membrane in human urine at a pH level of 7

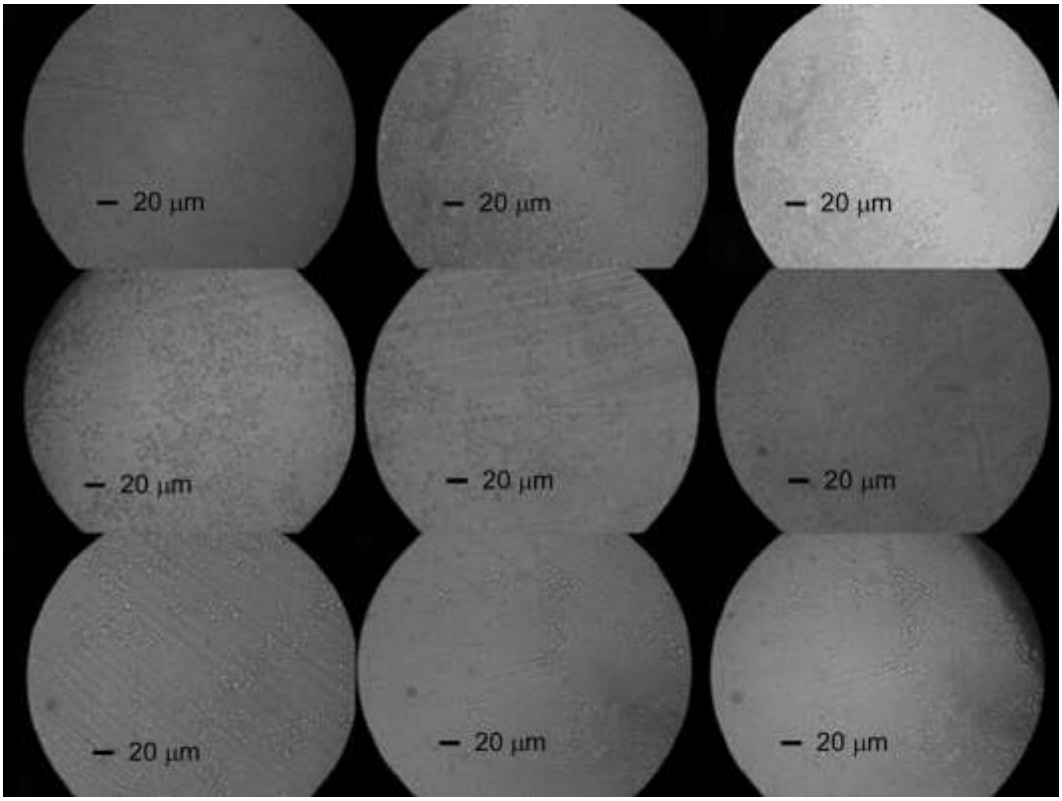

RT4 cells after 12 hours of incubation on the ultra-thin membrane in human urine at a pH level of 7

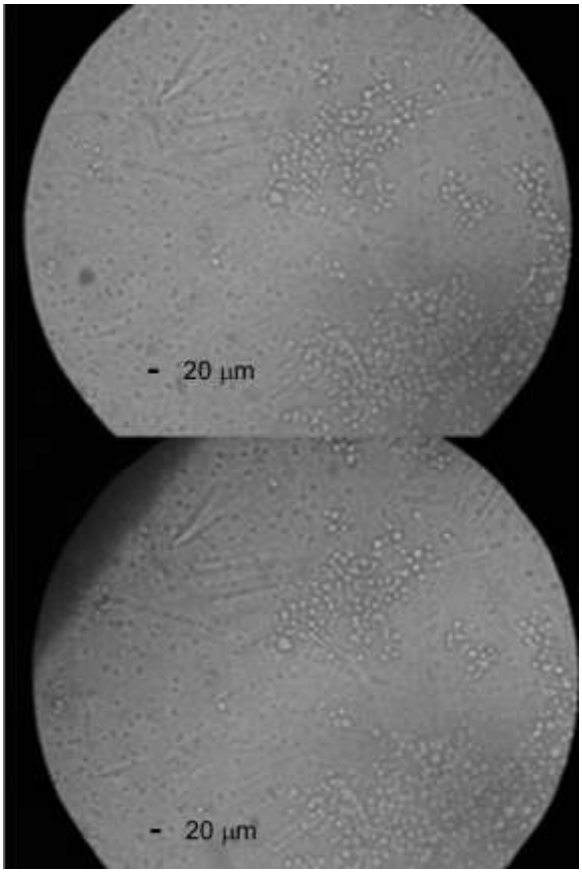

RT4 cells after 12 hours of incubation on the ultra-thin membrane in human urine at a pH level of 7

APPENDIX F

CELLOMICS MEMBRANE 8 HOUR INCUBATION WITH VARIOUS CELL TYPE AND MIXED CELLS

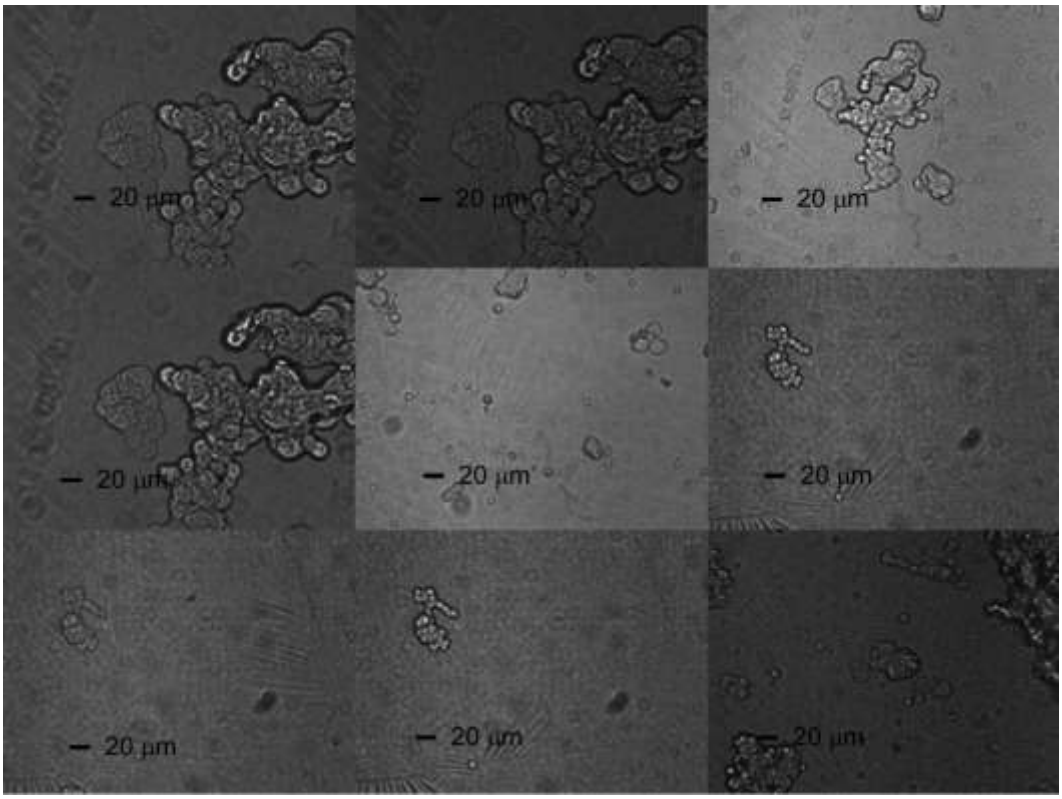

RT4 cells after 8 hours of incubation on the ultra-thin membrane

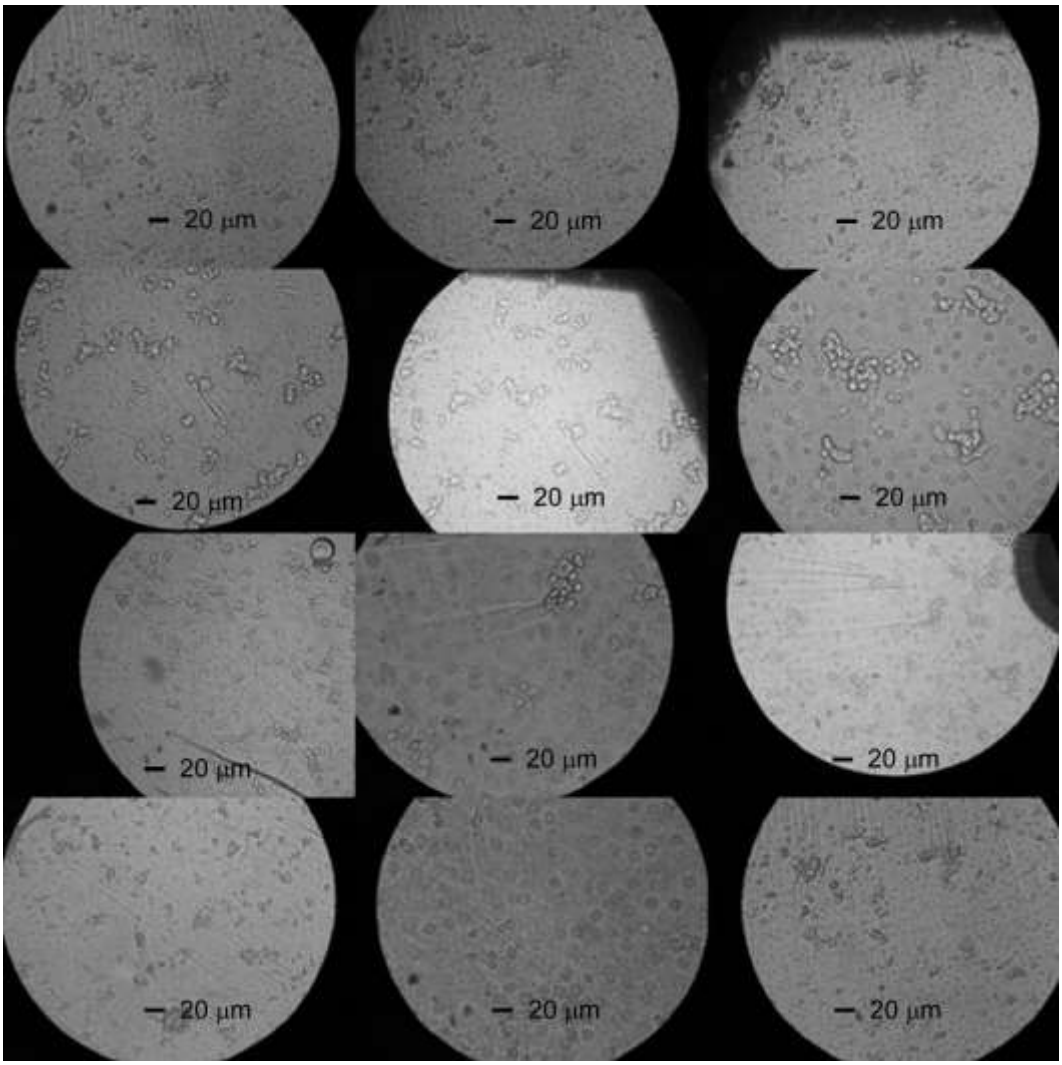

T24 cells after 8 hours of incubation on the ultra-thin membrane

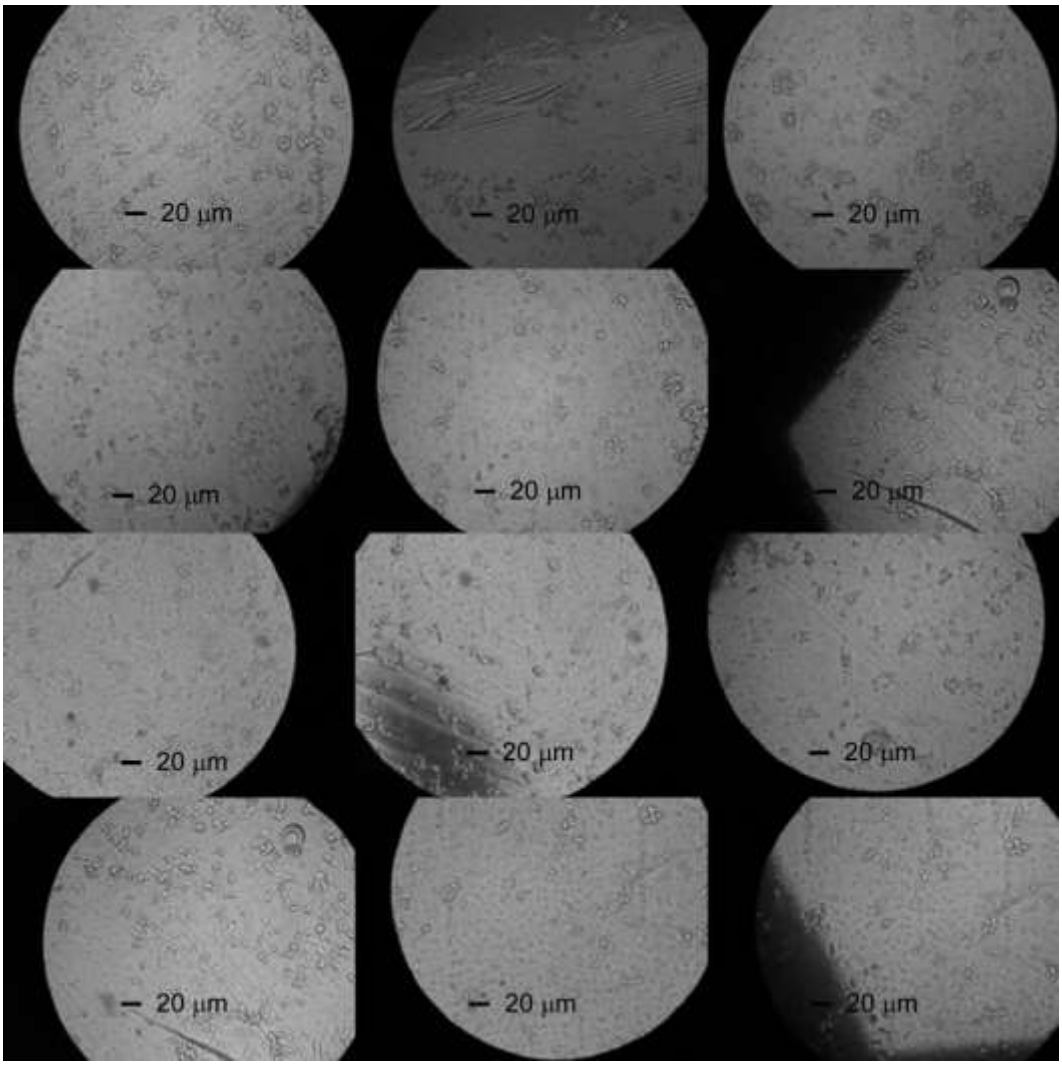

T24 cells after 8 hours of incubation on the ultra-thin membrane

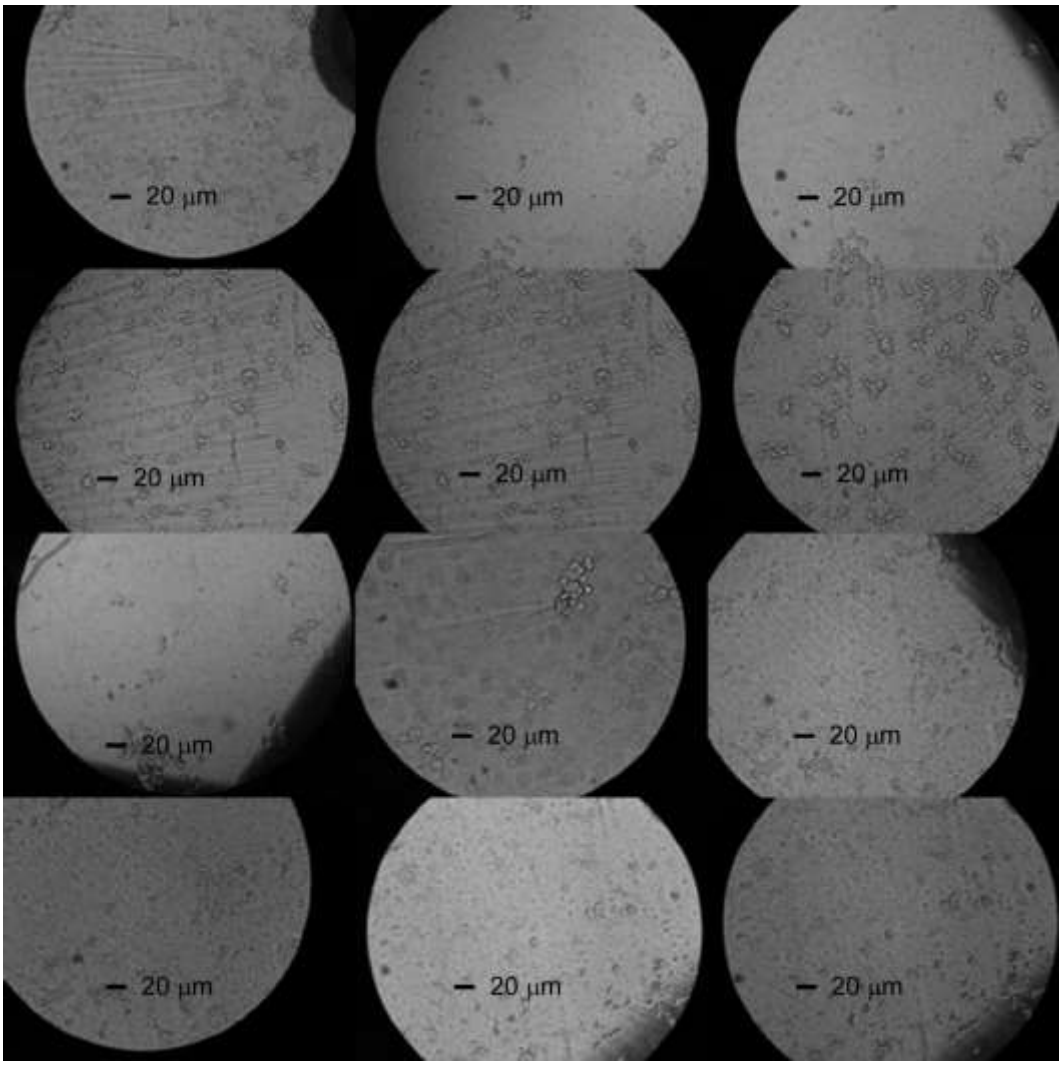

T24 cells after 8 hours of incubation on the ultra-thin membrane

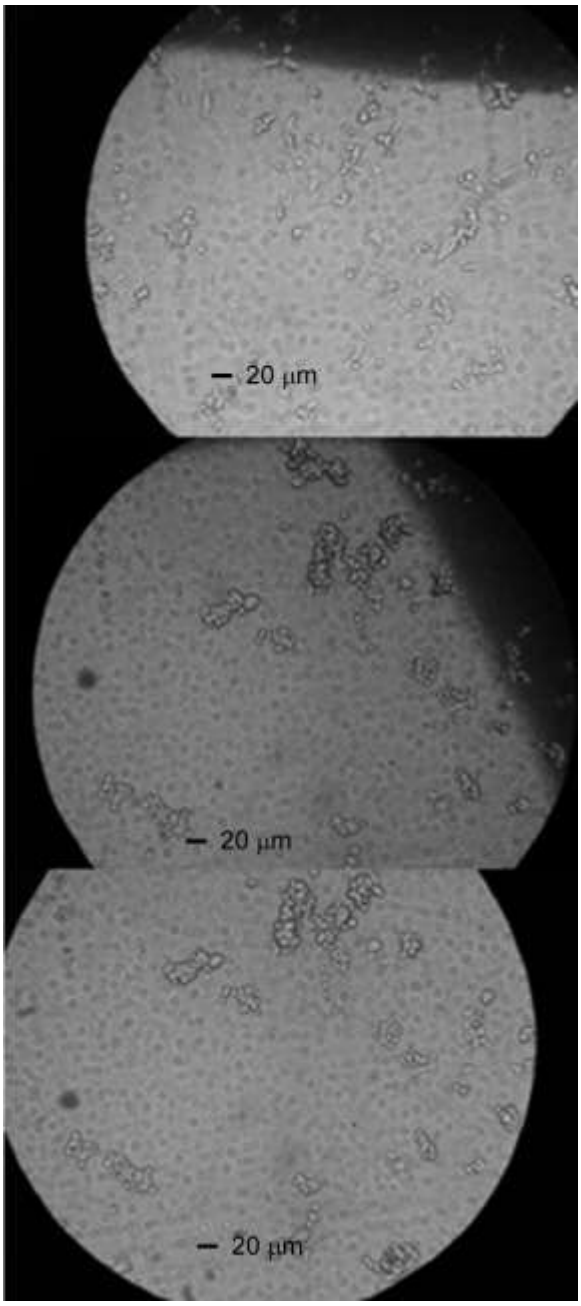

T24 cells after 8 hours of incubation on the ultra-thin membrane

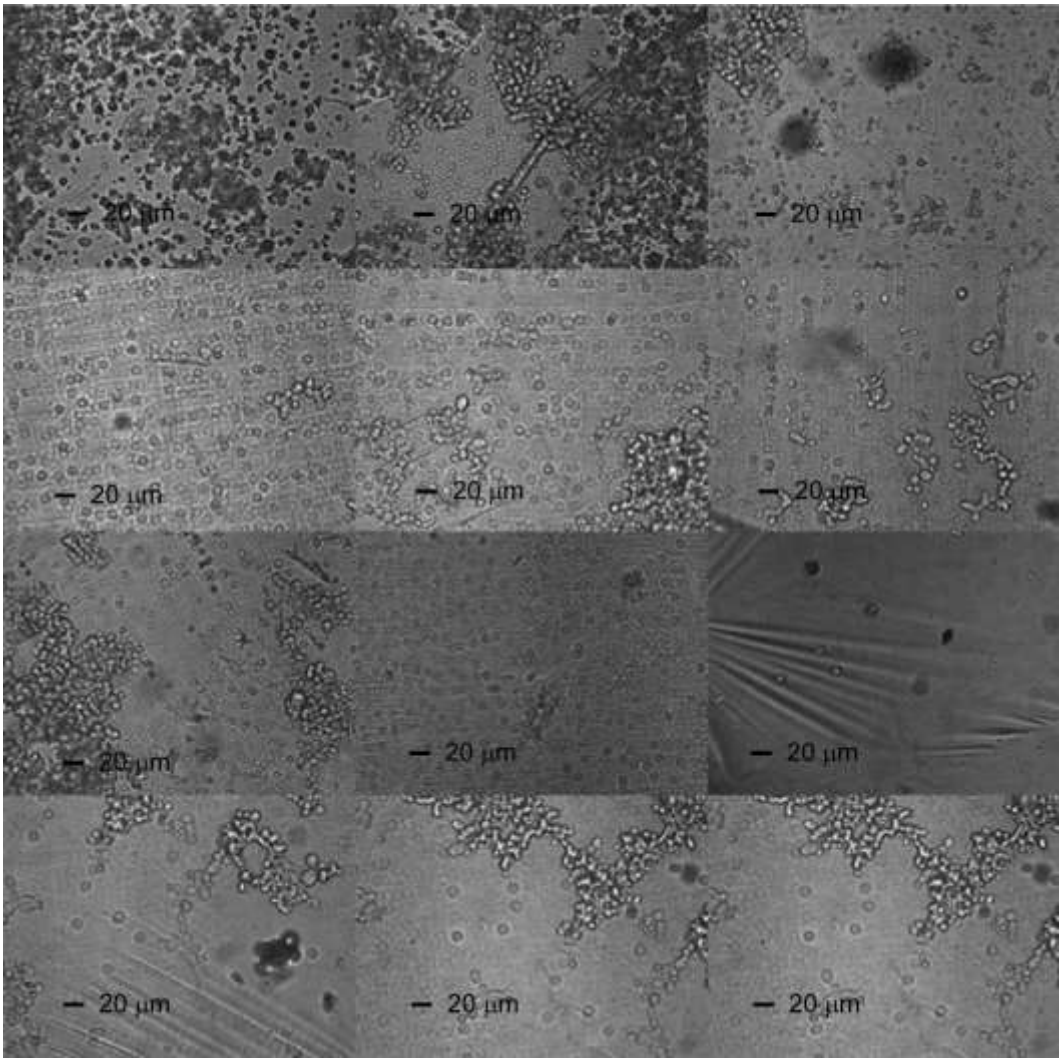

HEK293f cells after 8 hours of incubation on the ultra-thin membrane

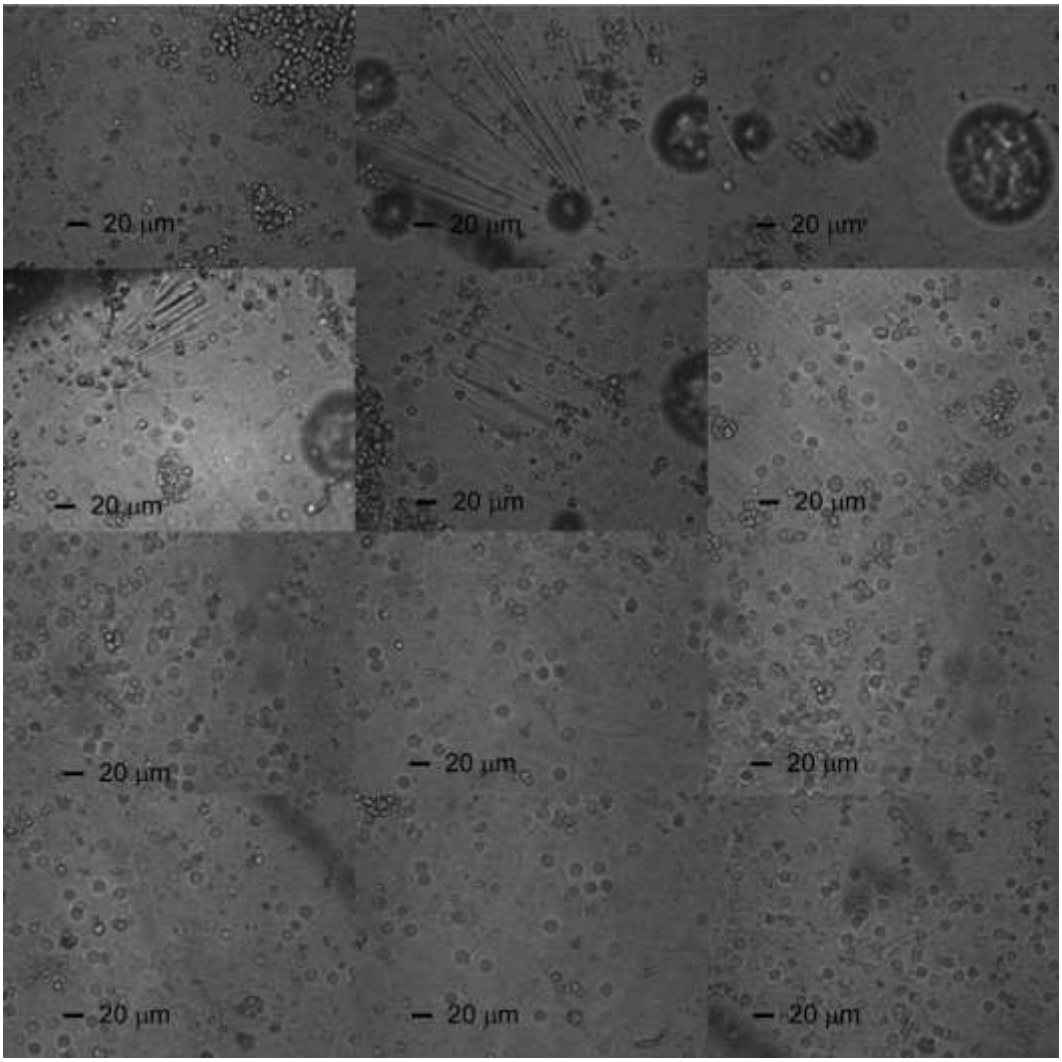

HEK293f cells after 8 hours of incubation on the ultra-thin membrane

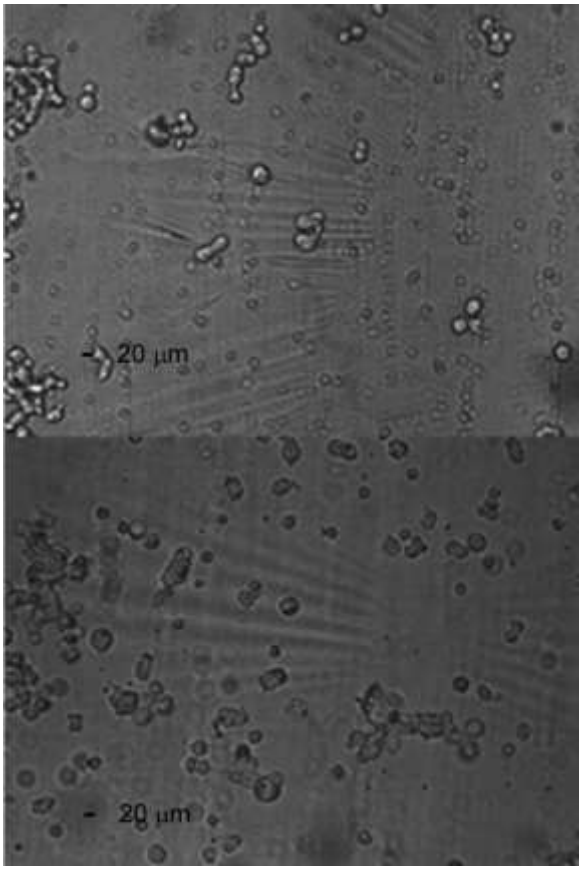

HEK293f cells after 8 hours of incubation on the ultra-thin membrane

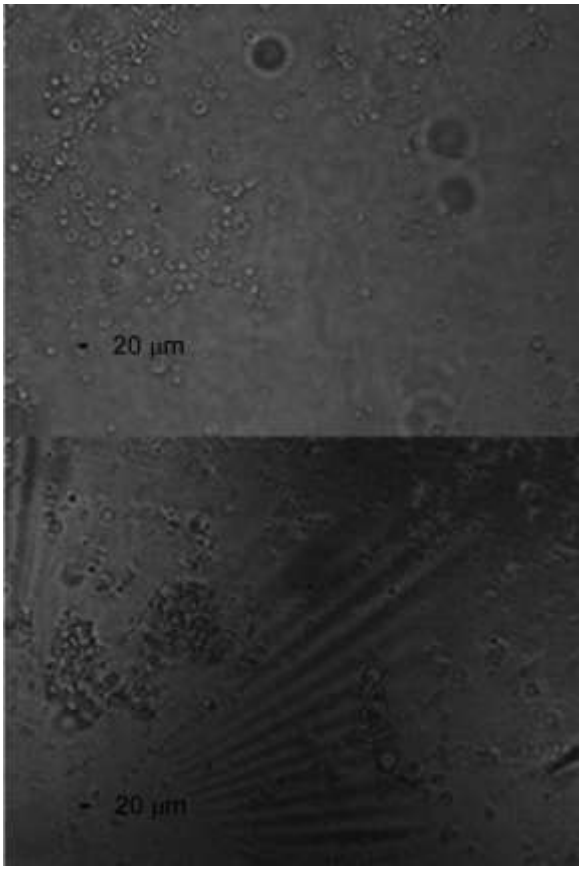

Buffy coat cells after 8 hours of incubation on the ultra-thin membrane

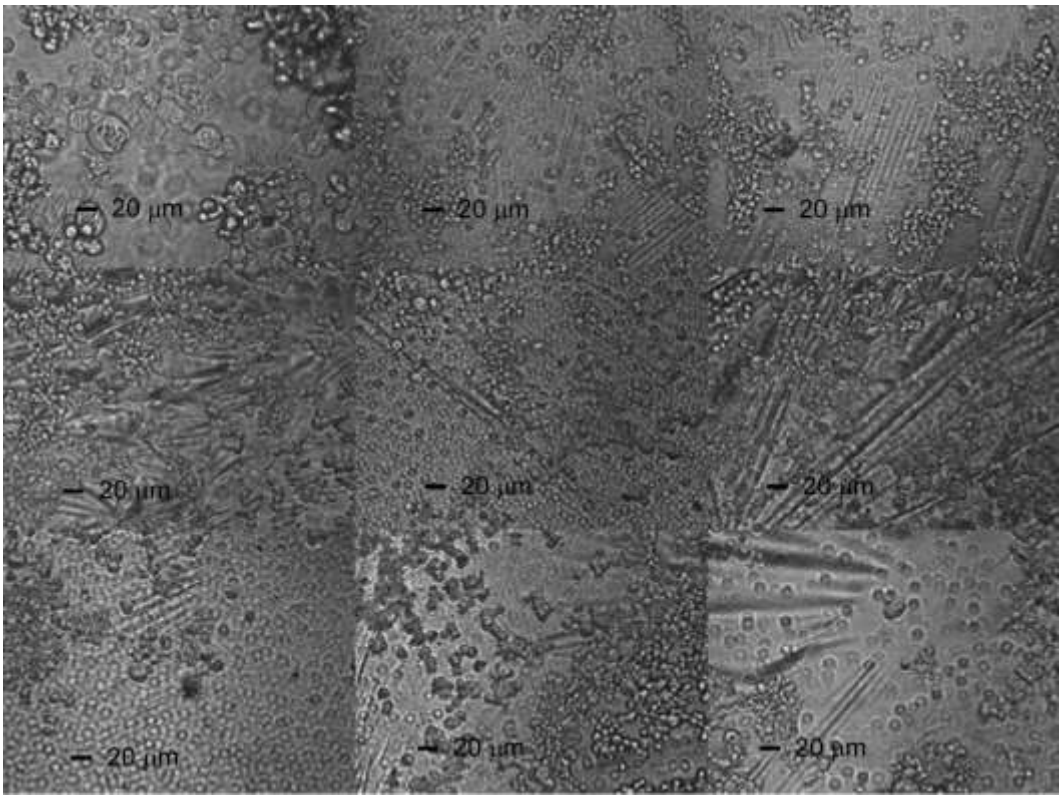

1:1 ratio of RT4 cells to HEK293f cells after 8 hours of incubation on the ultra-thin membrane

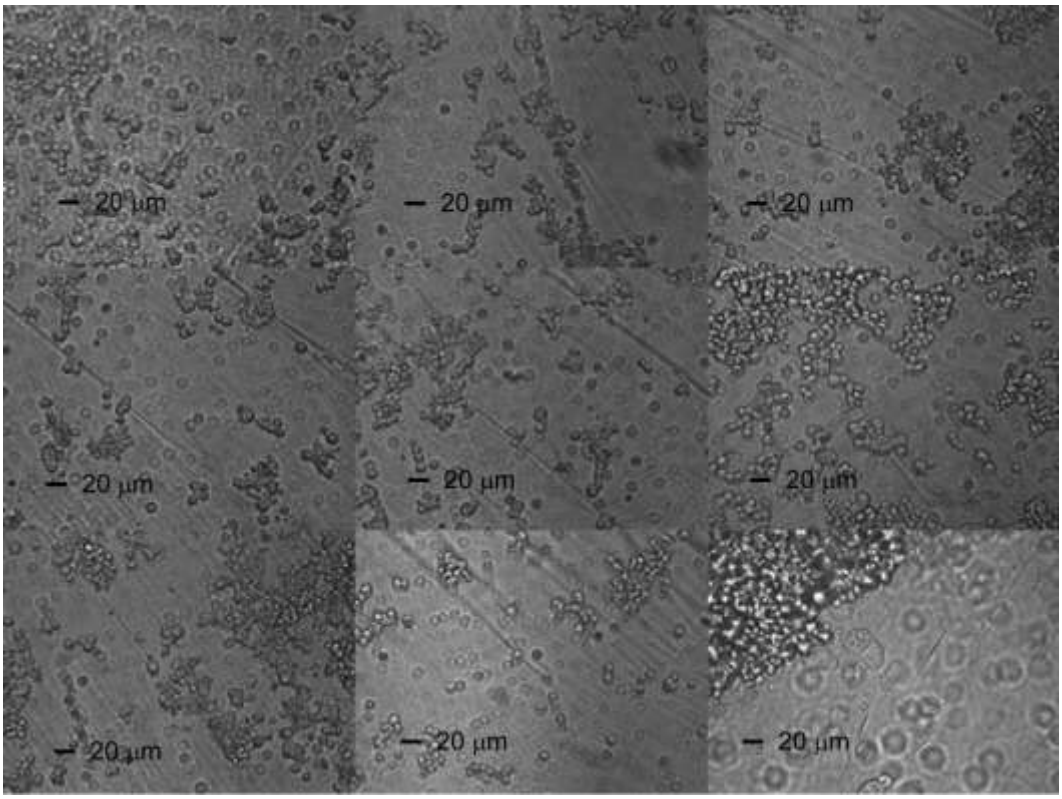

1:1 ratio of RT4 cells to HEK293f cells after 8 hours of incubation on the ultra-thin membrane

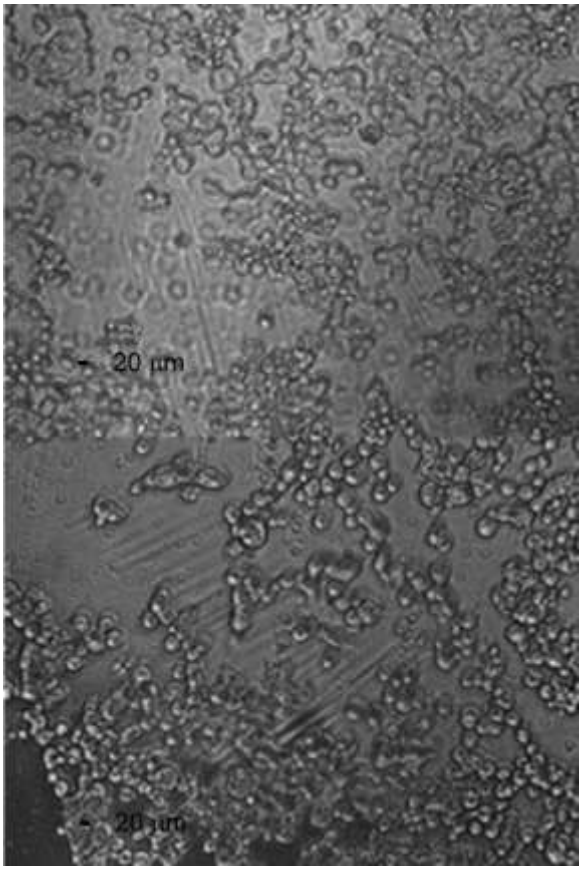

1:1 ratio of RT4 cells to HEK293f cells after 8 hours of incubation on the ultra-thin membrane

APPENDIX G

CELLOMICS MEMBRANE 24 HOUR INCUBATION WITH VARIOUS CELL TYPE AND MIXED CELLS

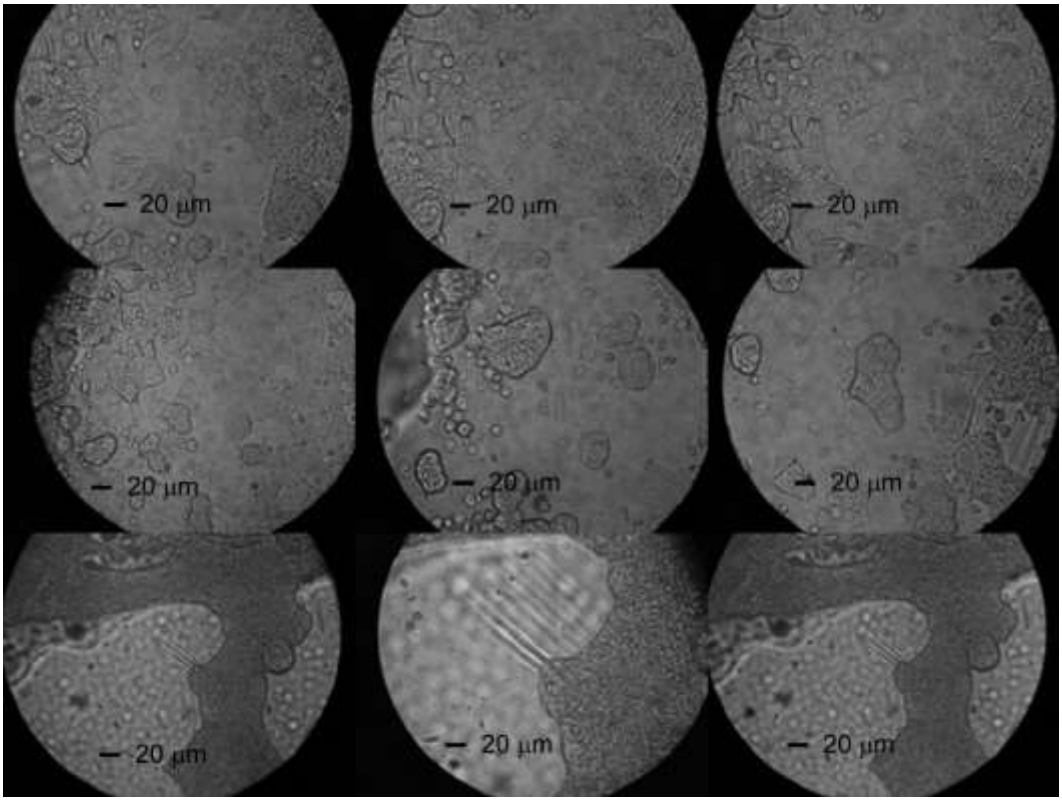

RT4 cells after 24 hours of incubation on the ultra-thin membrane

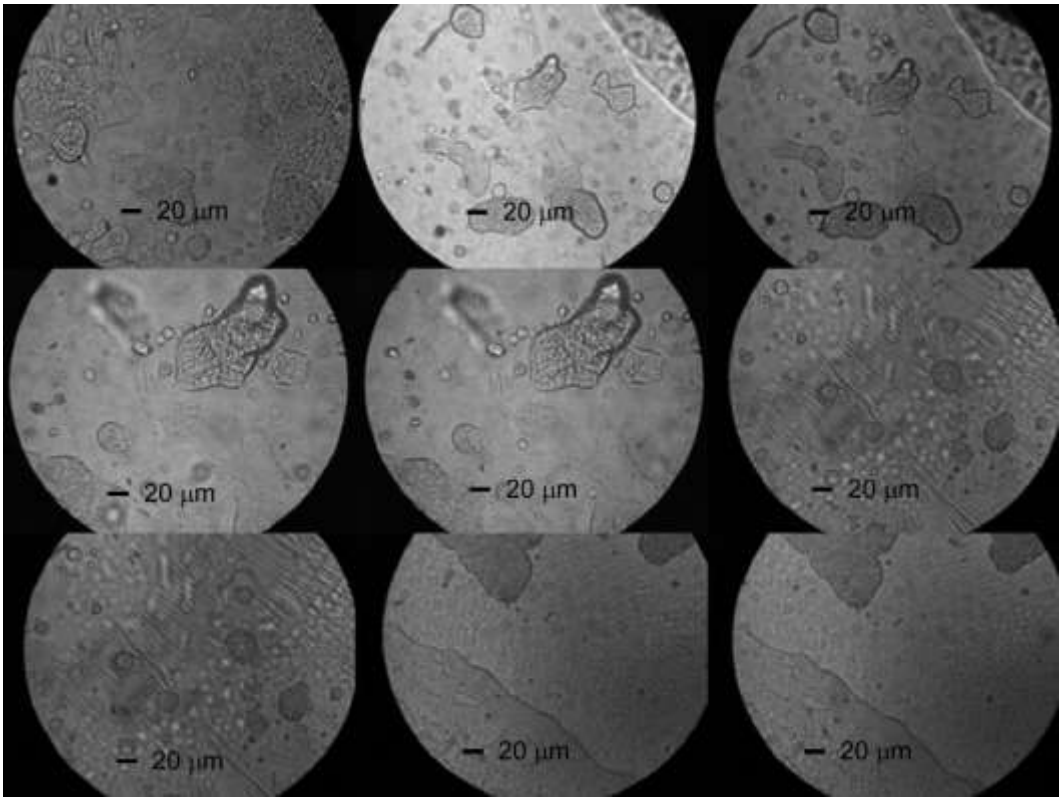

RT4 cells after 24 hours of incubation on the ultra-thin membrane

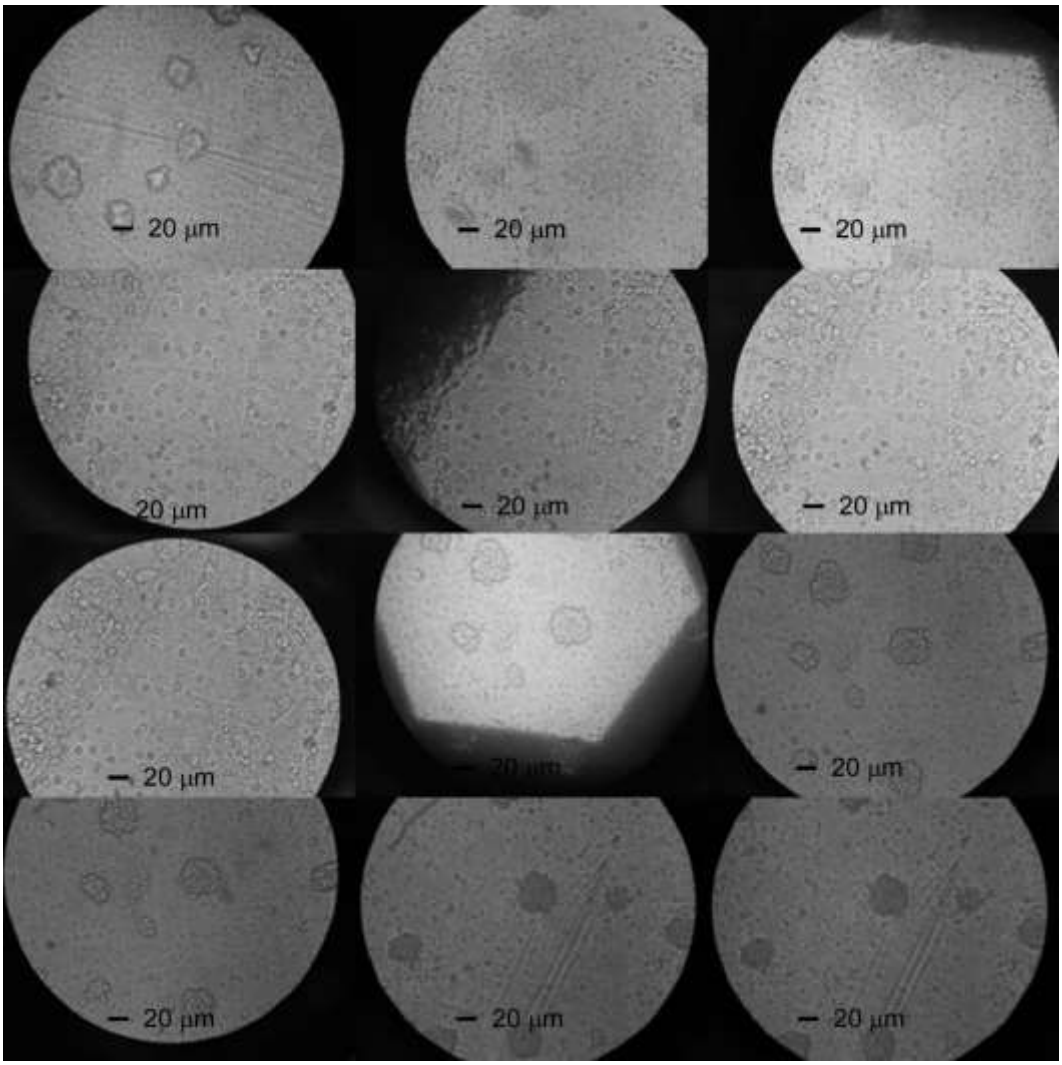

T24 cells after 24 hours of incubation on the ultra-thin membrane

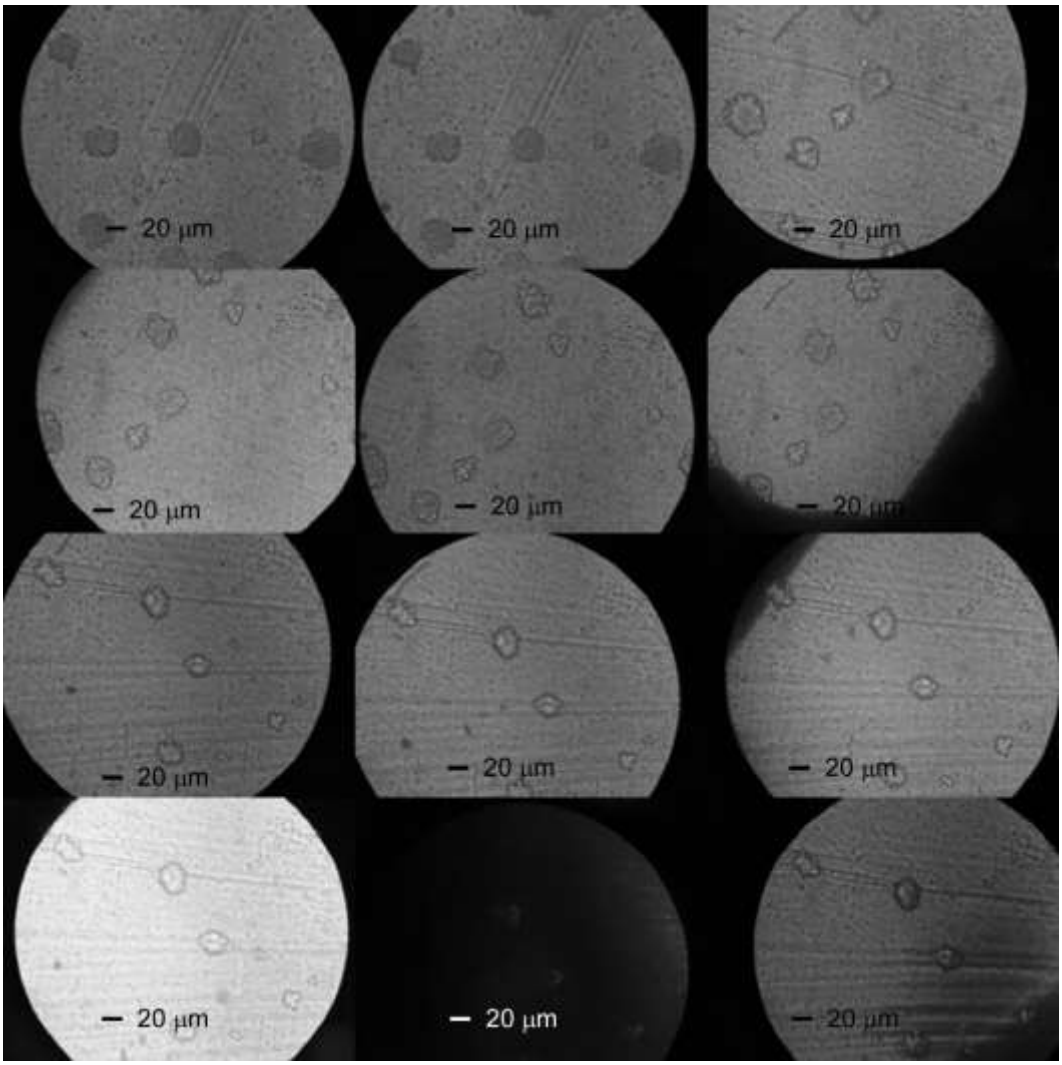

T24 cells after 24 hours of incubation on the ultra-thin membrane

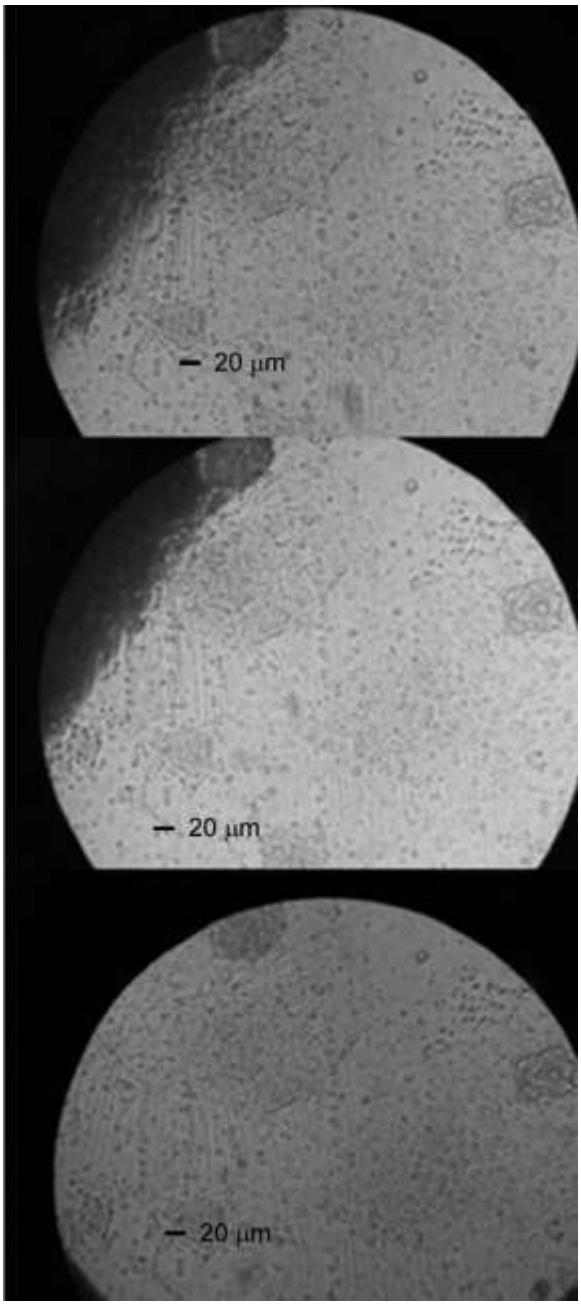

T24 cells after 24 hours of incubation on the ultra-thin membrane

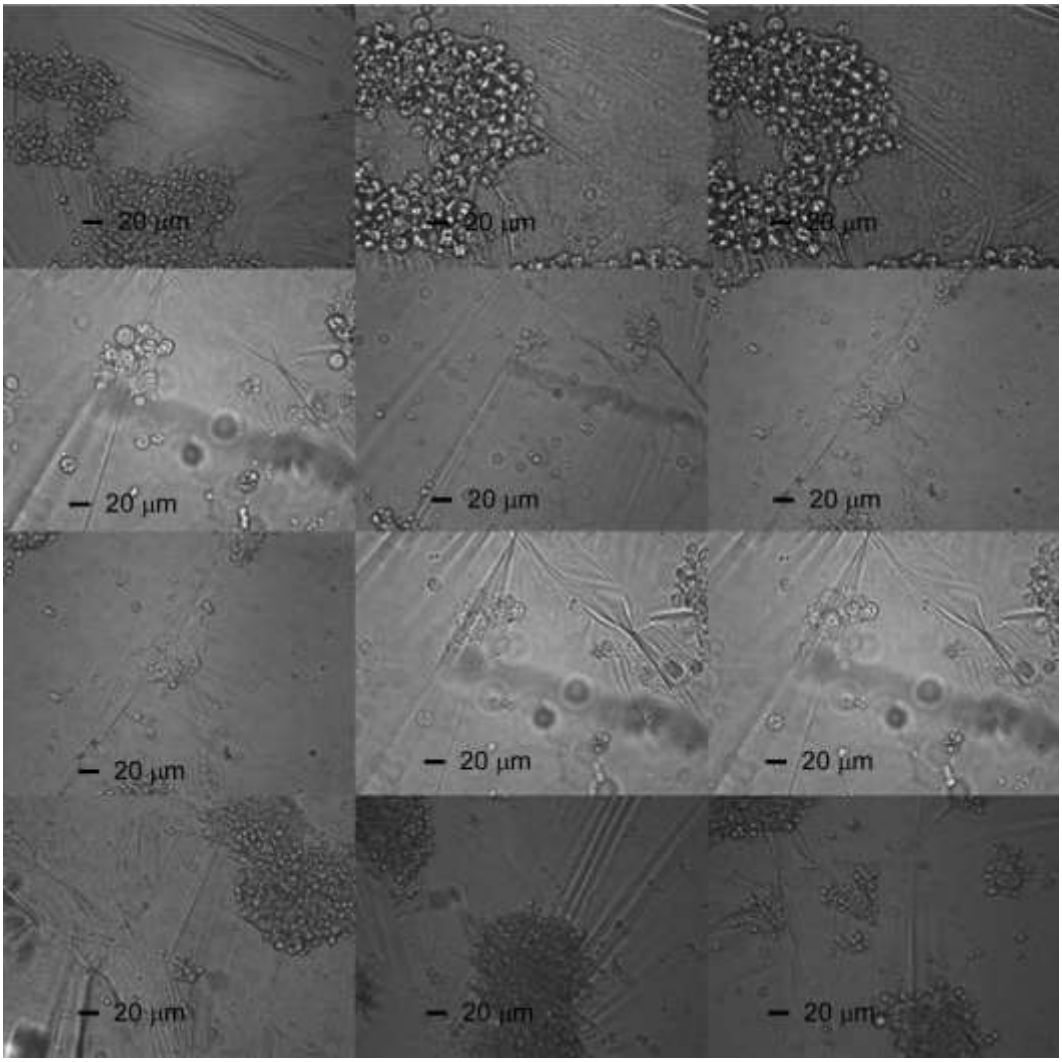

HEK293f cells after 24 hours of incubation on the ultra-thin membrane

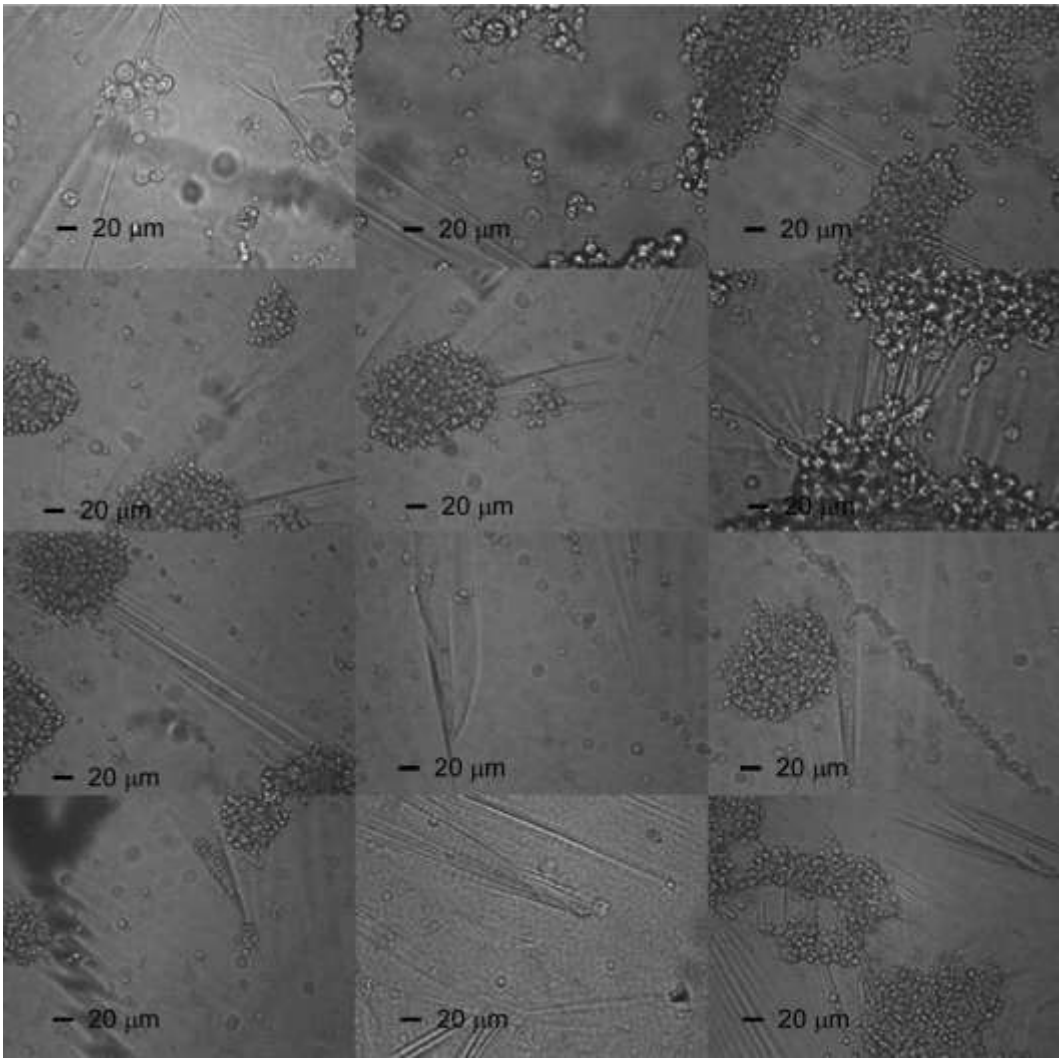

HEK293f cells after 24 hours of incubation on the ultra-thin membrane

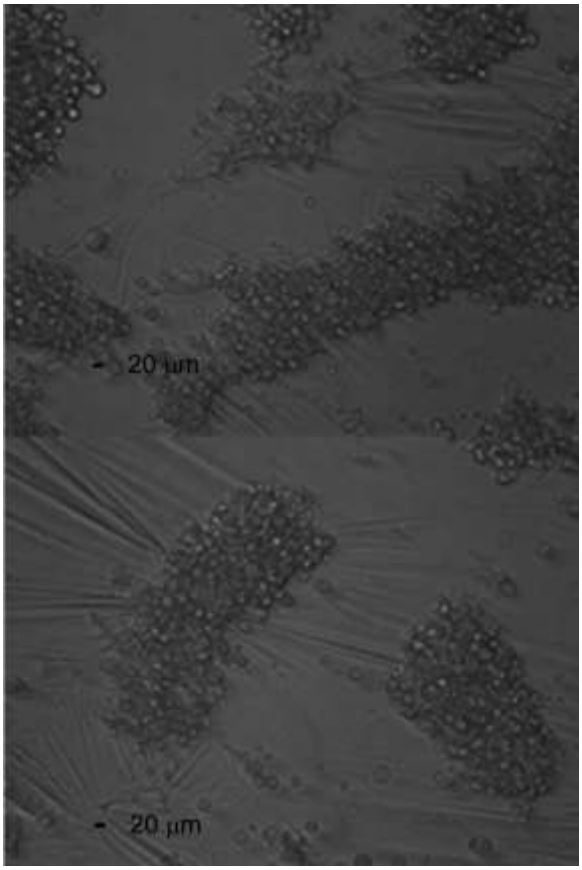

HEK293f cells after 24 hours of incubation on the ultra-thin membrane

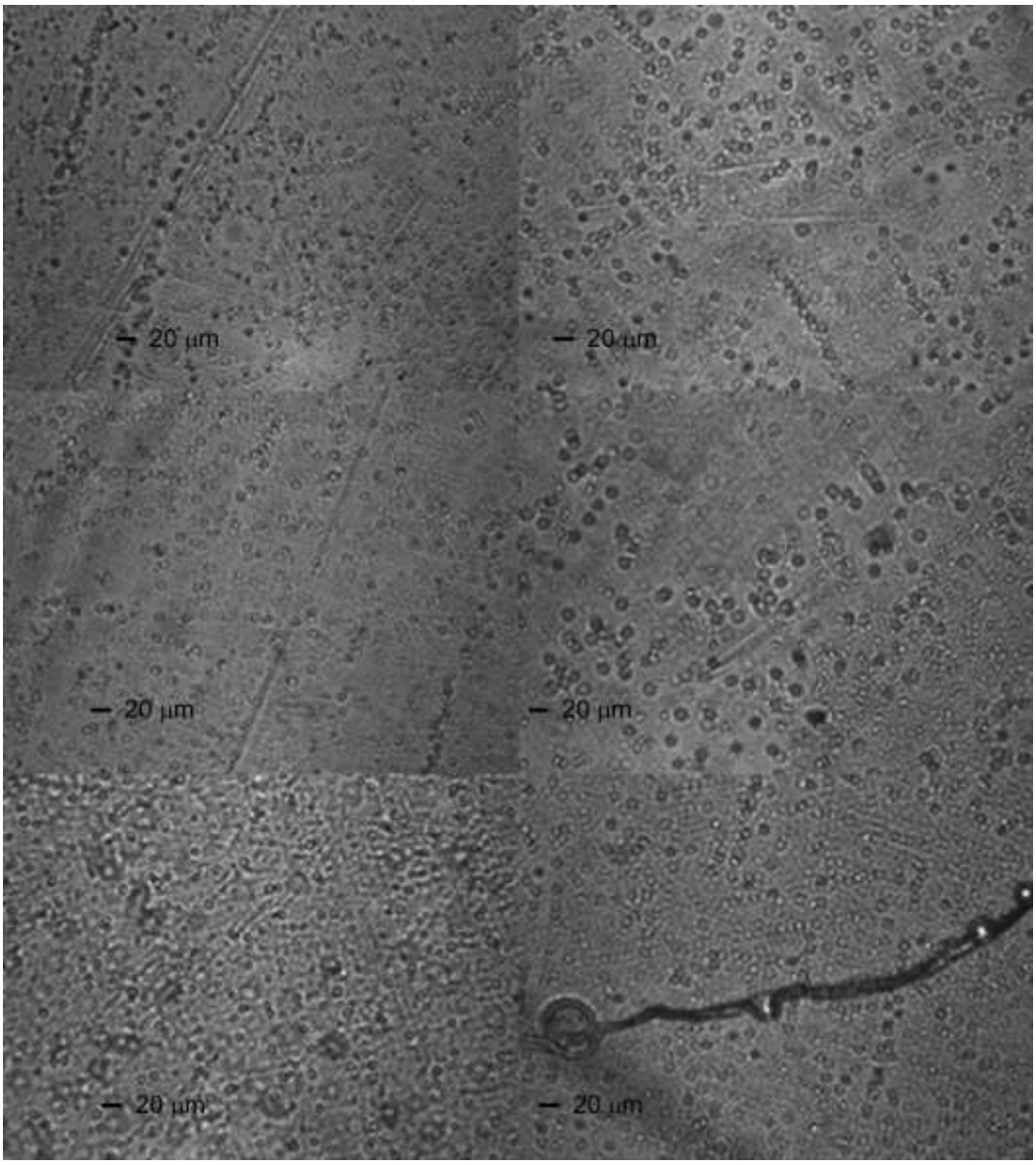

Buffy coat cells after 24 hours of incubation on the ultra-thin membrane

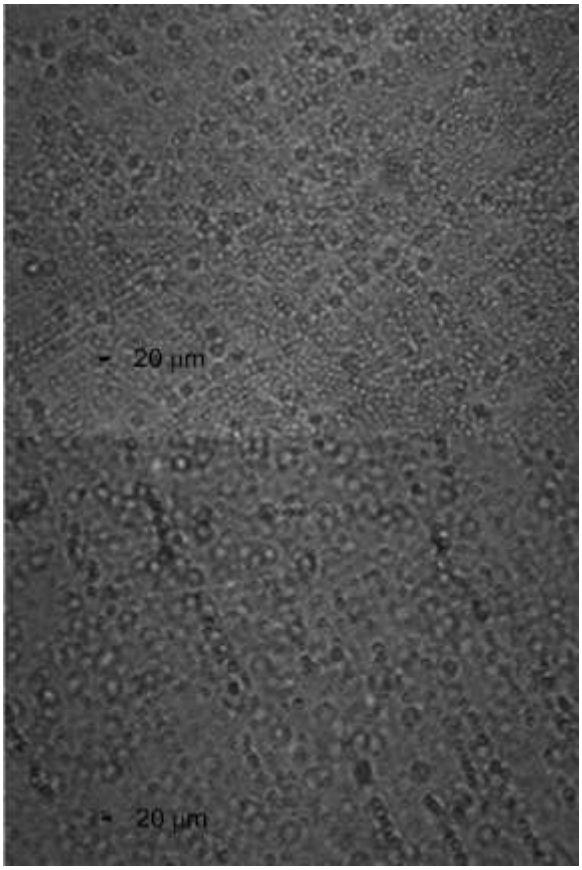

Buffy coat cells after 24 hours of incubation on the ultra-thin membrane

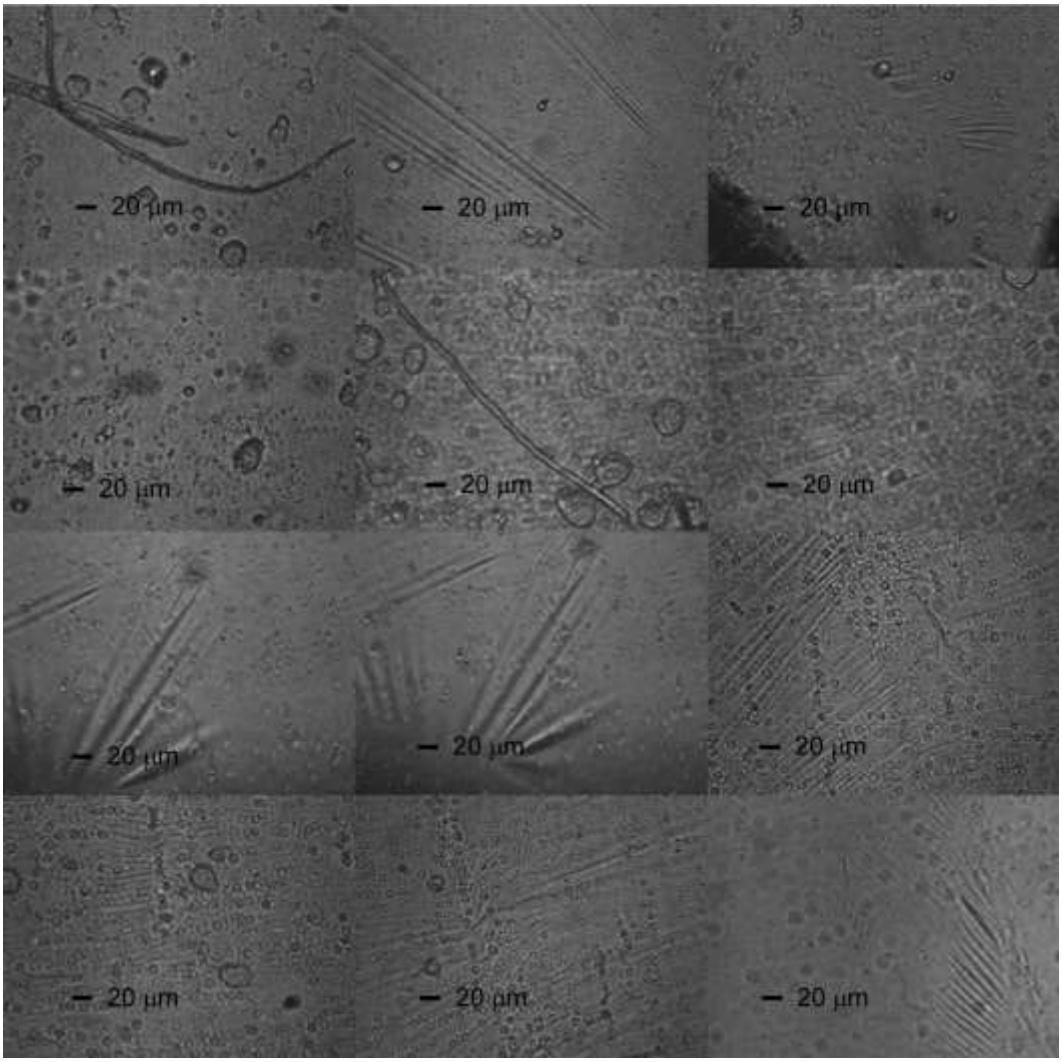

1:1 ratio of RT4 cells to HEK293f cells after 24 hours of incubation on the ultra-thin membrane

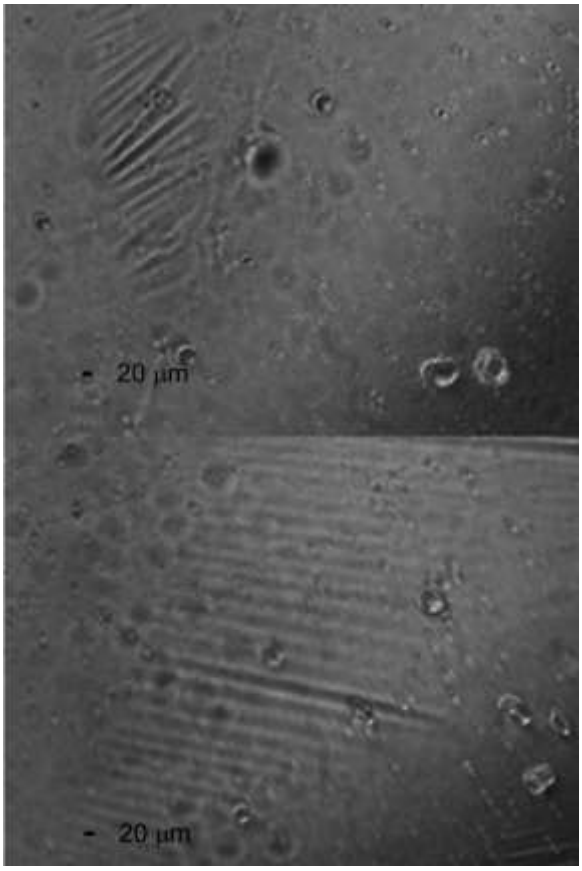

1:1 ratio of RT4 cells to HEK293f cells after 24 hours of incubation on the ultra-thin membrane

APPENDIX H

CELLOMICS MEMBRANE COMPARING CELL TRANSFER METHODS AFTER 4 HOURS INCUBATION

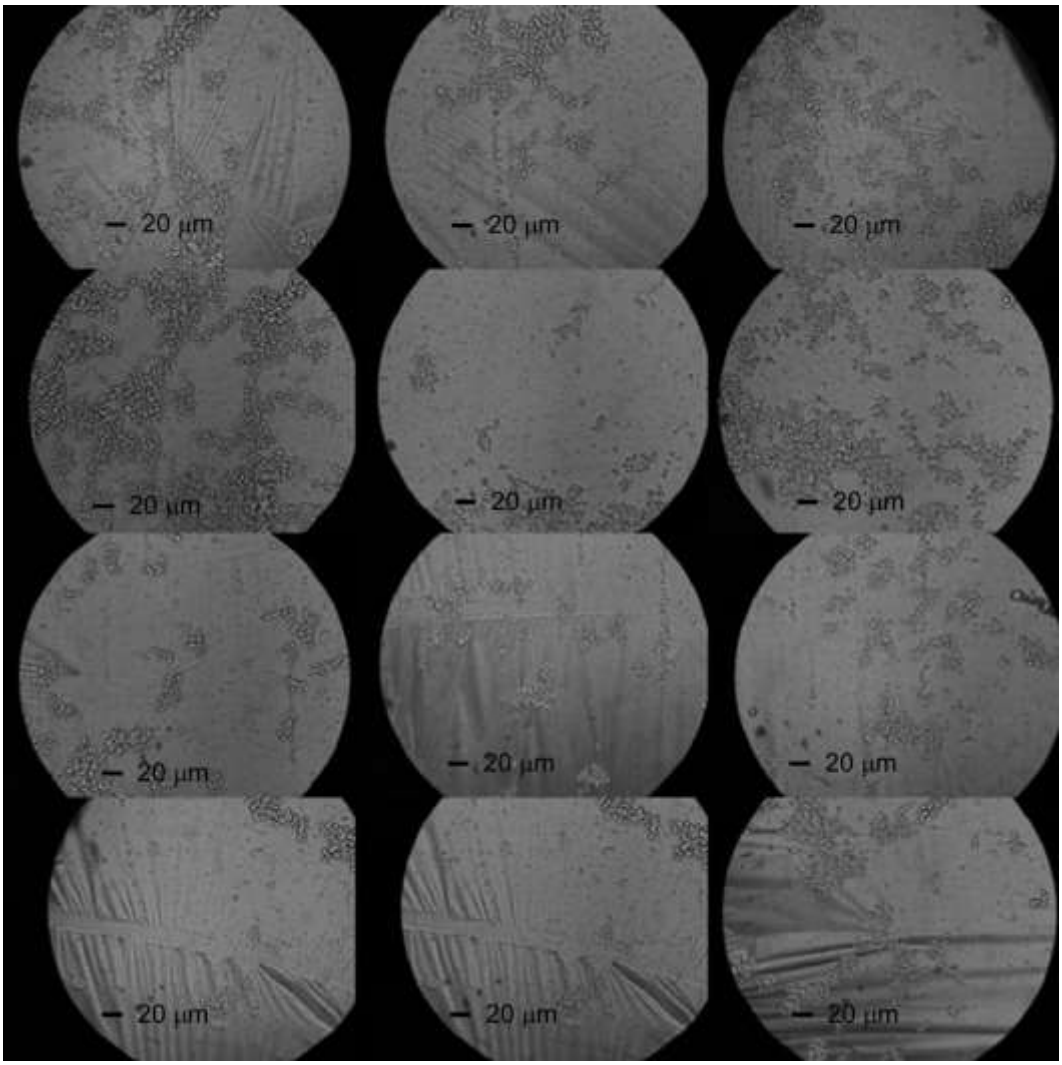

T24 cells transferred using trypsin and incubated for 4 hours on the ultra-thin membrane

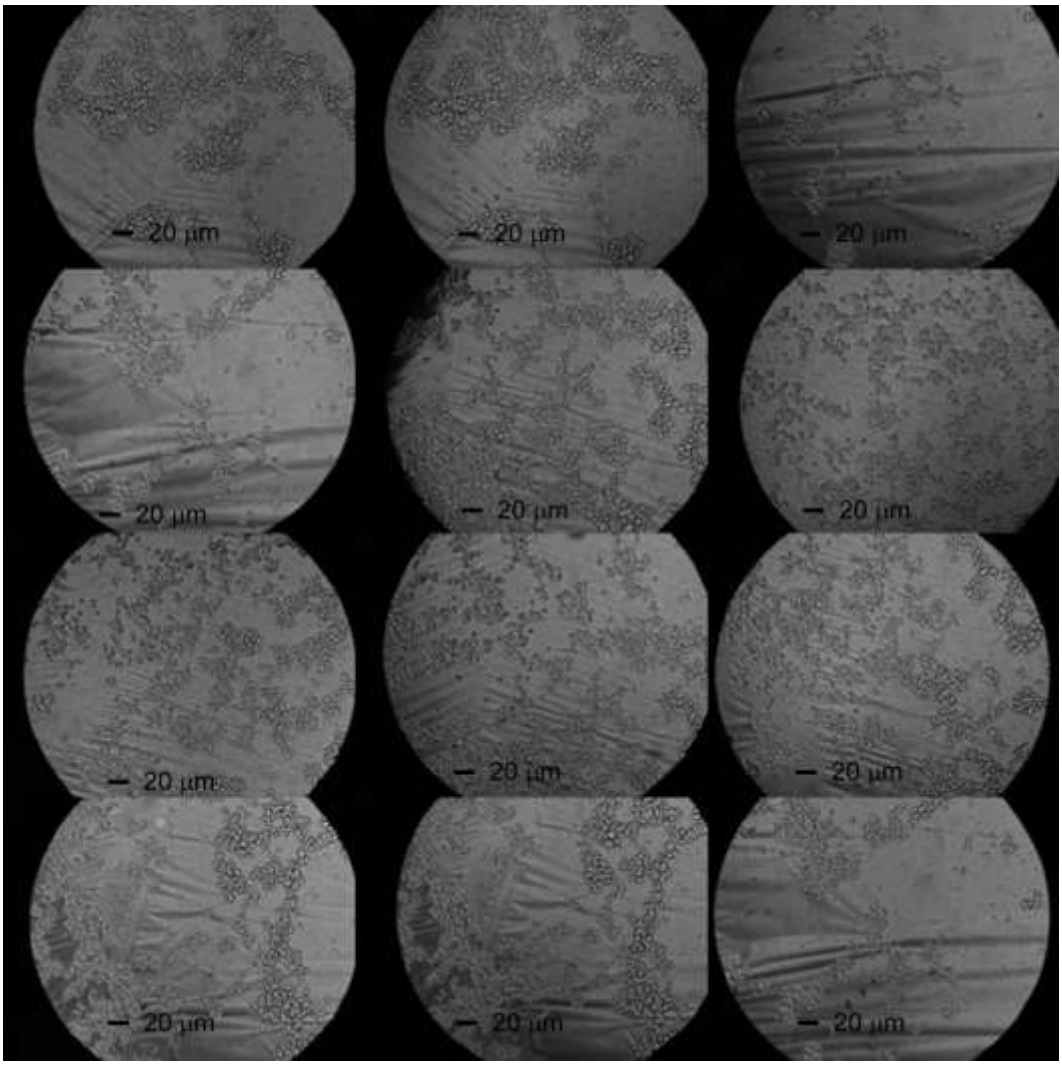

T24 cells transferred using trypsin and incubated for 4 hours on the ultra-thin membrane

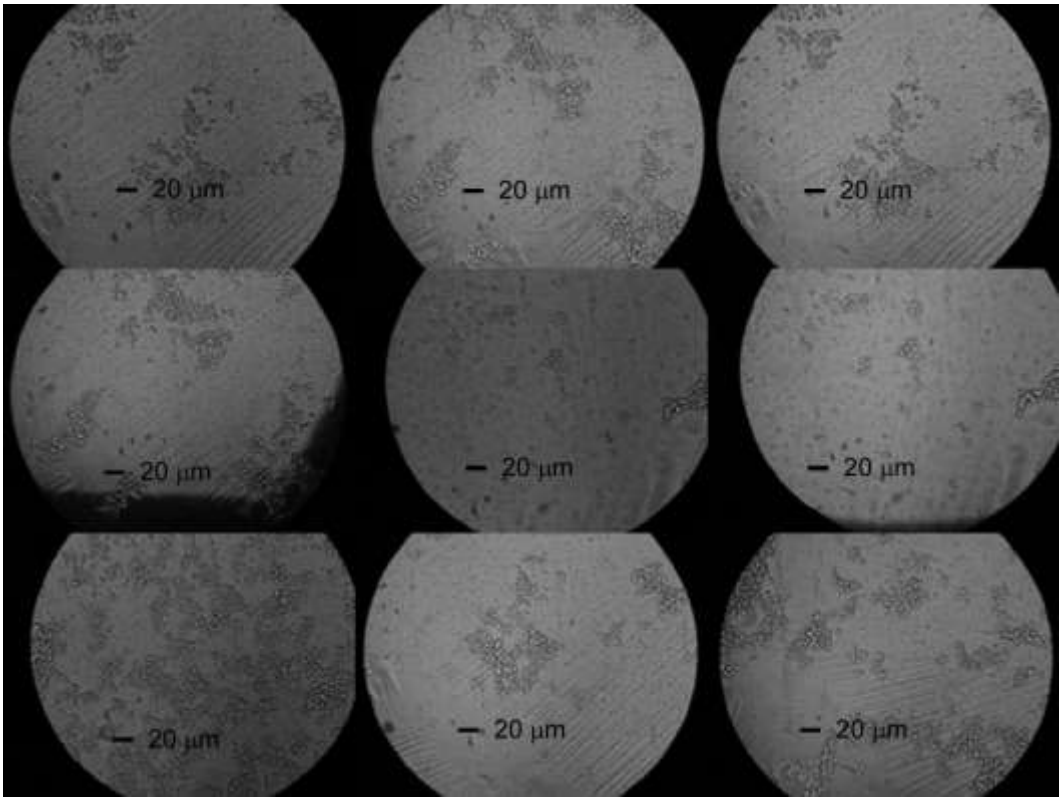

T24 cells transferred using trypsin and incubated for 4 hours on the ultra-thin membrane

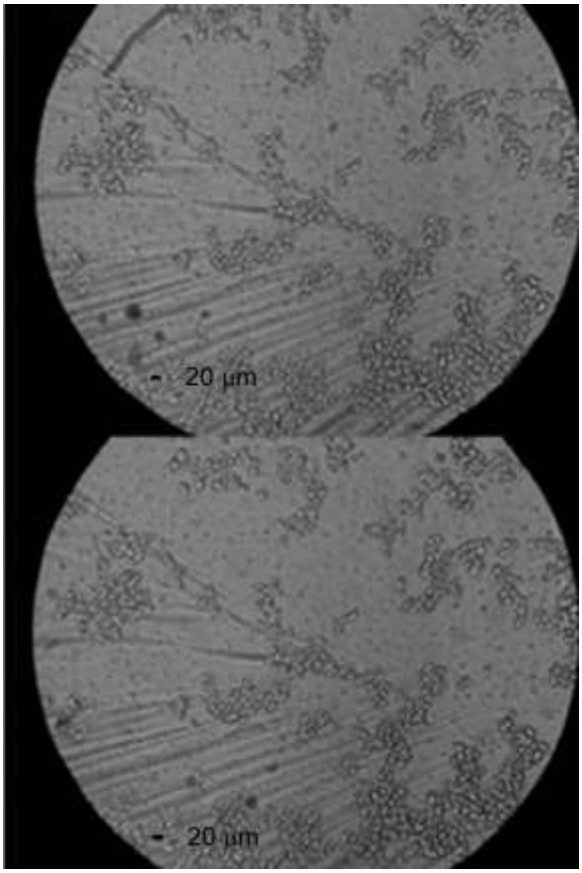

T24 cells transferred using trypsin and incubated for 4 hours on the ultra-thin membrane

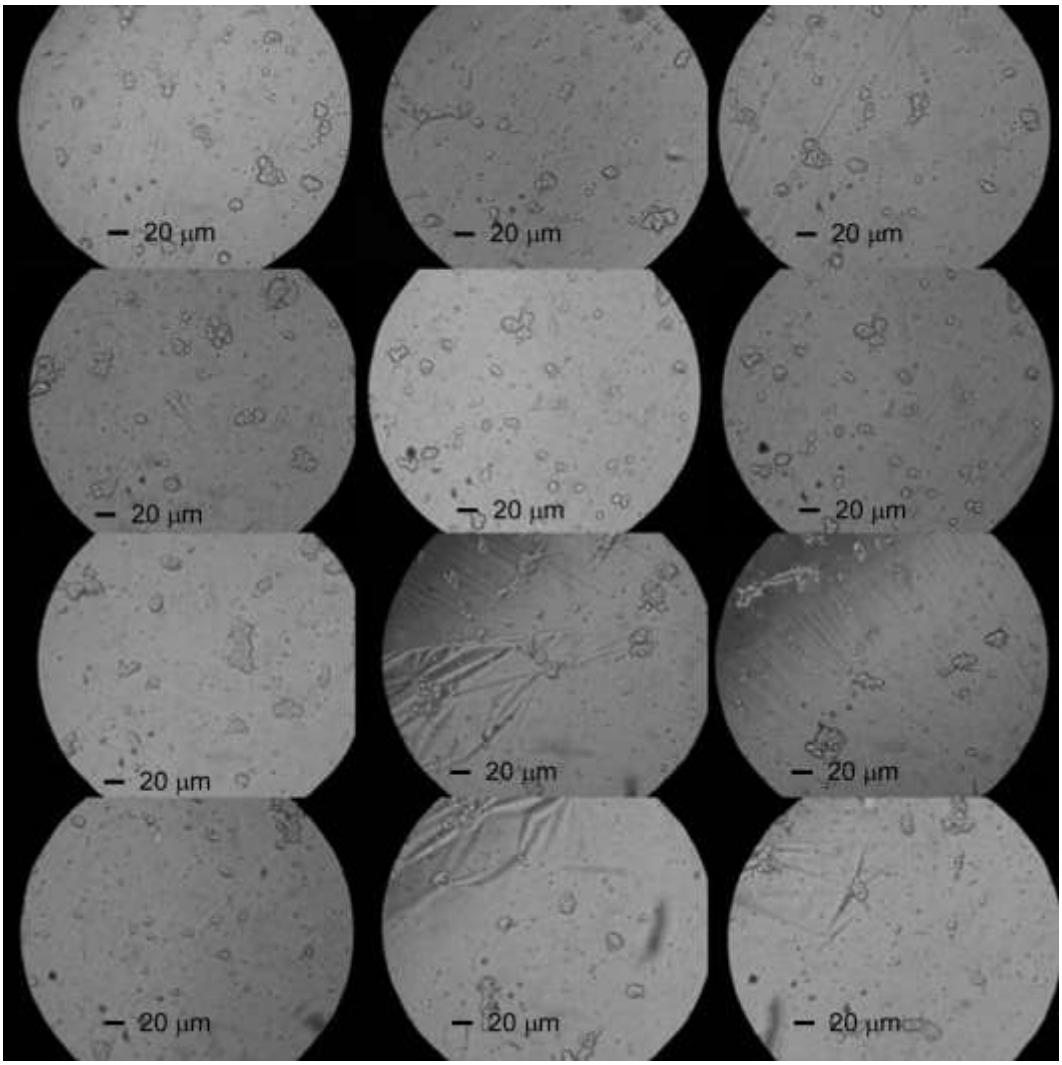

T24 cells transferred using cell dissociation buffer and incubated for 4 hours on the ultra-thin membrane

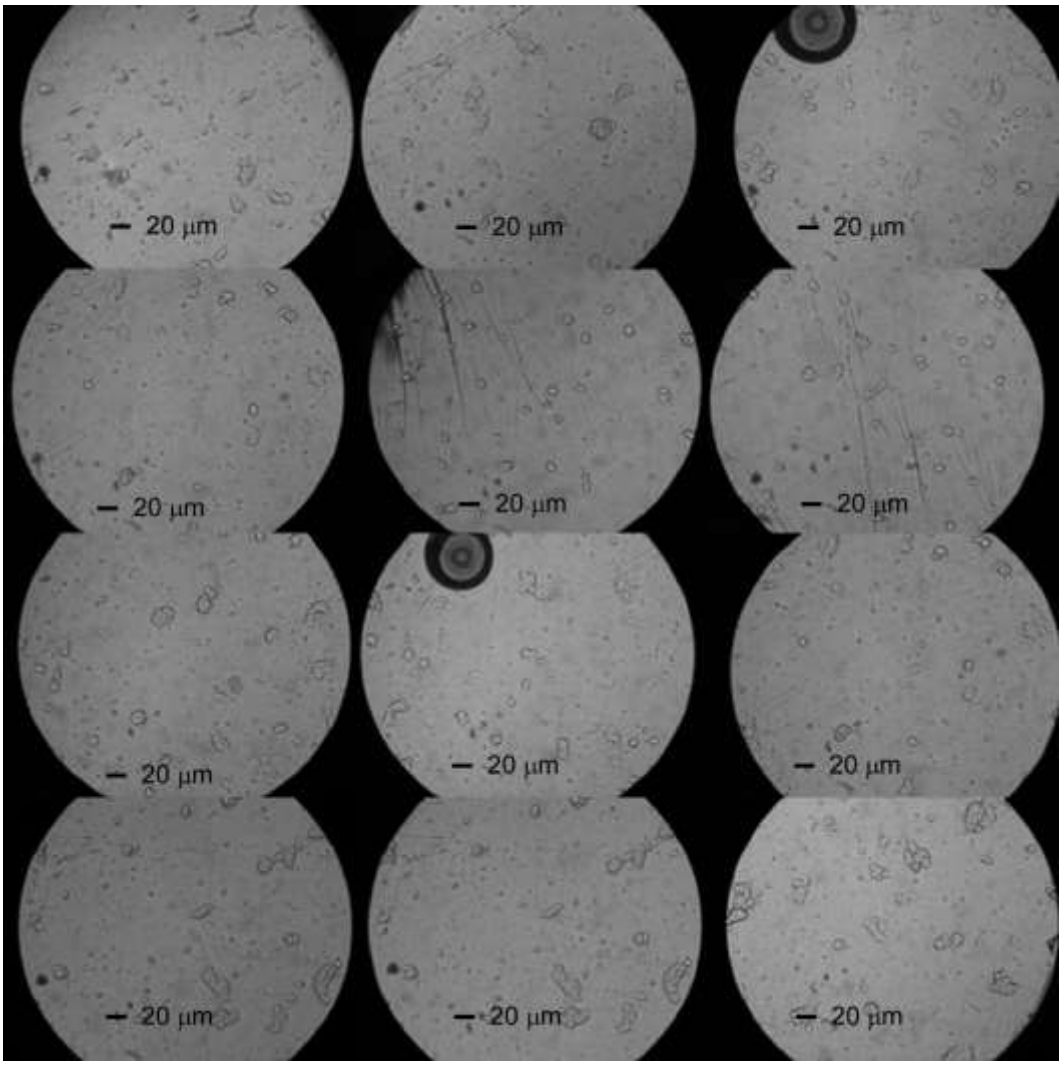

T24 cells transferred using cell dissociation buffer and incubated for 4 hours on the ultra-thin membrane

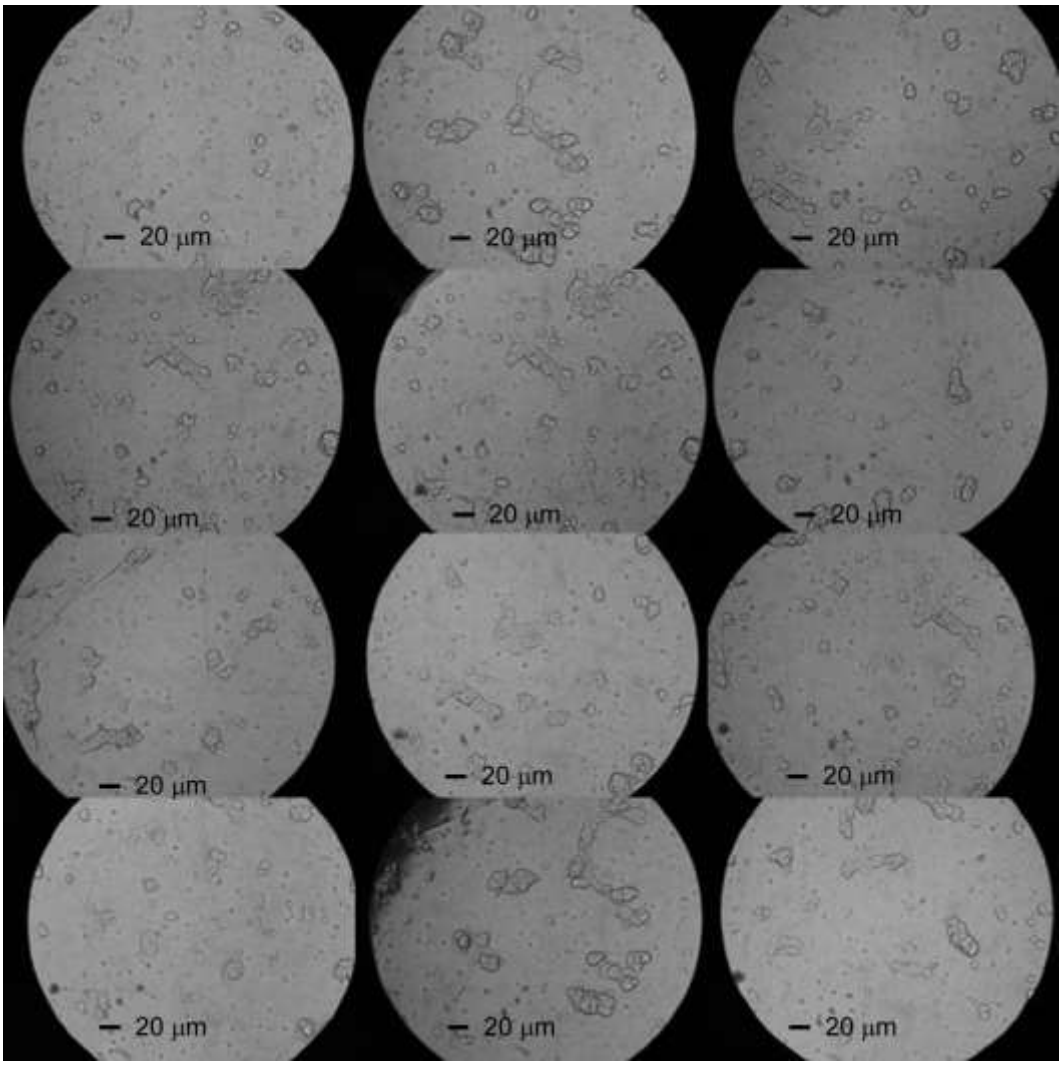

T24 cells transferred using cell dissociation buffer and incubated for 4 hours on the ultra-thin membrane

APPENDIX I

LIVE DEAD ASSAY OF 2D TRANSITION METAL DICHALCOGINIDES BIOCOMPATIBILITY

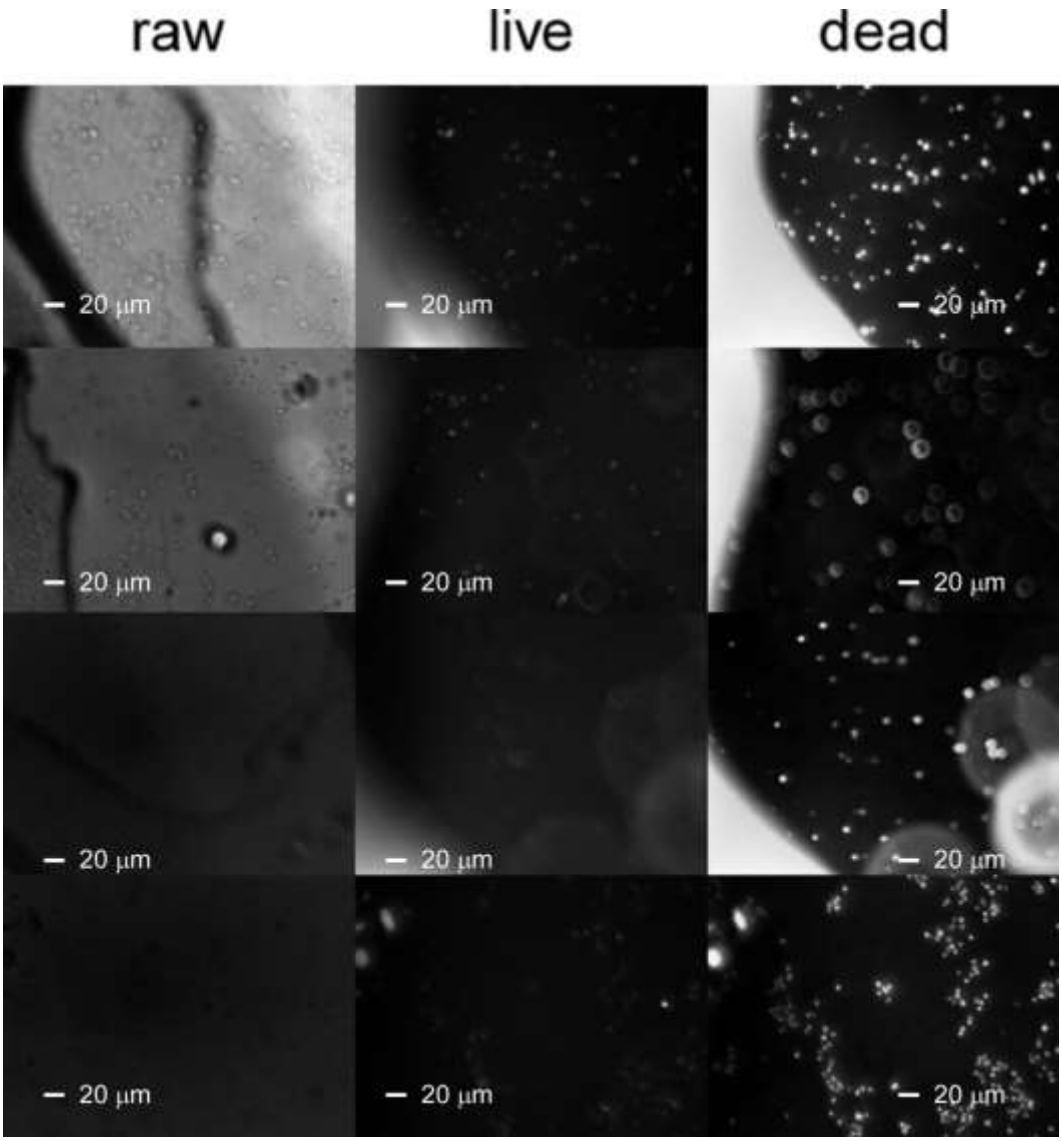

HEK293f cells exposed to epoxy for 48 hours and stained for cell viability

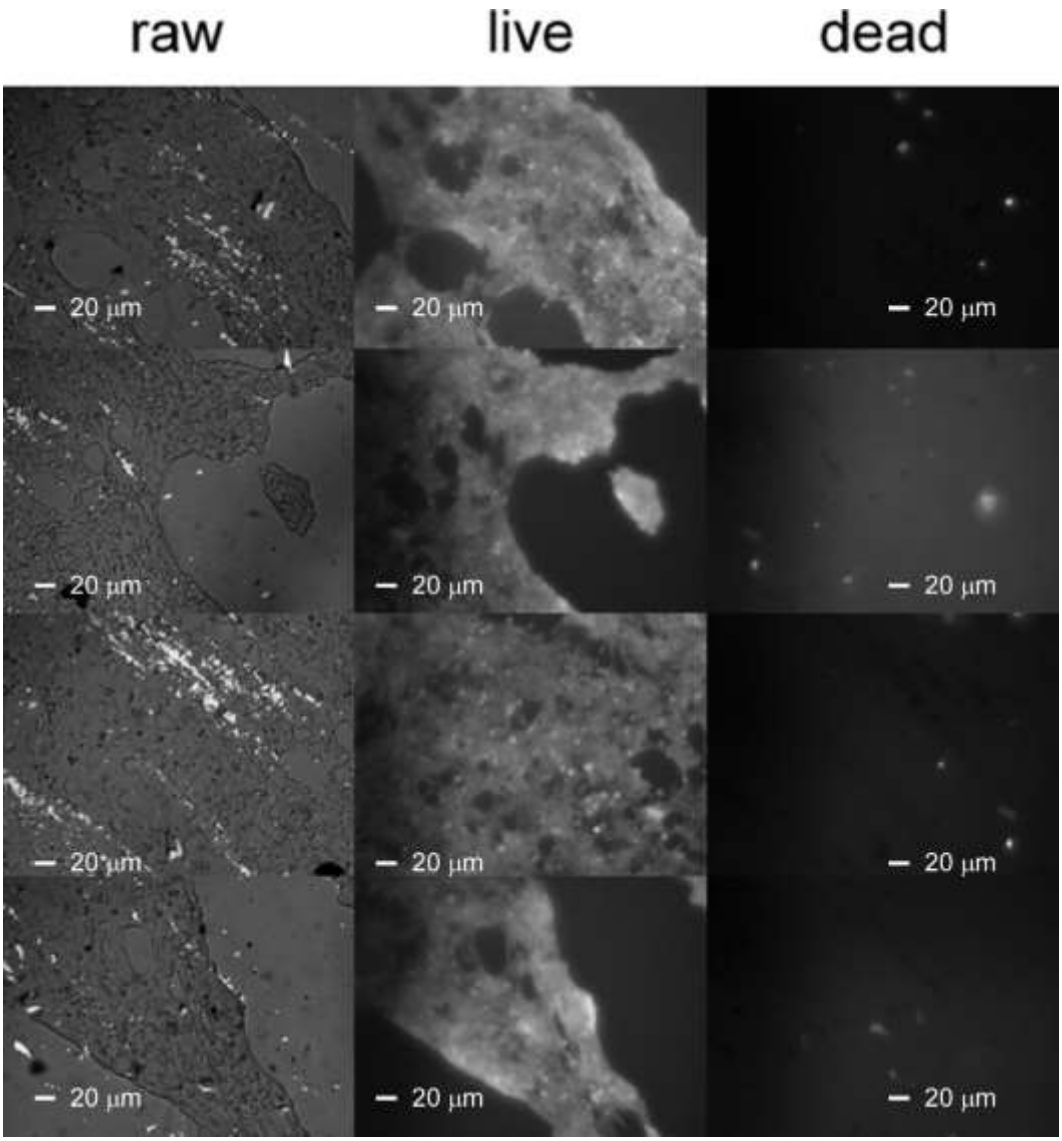

HEK293f cells exposed to gold for 48 hours and stained for cell viability

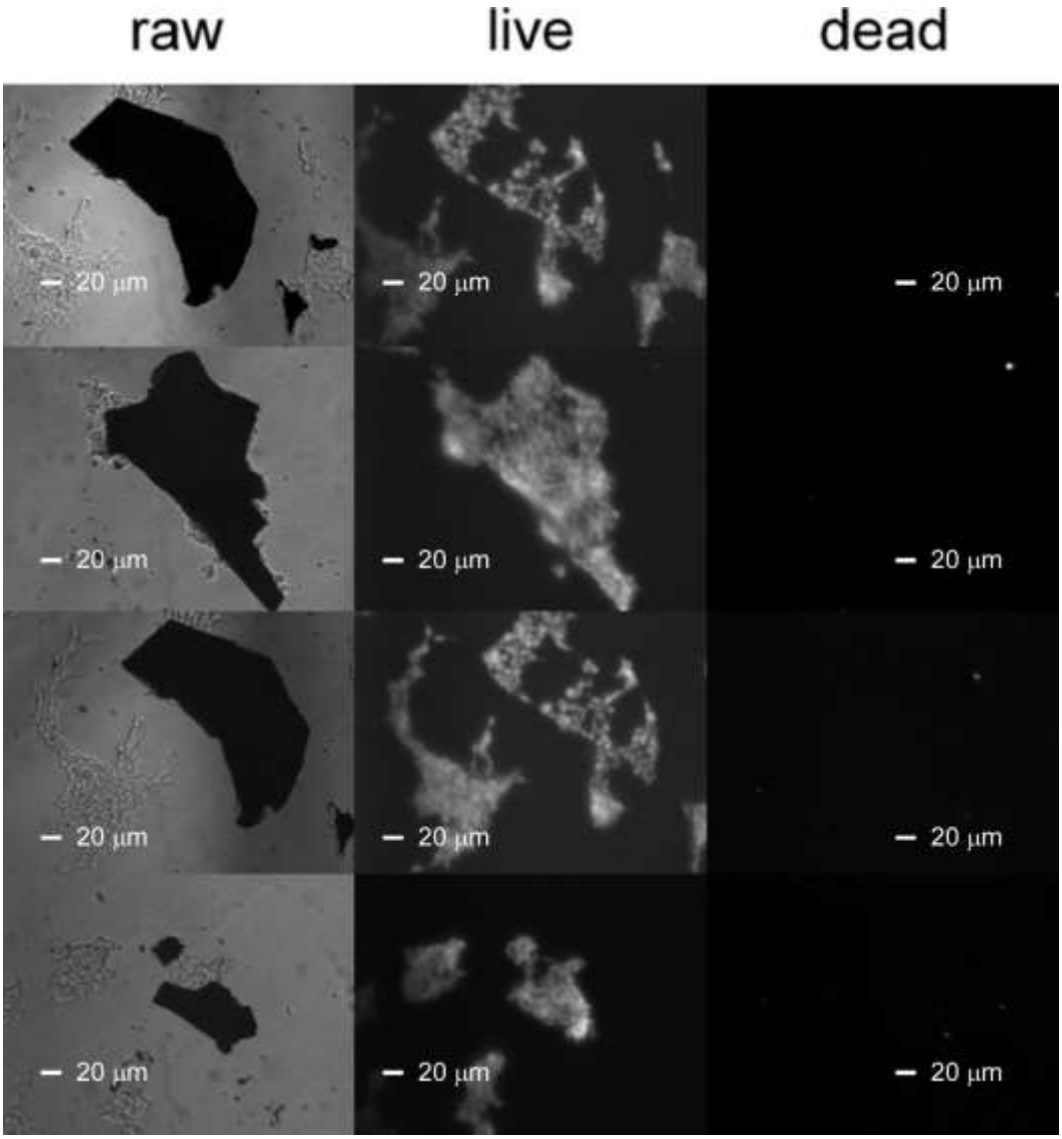

HEK293f cells exposed to graphite for 48 hours and stained for cell viability

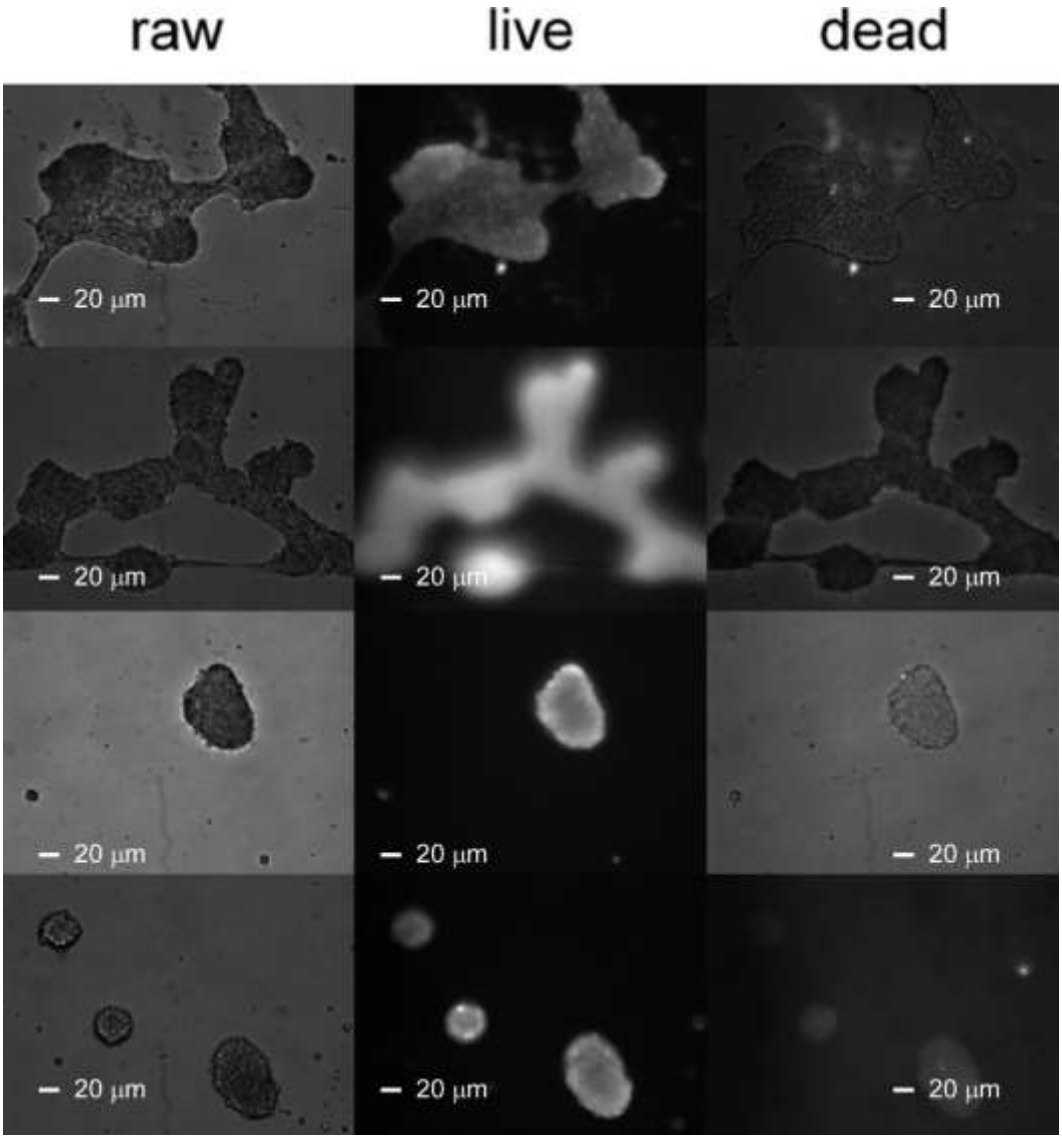

HEK293f cells exposed to PDMS for 48 hours and stained for cell viability

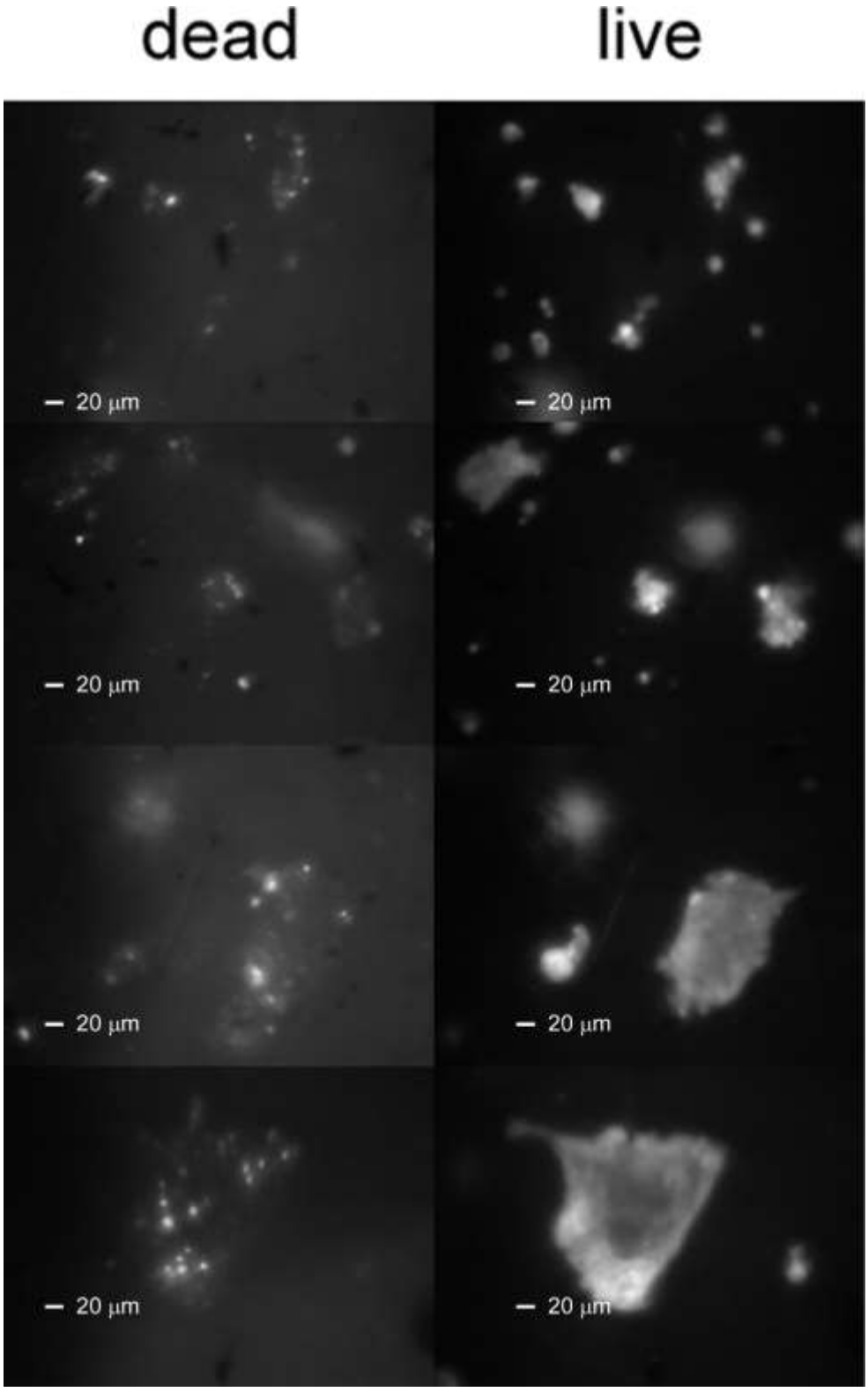

HEK293f cells exposed to silver for 48 hours and stained for cell viability

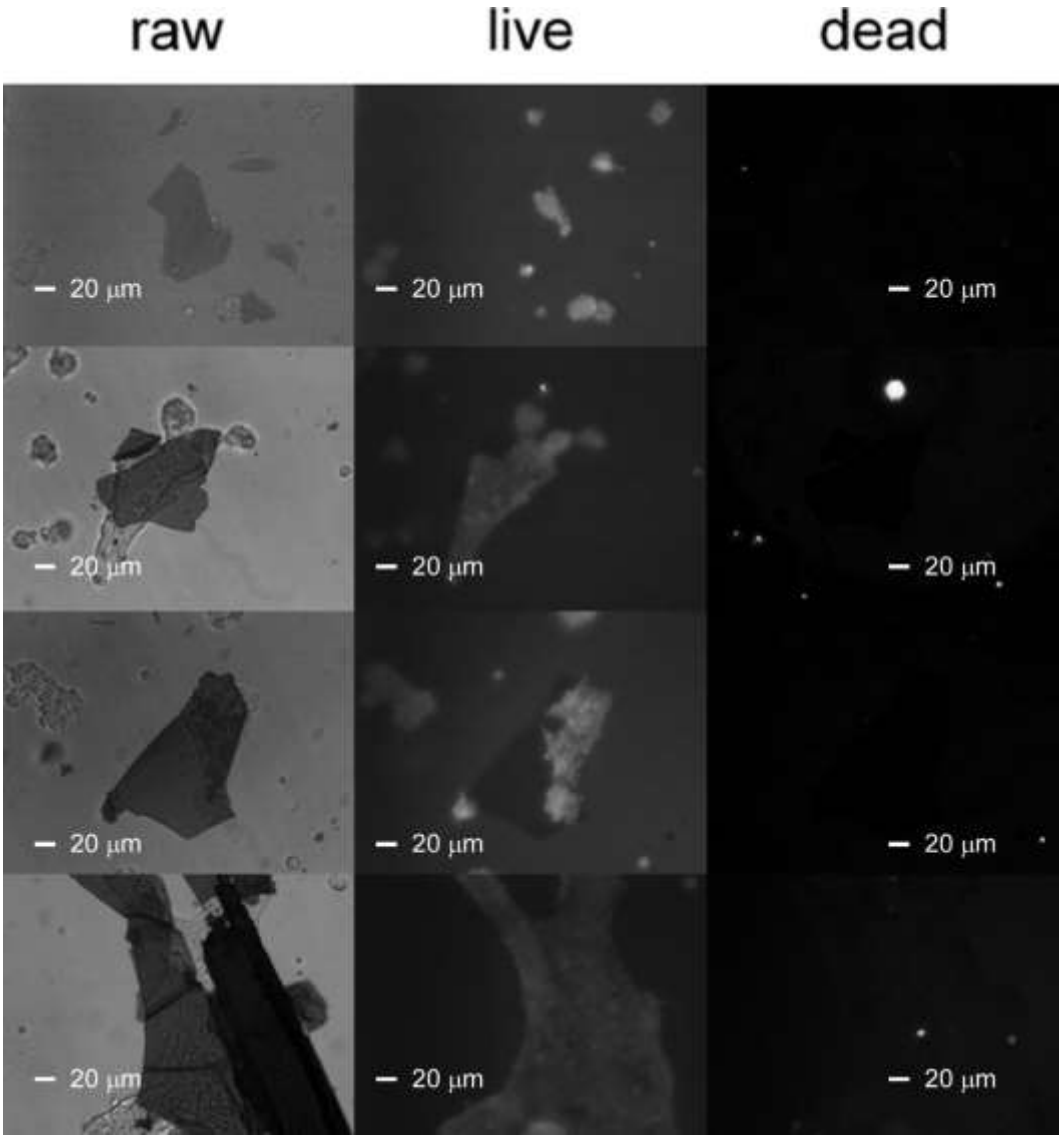

HEK293f cells exposed to mechanically exfoliated molybdenum disulfide for 48 hours and stained for cell viability

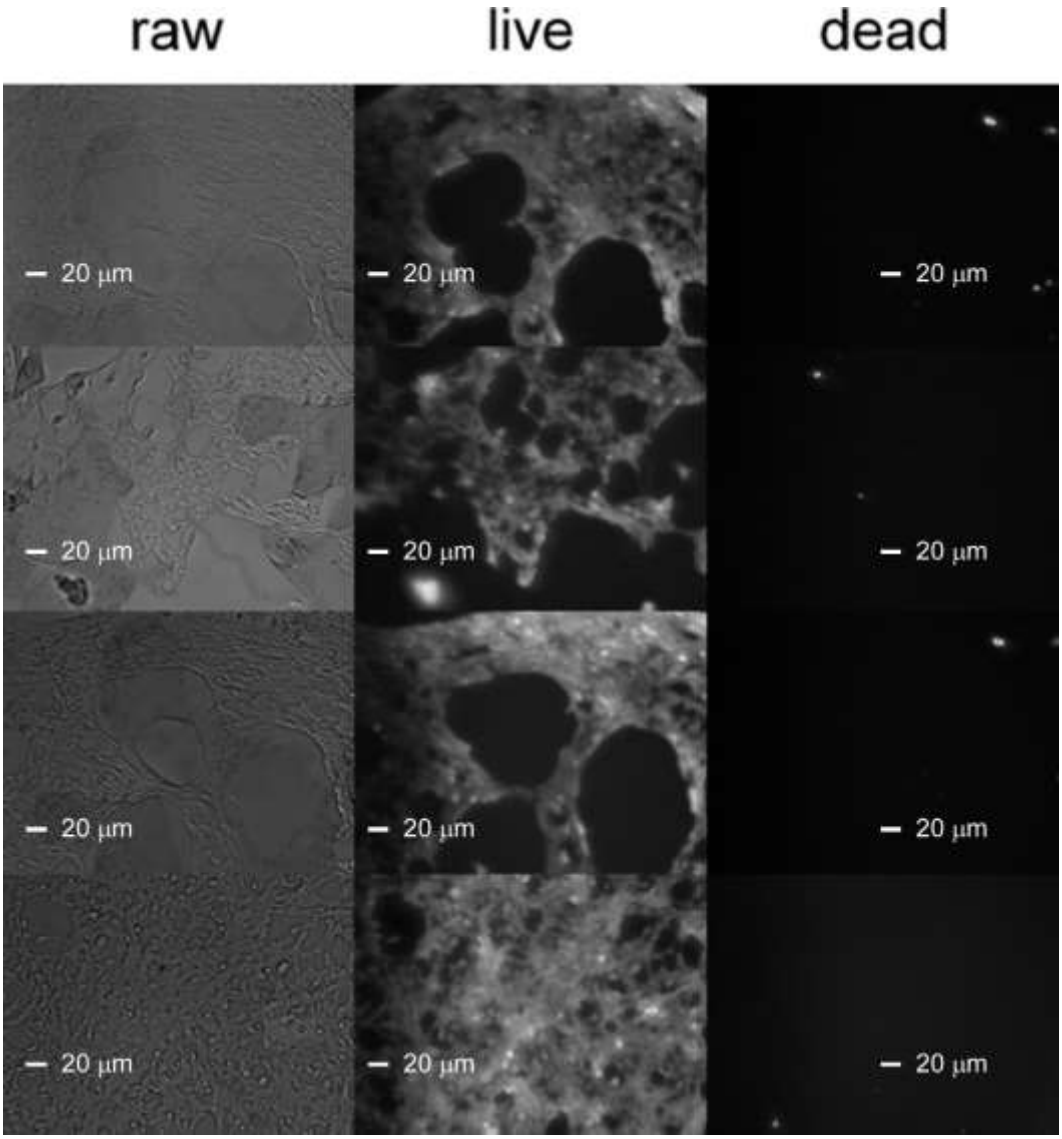

HEK293f cells exposed to CVD molybdenum disulfide for 48 hours and stained for cell viability

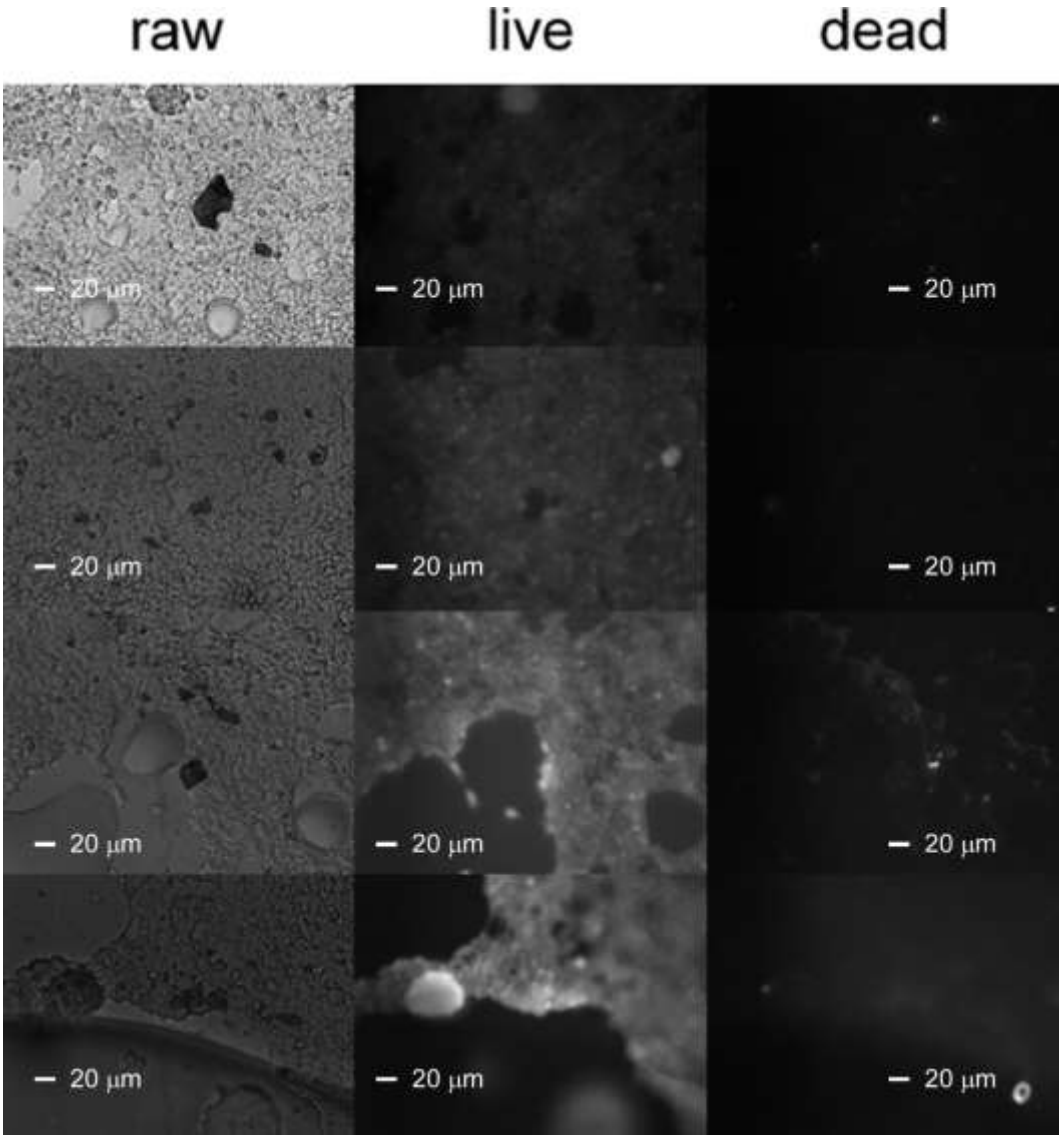

HEK293f cells exposed to mechanically exfoliated tungsten disulfide for 48 hours and stained for cell viability

APPENDIX J

REACTIVE OXYGEN SPECIES GENERATION ASSAY OF 2D TRANSITION METAL DICHALCOGINIDES BIOCOMPATIBILITY

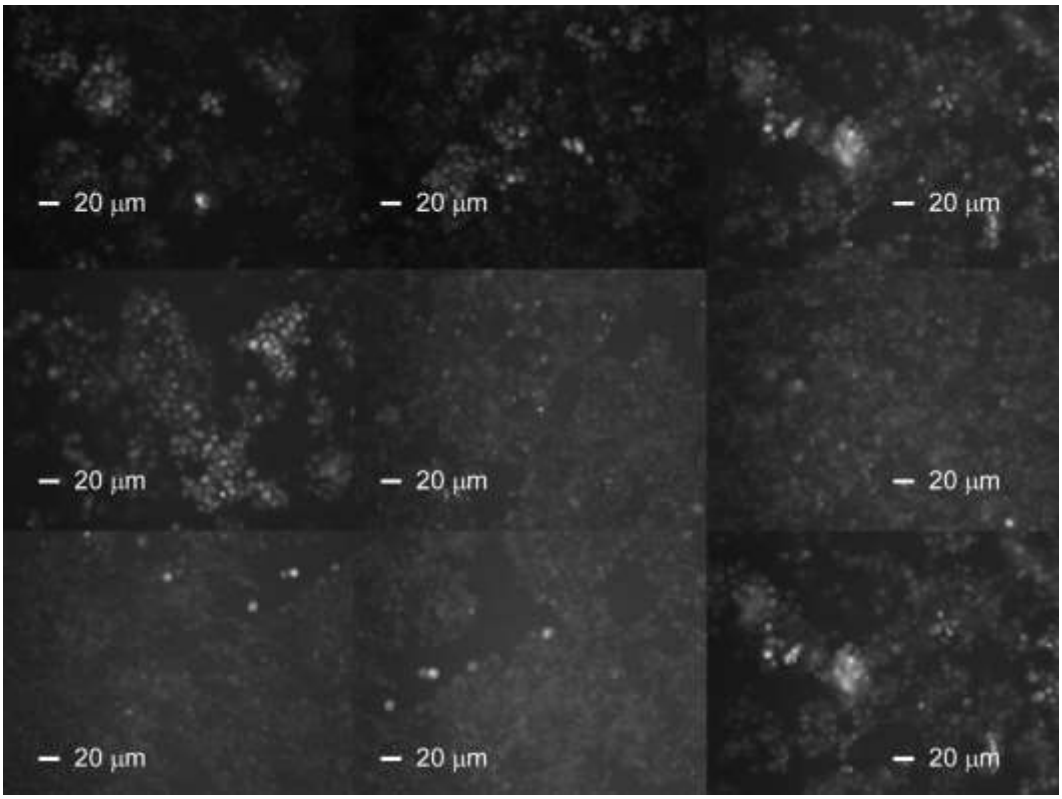

HEK293f cells exposed to copper for 48 hours and stained for reactive oxygen species formation

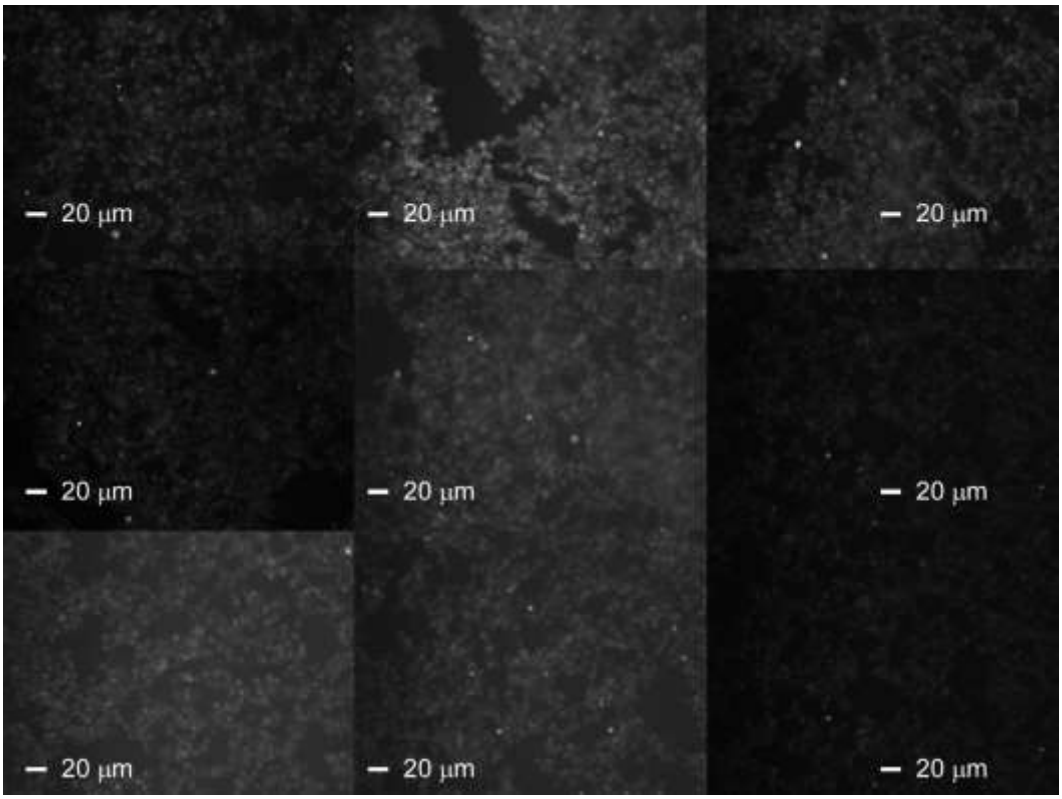

HEK293f cells untreated for 48 hours and stained for reactive oxygen species formation

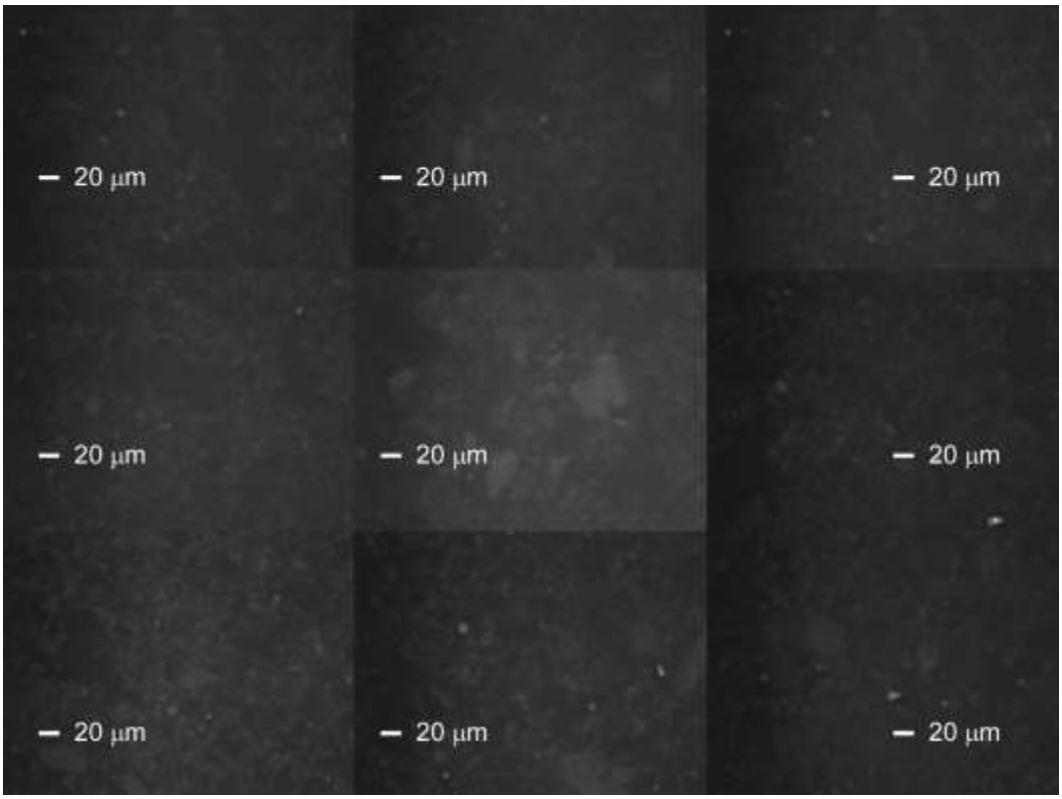

HEK293f cells exposed to mechanically exfoliated molybdenum disulfide at a concentration of 100 µg/mL for 48 hours and stained for reactive oxygen species formation

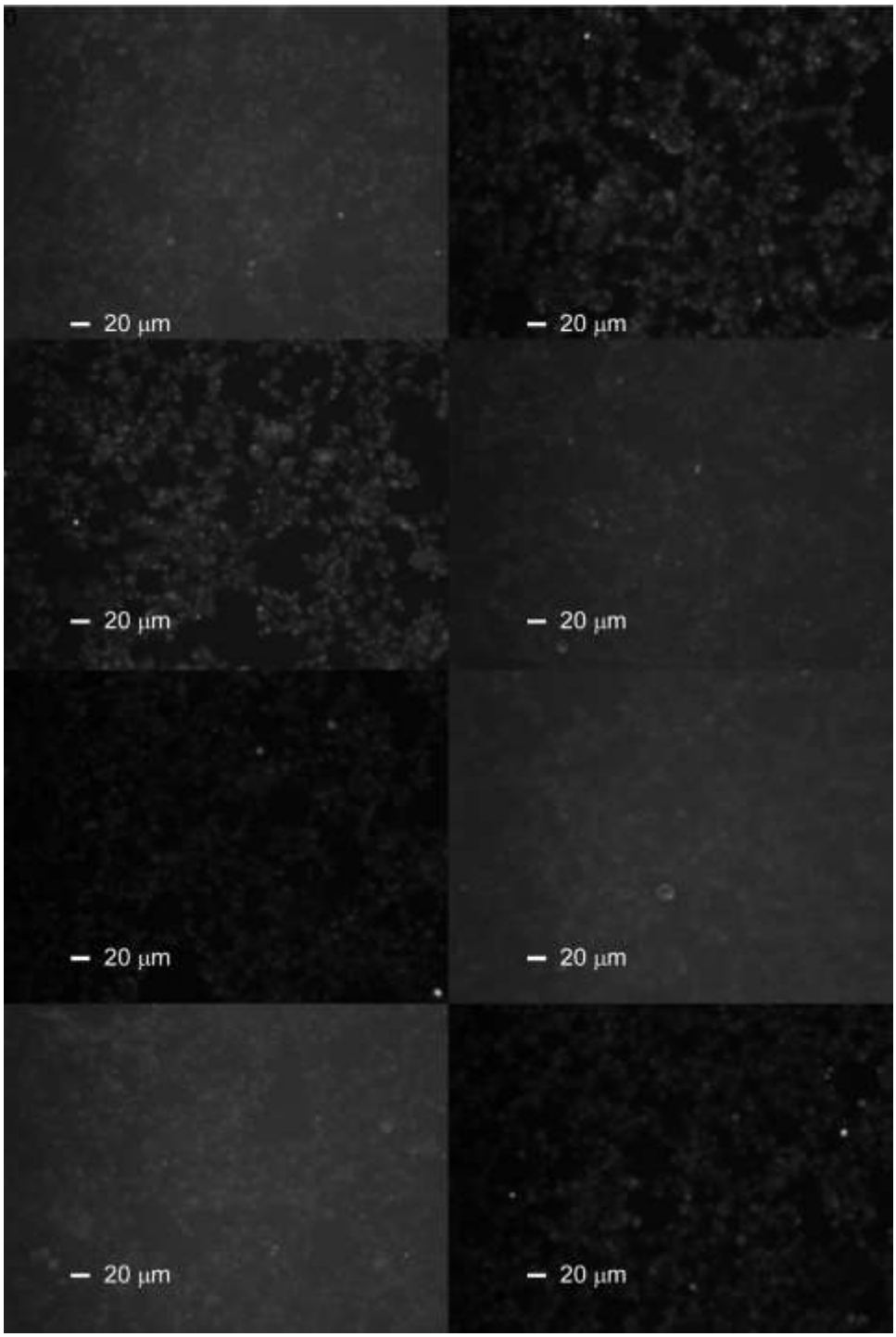

HEK293f cells exposed to mechanically exfoliated molybdenum disulfide at a concentration of 10 μg/mL for 48 hours and stained for reactive oxygen species formation

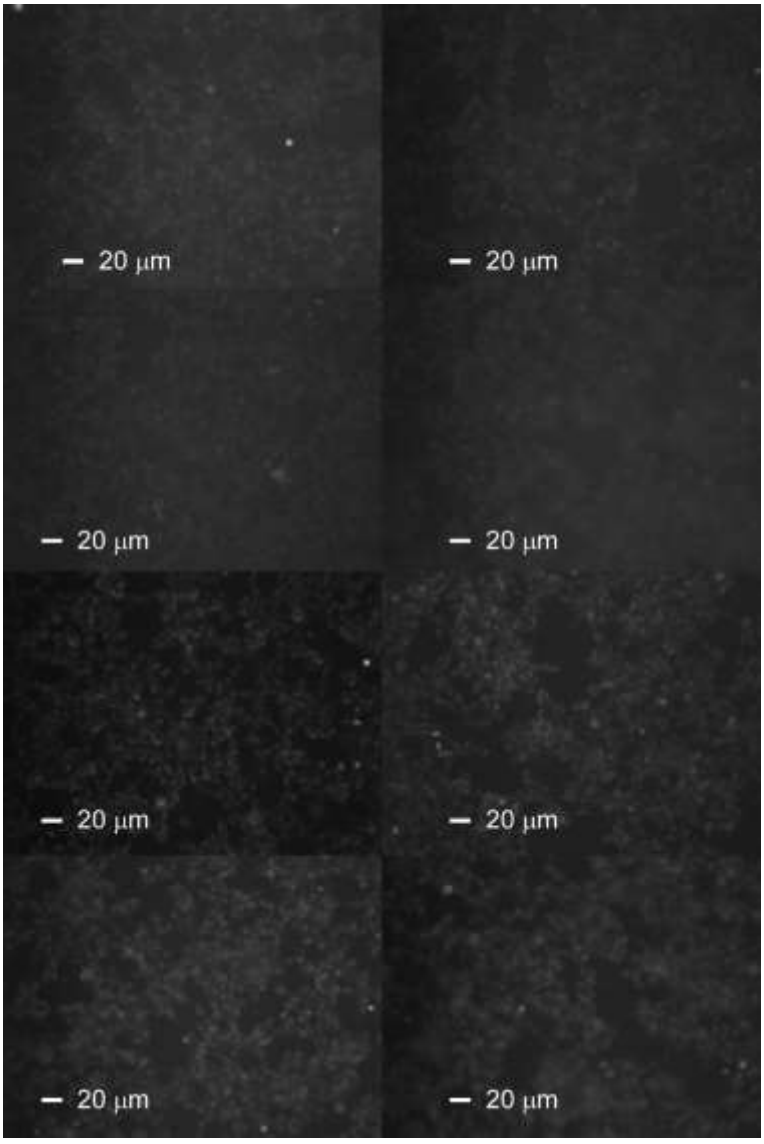

HEK293f cells exposed to mechanically exfoliated molybdenum disulfide at a concentration of 1 μg/mL for 48 hours and stained for reactive oxygen species formation

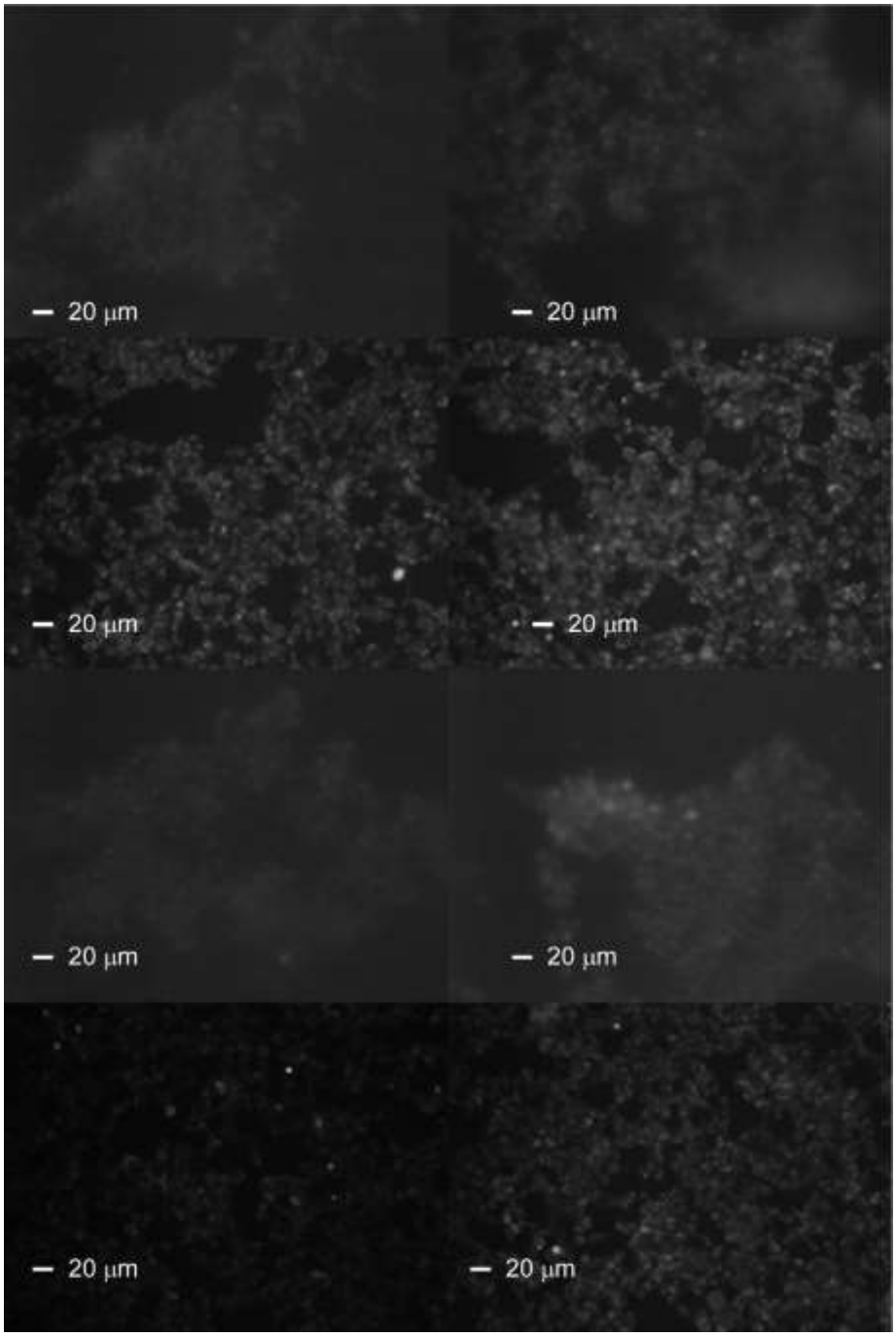

HEK293f cells exposed to mechanically exfoliated molybdenum disulfide at a concentration of 0.1 µg/mL for 48 hours and stained for reactive oxygen species formation